Development of Heusler-alloy-based Current-Perpendicular-to-Plane Giant Magnetoresistive Devices

Jiamin CHEN

November 2017

Development of Heusler-alloy-based Current-Perpendicular-to-Plane Giant Magnetoresistive Devices

Jiamin CHEN

Doctoral Program in Materials Science and Engineering

Submitted to the Graduate School of
Pure and Applied Sciences
in Partial Fulfilment of the Requirements
for the Degree of Doctor of Philosophy in
Engineering
at the
University of Tsukuba

TABLE OF CONTENTS

Chapter 1 Introduction

1.1 Spintronics

Spintronics is an exciting and rapidly developing new field, which is differs from traditional electronics, based on the fact that electrons have a further degree of freedom of spin as well as charge. In the past few decades, Moore's law has led the information technology (IT) industry, which the number of transistors on a chip doubles about every 2 years, but there will be a limit in conventional solid state electronics due to the increasing heat dissipation challenges of charge current and quantum size effects in small devices. The scale of the complementary metal-oxide semiconductor (CMOS) logic has been repeatedly miniaturized since its introduction in 1982. The semiconductor industry follows a roadmap. The minimum feature size in silicon circuits was 45 nm in 2008, and it is further decrease to 22 nm in 2011. The 14 nm technology is projected to be reached by semiconductor companies in 2014.[1] However, the new update Roadmap to the International Technology for Semiconductors predicted that the speed of this growth will slow down at the end of 2013, when transistor number and densities are to double only every three years. [2] It is unclear that what will take over at the end of the roadmap, when feature sizes of less than 10 nm will make CMOS impractical. In order to sidestep this limitation, researchers in the recent years have moved their interest to the field of *spintronic*. In the field of spintronics, the electrons are manipulated as spin not just their electrical charge within electronic circuits. These spintronic devices, taking advantage of the extra degree of freedom offered by magnetic materials, are expected to be versatile, fast, nonvolatile, low energy consumption and capable of data storage and processing. They are playing a gradually significant role in the development of high density data storage, magnetic sensors, quantum computing, microelectronics, biomedical applications, and so on. [3]

The discovery of the giant magnetoresistive effect (GMR) in 1988 is considered as the beginning of the new spin-based electronics. Today, spintronic devices are everywhere as you can find them on the desktop as the write and read head of most hard disk storage devices. Write heads are electromagnets making from thin film, while read heads are usually giant magnetoresistance (GMR) or tunnelling magnetoresistance (TMR) spin-valves.[4] The resistance change in these two MR phenomena originates from the parallel and anti-parallel magnetization configurations that result in different electric spin-dependent scattering in the multilayer hetero-structure. In fact, a TMR read head was commercialized by Seagate in 2005. Since then, it had been used as read head senor in hard disk drive to provide a higher sensitivity. Unfortunately, TMR may prove to be a short-lived option, because TMR have an intrinsic high resistance due to the usage of insulator barrier (typically resistance – area products above 1 $\Omega \cdot cm^2$), and with further downscaling it will become difficult to maintain a high signal-to-noise ratio with an rapid increase of sensor resistance. On the other hand, Current-perpendicular-to –plane giant magnetoresistance (CPP-GMR) is showing promising future due to its intrinsic low resistance by using metallic spacer.

1.2 Giant magnetoresistance (GMR) effect

1.2.1 History and background of GMR

Giant magnetoresistance (GMR) is a quantum mechanical effect of magnetoresistance, which can be observed in magnetic multilayered with a structures of alternating ferromagnetic and non-magnetic layer. It was discovered independently by the groups of Albert Fert from France, and Peter Grünberg from Germany. Their discovery, which triggered the development of the spin-valve sensor in the several decades that followed, was awarded the Nobel Prize in physics in 2007. The fundamental of GMR is the spin dependent scattering effects. It was first proposed to explain the anomalous resistivity tendency shown in bulk ferromagnetic materials with impurities dopant by Mott.[5] The "two-channel model", which regards spin up and down electrons as two different conduction channels, is developed to help people understand physics behind. In this model, spin-flip scattering between two channels is neglected to simply the model. Using this model, physics of GMR can be quantified and connection between magnetic properties and electrical transport can be understood. From then on, research interest on spin dependent scattering drastically increases, and some pioneering studies were performed by Fert and Campbell.[6] Since then, the discovery of the GMR effect opened a new door of exploring magnetic materials by means of spin-dependent transportation and generated a new field, which combine two conventional fields of magnetism and electronics together, named spintronics.

1.2.2 Classical experimental result

In 1986, the first study about antiferromagnetic interlayer exchange coupling in the Fe/Cr/Fe trilayers was reported by Grünberg et al.[7] Thereafter, they observed an improvement of MR up to 1.5% at room

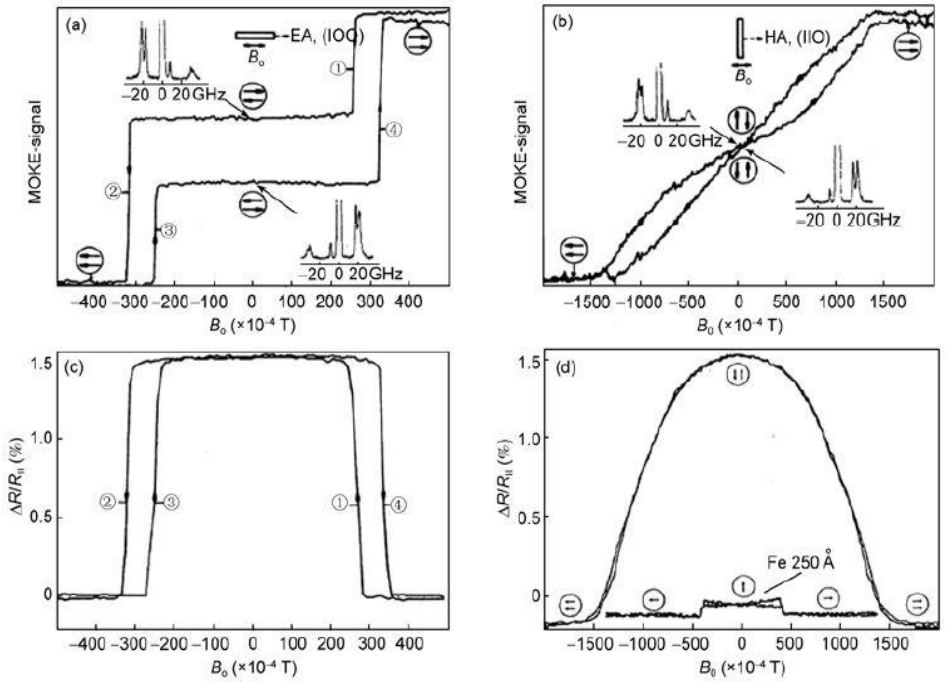

Fig. 1-1 GMR measurement in the Fe/Cr/Fe trilayers by the group of Peter Grünberg. [7]

temperature in the Fe/Cr/Fe trilayers (see **Fig. 1-1**). Two years later, Baibich et al.[8] also obtained a huge MR of ~ 50% at low temperature in Fe/Cr magnetic super lattices fabricated by molecular beam epitaxy (MBE) independently (**Fig. 1-2**). Their result indicated the spin-dependent transmission of the conduction electrons between Fe and Cr layers. In this paper, they observed not only huge GMR, but also pointed out promising future applications with this new spin-dependent phenomenon.

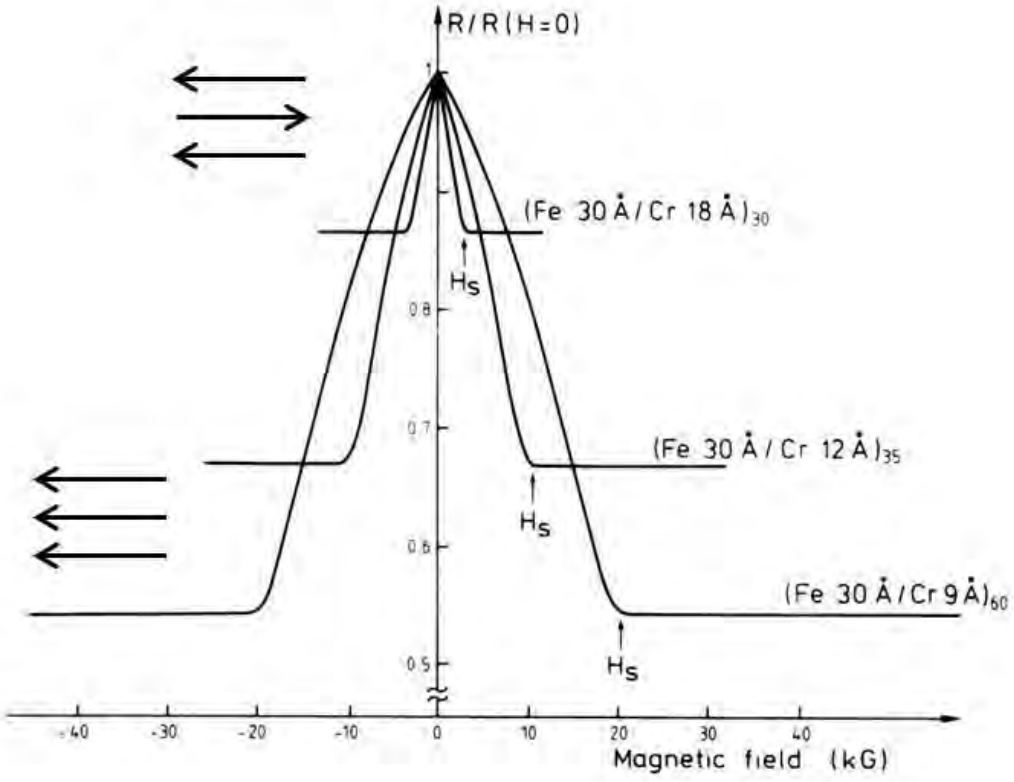

Fig. 1-2 Magnetoresistance of three Fe/Cr superlattice at 4.2 K. Courtesy of M. N. Baibich etc. [8]

A significant progress in the exploration of the GMR was reported by Parkin *et al*. They observed both the magnetoresistance and exchange coupling strength oscillate with non-magnetic interlayer thickness in metallic multilayers structure prepared by magnetron sputtering. As shown in **Fig. 1-3**, the oscillation could be observed even at room temperature.[9] The spin polarization oscillations in the Cu layers of Fe/Cu multilayers was directly observed by Jin Q Y *et al.* using nuclear magnetic resonance measurement.[10] Thereafter, GMR oscillation of interlayer coupling in multilayers with different materials, such as Co-Nb/Pd[11], Fe/Ag[12], Fe/Pd[13], Fe/Mo[14] and (Co-Ag)/Ag[15], have been widely explored. Among them, Co/Cu system is of special interest because of small lattice mismatch between Co and Cu. Small lattice mismatch is beneficial for low dislocation density at the interface. Thereafter, progresses keep reporting in this area. For instance, GMR greater than 65% has been obtained in Co/Cu multilayers at room temperature.[16] The substantially large room temperature GMR effects and the convenient thin film preparation technique have made GMR devices coming close to commercial application.

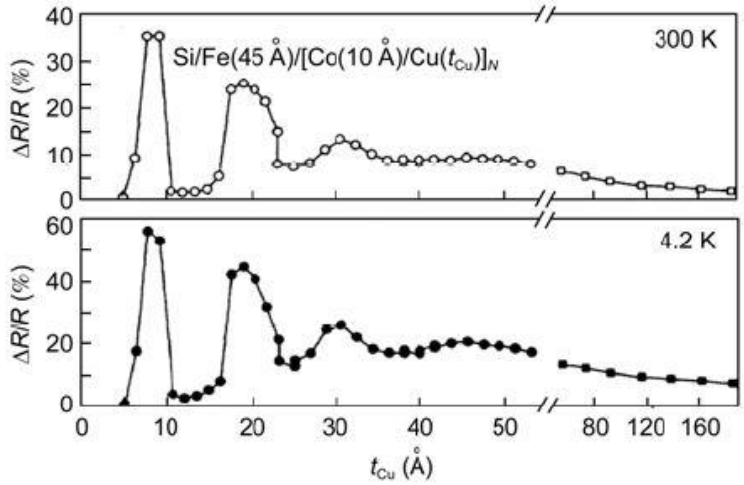

Fig. 1-3 Saturation MR ratio versus the Cu interlayer thickness for Si/Fe(45 Å)/[Co(10 Å)/Cu(t_{Cu})]$_N$ superlattices. N=16 for t_{Cu} below 55 Å and N=8 for t_{Cu} above 55 Å. [9]

1.2.3 Theoretical models

As mentioned previously, the GMR can be explained qualitatively using the "two current model" proposed by Mott.[17] In this model, there are two important assumptions: (1) conductivity in metals can be described with two independent parallel connection channels of spin-up and spin-down electrons, respectively. (2) scattering rates of the spin-up and spin-down electrons in ferromagnetic metals are very different, which means there is spin-dependent scattering. The so-called giant magnetoresistance (GMR) ratio is defined as the following simple equation:

$$MR\ ratio = \frac{\Delta R}{R_p} = \frac{R_{ap} - R_p}{R_p} \times 100\%$$

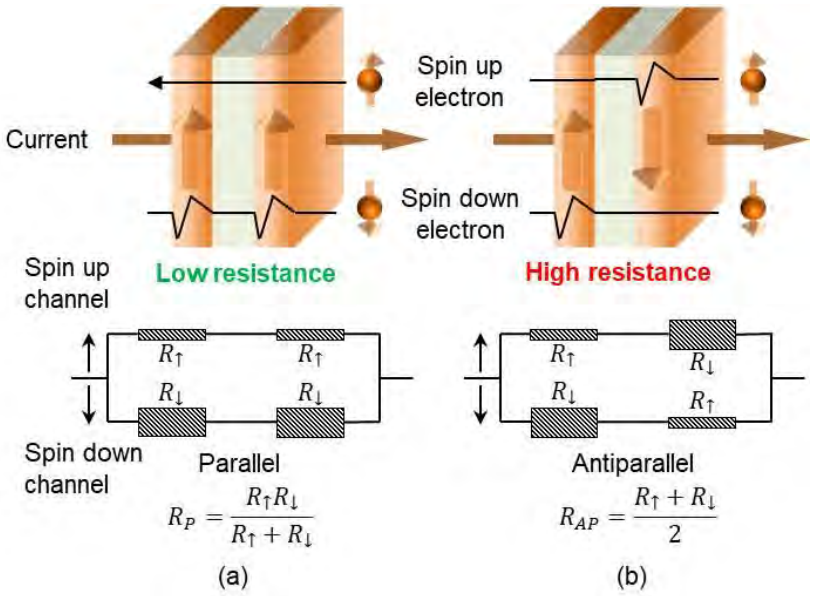

Fig. 1-4 Schematic of the two current series resistor model for GMR. (a) For the parallel state (b) For the antiparallel state.

Where R_{ap} represents the resistance of the multilayer in zero-field, and R_p represents the resistance of multilayer in a large saturation magnetic field. The origin of this magnetoresistance behaviour was later confirmed to originate from the difference of electron scattering asymmetry between the parallel and anti-parallel magnetization arrangement of the alternate ferromagnetic Fe layers. One simplified explanation of this phenomenon is showed in **Fig. 1-4**. Considering only the bulk scattering in ferromagnetic layers, the symbols $R_\uparrow$ and $R_\downarrow$ are the resistance of the ferromagnetic layers for the up and down spin electrons, arrows and stripes are the symbols for the magnetization and ferromagnetic layers, respectively. For the case of the anti-parallel state shown in **right panel**, the resistance of both the spin up channel and the spin down channel equals $(R_\uparrow + R_\downarrow)/2$, therefore the total resistance is given by

$$R_{ap} = (R_\uparrow + R_\downarrow)/4$$

while for the case of parallel state shown in **left panel**, the resistance of the up and down spin channels are in parallel connection, and the resistance is given by

$$R_p = (R_\uparrow^{-1} + R_\downarrow^{-1})^{-1} = \frac{R_\uparrow \cdot R_\downarrow}{R_\uparrow + R_\downarrow}$$

and the magnetoresistance can be expressed as following:

$$MR\ ratio = \frac{R_{ap} - R_p}{R_p} \times 100\% = \frac{(R_\uparrow - R_\downarrow)^2}{4R_\uparrow R_\downarrow} = \frac{(\rho_\downarrow - \rho_\uparrow)^2}{4\rho_\uparrow \rho_\downarrow}$$

where the resistivity of the up and down spin electrons, namely $\rho_\uparrow$ and $\rho_\downarrow$, is different in ferromagnetic materials. This two current series resistor model can not only explain GMR effect qualitatively, but also indicate the relation between magnetoresistance and scattering asymmetry. But this model appears to be too simple to analyse CIP-GMR in magnetic multilayer and spin-valve structure due to the limit of assuming mean free path of spin up and spin down electron are both larger than the thickness of each layer.

Apart from the two current series resistor model, researchers have proposed a lot of other theoretical models to investigate underlying physics of GMR effect. The main difference in these models is how to handle band structure of electron and how to deal with the electron transportation equation. Two principle approaches to handle band structure of electron are free electron approximation, which has a merit of great simplification of calculation while capturing the main feature of GMR effect, and accurate multiple band structure approximation, which are useful for quantitative analysis of GMR effect. To deal with electron transportation equation, semi-classical Boltzmann theory and quantum mechanics theory are mainly introduced. Boltzmann theory has been widely used but it cannot be applied especially when lift-time broadening effect coming from scattering and band splitting effect have similar contribution in the magnetic multilayer. On the other hand, quantum mechanics theory combined with accurate multiple band structure approximation becomes an effective method to treat electron transportation equation.[18] Following is a brief introduction of research progress mentioned above.

Camley *et al.*[19] first theoretically investigate the mechanism of GMR effect in multilayer system with antiferromagnetic coupling. They introduced spin dependent interfacial scattering into classical Boltzmann transportation equation and found GMR is strongly related to mean free path of electron, thickness of thin

film and scattering asymmetry for spin up and spin down electron. Later on, they further introduced bulk scattering into the previous model,[20] and found interfacial spin scattering mainly contribute to the GMR in Fe/Cr system while bulk spin scattering mainly contribute to the GMR in permalloy system. As shown in **Fig. 1-5**, Sheng *et al.* [21] successfully explained why multilayer structure can improve GMR effect in $(Fe/Cr)_n/Fe$ system by using path-integral method, which considered interfacial effect in Boltzmann transportation equation. Valet and Fert [22] proposed a semi-classical theoretical model based on free electron Boltzmann transportation equation, which is suitable for CPP configuration. This model can successfully distinguish contribution from bulk and interfacial spin scattering asymmetry but cannot describe electron band structure and quantum effect when mean free path is approximate to the layer dimension. Levy *et al.*[23] firstly presented a quantum model based on free electron, which took use of Kubo linear response theory. Camblong *et al.*[24] further gave out new method to treat interfacial scattering based on same model but using real space approach instead of local approximation. Vedyayev *et al.*[25] obtained similar result in the spin-valve structure.

Beside the theoretical model based on free electron mentioned above, single-band tight-binding model is another effective method to describe electron structure. Asano *et al.*[26] firstly use single band s-valent tight binding model to investigate the effect of interface roughness and bulk disorder on CIP-GMR and CPP-GMR effect. Thereafter, Itoh *et al.*[27] introduced single-cell coherent potential approximation to single-band tight-binding model, and explored the physical origin difference of CIP-GMR and CPP-GMR effect. To further study Ohmic resistivity and GMR effect, Todorov *et al.*[28] introduced real space Green function to depict scattering more accurately. In addition to that, Li *et al.*[29] successfully explained the oscillation behaviour against the nonmagnetic spacer thickness by considering contribution of band density of state in transition group and s-d scatter matrix to GMR effect.

Free electron model and sing-band tight-binding model both use approximation method to describe electron structure in the ferromagnetic multilayer. They both neglect the effect of ferromagnetic d band or sp-d coupling on electron transport, which are both significant to ferromagnetism and GMR. In order to obtain more intrinsic parameters of GMR effect theoretically, more accurate method needs to be developed to characterize electron structure in material system. Schep *et al.*[30] calculated a GMR of 120% based on the local spin density approximation method deliberating transport contribution of s and d electron. They also pointed out that the coupling of s and d electron will degrade conductivity of s conduction electron, leading to the fact that s electron will be trapped due to the existence of spin-dependent interfacial barrier. This model mainly suitable for system in which dimension shorter than electron mean free path (ballistic transport) and scattering from defect is neglected.

The first principle calculation integrated with quantum mechanics transport theory is the most powerful method to investigate electron transportation and GMR effect so far. This method can not only consider charge and spin transfer effect at the interface by using self-consistent method to describe electron band structure, but also build up reliable transport model based on quantum mechanics transport theory. Butler *et al.*[31,32] firstly reported the first principle calculation model which suitable for both CIP-GMR and spin-valve

structure. Blaas *et al.*[33] included spin orbital coupling into their calculation model and successfully deduced resistivity without introducing extra parameters by considering contribution of both electron band structure and impurity states in spin-dependent scattering to GMR effect. Nevertheless, how to accurate describe magnetic disorder, spin orbital coupling and real electron band structure in the material are still big issues to be overcome to let us have a deeper understanding of the underlying physics of GMR effect.

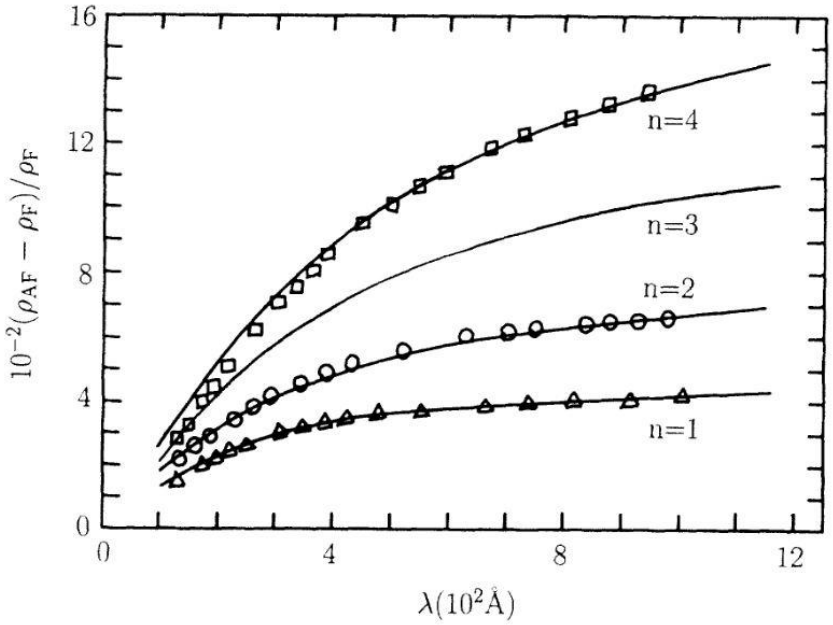

Fig. 1-5 MR ratio in epitaxial $(Fe/Cr)_n/Fe$ multilayer for experimental(points) and theoretical(lines). [21]

1.2.4 Current-perpendicular-to-plane giant magnetoresistance (CPP-GMR)

The GMR effect was originally discovered in a current-in-plane (CIP) configuration; however an even larger effect is found for the current-perpendicular-to-plane (CPP) configuration. The intrinsic larger MR output in CPP-GMR is mainly coming from the different mechanism of the current flow in the layer structure.

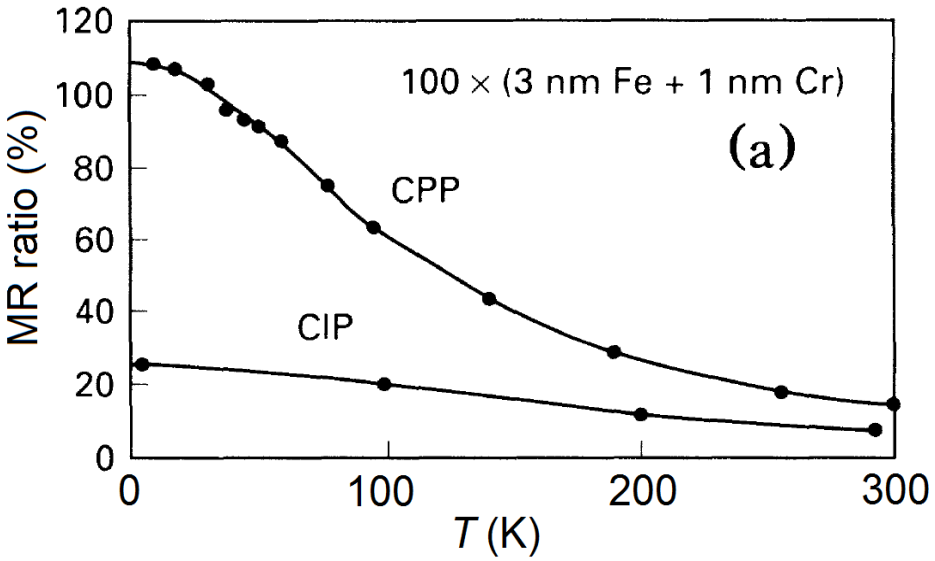

Fig. 1-6 Temperature dependence of GMR ratio in CPP and CIP geometry for Fe/Cr multilayer structure. [36]

In CIP geometry, the current is prone to flow in the spacer layer because spacer has relative lower resistivity than that of the magnetic layer. While for the CPP case, the current is expected to flow uniformly through the F/N/F layer, if the cross-section current path is sufficiently small, thus the spin-dependent scattering both in bulk and at the interface could be utilized more efficiently. The larger MR ratio for the CPP-GMR than that of the CIP-GMR has been experimentally demonstrated in Co/Ag multilayer by Pratt, Jr. *et al*[35] and in Fe/Cr multilayer by Gijs *et al*[36], as shown in **Fig. 1-6**.

Here the mechanism of CPP-GMR will be briefly discussed. A main difference between CPP-GMR and CIP-GMR is the existence of so-called spin accumulation effect in CPP configuration. Because of the spin-asymmetry of the electric resistivity in ferromagnetic layer, one spin electron is more than the other spin electron in a spin-polarized ferromagnetic material ($\rho_\uparrow < \rho_\downarrow$ or $\rho_\uparrow > \rho_\downarrow$). However, in nonmagnetic materials, they are the same ($\rho_\uparrow = \rho_\downarrow$). With the assumption of no spin-flipping at the interface between ferromagnetic and nonmagnetic material, the current including both up and down spins electrons should be continued at the interface. Therefore, there will be a deviation of the electronic chemical potential near the interface, resulting in spin accumulation. Such spin accumulation generates a voltage drop at the F/N interface. Depending on the magnetization configuration of F/N/F tri-layer, the resistance change can be observed from the parallel (P) to antiparallel (AP) state and vice versa.

By using a two current series resistance model established by Mott, we obtain the resistance-change area product ΔRA roughly expressed as follows:

$$\Delta RA \sim 2\frac{\beta^2}{1-\beta^2}\rho_F + 2\frac{\gamma^2}{1-\gamma^2}AR_{F/N}$$

where β and γ are the spin scattering asymmetries in bulk F metals and at the F/N interface defined by

$$\beta = \frac{\rho_\downarrow - \rho_\uparrow}{\rho_\downarrow + \rho_\uparrow}$$

$$\gamma = \frac{AR_{F/N\downarrow} - AR_{F/N\uparrow}}{AR_{F/N\downarrow} + AR_{F/N\uparrow}}$$

in which $\rho_\downarrow$ and $\rho_\uparrow$ are the resistivity of the down and up spins, and ρ_F and $AR_{F/N}$ are the resistivity of the F layer and the interfacial resistance-area product. Due to the fact that β and γ are in the denominators of the formula for the ΔRA expression, β and γ have to be as large as possible in order to attain the largest ΔRA value. From this perspective, F/N interface with large γ and materials with high spin polarization (β) such as Heusler alloy should be beneficial to increase the CPP-GMR ratio.

1.3 Co-based Heusler alloy

1.3.1 Introduction

The discovery of Heusler alloys can be traced back to 1903. At that time, A. Heusler firstly found that adding sp elements (Al, In, Sn, Sb or Bi) into a Cu-Mn alloy can turn it into a ferromagnetic material, although there is no ferromagnetic element in this alloy.[37] After this discovery, the basic understanding composition and crystal structure of these alloys remained unknown for a long time until 1929, when Potter

et al.[38] reported a study on a Cu-Mn-Al alloy by X-ray measurement to reveal that this system were ordered in a fcc lattice. Bradley *et al* .[39] further investigated the Cu-Mn-Al system specifically using X-ray and anomalous X-ray scattering, from which a relationship between composition, magnetic properties and chemical order was established. After this study, an interpretation of the crystal structure was successfully presented. Thereafter, numerous researches followed up these systems. Heusler alloys attracted a lot of research interests due to the theoretically predicted half metallic property, in which majority spin band shows typical metallic behaviour while minority spin band exhibits a gap at the Fermi level. In other word, spin polarization at Fermi level can be 100%. The first Heusler alloy was found with a $L2_1$ structure consisting four fcc sublattices. Later on, it was also discovered that $C1_b$ structure could be obtained by leaving one of the four sublattices unoccupied. The $L2_1$ structure compounds are often named full-Heusler alloys while the $C1_b$ structure compounds are referred to half- or semi-Heusler alloys. Among the huge Heusler alloys family, Co-based Heusler alloy, where Co occupies X site in the crystal structure as shown in **Fig. 1-7**, is showing promising future due to their relatively high Curie temperature and high spin polarization.

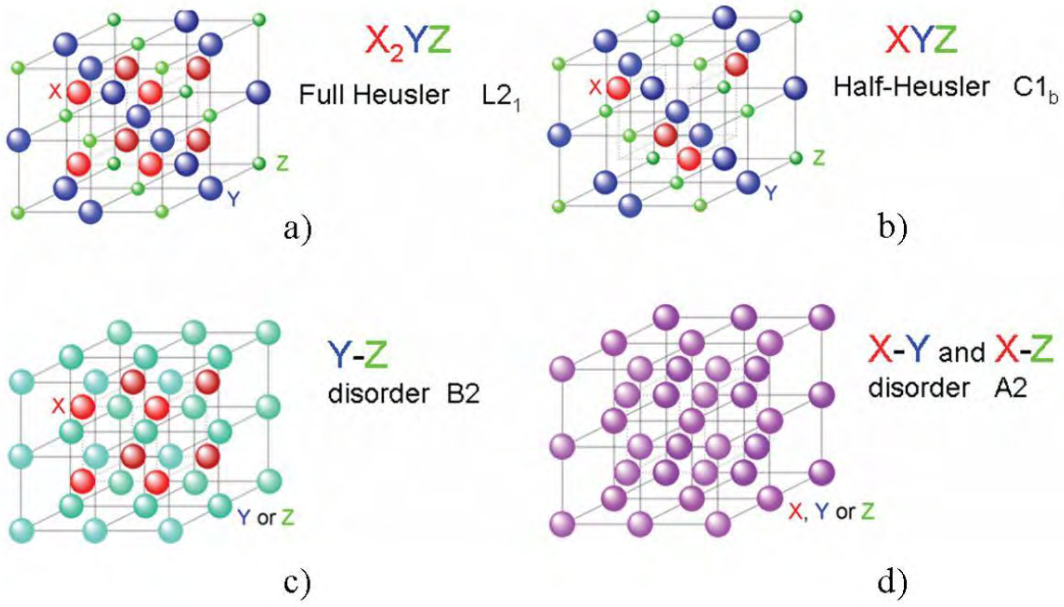

Fig. 1-7 (a) $L2_1$ ordered structure full-Heusler, (b) $C1_b$ ordered structures half-Heusler. (c) B2 disorder due to the Y-Z randomly occupied and (d) A2 disorder caused by the X-Z or X-Y intermixing.

1.3.2 Crystal structure

Heusler alloys are mainly assorted with full Heusler alloys (X_2YZ) and half Heusler alloys (XYZ) crystallize in $L2_1$ and $C1_b$ structures (see **Fig. 1-7**). One unit cell normally consists of four interpenetrating fcc sublattices, in which X occupies the positions of (000) and (1/2, 1/2, 1/2), Y occupies the positions of (1/4, 1/4, 1/4) and Z occupies the positions of (3/4, 3/4, 3/4). For half Heusler compounds, the site (1/2, 1/2, 1/2) is vacant. The structure factors are:

$$F_{L21} = |4(f_X - f_Z)| \qquad \text{for } L2_1 \text{ structure } (h, k, l \text{ odd})$$

$F_{B2} = |4(2f_X - f_Y - f_Z)|$ for B2 superlattice (h, k, l even, $h + k + l = 4n + 2$)

$F_{fund} = |4(2f_X + f_Y + f_Z)|$ for A2 structure (h, k, l even, $h + k + l = 4n$)

in which f is the atomic factor and n is an integer. The highly chemically-ordered $L2_1$ structure degrades to B2 ordered structure by mixing the elements Y and Z, and the B2 structure degrades to disordered A2 structure by further mixing the X and Y (Z) elements.

1.3.3 Half-metallic

The concept of half-metallic property was first introduced by Groot *et al.* [40], originated from band structure calculations of NiMnSb and PtMnSb half Heusler alloys. In these kinds of materials one of the spin sub-bands (usually majority spin band) presents metallic behaviour, whereas the other sub-band forms a gap at the Fermi level (see **Fig. 1-8**). Not only half Heusler alloy, full-Heusler alloys of the type Co_2MnZ, (Z=Si,Ge) were also proposed to be half-metal by Ishida *et al.*.[34]

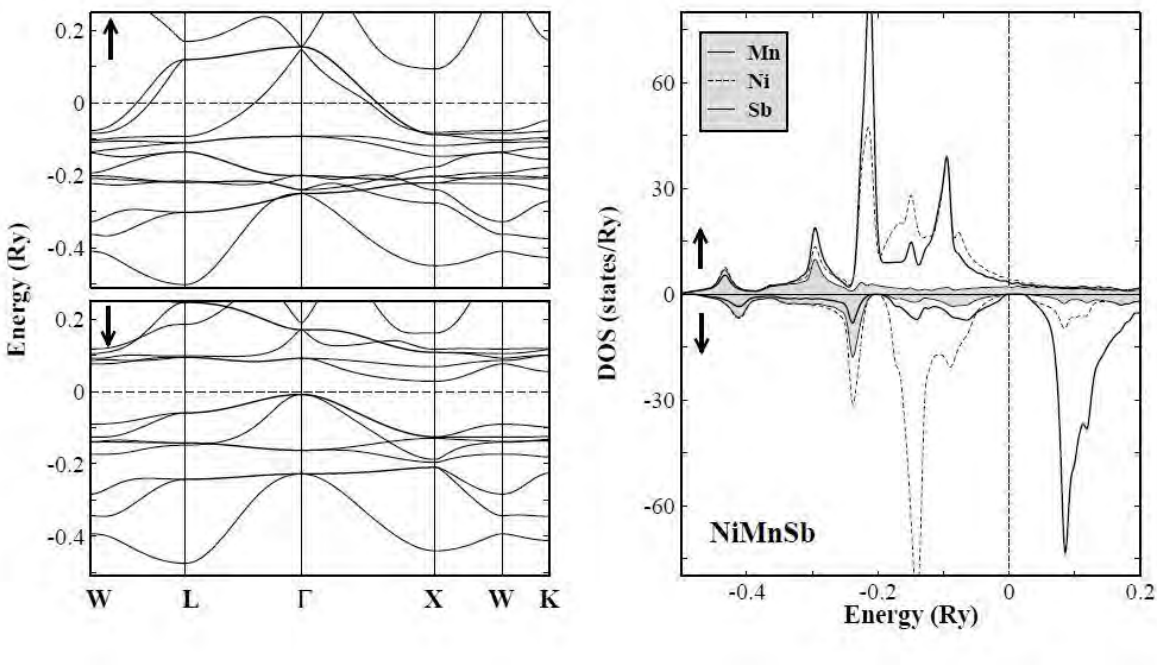

Fig. 1-8 In the left, band structure of half-metallic in ferromagnet NiMnSb. The dashed line represents the Fermi level. In the right, atom-resolved density of states (DOS) of NiMnSb. The DOS of Sb is shown with shaded color. [40]

1.3.4 Order-Disorder transformation

Heusler alloys have order-disorder transformations below the melting points during annealing process. The $L2_1$ structure can be achieved by two steps: A2→B2→$L2_1$ with increasing annealing temperature as shown in **Fig. 1-7**. Webster[41] studied the chemical ordering of the Co_2MnAl Heusler alloy using a high

temperature x-ray diffractometer. **Fig. 1-9** shows the (111) $L2_1$ and (200) B2 diffraction peaks of the Co_2MnAl alloy as a function of temperature. The $L2_1$ super lattice peak disappears at around 1000 K, signifying the $L2_1$-B2 transformation. Similarly, the B2-A2 transformation appears at 1250 K. A more recent result of the order-disorder transformation for the Co-based Heusler alloy is shown in **Fig. 1-10**, Varaprasad *et al*[42] studied the differential thermal analysis (DTA) of the as-solidified $Co_2Fe(Ga_xGe_{1-x})$ Heusler alloys for x=0, 0.5 and 1. The DTA curves exhibit three endothermic peaks from 800 to 1600 K as indicated by arrows. The first weak endotherms represent the Curie temperature when ferromagnetic-to-paramagnetic transition occurs. The second peak observed from $Co_2Fe(Ga_{0.5}Ge_{0.5})$ is originated from the $L2_1 \leftrightarrow$ B2 structural transformation. The third endotherm is the melting point of the alloy.

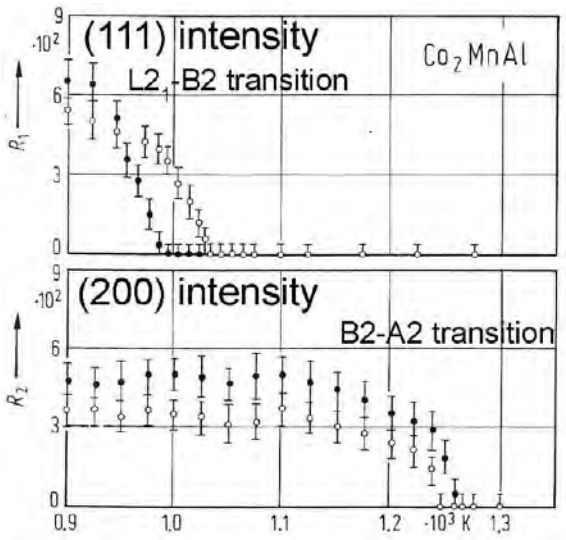

Fig. 1-9 Temperature dependence of (111) $L2_1$ and (200) B2 diffraction peak for Cu_2MnAl. Courtesy of Webster. [41]

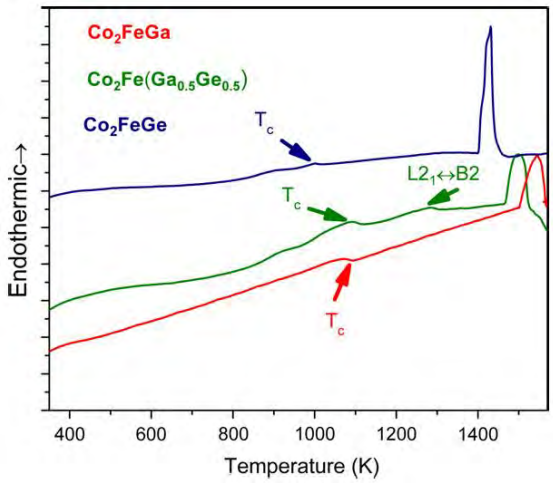

Fig. 1-10 DTA curves of $Co_2Fe(Ga_xGe_{1-x})$ (x=0, 0.5 and 1) bulk alloys.[42]

When the film was fabricated at the as-deposit state, they often exhibit disordered A2 or imperfect B2 structure, therefore heat treatment, namely annealing, is necessary to attain better ordering in Heusler alloys.

The Co_2MnSi alloy is regarded one of the best alloys for CPP-GMR devices due to the realization of $L2_1$ ordering at relatively low temperature of around 400°C.[43] On the other hand, the Co_2Fe-based alloys $Co_2Fe(Al_{0.5}Si_{0.5})$ and $Co_2Fe(Ga_{0.5}Ge_{0.5})$ are nominal for their high thermal stability that the best CPP-GMR output is achieved at annealing temperature of more than 500°C.[44,45] Thus the investigation on both the Co_2Mn-based and Co_2Fe-based alloys is necessary since we want to improve their chemical ordering as well as thermal stability.

1.3.5 Slater-Pauling behaviour

The total moment follows the rule $M_t = Z_t - 18(\text{for half})$ and $M_t = Z_t - 24(\text{for full})$ in the half- and full-Heusler alloys, where Z_t is the total number of valence electrons.[46] Z_t is given by the sum of spin-up and spin-down electrons as shown in equation: $Z_t = N_\uparrow + N_\downarrow$. And the total moment M_t is given by the subtraction of $M_t = N_\uparrow - N_\downarrow$. Since 9 minority bands in half Heusler alloys and 12 minority bands in full Heusler alloys are fully occupied, equation of $M_t = Z_t - 18(\text{for half})$ and $M_t = Z_t - 24(\text{for full})$ can be obtained. This equation is the well-known Slater-Pauling behaviour. In **Fig. 1-11**, the calculated total spin magnetic moments for both half and full Heusler alloys versus the total number of valence electrons are plotted. The rule of $M_t = Z_t - 18(M_t = Z_t - 24)$ fulfilled by these compounds are shown by the dash line. The total moment M_t is an integer quantity with the assumption of $Z_t \geq 18$.

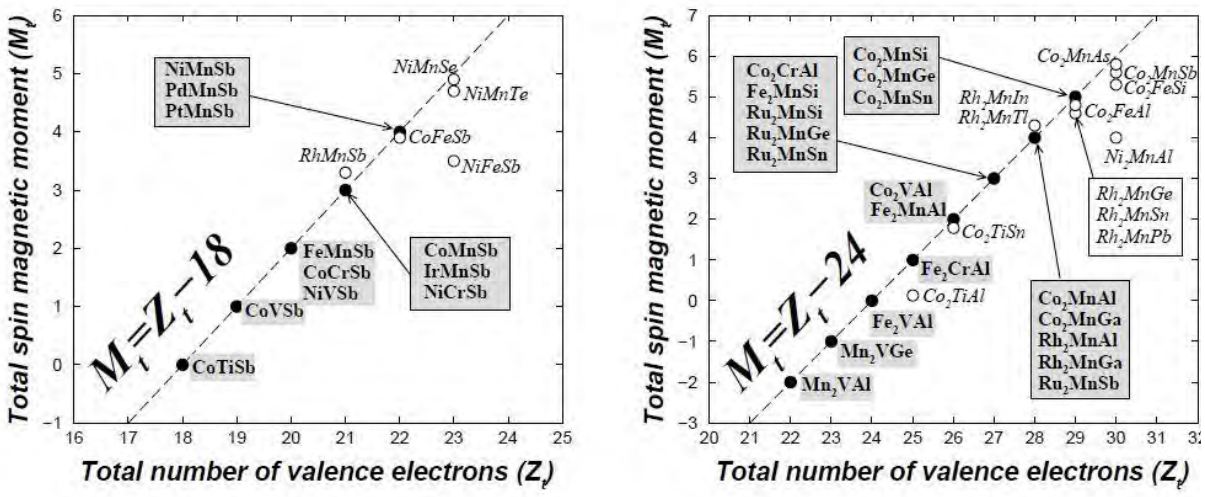

Fig. 1-11 Total spin moments for half-Heusler alloys (left) and full-Heusler alloys (right) as shown in ref.46. Slater Pauling behaviour are indicated by the dashed line.

The Slater-Pauling rule is a necessary condition for the full Heusler alloys to be half-metals. Nevertheless, for the ternary alloys in **Fig. 1-11** that deviate slightly from the linear relationship of the Slater-Pauling rule, for example Co_2FeAl and Co_2FeSi, there is also opportunity to turn them into half-metal by partially substituting the Z element, which is called *Fermi level tuning*. Fecher and Felser investigated the electronic structures[47] of the $Co_2Fe(Al_xSi_{1-x})$ alloys by *ab intio* calculations shown in **Fig. 1-12**. Although the

Fermi levels of the ternary alloys Co_2FeAl and Co_2FeSi were close to (or inside) the valence band and conduction band, respectively, by making a combination of Al and Si elements in the Z position, the quaternary alloy $Co_2Fe(Al_{0.5}Si_{0.5})$ had a Fermi level which was at the center of the minority band gap. In their report, they maintained that the half-metallicity of the alloys with Fermi level near the valence or conduction edge may be unstable against the increase of annealing temperature as well as chemical disordering. However, with Fermi level being at the center, the alloys may be stable against both. Nakatani *et al*[48] studied the spin polarization of the bulk $Co_2Fe(Al_xSi_{1-x})$ alloys by using the point contact Andreev reflection (PCAR) spectroscopy shown in **Fig. 1-13**, and for the case that x=0.5 the alloy $Co_2Fe(Al_{0.5}Si_{0.5})$ showed the highest spin polarization. This result was a nice confirmation of the *ab intio* calculations result in **Fig. 1-12**. By properly choosing the elements for the Fermi level tuning, the quaternary alloys are regarded as the spin-polarized source in the CPP-GMR devices.

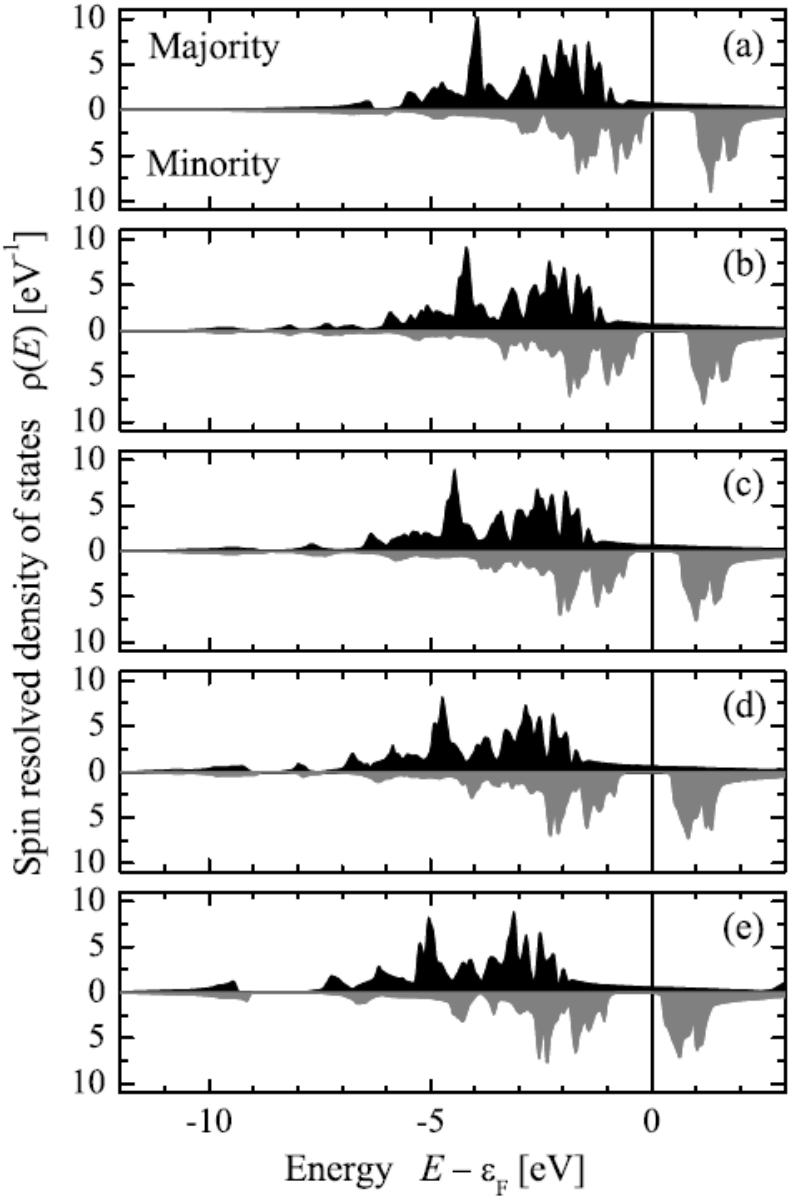

Fig. 1-12 Spin resolved density of states of $Co_2Fe(Al_{1-x}Si_x)$. By Fecher and Felser.[47]

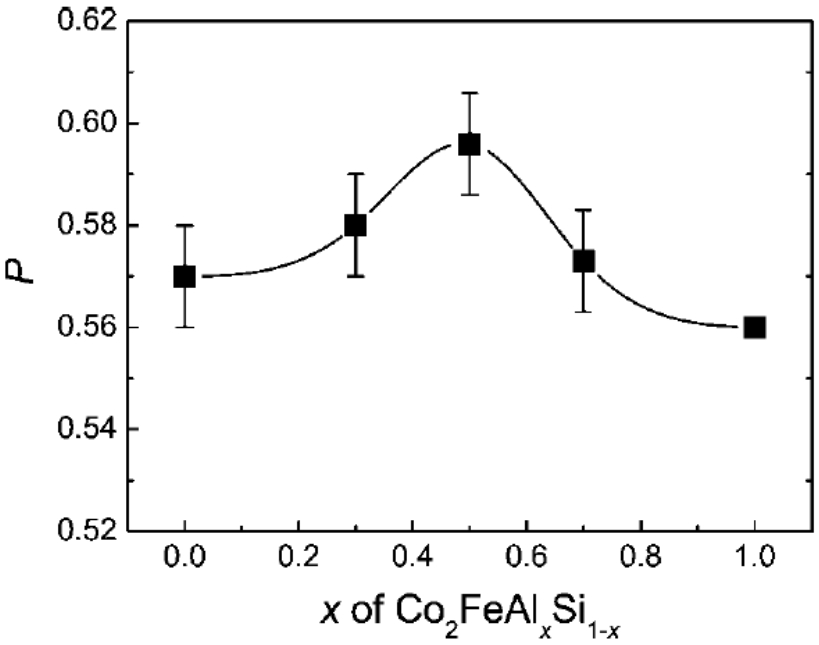

Fig. 1-13 The dependence of spin polarization on the Al concentration measured by PCAR. Courtesy of T. M. Nakatani *et al.*[48]

1.4 Review of previous work in CPP-GMR devices

1.4.1 Epitaxial CPP-GMR devices

The epitaxial CPP-GMR devices developed rapidly in the last decades, as shown in **Fig. 1-14**.[49-64] Back to 2006, the first epitaxial CPP-GMR devices was published with two Co_2MnSi electrodes separating by a 3-nm Cr spacer (Yakushiji et al., 2006).[51] In this paper, CPP-GMR pseudo spin-valves with Co_2MnSi/Cr/Co_2MnSi and obtained a large ΔRA of 19 $m\Omega\,\mu m^2$ and the MR ratio of 2.4% at room temperature. However, since they simply used 10 nm Cr as the underlayer, the value of ΔRA was later considered to be overestimated due to the current crowding phenomenon that was believed to occur in their devices. For this trilayer system a maximum MR ratio of 5.2% and ΔRA of 6.5 $m\Omega\,\mu m^2$ was obtained at RT (Sakuraba et al., 2009).[53] It is important to point out that the choice of the spacer layer is an essential issue. Spacer materials with a large spin-diffusion length and low resistivity are favourable to obtain large CPP-GMR values. With these considerations, silver appear to be an ideal spacer layer which can satisfy requirement mentioned above, combining with small lattice mismatch. As a result, a CPP-GMR ratio of 6.9% at RT (14% at 6K) was realized for a $Co_2Fe(Al_{0.5}Si_{0.5})$/Ag/$Co_2Fe(Al_{0.5}Si_{0.5})$ structure (Furubayashi et al., 2008).[52] Moreover, a further improvement of CPP-GMR ratio of 34% at 290K (80% at 14K) using the same system was reported by Nakatani et al. in 2010 afterward.[44] Very recently, the highest room-temperature MR ratio of 58% and ΔRA of ~12 mΩ μm^2 was obtained by Y. Sakuraba et al., by using Co-based Heusler alloy $Co_2Fe_{0.4}Mn_{0.6}Si$ (CFMS) in the ultrathin PSV stack of CFMS(4)/Ag(3)/CFMS(2) (unit in nm).[60] This PSV structure was regarded promising to be applied for the read head in the terabyte HDDs of the next generation.

By apply the post annealing process to the $Co_2Fe(Ga_{0.5}Ge_{0.5})/Ag/Co_2Fe(Ga_{0.5}Ge_{0.5})$ structure device, almost same level of MR output was achieved by S. Li et al as well.[62]

Other spacer material such as copper spacer has also been studied. Although there is large lattice mismatch between Cu and Heusler compounds, $Co_2MnSi/Cu/Co_2MnSi$ system showed CPP-GMR values of 8.6% at RT (30.7% at 6K) (Kodama et al., 2009).[54] To improve the interface scattering properties and optimize the lattice matching at the interface, CPP-GMR devices with "all-Heusler" structure were proposed like $Co_2MnSi/Ru_2CuSn/Co_2MnSi$. Unfortunately, these devices produced only a MR ratio of 6.7% at RT (Nikolaev et al., 2009). [65] Considering the highest MR output in the CPP-GMR devices that had been achieved, they can almost meet the requirement for next generation read head with data density of $2Tbit/in^2$. Nonetheless, the devices fabricated from epitaxial grown films cannot be applied in the industry presently, because for the mass fabrication process, polycrystalline films are required.

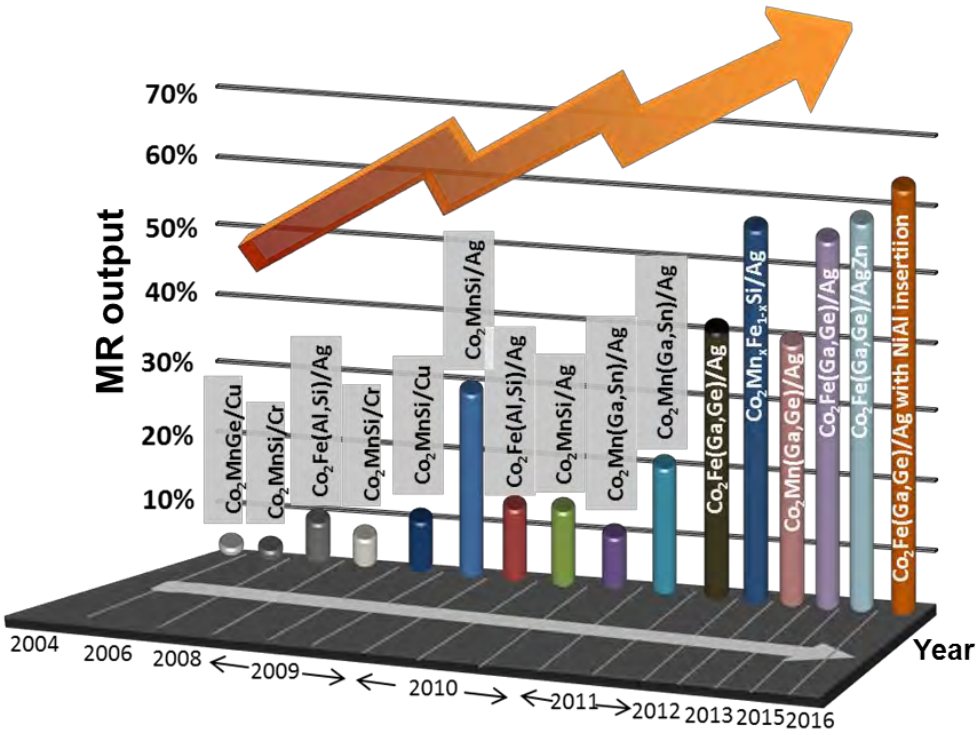

Fig. 1-14 Development of MR output for CPP-GMR devices. [49-64]

1.4.2 Polycrystalline CPP-GMR devices

When it comes to the perspective of application, there is no possibility of using (001) single-crystalline MgO substrate in industry: firstly the price of the MgO substrate is much higher than that of the thermally oxidized Si wafer which is more favourable in industry. Therefore, it is less possible to use MgO substrate for the mass production in HDD fabrication process considering the production cost. Moreover, the layered stack of CPP-GMR multilayer in real read head of HDDs would become polycrystalline due to the reason that the thin film structure would be deposited on polycrystalline soft magnetic shield with high saturation magnetic flux density. Therefore, the research on polycrystalline CPP-GMR devices becomes in demand especially in recent years. M. J. Carey et al in 2011 presented a systematic investigation on the CPP-GMR

spin valves sensors with full Heusler alloy Co_2MnGe and Cu spacer on glass or oxidized Si substrates.[66] They obtained ΔRA value of 4 mΩ μm^2 at relatively low temperature of 250°C by inserting CoFe nanolayers at the Co_2MnGe/Cu interface. On the other hand, structure and MR properties of CPP-GMR pseudo spin valves using polycrystalline Co_2Fe-based Heusler alloy thin films was reported very recently by T. M. Nakatani et al.[67] Similar MR output was achieved by using $Co_2Fe(Al_{0.5}Si_{0.5})$ and $Co_2Fe(Ga_{0.5}Ge_{0.5})$ electrode annealed at 450°C and 350°C, separately. As mentioned in these papers, the MR output of the devices prepared on the polycrystalline substrate show naturally 110-textured and much less values of ΔRA compared to those of epitaxial devices.

1.5 Purpose of this study

As introduced at the beginning of this chapter, the realization of CPP-GMR devices with sufficient high MR output is significant because it has been considered to be the next generation of read head for ultrahigh density magnetic recording. Up to now, highly spin polarized Heusler alloys such as Co_2MnSi (CMS), $Co_2Mn(Ga_{0.25}Ge_{0.75})$ (CMGG), $Co_2(Fe_{0.4}Mn_{0.6})Si$ (CFMS)and $Co_2Fe(Ga_{0.5}Ge_{0.5})$ (CFGG) have been utilized to provide large bulk spin polarization, and substantially large magnetoresistance (MR) ratios have been realized. However, a room-temperature (RT) ΔRA of at least 15 mΩ μm^2 is required for using CPP-GMR as read sensors for areal density over 2 Tbit/in^2. Therefore, further improvement of the MR output is essential. For instance, finding a new Heusler alloy which has both high spin polarization and high driving force for $L2_1$-ordering even at low annealing temperature is strongly desired to attain compatibility with the current fabrication process. On the other hand, from a practical point of view, the study on industrially viable high performance epitaxial CPP-GMR devices on a Si single crystalline substrate is also necessary. Proper choice of crystallographic orientation in ferromagnetic (FM) and non-magnetic (NM) materials may affect the thermal stability of the CPP-GMR stack against interlayer atomic diffusion and multilayer delamination. Multilayer engineering of the CPP-GMR stack is in strong need to satisfy rapid development of next generation read head sensors. Last but not least, new concept of processing is strongly required to solve the problem of annealing temperature limit, so that more freedom of material selection can be obtained to achieve higher CPP-(G)MR output.

In short, the motivation of the thesis is as below:

(1) To establish a fabrication process for (110)-oriented epitaxial CPP-GMR devices and investigate its crystallographic orientation dependence of MR output.

(2) To search for new highly spin-polarized Heusler alloy with high driving force for L21-order even at low annealing temperature for CPP-GMR device application.

(3) To grow high quality epitaxial CPP-GMR device on Si(001) wafer by selecting appropriate buffer materials.

(4) To fabricate single crystalline CPP-GMR device on polycrystalline electrode using wafer bonding technology.

1.6 Outline of this thesis

The thesis consists of seven chapters.

Chapter 1 introduces the general background on spintronics, giant magnetoresistance (GMR) effect, Co-based Heusler alloy and the issues that motivate the work in the thesis.

Chapter 2 provides experimental procedures including sample preparation, device fabrication and analysis methods.

Chapter 3 describes the work on CPP-GMR epitaxial spin-valves with (110)-oriented Heusler alloy $Co_2Fe(Ga_{0.5}Ge_{0.5})$ (short as CFGG) and different spacers (Ag, Cu and NiAl), in which orientation dependence of MR output has been investigated.

Chapter 4 describes the development of a new series of Heusler alloys prepared by the co-sputtering technique, $Co_2(Fe_{1-x}Ti_x)Si$, which have a strong merit of high spin-polarization together with high driving force for $L2_1$-ordering even at low annealing temperature.

Chapter 5 shows the work of realizing high quality epitaxial CPP-GMR pseudo spin-valves on Si(001) single crystalline wafer using NiAl buffer layer. It is the first demonstration of epitaxial spintronic devices with NiAl template for various practical applications in the field of ultra-high density hard disk drive (HDDs), magnetic sensor and so on.

Chapter 6 describes the work of fabricating single crystalline magnetoresistive sensors on polycrystalline electrode using a three-dimensional integration technology, which enables the integration of Heusler-alloy-based epitaxial CPP-GMR devices to high sensitive magnetic sensors regardless of the limitation of high temperature processing.

Chapter 7 provides summary of the thesis and future perspectives.

Reference

[1] http://www.bit-tech.net/news/hardware/2012/03/16/common-platform-finfet-14nm/1.

[2] "Overall Technology Roadmap Characteristics". International Technology Roadmap for Semiconductors. 2010.

[3] J.M.D. Coey, *Magnetism and Magnetic Materials* (Cambridge University Press, 2010).

[4] C. Chappert, A. Fert, and F.N. Van Dau, Nat. Mater. **6**, 813 (2007).

[5] N.F. Mott, Proc. R. Soc. Math. Phys. Eng. Sci. **156**, 368 (1936).

[6] Campbell I A, Fert A. Transport properties of ferromagnetis. In: Wohlfarth E P, ed. Ferromagnetic Materials. Amsterdam: North-Holland, 1982. 3: 747.

[7] P. Grünberg, R. Schreiber, Y. Pang, M.B. Brodsky, and H. Sowers, Phys. Rev. Lett. **57**, 2442 (1986).

[8] M.N. Baibich, J.M. Broto, A. Fert, F.N. Van Dau, F. Petroff, P. Etienne, G. Creuzet, A. Friederich, and J. Chazelas, Phys. Rev. Lett. **61**, 2472 (1988).

[9] Parkin S S P, Bhadra R, Roche K P. Osillatory magnetic exchange coupling through thin copper layers. Phys Rev Lett, 1991, 66(16): 2152–2155.

[10] Jin Q Y, Xu Y B, Zhai H R, et al. Direct evidence of spin polarization oscillations in the Cu layers of Fe/Cu multilayers observed by NMR. Phys Rev Lett, 1994, 72(5): 768–771.

[11] Yan S S, Liu Y H, Mei L M. Polarization and interlayer coupling in Co-Nb/Pd multilayers. Phys Rev B, 1995, 52(2): 1107–1111.

[12] Yu C T, Li S X, Lai W Y, et al. Giant magnetoresistance in Fe/Ag multilayers and its anomalous temperature dependence. Phys Rev B, 1995, 52(2): 1123–1132.

[13] Li M, Ma X D, Peng C B, et al. Magnetic-polarization effect of Pd layers in Fe/Pd multilayers. Phys Rev B, 1994, 50(14): 10323–10326.

[14] Yan M L, Lai W Y, Wang Y Z, et al. Giant magnetoresistance in Fe/Mo multilayers formed by magnetron sputtering. J Appl Phys, 1995, 77(4): 1816–1818.

[15] Zhou S M, Wang Y, Zhu W R, et al. Giant magnetoresistance properties in granular type (Co-Ag)/Ag multilayers. J Appl Phys, 1998, 83(2): 900–904.

[16] Parkin S S P, Li Z G, Smith D J. Giant magnetoresistance in antiferromagnetic Co/Cu multilayers. Appl Phys Lett, 1991, 58(23): 2710–2712.

[17] N. F. Mott, H. Jones, The Theory of the Properties of Metals and Alloys 1936

[18] E.Y. Tsymbal and D.G. Pettifor, in *Solid State Phys.* (Elsevier, 2001), pp. 113–237.

[19] R.E. Camley and J. Barnaś, Phys. Rev. Lett. **63**, 664 (1989).

[20] J. Barnaś, A. Fuss, R.E. Camley, P. Grünberg, and W. Zinn, Phys. Rev. B **42**, 8110 (1990).

[21] L. Sheng and D.Y. Xing, Phys. Rev. B **50**, 1001 (1994).

[22] T. Valet and A. Fert, Phys. Rev. B **48**, 7099 (1993).

[23] P.M. Levy, S. Zhang, and A. Fert, Phys. Rev. Lett. **65**, 1643 (1990).

[24] H.E. Camblong and P.M. Levy, Phys. Rev. Lett. **69**, 2835 (1992).

[25] A. Vedyayev, B. Dieny, and N. Ryzhanova, Europhys. Lett. EPL **19**, 329 (1992).

[26] Y. Asano, A. Oguri, and S. Maekawa, Phys. Rev. B **48**, 6192 (1993).

[27] H. Itoh, J. Inoue, and S. Maekawa, Phys. Rev. B **51**, 342 (1995).

[28] T.N. Todorov, E.Y. Tsymbal, and D.G. Pettifor, Phys. Rev. B **54**, R12685 (1996).

[29] L.-M. Li, F.-C. Pu, G.-L. Yang, and B.-Z. Li, Phys. Rev. B **51**, 12833 (1995).

[30] K.M. Schep, P.J. Kelly, and G.E. Bauer, Phys. Rev. Lett. **74**, 586 (1995).

[31] W.H. Butler, X.-G. Zhang, D.M.C. Nicholson, and J.M. MacLaren, Phys. Rev. B **52**, 13399 (1995).

[32] W.H. Butler, X.-G. Zhang, D.M.C. Nicholson, T.C. Schulthess, and J.M. MacLaren, Phys. Rev. Lett. **76**, 3216 (1996).

[33] C. Blaas, P. Weinberger, L. Szunyogh, P.M. Levy, and C.B. Sommers, Phys. Rev. B **60**, 492 (1999).

[34] S. Ishida, S. Akazawa, Y. Kubo, and J. Ishida, J. Phys. F Met. Phys. **12**, 1111 (1982).

[35] W. P. Pratt, Jr., S. -F. Lee, J. M. Slaughter, R. Loloee, P. A. Schroeder, J. Bass, Phys. Rev. Lett. **66** (1991) 3060

[36] M. A. M. Gijs, S. K. J. Lenczowski, J. B. Giesbers, Phys. Rev. Lett. 70 (1993) 3343

[37] F. Heusler Verh. Dtsch. Phys. Ges. , vol. 5, p. 219, (1903).

[38] H. H. Potter Proc. Phys. Soc. , vol. 41, p. 135, (1929).

[39] A. J. Bradley and J. W. Rodgers Proc. R. Soc. London Ser. A , vol. 144, p. 340, (1934).

[40]R. A. de Groot, F. M. Mueller, P. G. van Engen, and K. H. J. Buschow Phys. Rev. Lett, vol. 50, p. 2024, (1983).

[41] P. J. Webster, J. Phys. Chem. Solids **32** (1971) 1221

[42] B. S. D. Ch. S. Varaprasad, A. Srinivasan, Y. K. Takahashi, M. Hayashi, A. Rajanikanth, K. Hono, Acta Mater. **60** (2012) 6257

[43] H. Kijima, T. Ishikawa, T. Marukame, H. Koyama, K. Matsuda, T. Uemura, M. Yamamoto, IEEE Trans. Magn. **42** (2006) 2688

[44] T. M. Nakatani, T. Furubayashi, S. Kasai, H. Sukegawa, Y. K. Takahashi, S. Mitani, K. Hono, Appl. Phys. Lett. **96** (2010) 212501-1

[45] Y.K. Takahashi, A. Srinivasan, B. Varaprasad, A. Rajanikanth, N. Hase, T.M. Nakatani, S. Kasai, T. Furubayashi, and K. Hono, Appl. Phys. Lett. **98**, 152501 (2011).

[46] I. Galanakis, P. H. Dederichs, and N. Papanikolaou Phys. Rev. B , vol. 66, p. 134428, (2002).

[47] G. H. Fecher, C. Felser, J. Phys. D: Appl. Phys. 40 (2007) 1582.

[48] T. M. Nakatani, A. Rajanikanth, Z. Gercsi, Y. K. Takahashi, K. Inomata, K. Hono, J. Appl. Phys. 102 (2007) 033916

[49] J.A. Caballero, A.C. Reilly, Y. Hao, J. Bass, W.P. Pratt, F. Petroff, and J.R. Childress, J. Magn. Magn. Mater. **198**, 55 (1999).

[50] H. Hoshiya and K. Hoshino, J. Appl. Phys. **95**, 6774 (2004).

[51] K. Yakushiji, K. Saito, S. Mitani, K. Takanashi, Y.K. Takahashi, and K. Hono, Appl. Phys. Lett. **88**, 222504 (2006).

[52] T. Furubayashi, K. Kodama, H. Sukegawa, Y.K. Takahashi, K. Inomata, and K. Hono, Appl. Phys. Lett. **93**, 122507 (2008).

[53] Y. Sakuraba, T. Iwase, K. Saito, S. Mitani, and K. Takanashi, Appl. Phys. Lett. **94**, 012511 (2009).

[54] K. Kodama, T. Furubayashi, H. Sukegawa, T.M. Nakatani, K. Inomata, and K. Hono, J. Appl. Phys. **105**, 07E905 (2009).

[55] T. Iwase, Y. Sakuraba, S. Bosu, K. Saito, S. Mitani, and K. Takanashi, Appl. Phys. Express **2**, 063003 (2009).

[56] T. Furubayashi, K. Kodama, T.M. Nakatani, H. Sukegawa, Y.K. Takahashi, K. Inomata, and K. Hono, J. Appl. Phys. **107**, 113917 (2010).

[57] N. Hase, B.S.D.C.S. Varaprasad, T.M. Nakatani, H. Sukegawa, S. Kasai, Y.K. Takahashi, T. Furubayashi, and K. Hono, J. Appl. Phys. **108**, 093916 (2010).

[58] N. Hase, T.M. Nakatani, S. Kasai, Y.K. Takahashi, and K. Hono, J. Appl. Phys. **109**, 07E112 (2011).

[59] Y.K. Takahashi, A. Srinivasan, B. Varaprasad, A. Rajanikanth, N. Hase, T.M. Nakatani, S. Kasai, T. Furubayashi, and K. Hono, Appl. Phys. Lett. **98**, 152501 (2011).

[60] Y. Sakuraba, M. Ueda, Y. Miura, K. Sato, S. Bosu, K. Saito, M. Shirai, T.J. Konno, and K. Takanashi, Appl. Phys. Lett. **101**, 252408 (2012).

[61] Y.K. Takahashi, N. Hase, M. Kodzuka, A. Itoh, T. Koganezawa, T. Furubayashi, S. Li, B.C.S. Varaprasad, T. Ohkubo, and K. Hono, J. Appl. Phys. **113**, 223901 (2013).

[62] S. Li, Y.K. Takahashi, T. Furubayashi, and K. Hono, Appl. Phys. Lett. **103**, 042405 (2013).

[63] Y. Du, T. Furubayashi, T.T. Sasaki, Y. Sakuraba, Y.K. Takahashi, and K. Hono, Appl. Phys. Lett. **107**, 112405 (2015).

[64] J.W. Jung, Y. Sakuraba, T.T. Sasaki, Y. Miura, and K. Hono, Appl. Phys. Lett. **108**, 102408 (2016).

[65] K. Nikolaev, P. Kolbo, T. Pokhil, X. Peng, Y. Chen, T. Ambrose, and O. Mryasov, Appl. Phys. Lett. 94, 222501 (2009).

[66] M.J. Carey, S. Maat, S. Chandrashekariaih, J.A. Katine, W. Chen, B. York, and J.R. Childress, J. Appl. Phys. 109, 093912 (2011).

[67] T. M. Nakatani, Ye Du, Y. K. Takahashi, T. Furubayashi, K. Hono, Acta. Mater 61 (2013) 3695.

Chapter 2 Experimental procedure

2.1 Thin film fabrication

2.1.1 Magnetron sputtering

Sputtering is a process by which atoms are dislodged from the surface of a material due to the collision with target by high-energy particles. It is a physical vapour deposition (PVD) method used to fabricate thin films in nano-meter scale[1]. This process involves ejecting atoms from a target material onto a certain substrate such as MgO or Si wafer, as shown in **Fig. 2-1**[2]. Inertia ions (e.g. Ar+) are usually used for this atom-ejecting process.

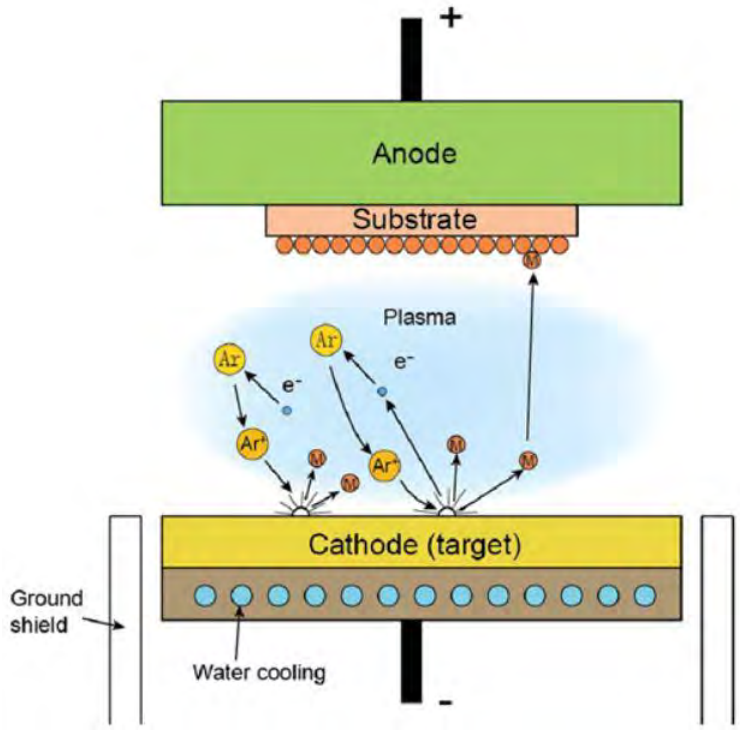

Fig. 2-1 Schematic demonstration of Magnetron sputtering.[2]

Sputtered atoms have wide energy distributions, typically up to tens of eV. After being detached from the target, only a very small amount of them (around 1%) can eventually reach the substrates or vacuum chamber. The atomic weight of the sputtering gas chosen should be close to the atomic weight of the target atom for efficient momentum transfer. Therefore, for light elements neon gas is desirable while for heavy elements Krypton or Xenon gas are used. In a sputtering chamber the substrate is usually placed on the top surface and acts as the anode, and the target is electrically connected as cathode. When voltage is applied between them, the inertia gas is ionized and forms plasma, which eventually causes the bombardment of the gas onto the target leading to the phenomenon of sputtering. One interesting about it is the colour of the plasma. To name a few, Argon: purple, Nitrogen: red, Fluorocarbon: blue.

As for the sputtering power there are normally two modes: DC (direct current) and RF (radio frequency). DC mode is the most common mode used for most metals. But it may cause charge build-up at the target. RF mode can solve this problem. Most RF sputtering is used for insulators and can be operated at a lower Ar

pressure. In our sputtering facility shown in **Fig. 2-2,** [3] the DC/RF power modes are also coupled with magnets. This set-up facilitates the lower-pressure sputtering process.

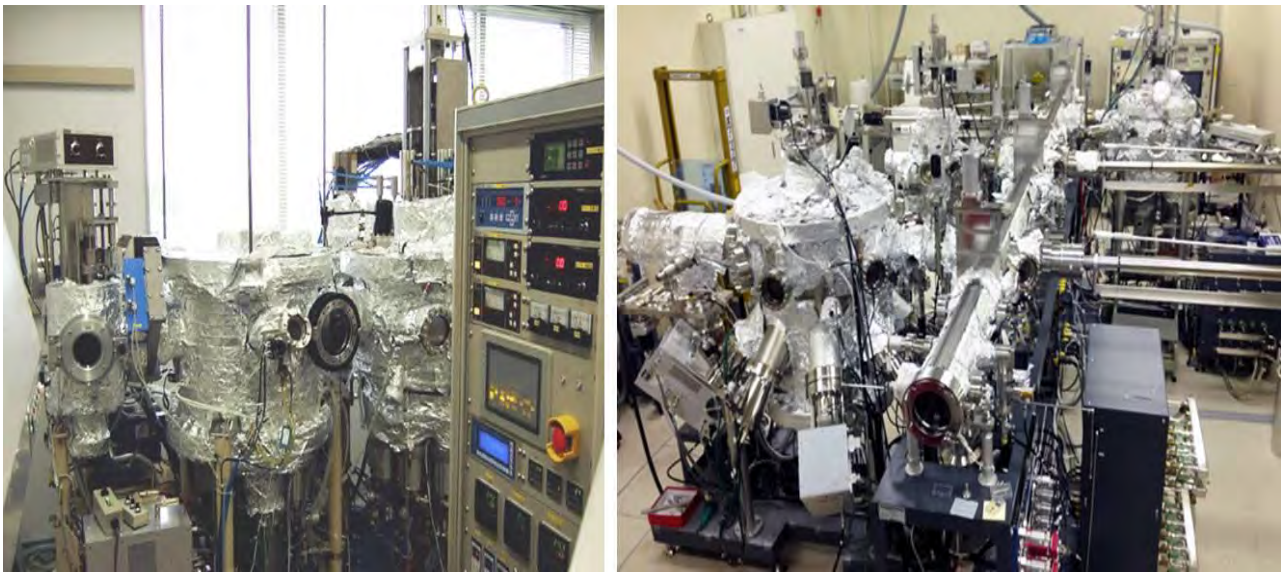

Fig. 2-2 UHV sputtering machine

In order to precisely control the thickness and quality of the deposited films, we have to measure and optimize the sputtering rate before depositing multilayer thin films. Table 2-1 summarizes the sputtering rate at different sputtering power/mode for different materials.

Material	Power	Gas flow/pressure	Sputtering rate
Ta	DC30	22.3 sccm/0.1 Pa	0.31 Å/s
W	DC30	22.3 sccm/0.1 Pa	0.27 Å/s
Ag	RF20	22.3 sccm/0.1 Pa	0.35 Å/s
Cu	DC12	22.3 sccm/0.1 Pa	0.32 Å/s
Ru	RF50	9.5 sccm/0.1 Pa	0.18 Å/s
Cr	DC40	22.3 sccm/0.1 Pa	0.38 Å/s
NiAl	DC30	22.3 sccm/0.1 Pa	0.35 Å/s
$Co_2Fe(Ga_{0.5}Ge_{0.5})$	DC30	22.3 sccm/0.1 Pa	0.29 Å/s

Table 2-1 Sputtering rate for different sputtering mode.

2.2 Microfabrication

The microfabrication process was implemented by the combination of photo and electron beam lithography and Ar ion etching. The photo lithography was used for the patterning of the bottom electrode, isolation slot, SiO_2 isolation pad and top electrode. The electron beam lithography was used for the build-up of the CPP-GMR pillar. The detail of microfabrication process was demonstrated in **Fig. 2-3** schematically.

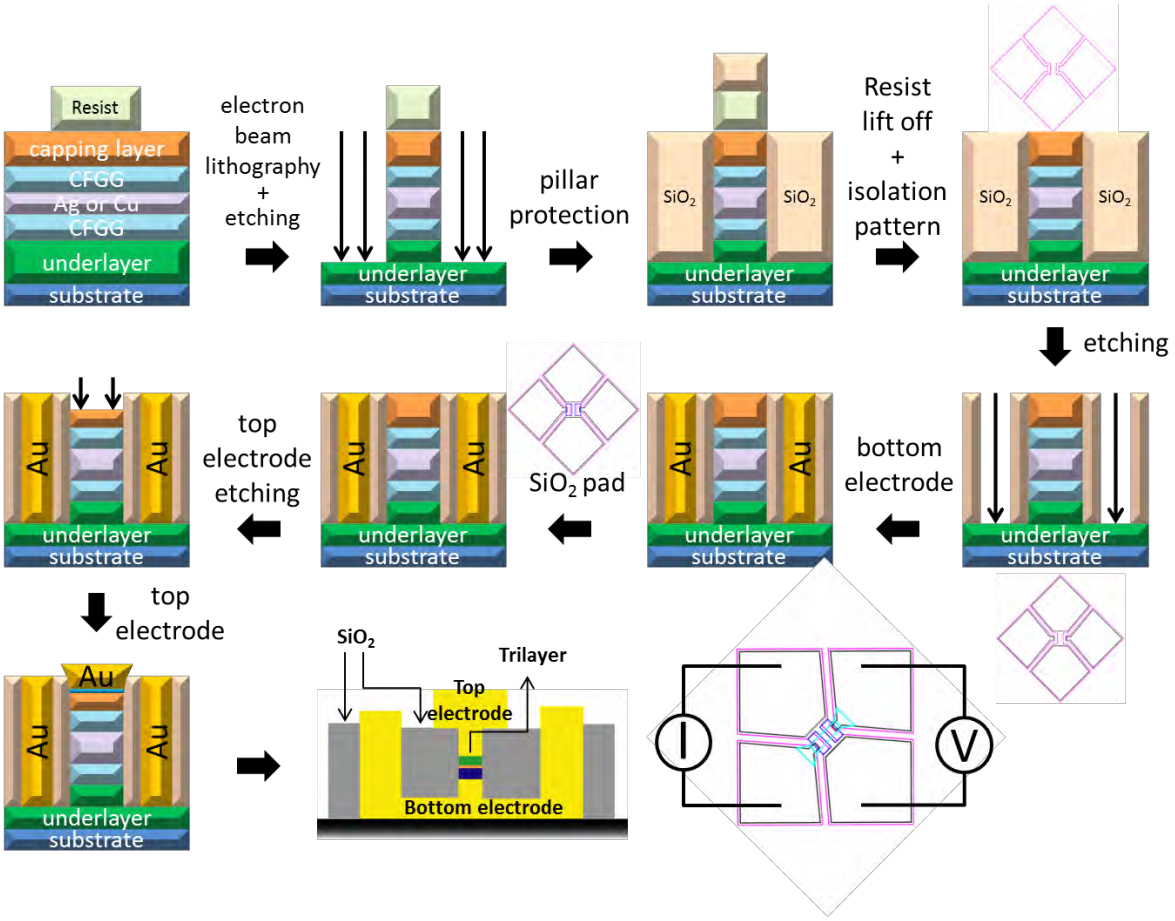

Fig. 2-3 Whole microfabrication process.

2.2.1 Photo lithography and electron beam (EB) lithography

Photo lithography

Resist: ma-N1407 negative resist Promotor of adhesion: Hexamethyldisilazane (HMDS)

Process:

(1) Spin coating of HMDS at 3500 rpm for 45 sec

(2) Baking at 90°C for 2 min

(3) Spin coating of ma-N1407 at 3500 rpm for 45 sec

(4) Baking at 90°C for 1.5 min

(5) Exposure for 90 sec

(6) Development with ma-D533* for 80 sec

(7) Ar ion milling or sputtering

*Ma-D533 is a developer for ma-N1407 negative resist.

EB lithography

Resist: ma-N2403 negative resist Promotor of adhesion: Hexamethyldisilazane (HMDS)

Process:

(1) Spin coating of HMDS at 3500 rpm for 45 sec

(2) Baking at 90°C for 3 min

(3) Spin coating of ma-N2403 at 3500 rpm for 45 sec

(4) Baking at 90°C for 2 min

(5) Spin coating of E-spacer at 3500 rpm for 45 sec, no post baking

(6) Electron beam exposure

(7) Development with ma-D532* for 80 sec

(8) Ar ion milling and sputtering

*Ma-D532 is a developer for ma-N2403 negative resist.

The most important part of the whole microfabrication process is to make the CPP-GMR pillar by EB lithography and Ion milling. During the pillar fabrication, a milling angle of 5 degree was applied to avoid the side wall damage and re-deposition problem. The control of proper stopping point for pillar milling is decided by the appearance of buffer layer material signal monitored by end point detection technique called secondary ion mass spectroscopy (SIMS). For the fabrication of electrode, Ta(2 nm)/Au(100 nm) layers were deposited. The pre-sputtered 2 nm Ta layer is to get better adhesion of the Au layer. The samples were Ar ion etched for 30 sec (Ru capping etched thickness of ~4 nm) after photolithography of the electrode. Then the Ta/Au electrode was deposited subsequently. This etching process is to clean the interface between Ru and the electrode for better contact. Otherwise, the devices contain a large parasitic resistance, which will strongly affect the magneto-transport properties. The whole process required for fabricating one sample costs more than 10 hours.

2.3 Experiment analysis methods

2.3.1 X-ray diffraction (XRD)

X-ray is a wave of electromagnetic essentially. In material, crystals can be considered as arrays of atoms. [4] X-ray is utilized for crystal analysis because the wavelength of X-ray has the similar dimension with atom distance in the crystal cell, which means crystal cell can be regarded as space diffraction grating of X-ray. When X-ray is applied to a material, because of the scattering with atom inside, each atom generates scattering wave. These waves interfere each other resulting in diffraction. And the superposition of diffraction waves gives result of intensity increment in some direction and intensity decrement in others. By analysing the diffraction patterns, information of crystal structure can be obtained. This diffraction follows an equation given by Bragg's law:

$$2d \sin\theta = n\lambda$$

where d is the distance between nearest diffraction planes, θ is an incident angle, n is any positive integer, λ is the beam's wavelength. See **Fig. 2-4**.

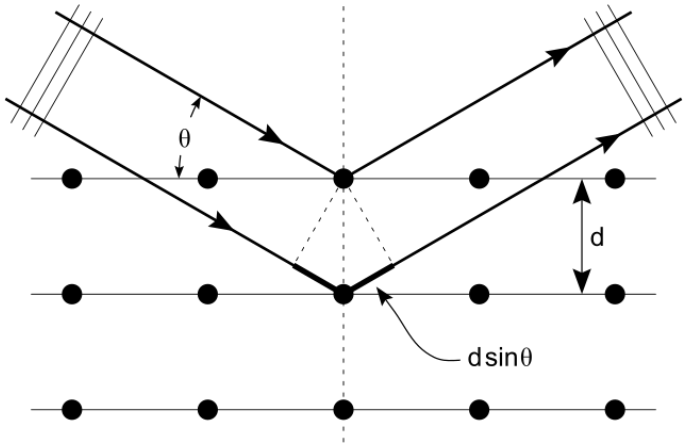

Fig. 2-4 Bragg's law

Fig. 2-5 Rigaku Smartlab 4-axis XRD

X-ray diffraction is one of the powerful non-destructive methods for structural characterization. Diffracted x-rays from periodic structures will make some diffraction patterns (peaks or spots). The diffraction patterns are useful to evaluate crystal structure, lattice parameters, crystal orientation, and the degree of atomic ordering. In this work, 4-axis x-ray diffraction (**Fig.2-5**) was used to check the crystal structure and the orientation relationship of our film stacks in the out-of-plane direction. And XRD pole-figure measurement was applied to study the orientation relationship between different layers in the in-plane direction.

2.3.2 Atomic Force Microscopy (AFM)

Atomic force microscopy (AFM) is a type of scanning probe microscopy, which enables very high-resolution with the order of nanometer. Its resolution is normally more than 1000 times better than the typical optical diffraction. So far, AFM is one of the principle tools for measuring, imaging, and manipulating matter at the Nano scale. The information obtained by AFM is from a cantilever with a sharp tip at its end which is used for scanning the specimen surface. The cantilever is typically made of silicon or silicon nitride with a tip radius of nanometre. According to Hooke's law, when the tip is brought close to a sample surface, a deflection of the cantilever occurs due to the forces between the tip and the sample. In this thesis, we used AFM for measuring the roughness of thin film surface after the film deposition.

2.3.3 Vibrating Sample Magnetometer (VSM)

The vibrating sample magnetometer (VSM) is common used scientific equipment which can measure magnetic properties. The first VSM was invented by Simon Foner at Lincoln Laboratory MIT in 1955. It is a widely used instrument for probing into the magnetic properties of various materials: ferromagnetic, antiferromagnetic, diamagnetic, paramagnetic and the like. The VSM used in the present study is Lake Shore Systems' Model 740 as shown in **Fig. 2-6**. Measurements of magnetic moments as small as 5×10^{-5} emu or even less are possible in magnetic field ranging from 0 to several Tesla. Both bulk and thin films can be measured from several K to approximately 1000 K.

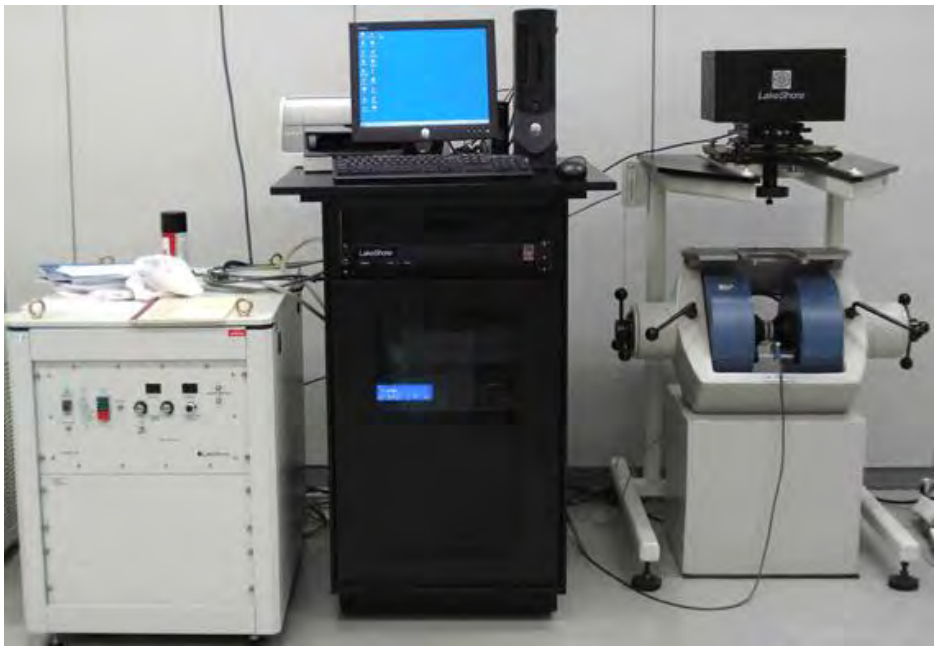

Fig. 2-6 Image of a high sensitivity VSM.

2.3.4 Scanning electron microscopy (SEM)

Scanning electron microscope (SEM)[5] is a type of electron microscope which scans sample with a focused beam of electrons to produce image. During the scanning, electrons interact with atoms in the

sample, producing various signals. These signals, which contain information about the sample's surface composition and topography, can be detected by detector to display related image in the computer. Resolution of SEM is very high, typically better than 1 nanometer. In addition, Specimens can be observed in different conditions such as in low vacuum, in high vacuum, in wet conditions, at low temperature or elevated temperatures.

Fig. 2-7 shows the SEM facility in our group. In this thesis, SEM is used for measuring the area of the reference pillars in CPP-GMR devices to calculate the accurate ΔRA value.

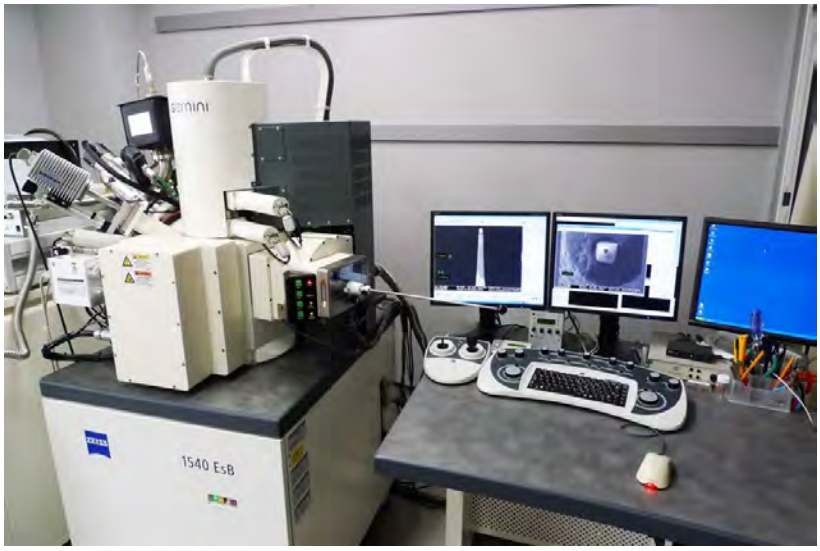

Fig. 2-7 Image of the CarlZeiss1540EsB SEM in our group.

2.3.5 Transmission electron microscopy (TEM)

Transmission electron microscopy (TEM) is a microscopy technique widely used for microstructure analysis. When a beam of electrons passes through an ultra-thin specimen, image can be formed owing to the interaction of the electrons transmitted through the specimen. The image is detected by imaging detectors, such as a fluorescent screen, a layer of photographic film or a CCD camera.[6] TEMs are capable of a very high resolution of imaging, owing to the small *de Broglie* wavelength of electrons. Even a single column of atoms could be carefully examined in a TEM, while the smallest object observable in a light microscope is tens of thousands times larger. When observing an ultra-thin specimen, the crystallographic structure of a multilayer thin film can be obtained by using the high-resolution (HR) TEM imaging mode. High-angle annular dark-field scanning TEM (HAADF-STEM) imaging offers contrast which is sensitive to the atomic number of atoms of each layer in thin films as well as the layer thickness of each material. Energy-dispersive X-ray spectroscopy (EDS) technique provides information about elemental analysis or chemical characterization of a sample. The imaging techniques mentioned above will be used for thin film microstructure analysis in the experiment part.

The TEM specimens in this work were prepared by Focused Ion Beam (FIB) for ion milling and surface cleaning was done by using Precision Ion Polishing System. Two different TEM facilities (**Fig. 2-8 and Fig. 2-9**) were used for the specimen observation. HAADF-STEM image and EDS mapping were taken from Titan G2 80-200. The HRTEM images were taken from Tecnai F30 due to its higher accelerating voltage.

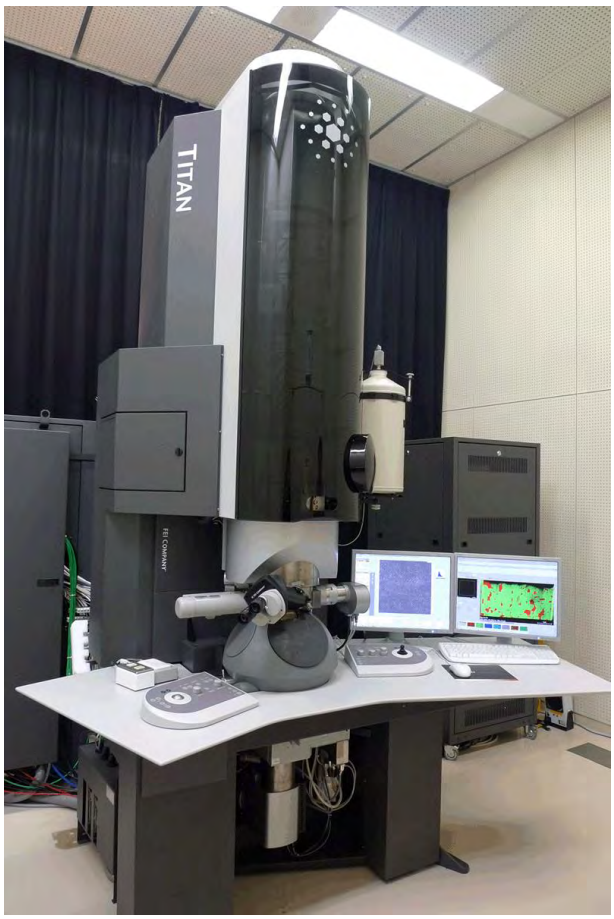

Fig. 2-8 Image of Titan G2 80-200 TEM

Fig. 2-9 Image of Tecnai F30 TEM

2.3.6 Four-probe measurement

The CPP-GMR property is measured by the dc 4-probe device with a constant current source at the range of mA. The set-up[7] is demonstrated in **Fig. 2-10**. The low temperature measurement is performed with a helium compressor refrigerator to reach around 5 K. The temperature control was done by manually adjustment of the heat power.

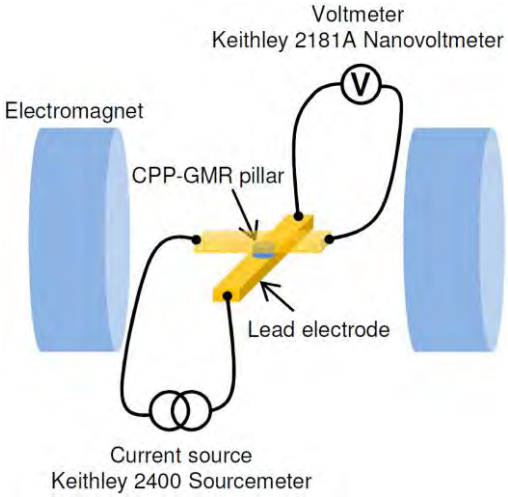

Fig. 2-10 Set up of 4-probe measurement.

[1] http://en.wikipedia.org/wiki/Magnetron_sputtering

[2] http://www.directvacuum.com/PDF/what_is_sputtering.pdf

[3] http://www.nims.go.jp/apfim/gif/ULVAC10THelicon.gif

[4] http://en.wikipedia.org/wiki/X-ray_diffraction#X-ray_analysis_of_crystals

[5] http://en.wikipedia.org/wiki/Scanning_electron_microscope

[6] http://en.wikipedia.org/wiki/Transmission_electron_microscopy

[7] T. M. Nakatani, spin-dependent scattering in CPP-GMR using Heusler alloy and the selection of the spacer material, PhD thesis

Chapter 3 CPP-GMR epitaxial spin-valves with (110)-oriented Heusler alloy $Co_2Fe(Ga_{0.5}Ge_{0.5})$ and different spacers (Ag, Cu and NiAl)

3.1 Introduction

This chapter describes:

(1) Fabrication of (110)-oriented CPP-GMR devices with Ag and Cu spacer and their various properties

(2) Fabrication of (110)-oriented CPP-GMR devices with NiAl spacer and their various properties

As discussed in chapter 1, all-metallic current-perpendicular-to-plane (CPP) giant magnetoresistance (GMR) device has been considered to be an attractive alternative read head for future high density hard disk drives (HDD) exceeding 2Tbit/in^2 owing to its intrinsic low device resistant. Although there are many investigations on CPP-GMR, no one has ever demonstrated orientation dependence of MR output of CPP-GMR devices. With this motivation, we prepared CPP-GMR pseudo-spin-valves (PSVs) consisting of epitaxial layers of the Heusler alloy $Co_2Fe(Ga_{0.5}Ge_{0.5})$ (CFGG) with the (110) orientation. Three nonmagnetic materials, Ag, Cu and NiAl, were used for the spacer layer, and the effects of the crystal orientation upon the MR properties were examined by comparing these devices with those comprising (001) epitaxial layers.

3.2 (110)-oriented CPP-GMR devices with Ag and Cu spacer

3.2.1 The choice of substrate and buffer layer

For the epitaxial thin film, the crystal orientation strongly depends on that of the substrate, which means that we can obtain the orientation that we want by selecting an appropriate substrate. In fact, many papers have reported a successful growth of (110)-oriented film by using different single crystal substrates like MgO (111) or sapphire$(11\bar{2}0)$[1–6]. Based on their study, we try to fabricate CPP-GMR film stack with $Co_2Fe(Ga_{0.5}Ge_{0.5})$ (110) electrode by using these two different substrates.

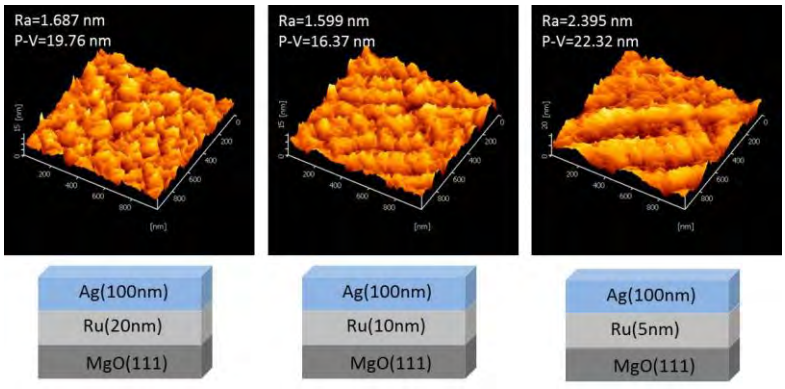

Fig. 3-1 AFM result of MgO/Ru(5,10,20)/Ag(100).

For CPP-GMR devices, a certain underlayer is needed to act as a buffer layer for the growth of the films on it and a lead electrode for the transport property measurement. This requires the underlayer to have a good wetness with the substrate, a small lattice mismatch with Heusler alloy and a low resistivity to avoid the current crowding effect. In the previous study in our group, there is a well-established system of using

Cr(10)/Ag(100) underlayer deposited on MgO substrate for film characterization and CPP-GMR devices in (001) orientation. However for (110) orientation, due to the fact of different lattice mismatch at the layer interface, the choice of underlayer should be reconsidered.

For MgO (111) substrate, we proposed MgO/Ru(5,10,20 nm)/Ag(100 nm) underlayer structure to obtain the fully (110)-oriented film stack. The roughness of the film surface after depositing 100 nm silver was measured by AFM. Unfortunately, the roughness of the surface after depositing the 100 nm Ag was frustratingly too bad, as can be seen from **Fig. 3-1**. Both R_a and p-v value were too large to provide a flat surface for the growth of Heusler layer.

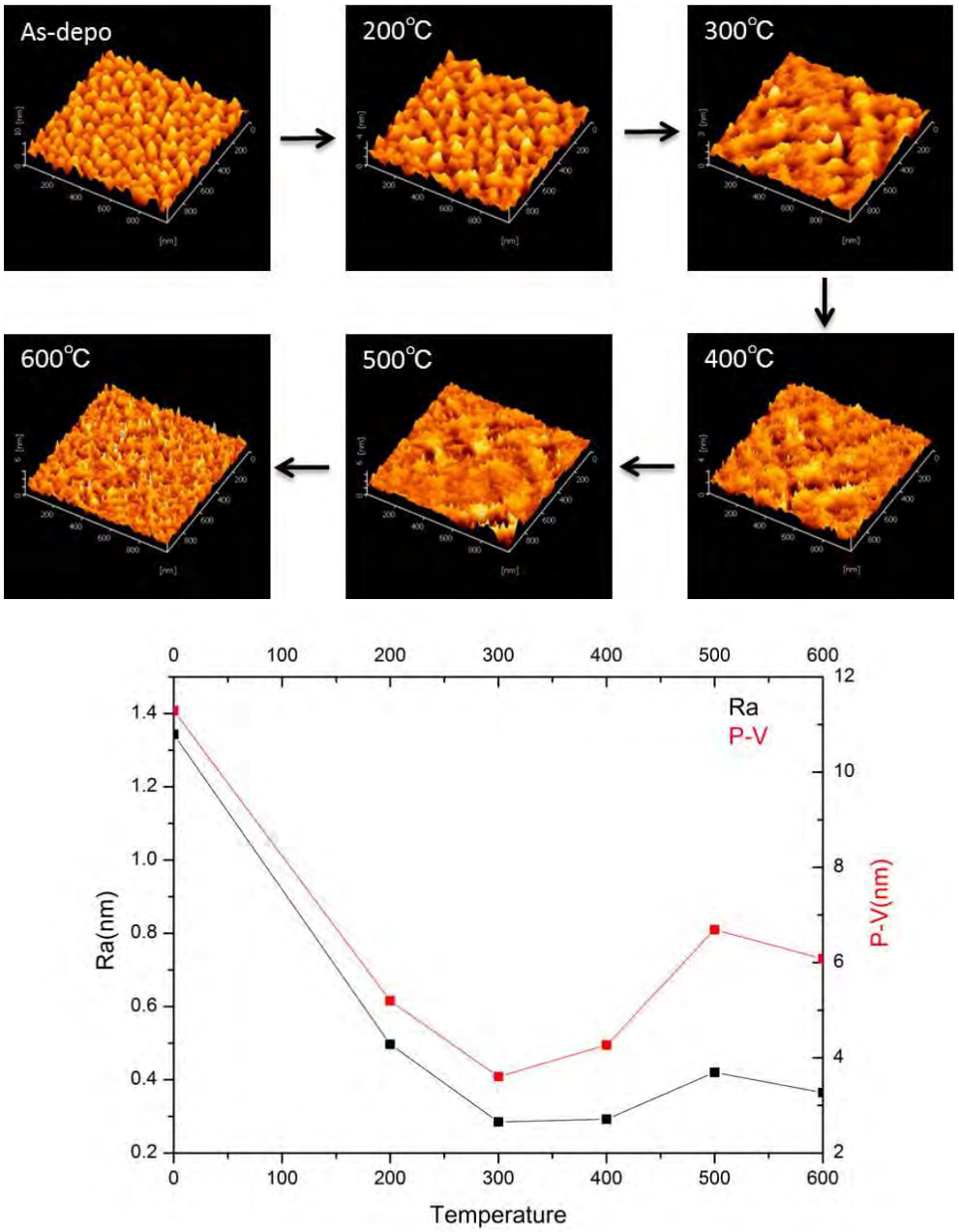

Fig. 3-2 Surface roughness of Sapphire/Ta(20)/W(20)/Ag(100) anneal at different temperature.

On the other hand, by using sapphire $(11\bar{2}0)$ single crystal substrate, M. Hattori et al.[7] reported a fabrication of Magnetic Tunnel Junctions with high-quality (110)-oriented Co_2MnSi electrodes. Since CPP-GMR and TMR device have a similar film structure, we borrowed their ideas of using Ta and W as seed layer on top of sapphire substrate for our (110)-oriented CPP-GMR fabrication. **Fig. 3-2** shows the average roughness (R_a) and the peak-to-valley height (p-v) of the sapphire/Ta(20)/W(20)/Ag(100) films for various annealing temperatures. We can see the surface flatness improve with increasing the annealing temperature. The improvement is presumably due to the atomic diffusion on the surface of the film. At the annealing temperature of 300°C, the film exhibits the best surface condition. The crystal structure of the previous films was examined by XRD. The result was shown in **Fig. 3-3**. All the films showed good (110) epitaxial growth for the underlayer in the out-of-plane direction. Therefore, we chose to use sapphire substrate with Ta/W/Ag underlayer and the annealing process of 300°C for 30 min was applied for all the films with Ta/W/Ag underlayer in the following experiment.

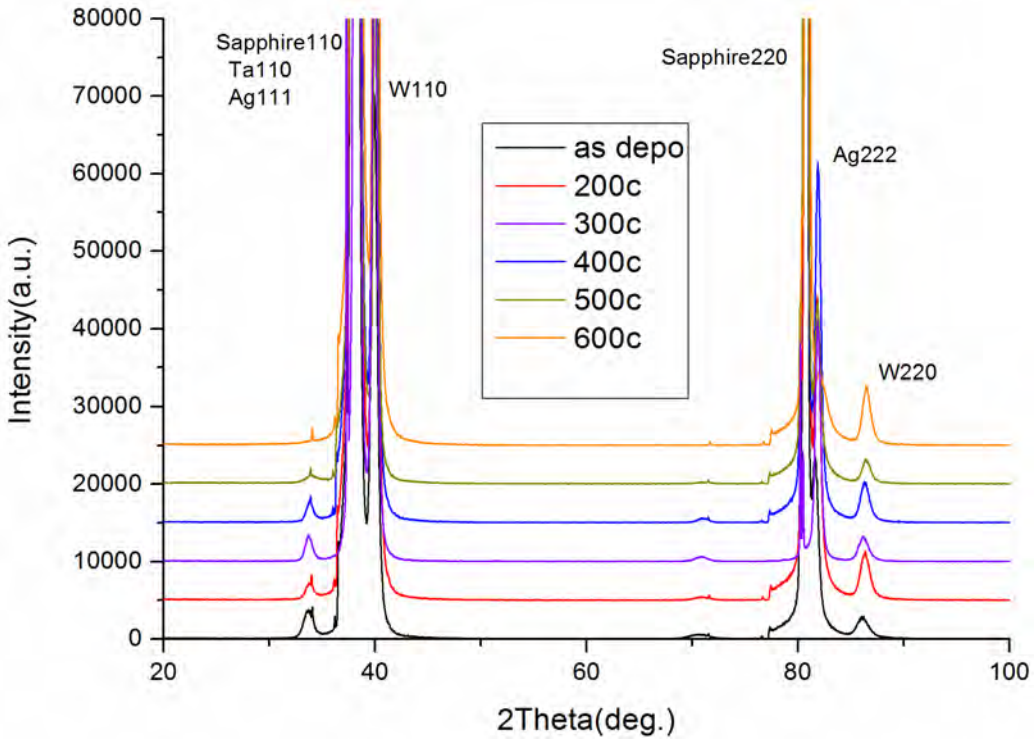

Fig. 3-3 XRD result of Sapphire/Ta(20)/W(20)/Ag(100) at different annealing temperatures.

3.2.2 The quaternary alloy $Co_2Fe(Ga_{0.5}Ge_{0.5})$

According to *ab initio* calculations, Co_2FeGa have high spin polarization, but not a half-metal[8]. The Fermi level (E_f) of $L2_1$ - Co_2FeGa is in the higher edge of the band gap. However, the single $L2_1$ phase is not obtained and unknown secondary phase forms in the Co_2FeGa system. On the other hand, Co_2FeGe forms a stable $L2_1$ phase with a band structure similar to that of Co_2FeGa. Hence, the substitution of Ge in Co_2FeGe with Ga may form stable $L2_1$ phase with Fermi level in the band gap. Since the melting temperature of Ga is

lower than Ge, we can expect the quaternary $Co_2Fe(Ga_xGe_{1-x})$ to order at relatively lower annealing temperature.

In 2011, Y. K. Takahashi *et al*[9] reported large magnetoresistance in CPP-GMR pseudo spin-valves using $Co_2Fe(Ga_{0.5}Ge_{0.5})$ Heusler alloy, the room-temperature MR and ΔRA value were ~42% and 9.5 $m\Omega\,\mu m^2$ (**Fig. 3-4**), respectively. The composition of $Co_2Fe(Ga_xGe_{1-x})$ was optimized experimentally by PCAR measurement to obtain the highest spin polarization, shown in **Fig. 3-5**. For the case where x=0.5, the spin polarization of the full Heusler alloy $Co_2Fe(Ga_{0.5}Ge_{0.5})$ reached nearly 70%, which was almost the highest value for the Co_2Fe-based Heusler alloys investigated by PCAR so far (**Table. 3-1**).

Quaternary alloys	P	T_c (K)	Ternary alloys	P	T_c (K)
$Co_2Mn(Ge_{0.75}Ga_{0.25})$	0.74	895	Co_2CrAl	0.62	600
$Co_2Mn(Ga_{0.5}Sn_{0.5})$	0.72	770	Co_2CrGa	0.61	
$Co_2Fe(Si_{0.75}Ge_{0.25})$	0.70	990	Co_2MnSn	0.60	800
$Co_2Fe(Ga_{0.5}Ge_{0.5})$	0.69	1080	Co_2MnAl	0.60	
$Co_2(Cr_{0.02}Fe_{0.98})Ga$	0.67		Co_2MnGa	0.60	700
$Co_2Mn(Ge_{0.25}Sn_{0.75})$	0.67		Co_2FeSi	0.60	1100
$Co_2(Mn_{0.95}Fe_{0.05})Sn$	0.65		Co_2FeAl	0.59	
$(Co_{1.93}Fe_{0.062})MnGe$	0.68		Co_2MnGe	0.58	900
$Co_2(Mn_{0.5}Fe_{0.5})Ga$	0.70	990	Co_2FeGe	0.58	1000
$Co_2(Cr_{0.02}Fe_{0.98})Si$	0.65	990	Co_2FeGa	0.58	1100
$Co_2Mn(Ti_{0.25}Sn_{0.75})$	0.64	480	Co_2TiSn	0.57	364
$Co_2Mn(Al_{0.5}Sn_{0.5})$	0.63		Co_2MnSi	0.56	900
$Co_2Mn(Ga_{0.25}Si_{0.75})$	0.63		Fe_2VAl	0.56	
$Co_2Mn(Si_{0.25}Ge_{0.75})$	0.63		Co_2VAl	0.48	
$Co_2(Mn_{0.5}Fe_{0.5})Si$	0.61				
$Co_2Mn(Al_{0.5}Si_{0.5})$	0.60				
$Co_2Fe(Ga_{0.5}Si_{0.5})$	0.60				
$Co_2Fe(Al_{0.5}Si_{0.5})$	0.60				

Table. 3-1 Spin polarization of different ferromagnetic materials by PCAR.[10]

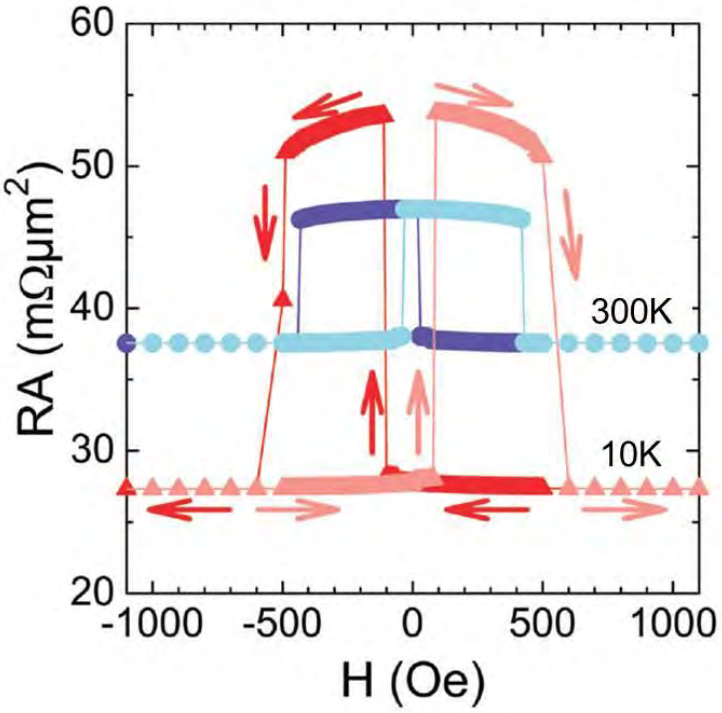

Fig. 3-4 MR curves of CFGG/Ag/CFGG PSV at 10 K and 300 K.[9]

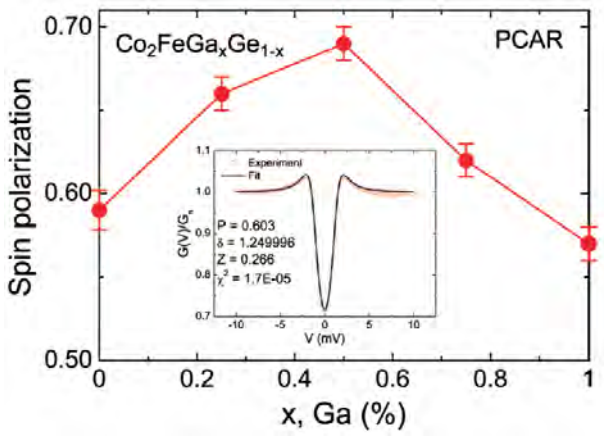

Fig. 3-5 Dependence of spin polarization of $Co_2Fe(Ga_xGe_{1-x})$ on x (Ga) content.[9]

Apart from the high spin polarization, another merit of the $Co_2Fe(Ga_{0.5}Ge_{0.5})$ is its occurrence of half-metallicity even in the B2 structure. B. S. D. Ch. S. Varaprasad *et al*[10] performed *ab initio* Density of States (DOS) calculations for Co_2FeGe, $Co_2Fe(Ga_{0.5}Ge_{0.5})$ and Co_2FeGa alloys with the $L2_1$ and B2 structures (shown in **Fig. 3-6**). The DOS of $Co_2Fe(Ga_{0.5}Ge_{0.5})$ demonstrates no minority electron states at E_F with both the $L2_1$ and B2 ordering, suggesting that the alloy is half-metallic at 0 K. Additionally, due to the fact that E_F of B2 $Co_2Fe(Ga_{0.5}Ge_{0.5})$ is at the center of the band gap, the alloy may be capable of reducing the minority state even with some A2 disorder at finite temperature. With high spin polarization as well as high thermal stability, the $Co_2Fe(Ga_{0.5}Ge_{0.5})$ has been identified as a promising material for the fabrication of CPP-GMR.

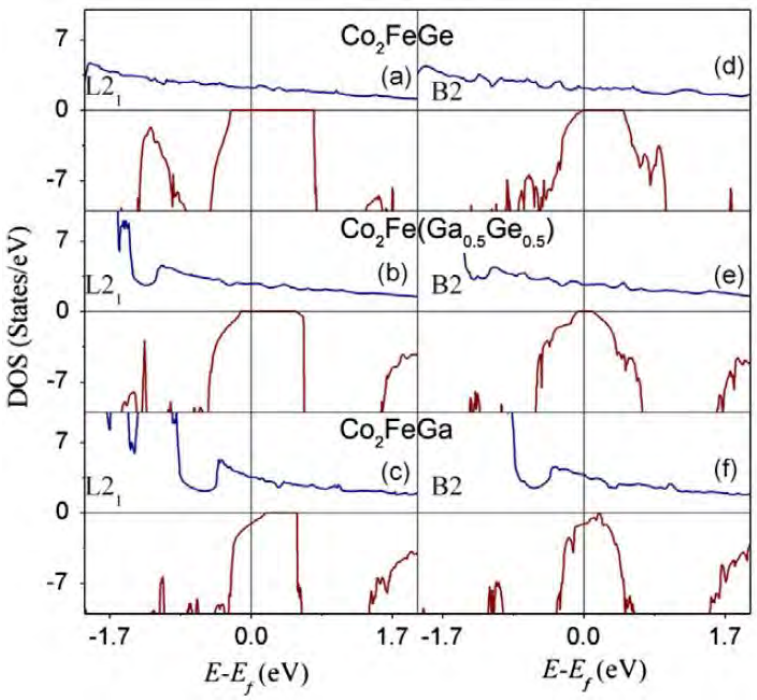

Fig. 3-6 Spin-resolved DOS of Co_2FeGe, $Co_2Fe(Ga_{0.5}Ge_{0.5})$ and Co_2FeGa alloys with the $L2_1$ and B2 structures. Courtesy of Varaprasad *et al.*[10]

3.2.3 Experiment details

Epitaxial multilayered films for pseudo spin valves (PSVs) with the layer structure of Ta(20)/W(20)/Ag(100)/$Co_2FeGa_{0.5}Ge_{0.5}$(10)/spacer(5)/$Co_2FeGa_{0.5}Ge_{0.5}$(10)/Ag(5)/Ru(8), where the numbers in the parentheses represent the thickness of each layer in nm and the spacer is either Ag or Cu, were fabricated on single-crystalline sapphire $(11\bar{2}0)$ substrates using an ultrahigh vacuum magnetron sputtering machine. The film stacking structure is showed in **Fig. 3-7**. The CFGG films were deposited using an alloy target with the composition of $Co_{45.2}Fe_{22.6}Ga_{14.2}Ge_{18}$. The chemical composition of the CFGG films was measured to be $Co_{49.3}Fe_{24.6}Ga_{12.9}Ge_{13.2}$ by inductively coupled plasma analysis. The Ta(20)/W(20) bi-layers were deposited at 200°C for buffer layers, on which 100 nm thick Ag layer was deposited at room temperature (RT) to form an electrode for measuring MR. *In-situ* annealing at 300°C was applied after the deposition of 100 nm thick Ag bottom electrode to improve the surface roughness and the rest of the films were deposited at RT. After the depositions of all the layers, the films were then *ex-situ* annealed at 250-600°C for 30 min in vacuum furnace to promote the chemical order of the CFGG layers. The films with structure of sub/Ta(20)/W(20)/Ag(100)/CFGG(10)/Ag or Cu(5)/Ru(5) were for XRD measurement, with structure of sub/Ta(20)/W(20)/Ag(100)/CFGG(5,10,30,50)/Ag(5)/Ru(5) were for VSM measurement and those with structure of sub/Ta(20)/W(20)/Ag(100)/CFGG(10)/Ag or Cu(5)/CFGG(10) /Ag(5)/Ru(8) (unit: nm) were for CPP-GMR device and TEM observation.

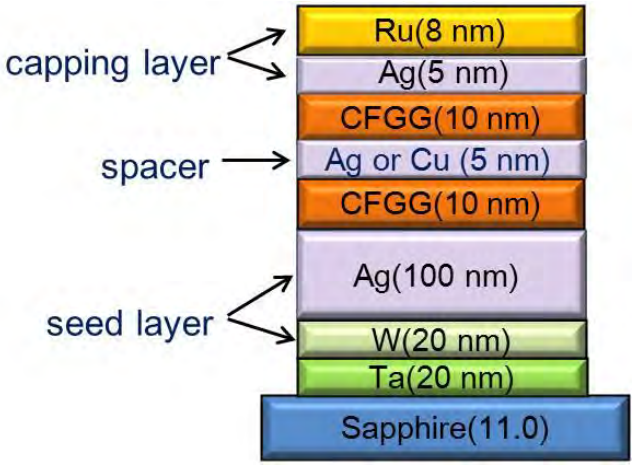

Fig. 3-7 Thin film stacking structure.

The crystal structure of the films was examined by 4-axis X-ray diffraction (XRD) using Cu-*K*α radiation. Cross-sectional transmission electron microscopy (TEM) and scanning TEM (STEM) were able to characterize the microstructure of the film stacks using images and energy dispersive X-ray spectrometry (EDS). Magnetization curves of the films were measured by a vibrating sample magnetometer (VSM). For CPP-GMR measurements, the film stacks were micro-fabricated into elliptical pillars with dimensions ranging from 70×140 to 300×600 nm^2 by electron beam lithography and Ar ion etching. The actual area of the pillar was measured by scanning electron microscopy (SEM) to enable the calculation of the resistance-

area product (RA) and the resistance change-area product (ΔRA). The magnetoresistance was measured by the direct current four-probe method in the temperature range 10–300K.

3.2.4 Crystal structure characterization

3.2.4.1 Crystal structure of multilayer films for CPP-GMR devices

As mentioned previously, the main purpose of this research is to obtain 110-oriented epitaxial CPP-GMR device. In order to check the crystal structure and confirm whether we get the orientation relationship as we design or not, we measured XRD. **Fig. 3-8** shows the 2θ-ω scan XRD profiles for the Ta(20)/W(20)/Ag(100)/CFGG(10)/spacer(5)/CFGG(10)/Ag(5)/Ru(8) film stack for both cases with Ag or Cu spacers, where the numbers in the parentheses represent the layer thickness in nm. The annealing temperature (T_a) for the device with the Ag spacer is 450°C and that for the device with the Cu spacer is kept at 350°C because the multi-layer structure of the Cu spacer deteriorates above this temperature. The W seed layer shows strong (110) peaks in both diffraction patterns, and the strong intensity of the Ag(111) peak suggests that the Ag bottom electrode for both samples and the Ag spacer are both (111)-oriented. The appearance of the CFGG(220) peaks at ~44.6° confirms that there is good (110)-oriented epitaxial growth in both films, while the Cu(111) peak indicates a similar (111) orientation for the Cu spacer.

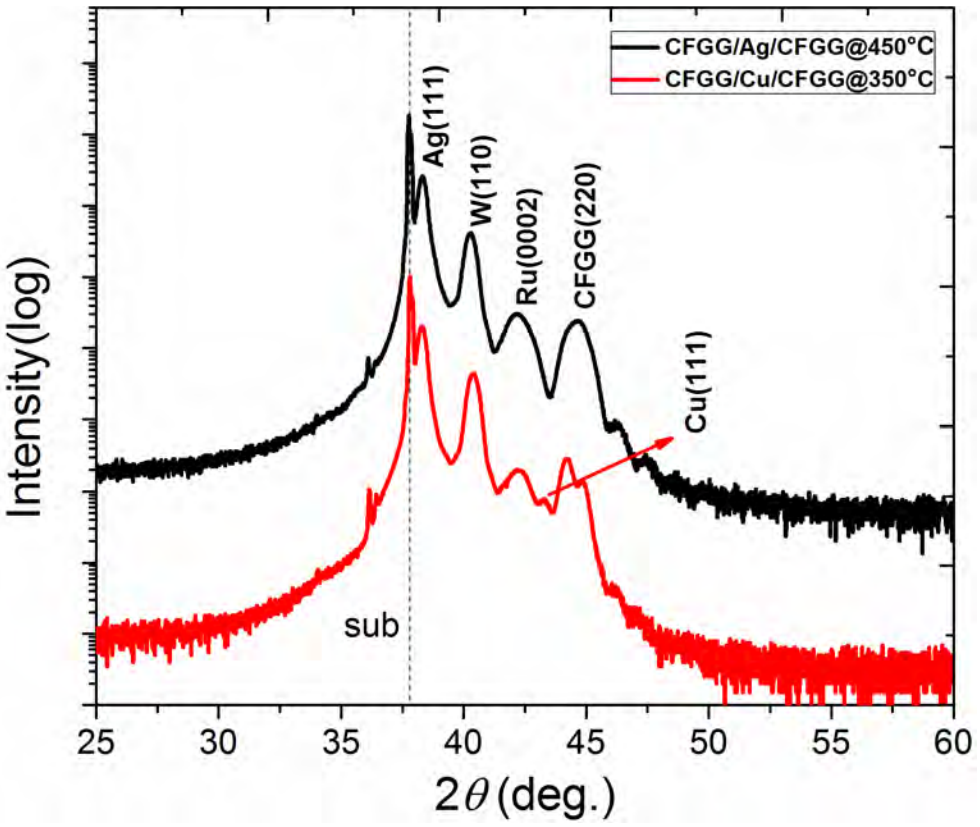

Fig. 3-8 The 2θ-ω XRD profiles of the film stacks Ta(20 nm)/W(20 nm)/Ag(100 nm)/CFGG(10 nm)/Ag annealed at 450°C and Cu(5 nm)/CFGG(10 nm)/Ag(5 nm)/Ru(8 nm) annealed at 350°C .[15]

To determine the in-plane crystallographic orientations, XRD pole-figure measurements are performed from the Ta(200), W(200), Ag(200), CFGG(400) and Cu(200) fundamental diffractions, as shown in **Fig. 3-9**. The ϕ scans of Ta(200) and W(200) show two sets of peaks, which indicate the presence of twin crystals with the [111] or $[11\bar{1}]$ direction parallel to the c-axis of sapphire. One set of (200) peaks are much stronger than the other, indicating a structure that is mostly single crystalline. However, 6-fold symmetric peaks appear in Ag and Cu, indicating two variants of the face-centered cubic crystals. The CFGG layer also exhibits 6-fold symmetric peaks corresponding to three variants with $[001]_{CFGG}$ parallel to the $[\bar{1}01]$, $[1\bar{1}0]$ and $[0\bar{1}1]$ directions of Ag, as shown in **Fig. 3-9**. The epitaxial relationship between the spacer and the Heusler alloy is the Nishiyama-Wasserman orientation relationship of $(110)[001]_{CFGG}//(111)[1\bar{1}0]_{Ag\ or\ Cu}$, which is the same as that observed in polycrystalline CFGG/Ag/CFGG devices.[11] The lattice mismatch of ~18.9% in the $[1\bar{1}0]_{CFGG}$ direction and 0.7% in the $[001]_{CFGG}$ direction are expected at the CFGG/Ag interface, which is a much larger mismatch than the 0.7% found in the (001)-oriented epitaxial PSVs. As for the device with the Cu spacer, the lattice mismatch for the (110)-oriented epitaxial film is 8.3% in the $[1\bar{1}0]_{CFGG}$ direction and 12.3% in the $[001]_{CFGG}$ direction and, overall, the mismatch is smaller than 12.3% for the (001)-oriented stack.

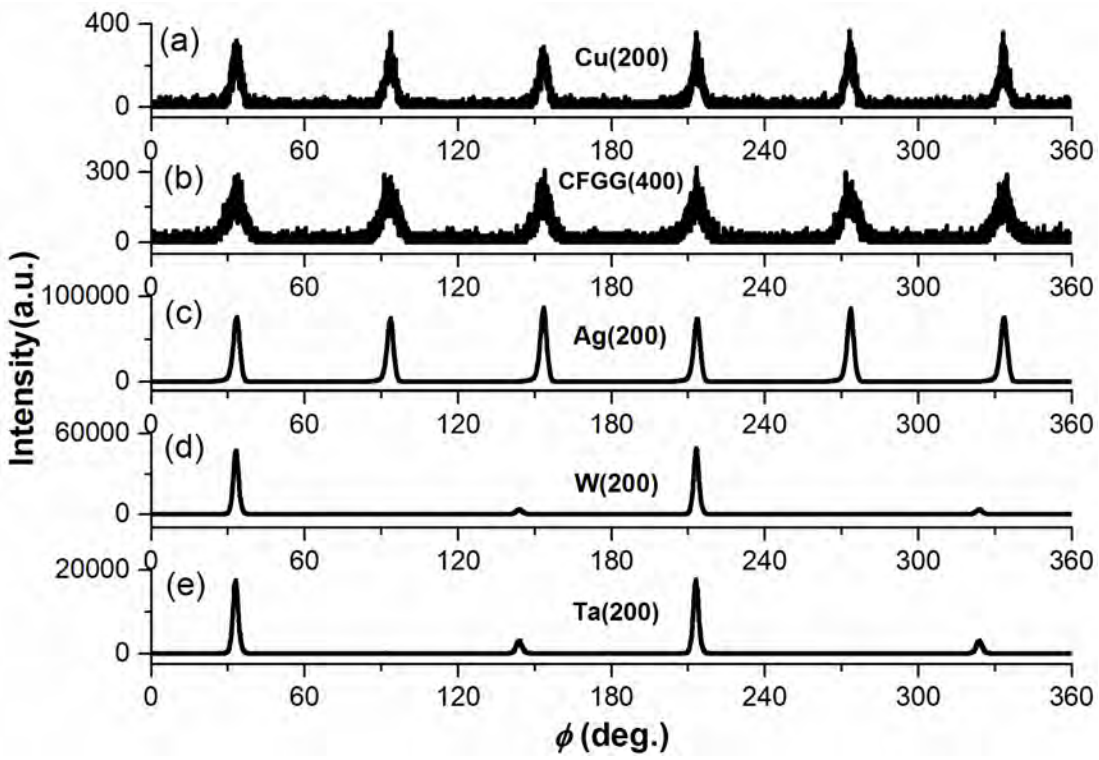

Fig. 3-9 The XRD pole-figure measurements for the (a) Cu(200), (b) CFGG(400), (c) Ag(200), (d) W(200) and (e) Ta(200) peaks for the same samples as Fig. 3-8.[15]

The chemical ordering parameter for B2 and L21 structure of the films was quantitatively evaluated from XRD profiles by calculating the peak intensity ratio of the superlattice peak to fundamental peak; (200)

to (400) for the B2 structure and (111) to (444) for the $L2_1$ structure. The ordering parameter can be defined as the following equation:

$$S_{B2} = \sqrt{\frac{(I_{002}/I_{004})_{experiment}}{(I_{002}/I_{004})_{simulation}}}$$

$$S_{L2_1} = \sqrt{\frac{(I_{111}/I_{444})_{experiment}}{(I_{111}/I_{444})_{simulation}}}$$

where I_{002} and I_{004} are the intensities of the 002 B2 superlattice and the 004 fundamental diffractions, $I_{111}$and I_{444} are the intensities of the 111 $L2_1$ superlattice and the 444 fundamental diffractions, the subscript of simulation means the simulated diffraction ratio for the perfectly ordered structure. **Fig. 3-10** shows the annealing temperature dependence of the ordering parameter estimated from the XRD profiles for CFGG single layer deposited on sapphire substrate. The degree of B2 ordering improves as increasing the annealing temperature, indicating the promotion of better ordering by applying the annealing process. In contrast, the degree of $L2_1$ ordering is not detectable until the temperature reach 500°C. At the temperature from 500°C to 600°C, even the $L2_1$ ordering parameter improve substantially, the decrement of B2 ordering suggests the occurrence of interdiffusion between the layer structure. The existence of interdiffusion will be discussed more specifically later by microstructure characterization.

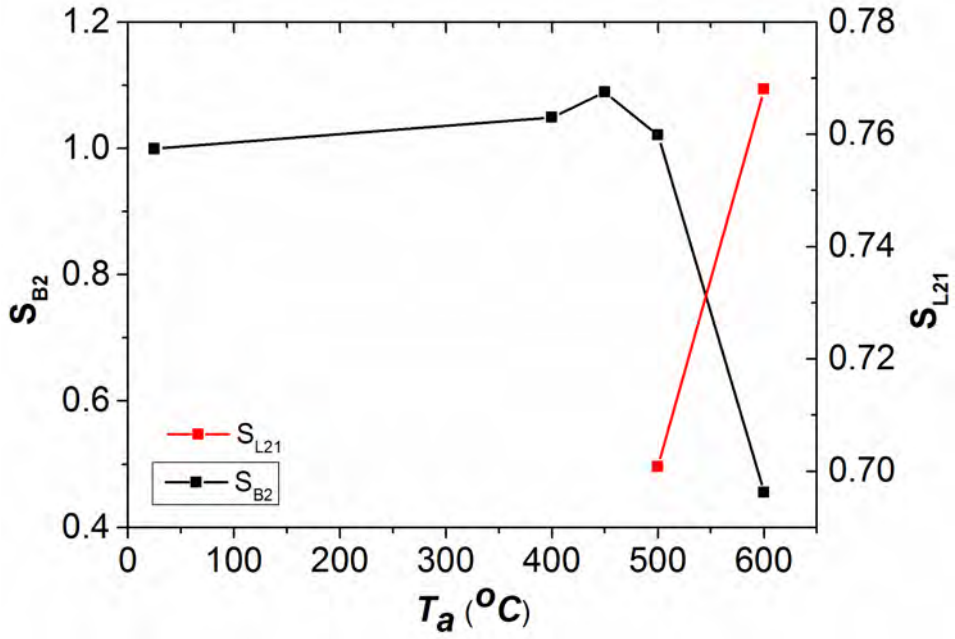

Fig. 3-10 Annealing temperature dependence of chemical ordering parameter for CFGG single layer.

3.2.4.2 Lattice matching between ferromagnetic layer and spacer

From the diffraction peak in the XRD profile, we calculated the out-of plane lattice parameter $a_\perp$ of Heusler alloy layer and the spacer. **Fig. 3-11(a)** summarized the dependences of $a_\perp$ of the CFGG and Ag films on the annealing temperature, respectively.

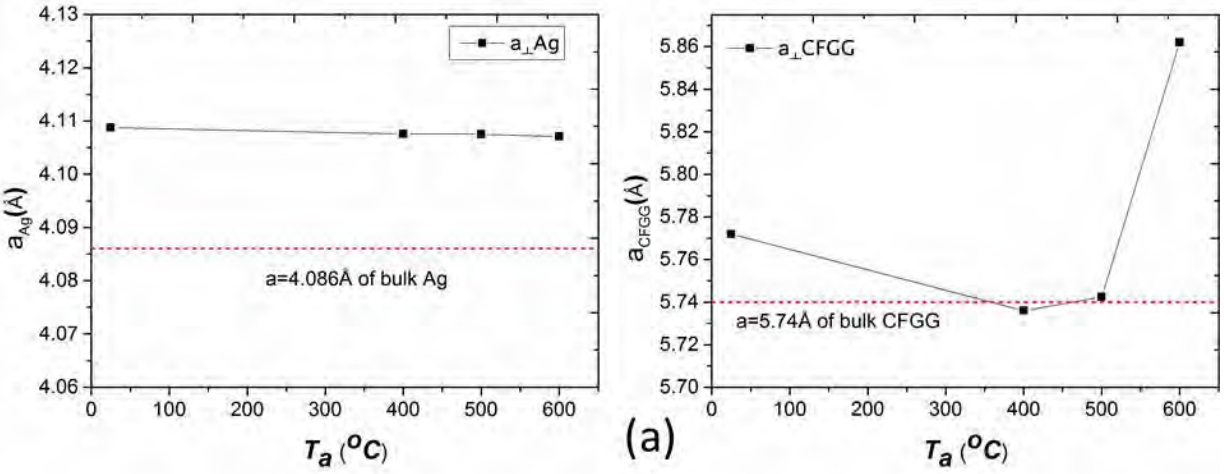

Fig. 3-11(a) Variations of out-of-plane lattice parameter of CFGG and Ag for different annealing temperature in (110)-oriented films.

For Ag spacer system, $a_\perp$ of Ag films are larger than that of the bulk material. This is probably because the in-plane lattice constant of Ag is larger than that of the CFGG layer so that the Ag crystal has to expand in out-of-plane direction and shrink in in-plane direction to match with CFGG crystal. At the same time, the CFGG crystal is try to shrink in out-of-plane direction and expand in in-plane direction to reduce the discrepancy at CFGG/Ag interface. The sudden jump of the lattice constant at high annealing temperature can be understood by the structure change by interdiffusion.

Fig. 3-11(b) summarized the dependences of $a_\perp$ of the CFGG and Cu films on the annealing temperature, respectively. For Cu spacer system, similar result can be seen with the Ag spacer system. Since the difference of the in-plane lattice constant between Cu and CFGG is smaller, the deformation of the crystal is not as obvious as the Ag spacer.

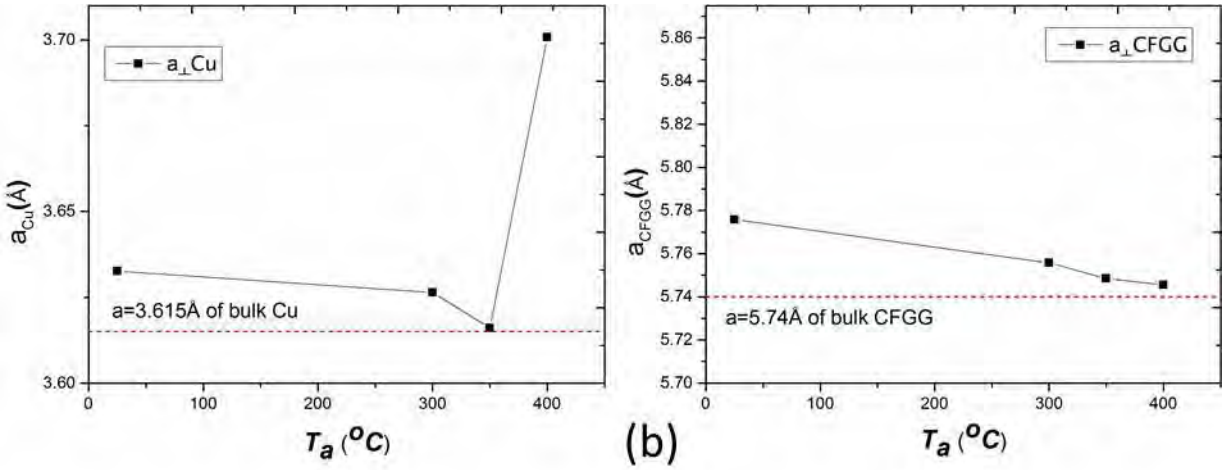

Fig. 3-11(b) Variations of out-of-plane lattice parameter of CFGG and Cu for different annealing temperature in (110)-oriented films.

The analysis of in-plane lattice mismatch at CFGG/spacer interface for (110) orientation devices was estimated, as shown in **Fig. 3-12(a)**. For comparison, lattice mismatch for (001)-oriented devices was presented as well, **Fig. 3-12(b).**

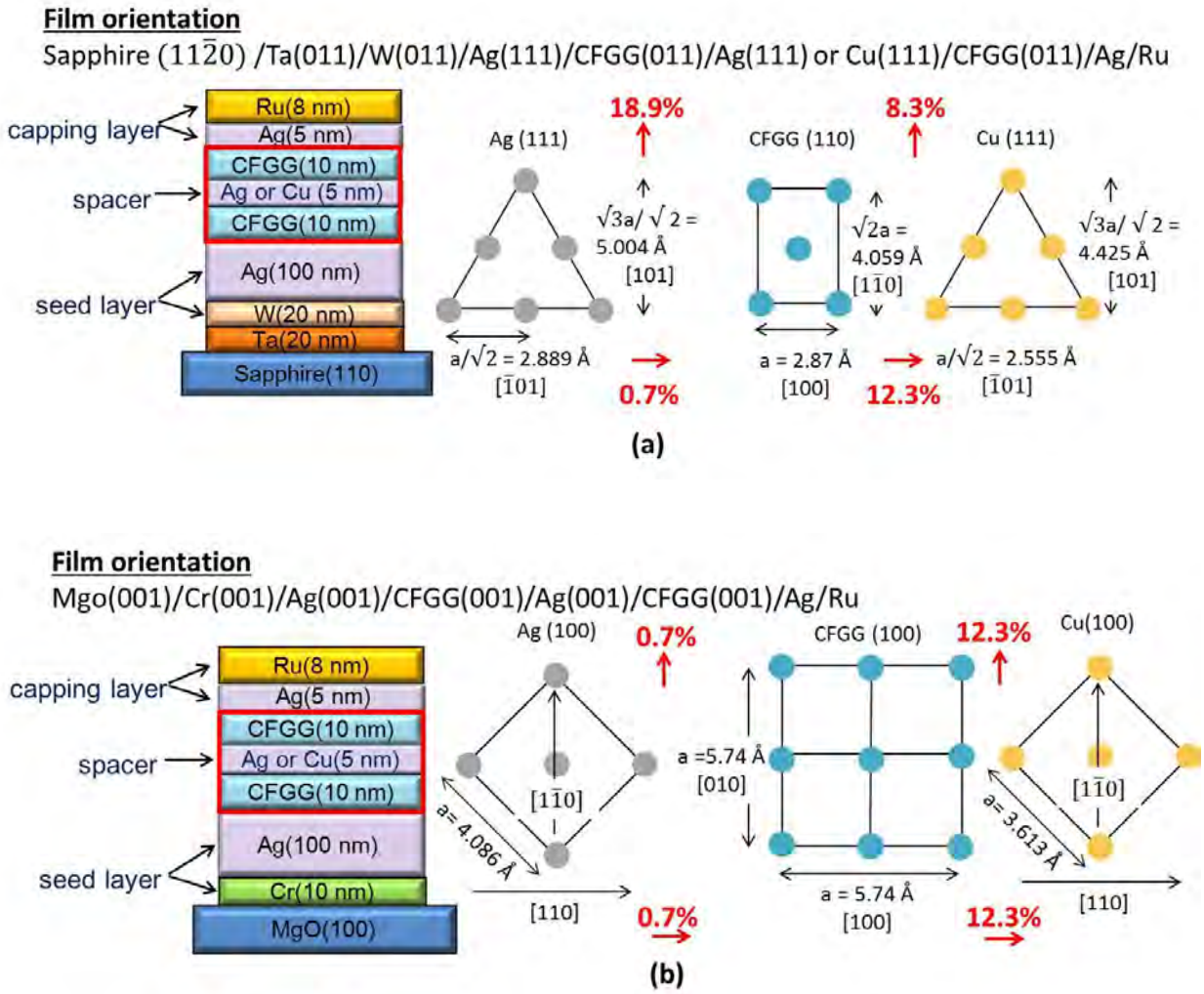

Fig. 3-12 The analysis of lattice mismatch for (a) (110)-oriented device (b) (001)-oriented device.

3.2.5 Magneto-transport properties

3.2.5.1 Measurement of the lead resistance

The actual pillar sizes were measured by scanning electron microscopy (SEM) for all the samples. **Fig. 3-13** shows the SEM image of typical reference pillars of sizes (a) 70×140 nm, (b) 100×200 nm, (c) 150×300 nm, (d) 200×400 nm (e) 300×600 nm. All the actual pillar areas were in good agreement of the designed value. In order to determine the lead resistance of the devices after microfabrication, the resistance of the devices was plotted as a function of the inverse of CPP-GMR pillar area (**Fig. 3-14**). According to the following formula:

$$R_{device} = \rho \cdot l \cdot \frac{1}{Area} + R_{lead}$$

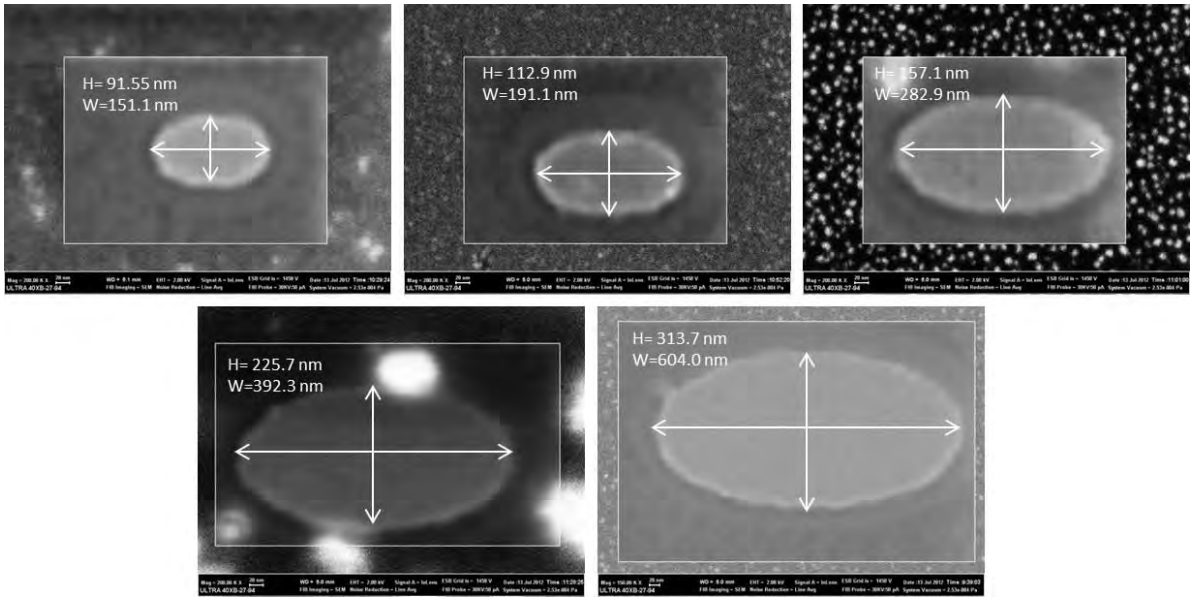

Fig. 3-13 SEM image of CPP-GMR reference pillar

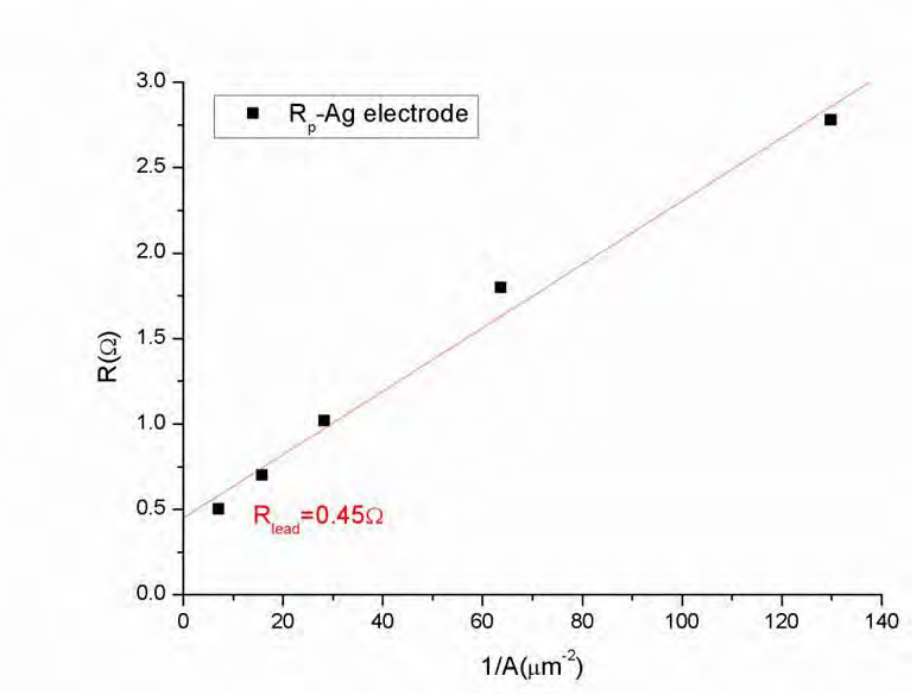

Fig. 3-14 Resistance of the CPP-GMR devices as a function of the inverse of CPP-GMR pillar area.

where the ρ was the average resistivity of the pillar, l was the thickness of the pillar. The lead resistance could be determined from the Y-axis intercept of **Fig. 3-14**, which was approximately 0.45 Ω. This resistance was slightly larger than that determined from the (001)-oriented epitaxial PSV devices, which was around 0.3 Ω. The reason for this increase was the different materials in the underlayer and the different interfacial resistance between the Ag bottom electrode and the tri-layer. Normally, in the (001)-oriented devices, Cr was used under the Ag electrode. But in these (110)-oriented devices, 20 nm Ta and W were used under the Ag electrode, which might give us a different contact resistance when current was applied. Moreover, the large

lattice mismatch between the Ag bottom electrode and the CFGG layer in (110)-oriented devices, which could generate the defect that scattered the electron, might contribute to the larger lead resistance as well.

3.2.5.2 Room temperature magneto-transport properties

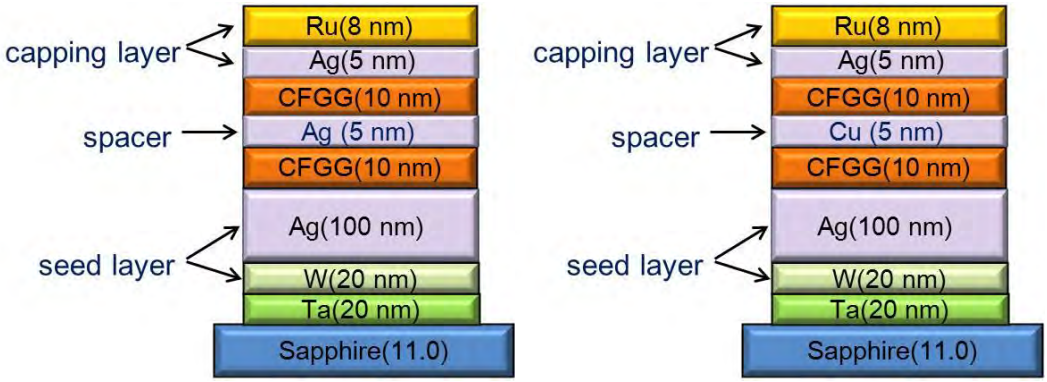

Fig. 3-15 Film structure for CPP-GMR devices.

The structure of CPP-GMR device for magneto-transport properties measurement was described in **Fig. 3-15**. The structure and the thickness of the tri-layers in (110)-oriented CPPGMR devices were designed as CFGG(10nm)/Ag or Cu(5nm)/CFGG(10nm) in this study, which is the same stacking structure as our previous study in (001)-oriented CPPGMR devices[12,13]. For comparison, the MR properties of the (001)-oriented CPPGMR devices with Ag and Cu spacer were plotted in **Fig. 3-16 and Fig. 3-17** as well, where the data for CFGG(001)/Ag(001)/CFGG(001) PSVs and CFGG(001)/Cu(001)/CFGG(001) PSVs were taken from our other works in Refs. 12,13.

a) Ag spacer

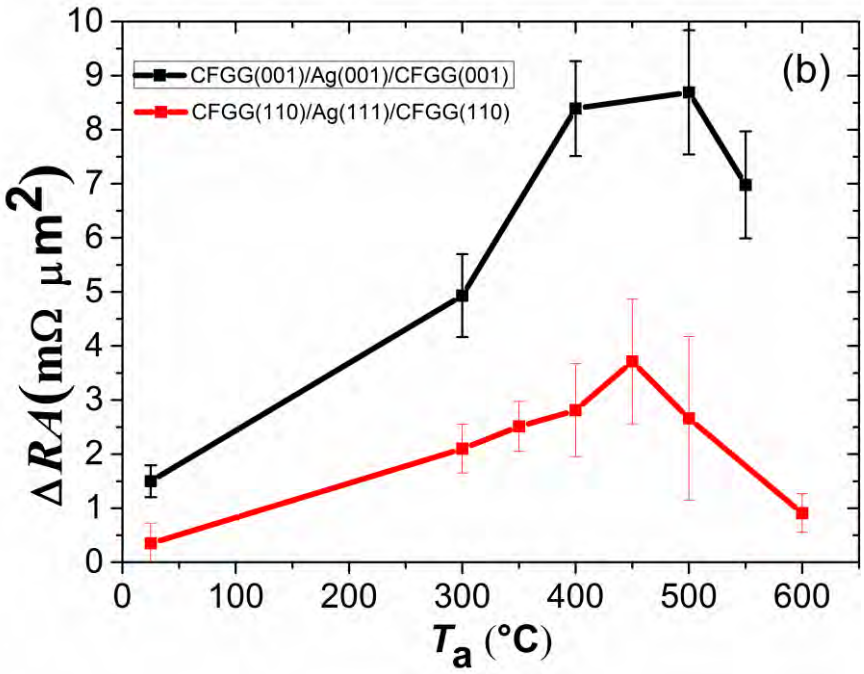

Fig. 3-16 Annealing temperature dependence of Δ*RA* for the epitaxial PSVs with Ag spacer.[15]

In **Fig. 3-16**, we plot the MR output as a function of annealing temperature in two different orientation devices both with Ag spacer. The black curve represents the 001 orientation and the red one stands for 110 orientation. After changing the orientation of the FM layer from (001) to (110), both the MR ratio and the ΔRA value of the CFGG(110)/Ag(111)/CFGG(110) PSVs drop significantly in the whole annealing temperature range. The MR output increases with raising the annealing temperature up to 450°C, thereafter it drops with a further increase in annealing temperature. The origin of this increment can be understood by the improvement of the B2 order of the CFGG film according to the same tendency results reported by Varaprasaed et.al.[10] And the decrement of the output above 450°C is because of the interdiffusion in the layer structure, which was shown by the EDS mapping. Note that the optimal annealing temperature of the (110)-oriented device with Ag spacer is 50°C lower than that of the (001)-oriented device, which indicates a less stability of the CFGG(110)/Ag(111) interface. This is mainly because a larger lattice mismatch of 18.9% in $[1\bar{1}0]_{CFGG}$ direction at the CFGG/Ag interface has also been introduced while we change the orientation from (001) to (110).

b) Cu spacer

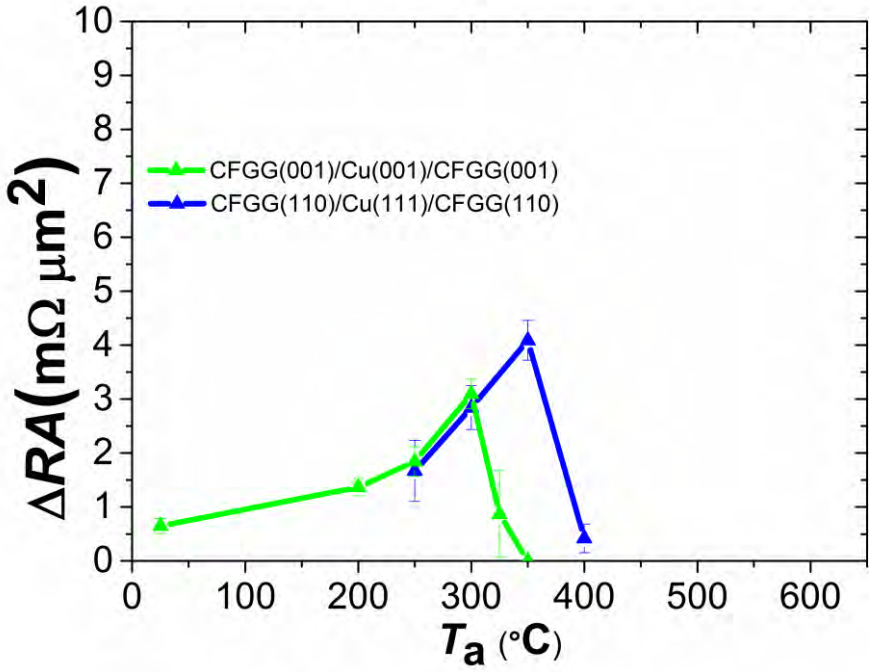

Fig. 3-17 Annealing temperature dependence of Δ*RA* for the epitaxial PSVs with Cu spacer.[15]

Fig. 3-17 summarizes ΔRA dependence on the annealing temperature for Cu spacer devices. For the samples with the Cu spacer, the MR output shows similar values for (110) and (001) oriented CFGG layers. Interestingly, unlike the deterioration of magneto-transport property in CFGG(110)/Ag(111)/CFGG(110) PSVs, an enhancement of MR output can be seen from the CFGG(110)/Cu(111)/CFGG(110) PSVs after varying the orientation. The MR output keep improving with increasing annealing temperature and reach a maximum at 350°C for CFGG(110)/Cu(111)/CFGG(110) device, while the CFGG(001)/Cu(001)/CFGG(001) device stops at

300°C. This enhancement can be explained by the improvement of interface stability of CFGG(110)/Cu(111) interface comparing with CFGG(001)/Cu(001) interface due to a better interface lattice matching as mentioned in the XRD section.

c) Discussion

In summary, after changing the orientation from (001) to (110), we have introduced a larger mismatch for Ag spacer but a smaller one for Cu spacer, as illustrated in **Fig. 3-18**. The difference of MR output in these four kinds of devices is strongly relative to lattice matching between the CFGG layer and the spacer. The result suggests that an improvement of GMR ratio can be obtained by selecting an appropriate orientation relationship between the FM layer and the spacer. It is worth mentioning that such improvement in the relative low annealing temperature region is valuable for practical application, because commercialized CPP read-back sensors (MTJs or CPP-GMR) cannot be subjected high temperatures above 400°C due to the current process limit[14].

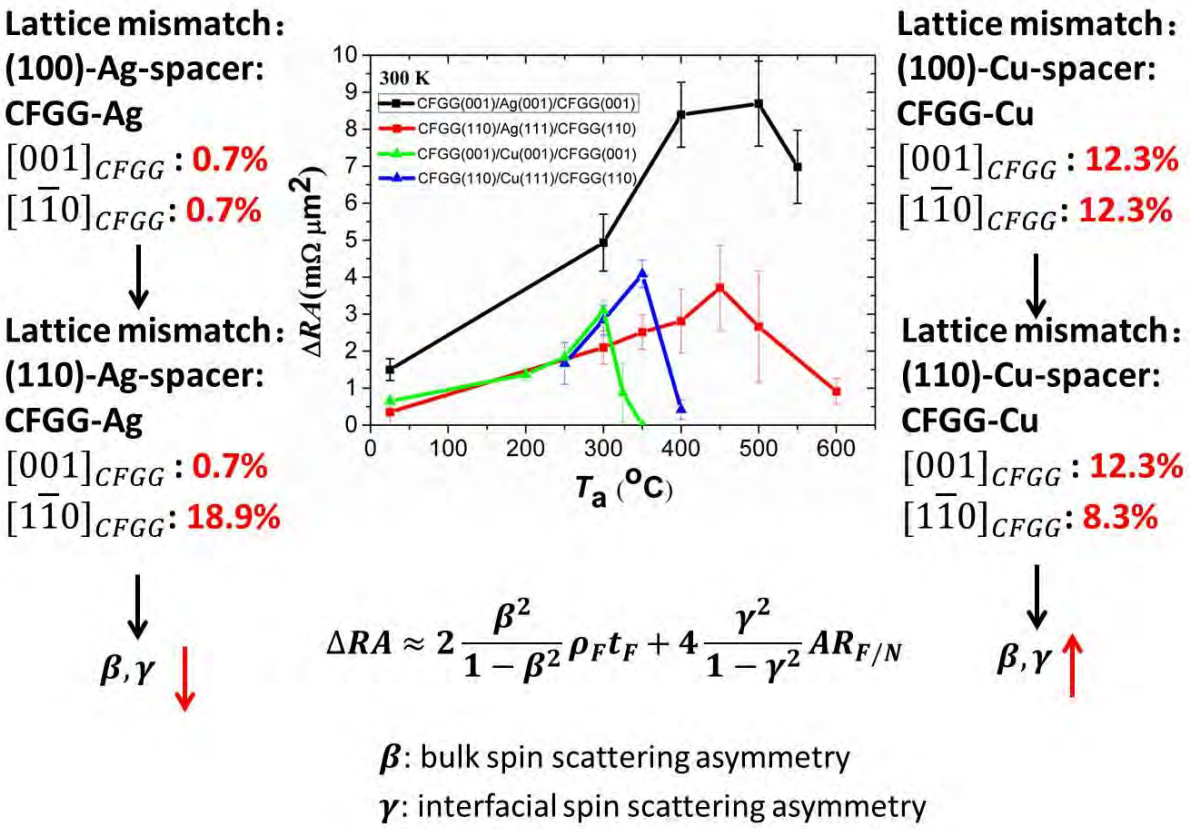

Fig. 3-18 Relation between the change of MR output and the change of lattice mismatch.

3.2.5.3 Low temperature magneto-transport properties

Fig. 3-19 shows the typical MR curves of an optimally annealed CFGG(10 nm)/Cu(5 nm)/CFGG(10 nm) and CFGG(10 nm)/Ag(5 nm)/CFGG(10 nm) PSVs measured at 10K and 300K, respectively. The CFGG(110)/Cu(111)/CFGG(110) device shows a maximum MR ratio and ΔRA value of 21.9% and 4.1 mΩ·μm^2 at 350°C, which is even higher than that of 19.8% and 3.7 mΩ·μm^2 at 450°C in

CFGG(110)/Ag(111)/CFGG(110) device. At 10K, both devices are enhanced giving a value of 53.9%, 10.1 mΩ·μm2 for Cu spacer and 45.7%, 8.1 mΩ·μm^2 for Ag spacer.

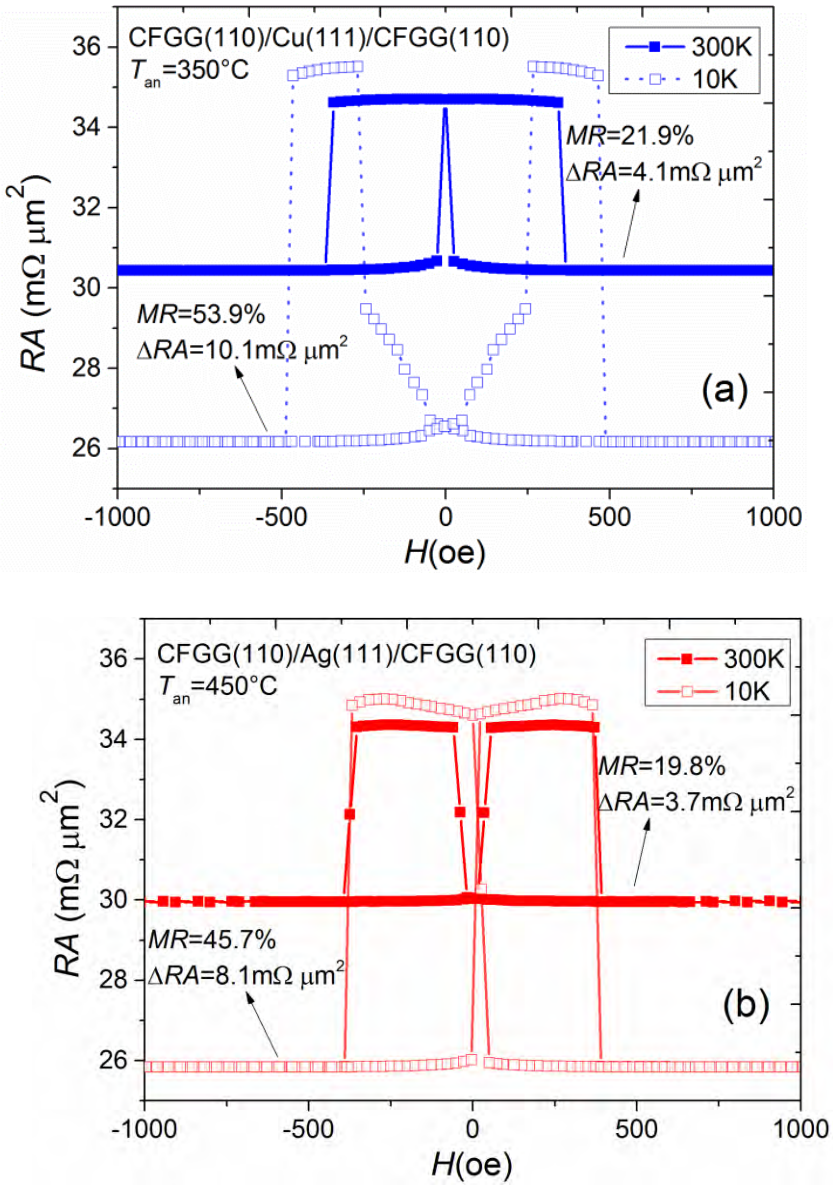

Fig. 3-19 The MR curve of the optimally annealed (a) CFGG(110)/Cu(111)/CFGG(110), (b) CFGG(110)/Ag(111)/CFGG(110) PSVs at 10K (open square) and 300K (solid square).[15]

The field dependence of the MR for the Cu spacer is somewhat different than that of the Ag spacer, and this difference may derive from the different temperature dependence of the magnetic anisotropy of the two materials or the interlayer exchange couplings, although the details are still unclear.

3.2.6 Magnetic property

3.2.6.1 Saturation magnetization and coercivity

The magnetization of magnetic Heusler alloys is strongly related to the degree of structural order, hence the film magnetization can be used as a parameter to represent the structural quality and the effect of annealing on structure. To further estimate the quality of the (110)-oriented CFGG films, we measured the annealing temperature dependence of the saturation magnetization M_s, coercivity H_c as shown in **Fig. 3-20**. The saturation magnetization value of two different spacer systems keep increasing as the annealing temperature increased, demonstrating the ordering improvement of the CFGG film, thereafter decrement started to occur at certain temperature, indicating the interdiffusion between the CFGG and spacer. In addition, the sudden increase of coercivity above 350°C for Cu spacer and 500°C for Ag spacer also explained the existence of interdiffusion. The annealing temperature dependence of saturation magnetization showed a similar changing tendency with the MR output of the devices shown in **Fig. 3-18**. but please note that there is a about 50°C delay of the performance decrement in the M_s, which is simply because the MR output that we measured in nano scale devices is more sensitive to interdiffusion. Apart from this, the maximum of M_s value of 868.6 emu/cc in Ag spacer films appeared at 500°C, while a slightly higher value of 882.7 emu/cc in Cu spacer films showed at 400°C. However, either of these two values is much smaller than the theoretical CFGG bulk value (~1100 emu/cc)[10] or the M_s value that measured in the (001)-oriented CFGG epitaxial film, which means that these two kinds of films are still far from the perfect structure.

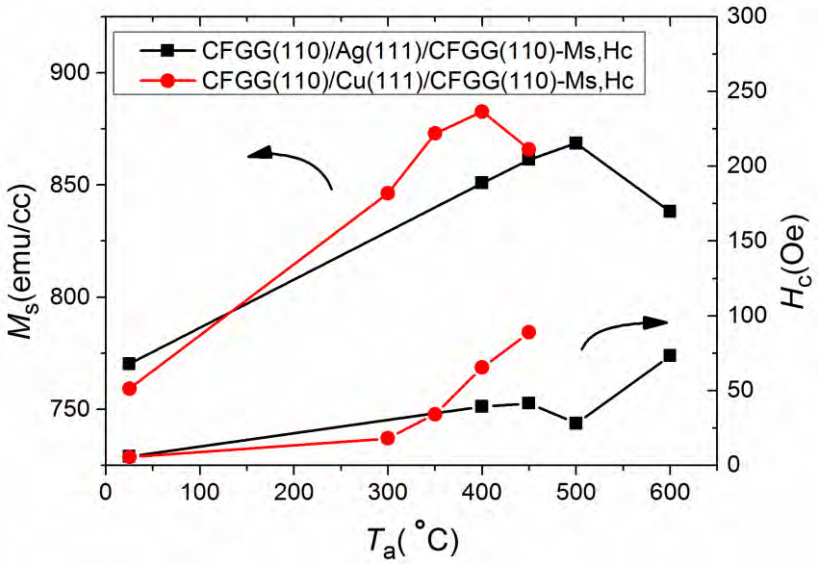

Fig. 3-20 Annealing temperature dependence of the saturation magnetization and coercivity in (110)-oriented devices with an Ag (black squares) or Cu (red circles) spacer.[15]

3.2.6.2 Magnetic dead layer

For very thin films, the degree of crystalline order in CFGG also depends greatly on the underlayer that it grows, especially in the as-deposited state. As we mentioned previously, a large lattice mismatch between Ag and CFGG layers has also been introduced after changing the orientation from (001) to (110). In order to investigate how this large lattice mismatch affected the CFGG layer quality, we fabricated two different oriented CFGG layers annealed at different temperatures to compare their magnetic properties. Their film structures are as follow:

① Ta(20nm)/W(20nm)/Ag(100nm)/CFGG(5,10,30,50nm)/Ag(5nm)/Ru(5nm) on sapphire a-plane substrate

② Cr(10nm)/Ag(100nm)/CFGG(5,10,30,50nm)/Ag(5nm)/Ru(5nm) on MgO(001) substrate

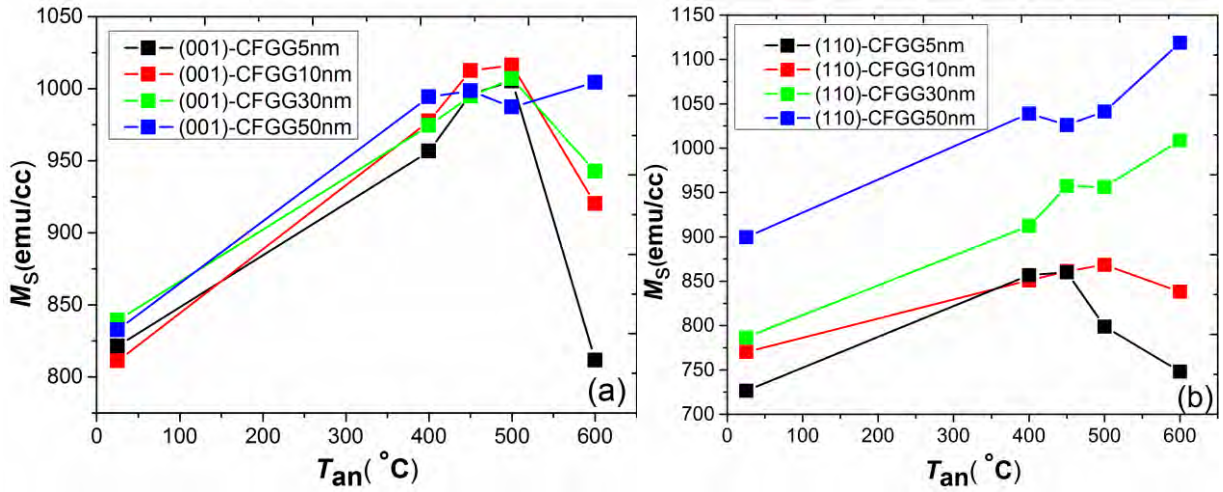

Fig. 3-21 Annealing temperature dependence of saturation magnetization in (a) (001)-oriented, (b) (110)-oriented CFGG single-layer films with different thickness.

Normally, for a perfect single CFGG thin film, the saturation magnetization value should be a constant no matter what thickness it is as shown in **Fig. 3-21(a)**. However, from **Fig. 3-21(b)**, we can see that the saturation magnetization increases not only with the increment of the annealing temperature, but also with the increment of the CFGG thickness in (110)-oriented films. At the thickness of 50 nm, the Ms is close to a bulk value of 1100 emu/cc. This result indicates that a large thickness of magnetically "dead" layer exists at the CFGG(110)/Ag(111) interface.

To calculate the actual thickness of the magnetic dead layer, we plot of the saturation magnetization/unit film area (M_s/A) value as a function of the CFGG layer thickness (t_F). The intercept of the M_s/A- t_F plot represents the thickness of the magnetic dead layer between CFGG and Ag under/capping layers as shown in **Fig. 3-22**. In **Fig. 3-22(a)**, the value of magnetic dead layer of the as-deposited CFGG(001) film is 0.07 nm. The dead layer thickness decreases to 0.03 nm by annealing at T_{an} = 450°C. Both these two magnetic dead layer thickness are negligibly small which indicates an almost perfect interface without defects between CFGG(001) and Ag(001) layer. This result is in good agreement with the TEM result reported in Ref.9. The dead layer thickness increases abruptly up to 0.63 nm at T_{an} = 600°C which can be understood by the occurrence of interdiffusion. In **Fig. 3-22(b)**, the temperature dependence of the magnetic dead layer thickness in CFGG(110) film shows the similar trend. That is the dead layer thickness decreases from 0.96 nm at as-deposited state to 0.78 nm at T_{an} = 450°C, then rise to 1.31 nm at T_{an} = 600°C. However, the dead layer thickness in CFGG(110) film is much larger than that in CFGG(001) film. This points out that the interface condition in (110)-oriented film is much inferior to that in (001)-oriented film due to the bad lattice matching. Although the samples shows well defined layered structure up to the optimal annealing temperature, the MR output is significantly lower than that obtained in the devices with (001) oriented epitaxial layers. This degradation would be attributed to the presence of large magnetic dead

layer at the interface of CFGG/Ag suggested by the magnetization measurements. The decrease of the magnetic moment results in the reduction of the interfacial spin asymmetry coefficient γ. In contrast, the magnetic moment at the interface is not dead and induces large value of γ in the (001)-oriented CFGG/Ag/CFGG devices. That is why we get a large difference of MR output even at the same annealing temperature after changing the orientation from (001) to (110) in the case of Ag spacer as shown in **Fig. 3-16**.

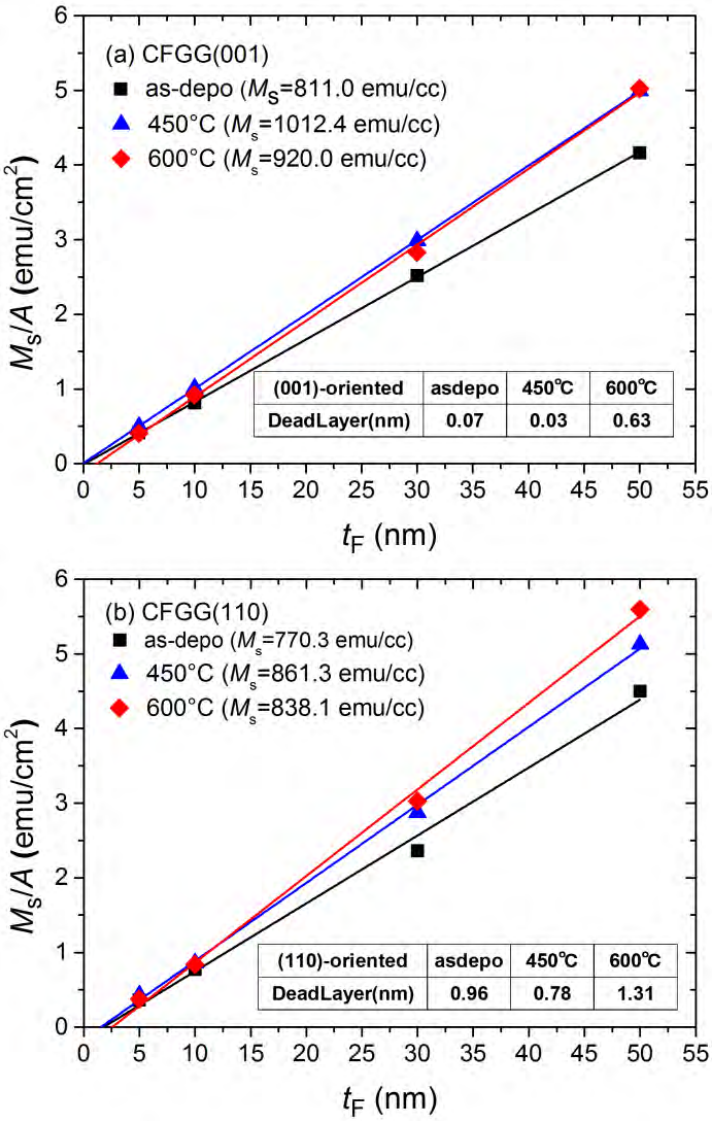

Fig. 3-22 Plots of M_s/A versus CFGG layer thickness (t_F) (a) in an (001)-oriented CFGG film and (b) in a (110)-oriented CFGG film.[15]

3.2.7 Microstructure

A TEM is used to characterize the samples in TEM and STEM modes, whereby it is possible to examine the device microstructure to aid in understanding its effect upon the MR properties. The specimen layer structure is Ta(20 nm)/W(20 nm)/Ag(100 nm)/CFGG(10 nm)/Ag or Cu(5 nm)/CFGG(10 nm)/Ag(5 nm)/Ru(8 nm), which is identical to that used for the CPP-GMR devices.

3.2.7.1 EDS mapping

a) Ag spacer

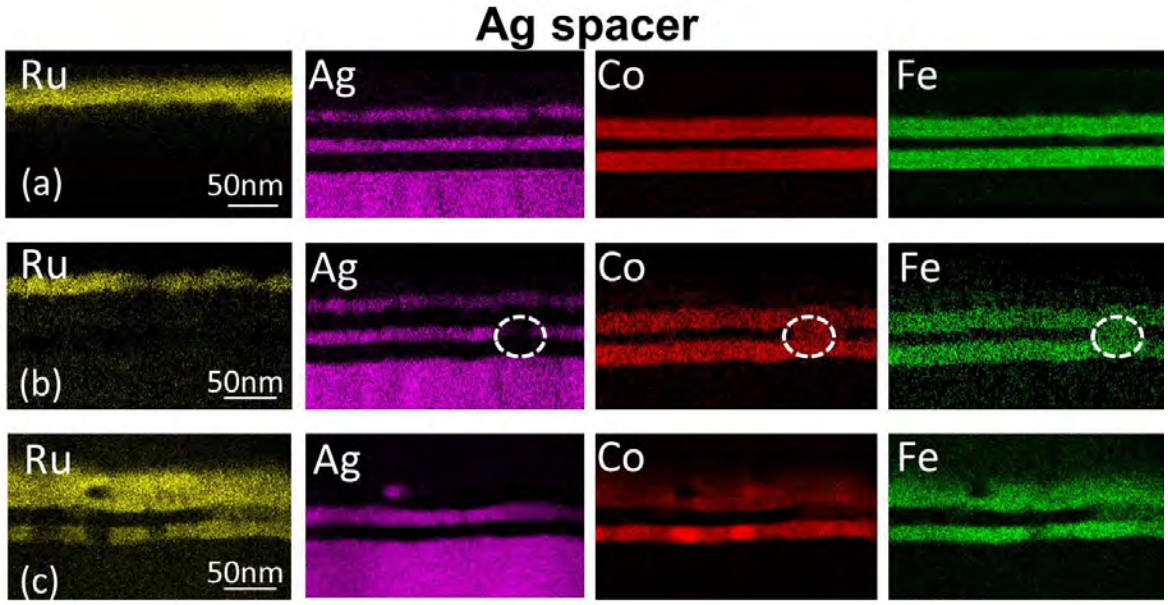

Fig. 3-23 EDS spectral mapping of Ru, Ag, Co and Fe in the CFGG(110)/Ag(111)/CFGG(110) film annealed at (a) 450°C, (b) 500°C, and (c) 600°C.[15]

Fig. 3-23(a)-(c) present EDS elemental mapping of the cross-section of the specimens for Ag spacer CPP-GMR devices. **Fig. 3-23(a)** shows the result derived from the CFGG(110)/Ag(111)/CFGG(110) PSVs annealed at the optimal Ta of 450°C. Here we can see a well-defined tri-layer structure with no visible interdiffusion. The sample annealed at 500°C (**Fig. 3-23(b)**) exhibits a small region in the Ag spacer that is void of Ag and in which Co, Fe and Ge are detected, which indicates the onset of diffusion between the CFGG layer and the Ag spacer. When we further increase Ta up to 600°C, serious deterioration of the layered structure is observed, as shown in **Fig. 3-23(c)**. The Ru and Ag layer diffuse toward the bottom CFGG layer while the upper CFGG layer diffuses toward the capping layer to reduce the large interfacial energy originating from the large misfit at the CFGG(110)/Ag(111) interface.

b) Cu spacer

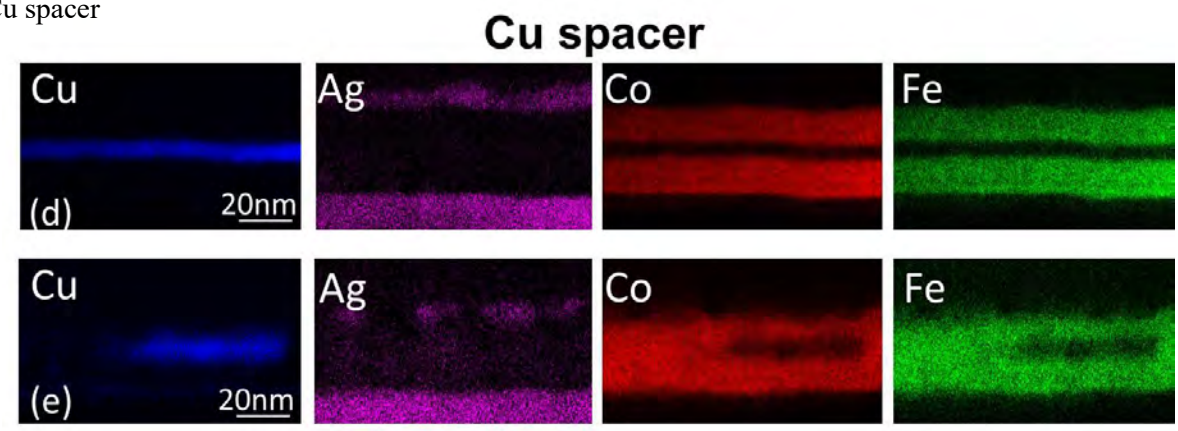

Fig. 3-23 EDS spectral mapping of Cu, Ag, Co and Fe in the CFGG(110)/Cu(111)/CFGG(110) film annealed at (d) 350°C and (e) 400°C.

In contrast, the CFGG(110)/Cu(111)/CFGG(110) PSVs annealed at 350°C exhibit a uniform and continuous tri-layer structure (**Fig. 3-23(d)**), which results in the higher MR output of these devices compared with the CFGG(001)/Cu(001)/CFGG(001) PSV. Note that serious interdiffusion has already occurred in the CFGG(001)/Cu(001)/CFGG(001) PSVs at the T_a reported in Ref.12. This provides further evidence of interface stability improvement in CFGG(110)/Cu(111)/CFGG(110) PSVs, which is achieved by changing the orientation to reduce the lattice mismatch at the interface. When T_a is raised to 400°C, serious interdiffusion occurs in the CFGG(110)/Cu(111)/CFGG(110) PSV as well, whereby the tri-layer structure is totally destroyed and the layers mix together (**Fig. 3-23(e)**).

3.2.7.2 TEM images

a) Ag spacer

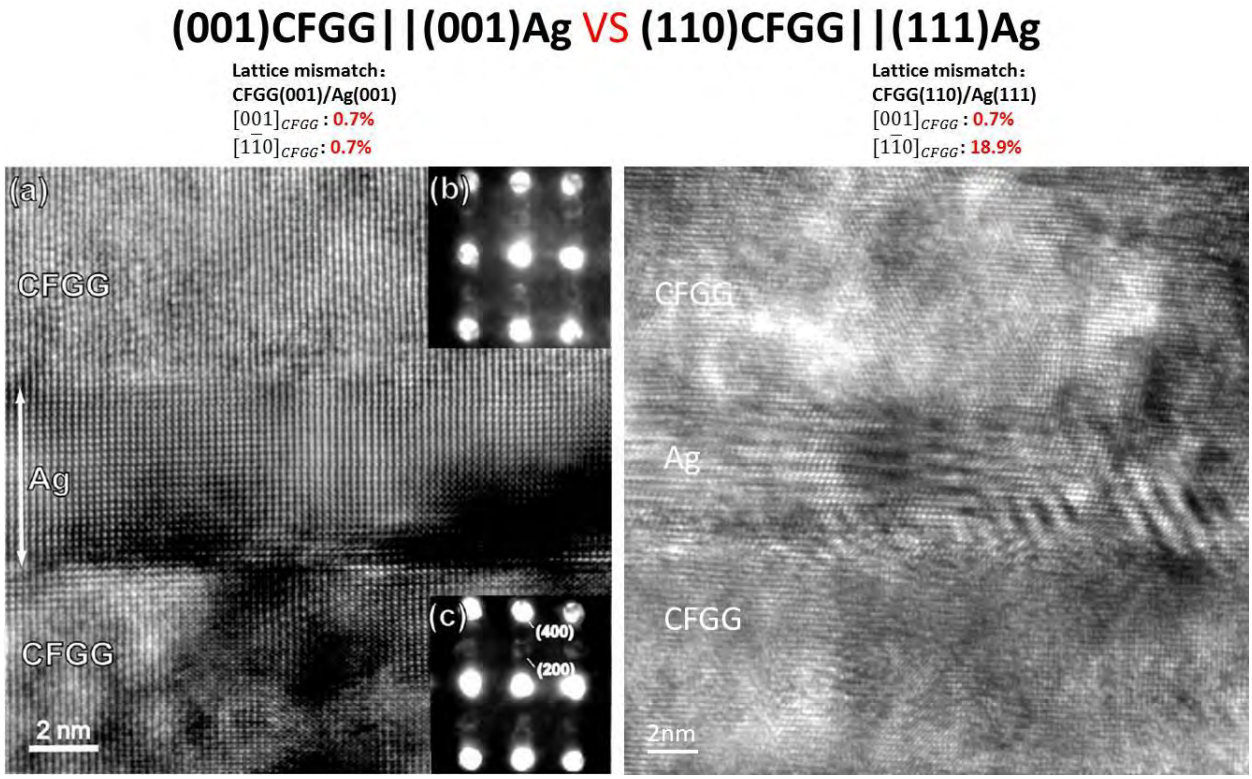

Fig. 3-24 Cross-sectional high resolution TEM images of CFGG/Ag/CFGG trilayer structure in left: (001)-oriented device[9], right: (110)-oriented device.

Fig. 3-24 compares the interface condition for trilayer structure in two different oriented devices. From the images, we can see the (001)-oriented devices give a much better layer structure than the (110)-oriented devices, which can explain the large differences of lattice matching, dead layer thickness and MR output well.

b) Cu spacer

In **Fig. 3-25**, we provide a cross-sectional TEM bright field image of CFGG(110)/Cu(111)/CFGG(110) PSVs annealed at the optimal temperature of 350°C. An unmistakable

tri-layer structure can be seen, which is in agreement with the EDS result. Many defects, including lattice distortions and dislocations, are observed at the CFGG/Cu and CFGG/Ag interfaces owing to the large lattice mismatch. Measuring from the high-resolution transmission electron microscopy (HRTEM) image, the defect interface region is as large as ~1 nm at the CFGG/Cu interface and ~1.3 nm at the CFGG/Ag interface, and is the reason for the large magnetic dead layer thickness in the magnetic properties result.

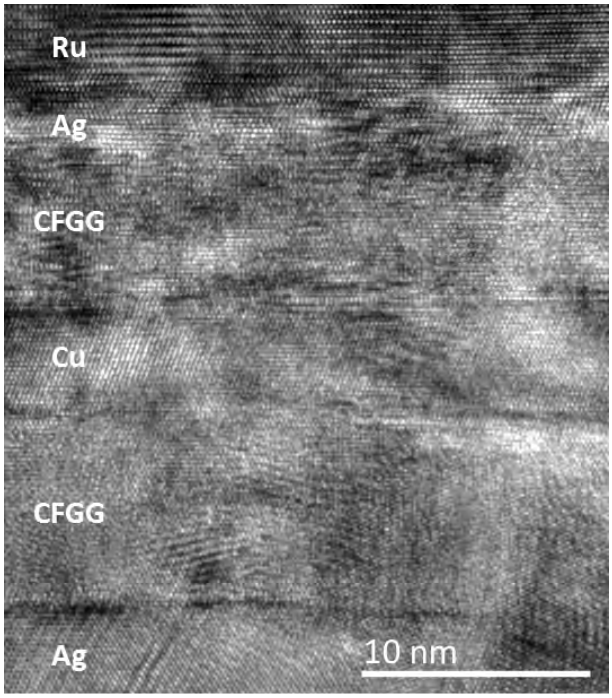

Fig. 3-25 Cross-sectional TEM bright field image of the (110)-oriented device with the Ag(100 nm)/CFGG(10 nm)/Cu(5 nm)/CFGG(10 nm)/Ag(5 nm)/Ru(8 nm) structure after annealing at 350°C.[15]

3.3 (110)-oriented CPP-GMR devices with NiAl spacer

In our previous study using epitaxial CPP-GMR devices, we found the change of crystal orientation in $Co_2FeGa_{0.5}Ge_{0.5}$(CFGG)/Ag system had introduced a different lattice mismatch at CFGG/Ag interface resulting in various MR outputs, i.e., the CPP-PSV with (001)CFGG/(001)Ag interface showed higher MR output than that with (011)CFGG/(111)Ag interface.[15] The influence of lattice matching on the interfacial spin scattering asymmetry is considered to be the main reason for the ΔRA value difference. However, how the band matching changes according to different crystal orientation is still unclear, because both lattice matching and band matching change when we alter the crystal orientation in the CFGG(bcc)/Ag(fcc) system. To focus only on the band matching influence, we prepared CPP-GMR PSVs consisting of CFGG and B2 NiAl alloy for a spacer for their good lattice and band matching demonstrated by Nakatani et al.[16] In addition, this combination is free of lattice matching influence depending on the crystal orientation because both alloys have the same crystallographic symmetry (see **Fig. 3-26**). The effects of the crystal orientation on

band matching were examined by comparing with the MR output in (001)CFGG and (110)CFGG orientations.

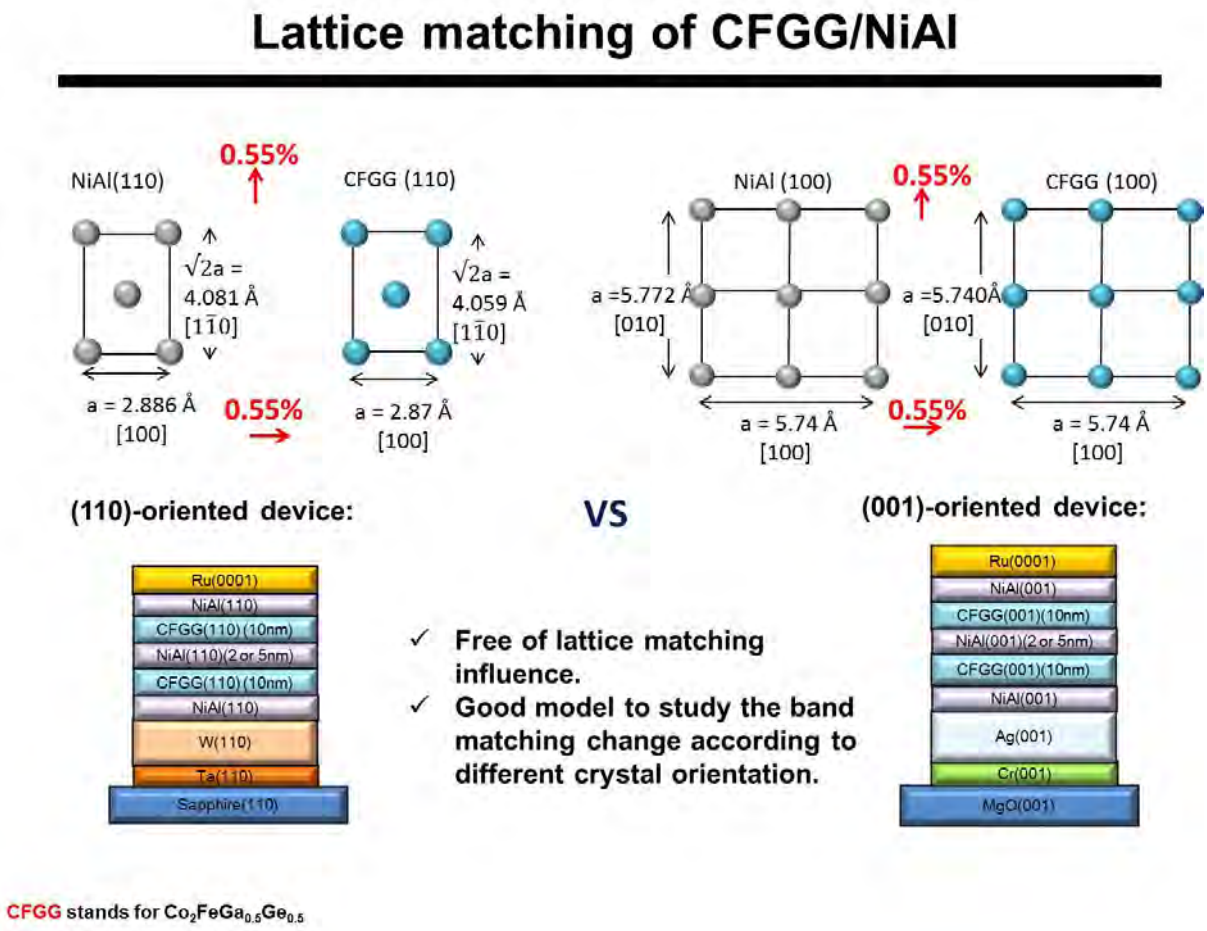

Fig. 3-26 Illustration of lattice matching between NiAl and CFGG in (110) and (001) orientation.

3.3.1 Usage of NiAl as buffer layer

NiAl is not only a good candidate for spacer material, but also a good choice to use as a buffer layer to provide flat surface and nice epitaxial growth with CFGG layer. This is because NiAl and CFGG have an almost perfect lattice matching as described in **Fig. 3-26**. In addition to that, NiAl is paramagnetic although it contains a ferromagnetic element since d-band of Ni is filled with electrons from Al. Therefore, NiAl can be used as a spacer as well as a buffer layer in CPP-GMR device. In fact, there is a previous report about using NiAl as underlayer for (001)-oriented CPP-GMR device to improve MR property and thermal stability of multilayer structure.[16] Hence, it could be interesting to apply NiAl as a buffer layer in our (110)-oriented CPP-GMR device as well.

The surface roughness of NiAl layer deposited on Sapphire (110) sub.//Ta(20 nm)/W(100 nm) template was investigated by AFM as shown in **Fig. 3-27**. When 5nm thick NiAl was deposited on the template, a pretty flat surface with R_a=0.31 nm and P_v=4.01 nm can be obtained. The roughness can be further improved by increasing NiAl layer thickness from 5 to 10 nm and by applying subsequently annealing process at 300°C. Therefore, buffer layer structure of Sapphire (110) sub.//Ta(20 nm)/W(100 nm)/NiAl(10 nm)@ 300°C was used for the following (001)-oriented NiAl spacer CPP-GMR study.

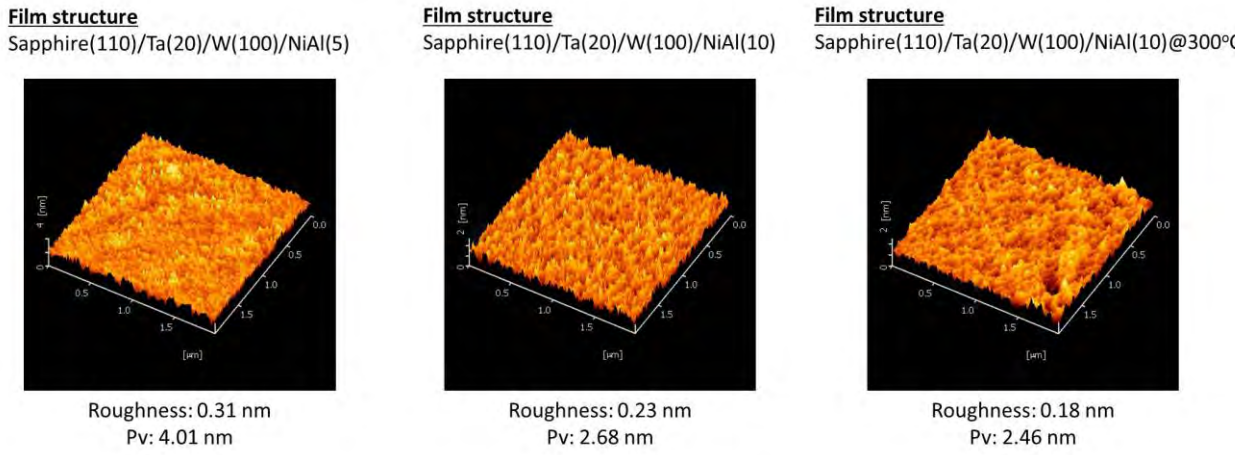

Fig. 3-27 Surface roughness of NiAl layer on Sapphire (110) sub.//Ta(20 nm)/W(100 nm) template.

The crystal structure of the previous films was examined by XRD. The result was shown in **Fig. 3-28**. In the sample with film structure of Sapphire(110)/Ta(20)/W(100)/NiAl(10), a clear NiAl (110) peak can be observed, indicating a nice epitaxial growth of (110) orientation in the out-of-plane direction.

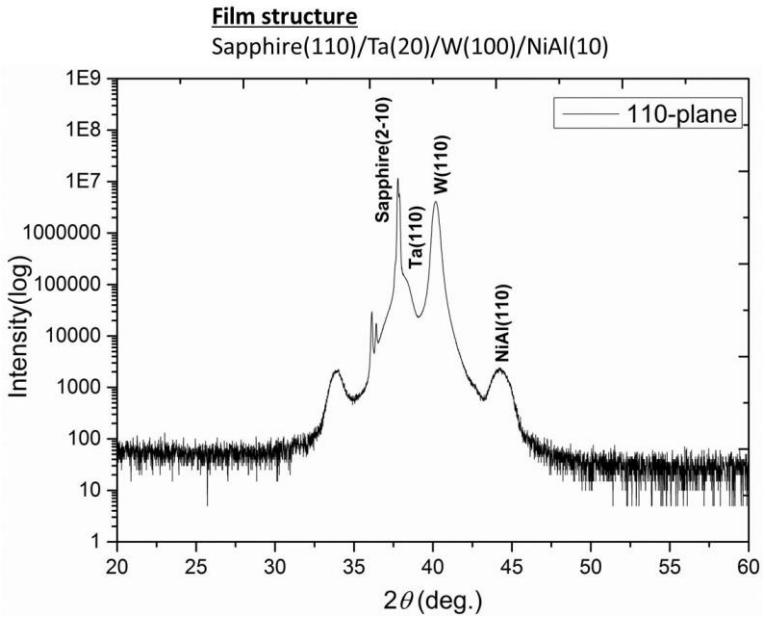

Fig. 3-28 Out-of-plane 2θ-ω scan XRD pattern for the sample of Sapphire(110)/Ta(20)/W(100)/NiAl(10).

In order to check the in-plane crystal structure of NiAl layer and orientations relationships, XRD pattern of (001)-plane and relative pole figure were measured by tilting the surface normal direction with 45° as shown in **Fig. 3-29**. NiAl(100), W(100) and Ta(100) peaks can be detected clearly in (001)-plane XRD pattern. In the pole figure pattern, a small satellite peak coming from variant at round 55° are observed from the phi-scan in Ta, W and NiAl layer. The intensity of such small satellite peak gradually decreases from Ta to NiAl layer. After annealing the sample at 300 °C, peak intensity in (001)-plane XRD pattern increases significantly and small satellite peaks in pole figure disappear in both W and NiAl layer, indicating a

structure of high quality single crystal (see **Fig. 3-30**). This result suggests that a high quality of (110)-oriented buffer layer was successfully achieved for the fabrication of (110)-oriented CPP-GMR device, which is superior to the previous Sapphire(110)/Ta/W/Ag buffer template (see **Fig. 3-9**) due to the suppression of variant formation.

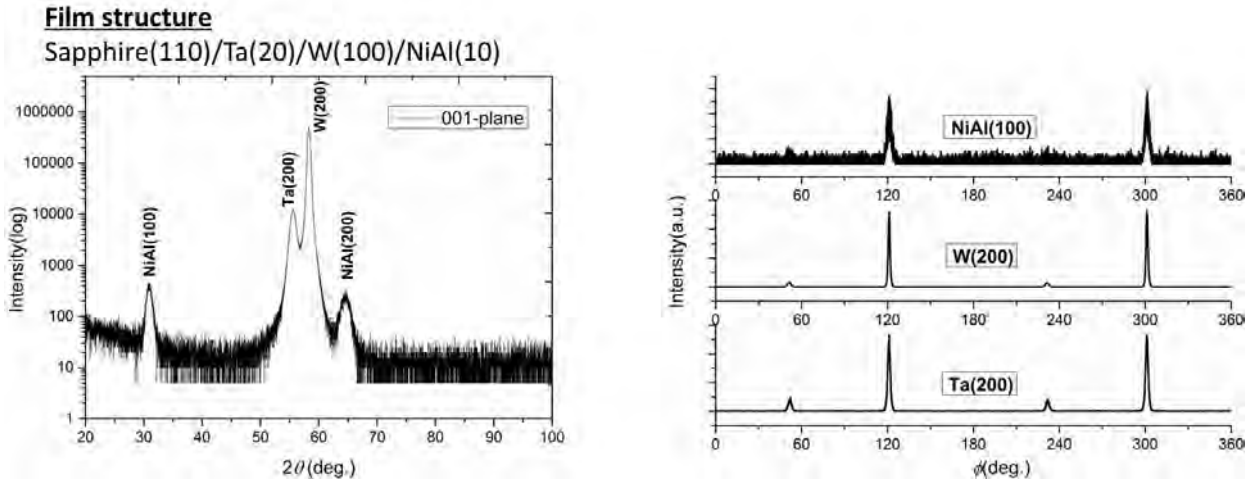

Fig. 3-29 Out-of-plane 2θ-ω scan XRD pattern and pole figure for the sample of Sapphire(110)/Ta(20 nm)/W(100 nm)/NiAl(10 nm).

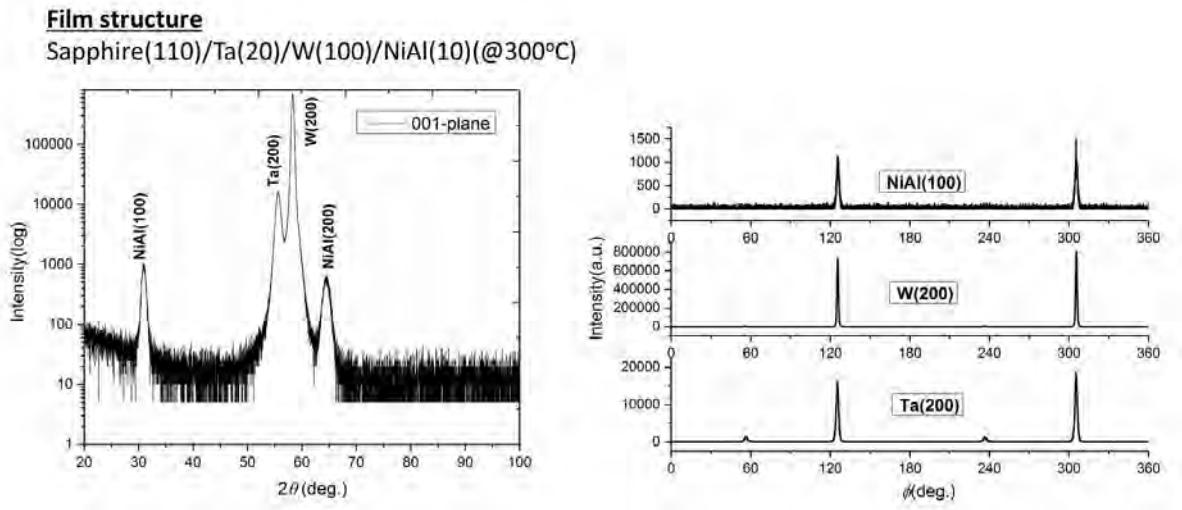

Fig. 3-30 Out-of-plane 2θ-ω scan XRD pattern and pole figure for the sample of Sapphire(110)/Ta(20 nm)/W(100 nm)/NiAl(10 nm)@(300°C).

3.3.2 Experiment details

By using high quality (110)-oriented Sapphire (110) sub.//Ta(20 nm)/W(100 nm)/NiAl(10 nm)@300°C template, all-B2-trilayer CPP-GMR pseudo spin-valves using $Co_2Fe(Ge_{0.5}Ga_{0.5})$ Heusler alloy and NiAl spacer was fabricated. Meanwhile, (001)-oriented CPP-GMR device with completely same tri-layer structure was also fabricated for comparison. The experiment details are as shown in **Fig. 3-31**.

For the (110)CFGG-oriented CPP-GMR devices, the films were deposited on a sapphire($11\bar{2}0$) single crystal substrate with the layer structure of Ta(20)/W(100)/NiAl(10)/CFGG(10)/NiAl(2 or

5)/CFGG(10)/NiAl(5)/Ru(8), where the numbers in the parentheses represent the thickness of each layer in nm. The Ta/W/NiAl underlayer was annealed at 300°C to obtain a flat surface as well. The details of buffer layer preparation can be found in our previous work.[15] For the (001)CFGG-oriented CPP-GMR devices, the films were deposited on a MgO(001) single crystal substrate by ultrahigh-vacuum magnetron sputtering system with the layer structure of Cr(10)/Ag(100)/NiAl(10)/CFGG(10)/NiAl(2 or 5)/CFGG(10)/NiAl(5)/Ru(8). The Cr/Ag/NiAl underlayer was annealed at 300°C to improve the surface roughness. The CFGG films were deposited using an alloy target with the composition of $Co_{45.2}Fe_{22.6}Ga_{14.2}Ge_{18}$, and the chemical composition of the resulting CFGG films was measured to be $Co_{49.3}Fe_{24.6}Ga_{12.9}Ge_{13.2}$ by inductively coupled plasma analysis. After the deposition of all layers, both films were then ex-situ annealed at 300–600°C for 30 min in a vacuum furnace to promote the chemical order of the CFGG layers.

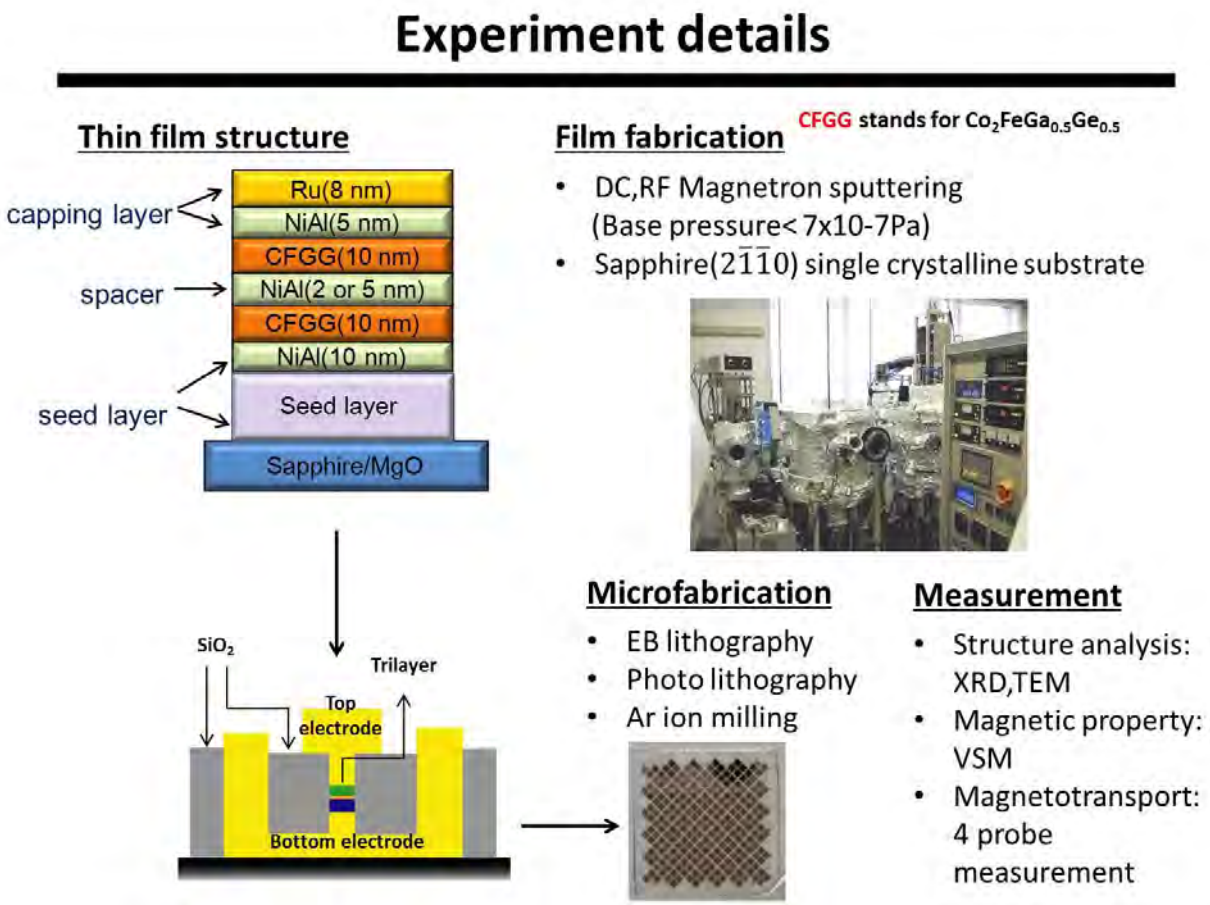

Fig. 3-31 Explanation of experiment details

3.3.3 Crystal structure characterization

The crystal structure of the multilayer films for CPP-GMR devices was examined by 4-axis X-ray diffraction (XRD) using Cu-Kα radiation as shown in **Fig. 3-31**.

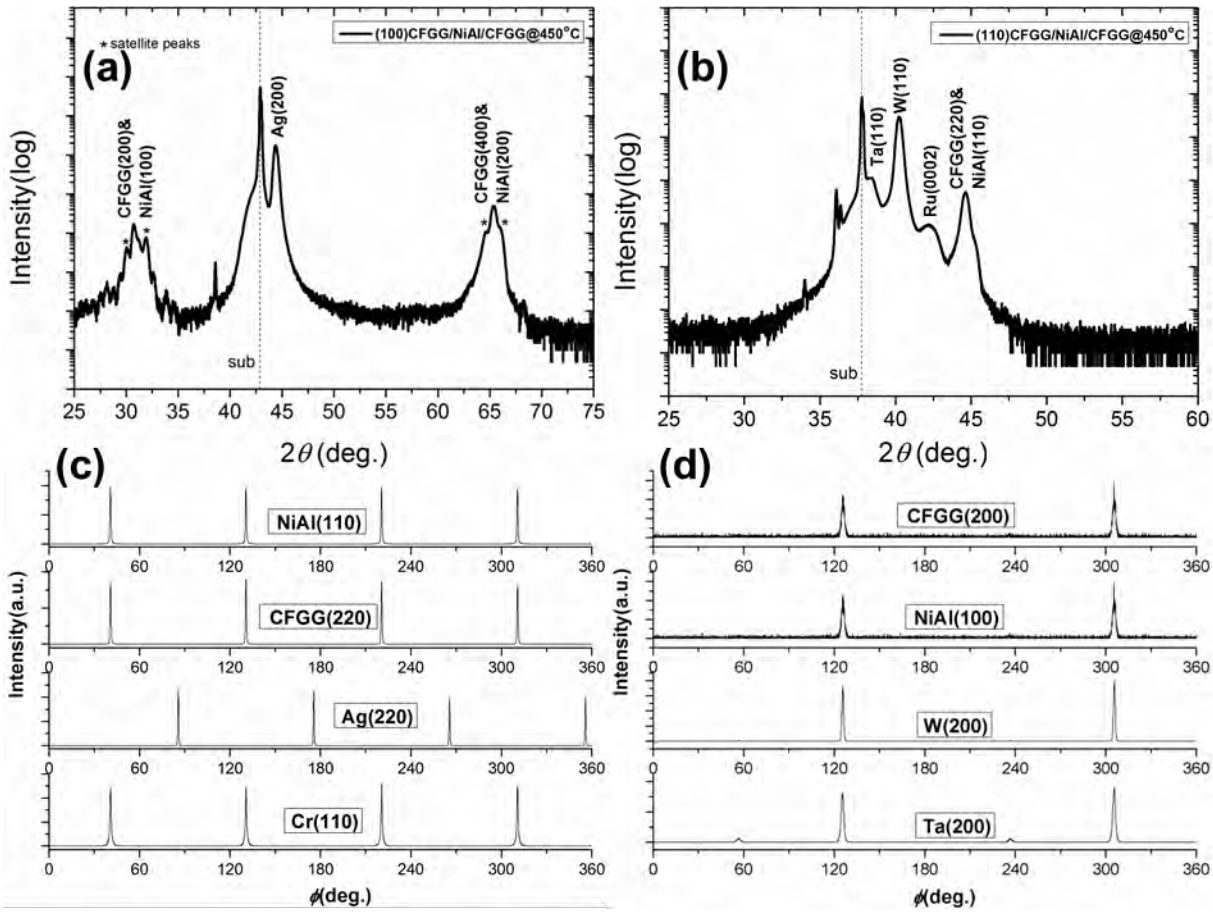

Fig. 3-32 Out-of-plane 2θ-ω scan XRD pattern for the samples in (a) (001) orientation and (b) (110) orientation. XRD pole-figure measurements for the samples in (c) (001) orientation and (d) (110) orientation.

Fig. 3-32(a) and (b) shows the out-of-plane XRD pattern for (001)-oriented film and (110)-oriented film respectively. The film structures are the same as what we had described in **section 3.3.2** and both of them are annealed at optimal temperature 450 °C. From the XRD profiles, we can confirm the out-of-plane orientations of the films are exactly the same as what we have designed. The in-plane crystallographic orientations relationships were determined by XRD pole-figure measurements as shown in **Fig. 3-32**(c) and (d). The epitaxial relationships for the tri-layers are (100)[011]CFGG//(100)[011]NiAl for (100)-oriented film and (110)[001]CFGG//(110)[001]NiAl for (110)-oriented film. No redundant peaks coming from different variants are observed from the phi-scan in CFGG and NiAl layers, indicating a structure of high quality single crystal in both films. Since the NiAl (001) and CFGG (002) superlattice peaks overlap due to the growth of CFGG/NiAl/CFGG trilayer with almost identical out-of-plane lattice parameters of $a_{CFGG} = 0.287nm$ and $a_{NiAl} = 0.289nm$, we have to check the ordering of these two layers by taking nanobeam diffraction pattern, which will be discussed in **section 3.3.6**.

3.3.4 Magneto-transport properties

3.3.4.1 Measurement of the lead resistance

In this study of (110)-oriented CPP-GMR devices with NiAl spacer, a new buffer template of Ta(20 nm)/W(100 nm)/NiAl(10 nm) was developed to obtain high quality (110) orientation epitaxial growth. Here 100nm thick W layer was used as a bottom electrode during micro-fabrication for (110)-oriented CPP-GMR device, which is different from that in (001)-oriented CPP-GMR device using Ag as bottom electrode. Normally, tungsten is not a good material for electrode because the resistivity of tungsten is 5.60×10^{-8} (Ω•m), which is around 3.5 times larger than that of silver (1.59×10^{-8}(Ω•m)). But as mentioned in **section 3.2.5.1**, the lead resistance of the devices can be calculated by the following formula:

$$R_{device} = \rho \cdot l \cdot \frac{1}{Area} + R_{lead}$$

Where the ρ was the average resistivity of the pillar, l was the thickness of the pillar. If lead resistance is subtracted correctly, the influence of bottom electrode can be eliminated so that meaningful MR property comparison can be done for two different orientations CPP-GMR device with NiAl spacer. The resistance of the device was plotted as a function of reciprocal of device pillar area in **Fig. 3-33**. The lead resistance could be determined from the Y-axis intercept, which was approximately 0.76 Ω for tungsten bottom electrode and 0.45 Ω for sliver bottom electrode, respectively.

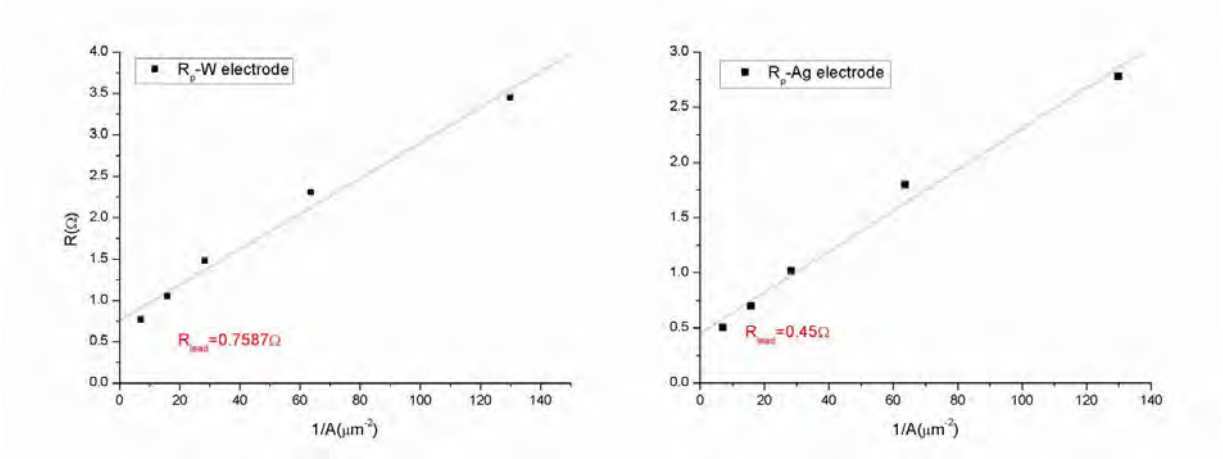

Fig. 3-33 Resistance of the CPP-GMR devices as a function of the inverse of CPP-GMR pillar area.

3.3.4.2 Room temperature magneto-transport properties

Fig. 3-34 summarizes ΔRA measured at RT as a function of the post annealing temperature Ta. The stacking structure of the tri-layers was fixed to CFGG(10 nm)/NiAl(2 or 5 nm)/CFGG(10 nm) in both (001) and (110) orientation devices for comparison. At the Ta ranging from 300 to 600 °C, we can see both (110)-orientated and (001)-oriented CPP-GMR devices show similar MR properties. Namely, the two devices with different orientations exhibit not only almost the same ΔRA value but also the same tendency of annealing temperature dependence of RA. At the Ta of 450°C, both orientations reach a maximum ΔRA value of 4.34 mΩ·μm^2 for the (001)-oriented device with RA of ~48 mΩ·μm^2 and 4.14 mΩ·μm^2 for the (110)-oriented

device with RA of ~50 mΩ·μm^2. When the spacer thickness reduces from 5 nm to 2 nm, the MR outputs improve slightly because of the short spin diffusion length (~8.1 nm) of the NiAl spacer. [16] However, the spacer thickness cannot be further reduced to obtain higher MR output due to the appearance of the strong interlayer exchange coupling. This result is the first experimental evidence suggesting there is no or little orientation dependence of band matching. Note that industrially-viable polycrystalline CPP-GMR devices always exhibit a natural (110) texture,[17–19] which is different from the (001)-oriented epitaxial CPP-GMR devices that have been well-studied in laboratory experiment. By using all-B2-trilayers structure, the orientation difference problem can be easily solved. Hence, this discovery is useful for read head sensor design.

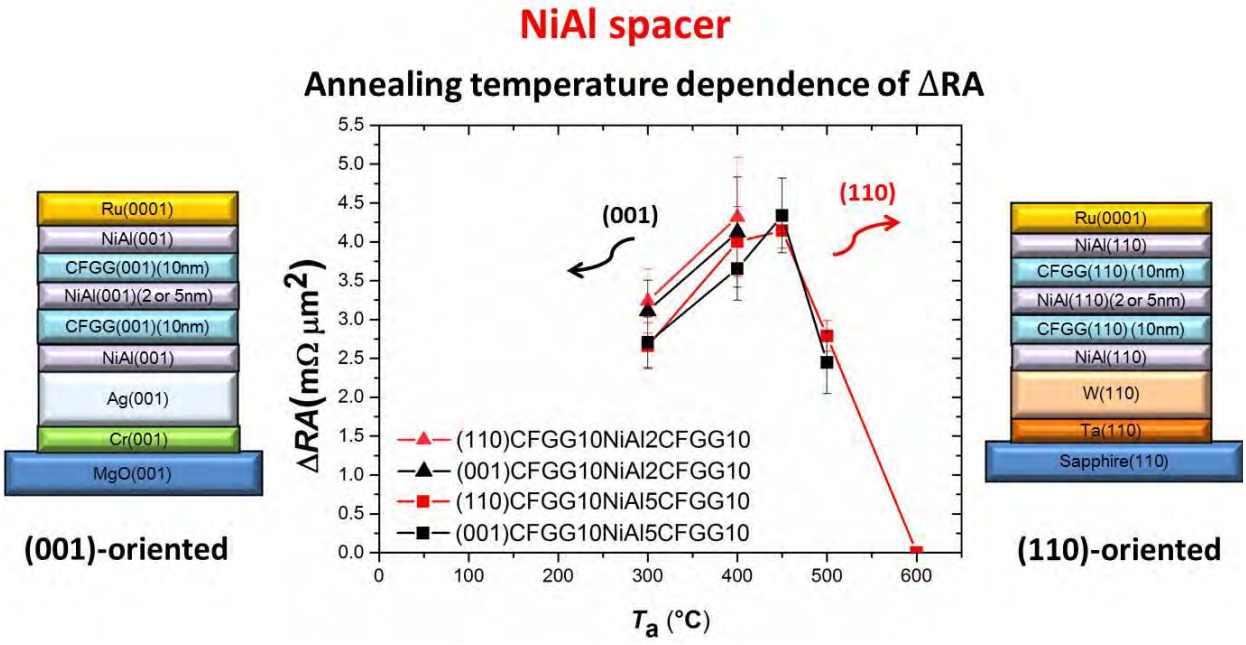

Fig. 3-34 Annealing temperature dependence of ΔRA of the film stack in (110) and (100) orientation with NiAl spacer.

3.3.5 Magnetic property

3.3.5.1 Magnetic dead layer

In order to check the magnetic property of CFGG layer near the CFGG/NiAl interface, the magnetizations of these two types of devices were measured for various thicknesses of the CFGG layer (t_f). We prepare the samples with (110)-oriented CFGG layers with a stack structure of Ta(20 nm)/W(100 nm)/NiAl(10 nm)/CFGG(t_f)/NiAl(5 nm)/Ru(5 nm) on sapphire(11 $\bar{2}$ 0) substrates. The samples with (001)-oriented CFGG layers were prepared with the structure Cr(10 nm)/Ag(100 nm)/NiAl(10 nm)/CFGG(t_f)/NiAl(5 nm)/Ru(5 nm) (t_f=5, 10, 30, 50 nm) on MgO(001) substrates. **Fig. 3-35** shows the plot of the saturation magnetization/unit film area (M_s/A) value as a function of t_F. The intercept of the t_F vs. M_s/A plot represents the thickness of the magnetic dead layer at CFGG/NiAl interface. The value of M_s of the as-deposited CFGG film with the (001) orientation is 846.7 emu/cc, which

increased to 996.0 emu/cc after annealing at 400 °C due to the progress of B2 order. For the (110)-orientated CFGG film, we can find similar value and trend, i.e. M_s increased from 850.5 emu/cc to 1013.6 emu/cc by annealing at 400 °C. Both films in two different orientations show negligibly small dead layer thickness as we can see in the inset table, which indicates a good lattice matching between the CFGG and NiAl layers, consistent with what we have expected from lattice mismatch calculation in **Fig. 3-26**. It is important to point out that the dead layer thickness difference for CFGG/Ag combination in two different orientations is quite obvious due to the lattice nature of BCC/FCC interface as reported in our previous work.[15] This VSM result gives clear evidence that two differently oriented films are comparable and free of lattice matching influence.

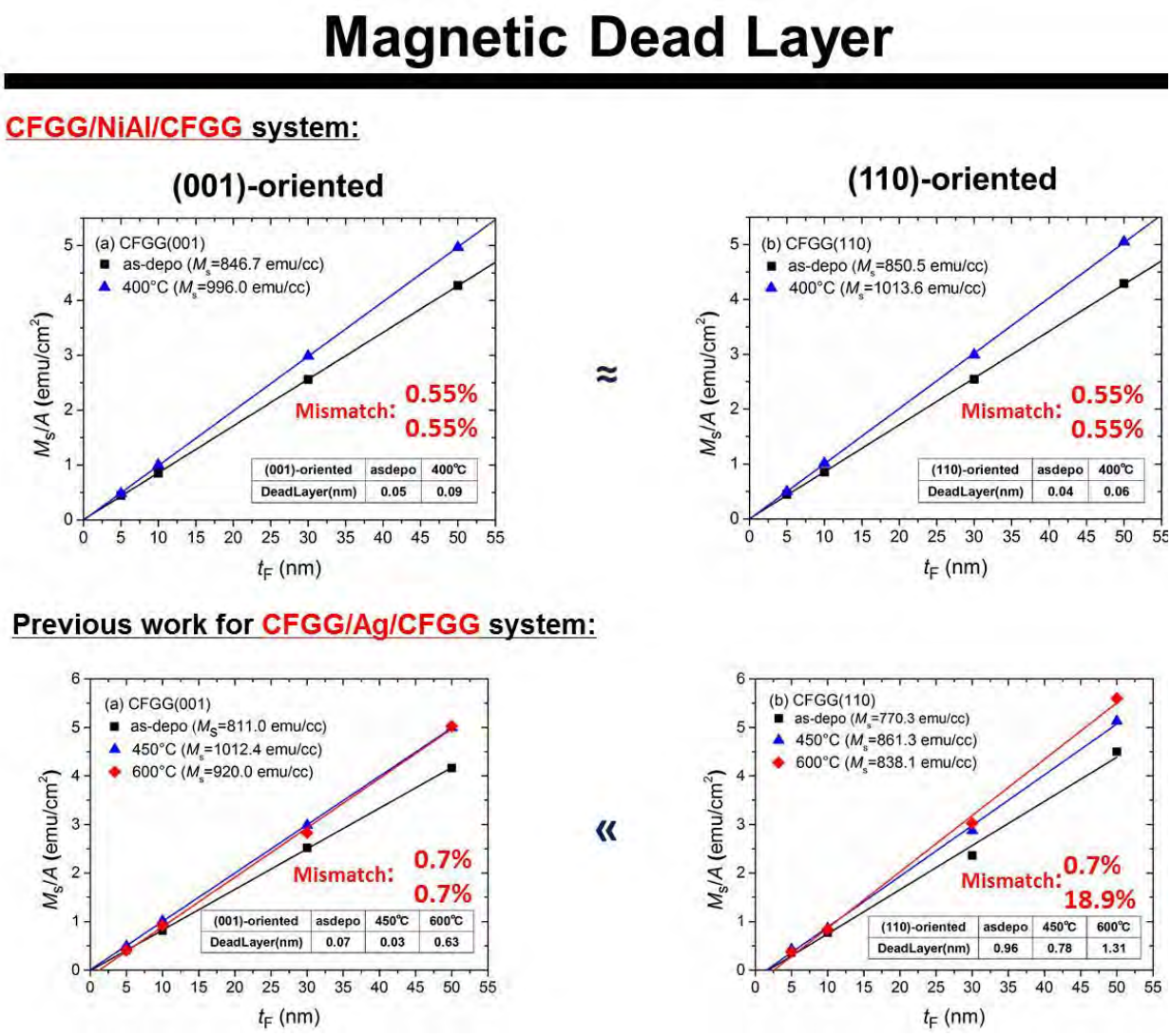

Fig. 3-35 Plots of M_s/A versus CFGG layer thickness (t_F) (a) in an (001)-oriented CFGG film and (b) in a (110)-oriented CFGG film.

3.3.6 Microstructure

Further structural characterization of the spin-valves was done by TEM observations to understand the interface condition and interdiffusion between the CFGG and NiAl layer. The bright field TEM image, high-angle annular dark-field (HAADF)-STEM image and related EDS mapping data of cross-sectional

specimens prepared from the (001)- and (110)-oriented devices are shown from **Fig. 3-36** to **Fig. 3-38**. In **Fig. 3-36**, the high resolution HAADF images show perfect lattice matching between CFGG and NiAl layer without any dislocations in the observed area. Nanobeam diffraction patterns clearly show the NiAl (001) and CFGG (002) B2-superlattice diffraction spots in both cases. Therefore, we can conclude that the structure of CFGG/NiAl/CFGG is all-B2-trilayer structure. In **Fig. 3-37**, a flat and sharp interface between CFGG and NiAl layer in both (001) and (110) oriented films can be seen. The EDS mapping data clearly shows a well-defined tri-layer structure with no visible interdiffusion. Likewise, the abrupt change in chemical composition at the CFGG/NiAl interface shown in EDS line scan indicates no significant interdiffusion as well. A bright field observation was excited with the two beam condition parallel to the film plane (g=[220]CFGG, [110]NiAl for the (001)-oriented sample and g=[200]CFGG, [100]NiAl for the (011)-oriented sample) to carry out further analysis of the misfit strain in a wide observation range. In this diffraction condition, the strain by the atomic displacement parallel to the film plane such as those by lattice misfit should show diffraction contrast.[20] The bright field image in **Fig. 3-38(a)** does not show any strain contrast within the CFGG/NiAl/CFGG trilayer or at the interfaces, indicating the absence of an appreciable strain by good lattice matching (only 0.55% lattice mismatch for CFGG/NiAl interface). We can see the strain contrast exists only at the Ru/NiAl capping interface due to the large lattice mismatch between them. In **Fig. 3-38(b)**, the strain contrasts are showed only at Ru/NiAl and NiAl/W interface but not at the CFGG/NiAl/CFGG trilayer region, suggesting a good lattice matching (0.55%) between CFGG and NiAl as well. The small lattice mismatch enables a good epitaxial growth of CFGG layer on NiAl layer. These TEM results demonstrate that NiAl could also be a good candidate for buffer layer which can provide a flat and good lattice matching interface for Heusler alloy in both orientations devices.

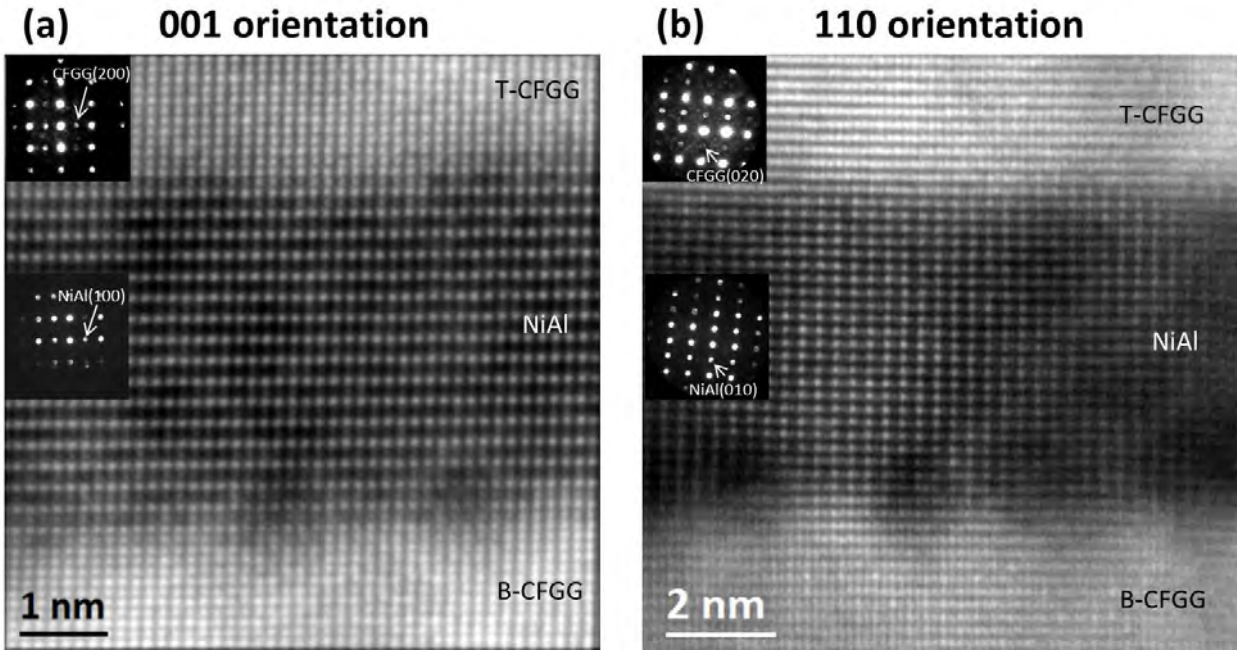

Fig. 3-36 High resolution HAADF-STEM images together with Nanobeam diffraction pattern from CFGG and NiAl layer of (a) CFGG(001)/NiAl(001)/CFGG(001) and (b) CFGG(110)/NiAl(110)/CFGG(110) both annealed at 450°C.

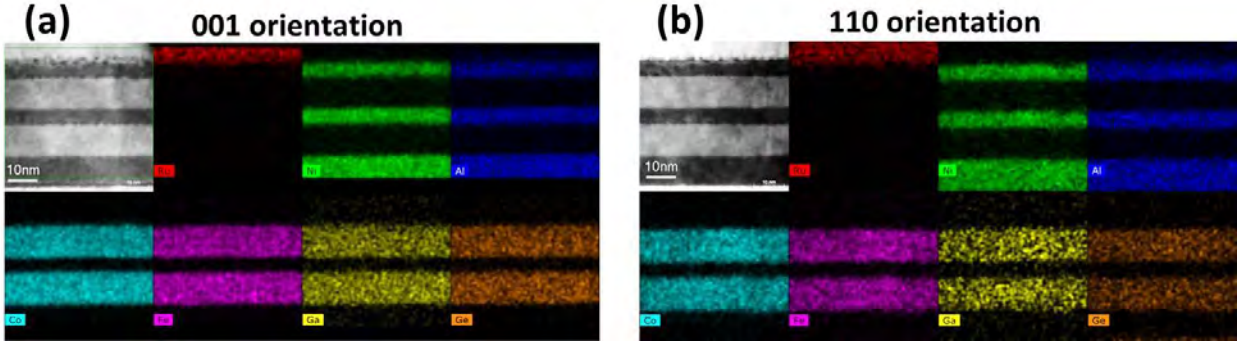

Fig. 3-37 EDS mapping images for (a) CFGG(001)/NiAl(001)/CFGG(001) and (b) CFGG(110)/NiAl(110)/CFGG(110) both annealed at 450°C.

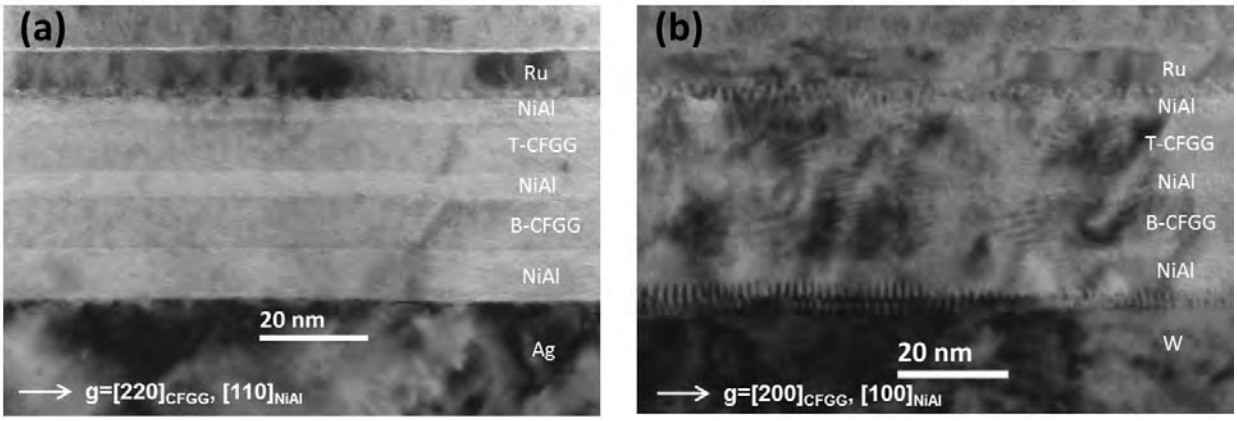

Fig. 3-38 Two-beam condition bright field image with the g vectors parallel to the film plane for (a) CFGG(001)/NiAl(001)/CFGG(001) film and (b) CFGG(110)/NiAl(110)/CFGG(110) film both annealed at 450°C.

3.4 Summary of this chapter

In this chapter, orientation dependence of MR output between (110)-oritentd CPP-GMR devices and (001)-oriented devices has been investigated by using Heusler alloy $Co_2Fe(Ga_{0.5}Ge_{0.5})$ and different spacers (Ag, Cu and NiAl). The summaries are as follow:

(a) (110)-oriented CPP-GMR devices with Ag and Cu spacer:

1) Fully epitaxial CPP-GMR device with a (110)-oriented CFGG Heusler alloy was successfully fabricated for the first time.
2) Significant degradation of the MR output is observed for the (110)-oriented devices with the (111)-oriented Ag spacer compared with the (100)-oriented devices. In contrast, the (110)-oriented device exhibits a higher MR output with a (111)-oriented Cu spacer, suggesting that an improvement of the GMR ratio can be obtained by selecting an appropriate orientation relationship to tune the lattice mismatch between the FM layer and the spacer.

3) The (110)-oriented CPP-GMR device demonstrate a ΔRA value of 4.1 $m\Omega \cdot \mu m^2$ with a Cu spacer at 350°C and 3.7 $m\Omega \cdot \mu m^2$ with an Ag spacer at 450°C.
4) In the case of CFGG/Ag/CFGG CPP-GMR devices, the (001)-oriented CFGG layer gives rise to a higher MR output. This suggests that the naturally-grown (110)-textured polycrystalline CFGG/Ag/CFGG PSV is not the ideal structure, and an alteration of the texture of the CFGG layer to the (100) planes appears to be an effective way to enhance the MR output of the polycrystalline device. In fact, Du *et al*.[21] have demonstrated that the (001)-textured polycrystalline PSVs give higher MR than the (110) textured polycrystalline PSVs.
5) For a naturally-grown (110) textured device, a Cu spacer is a good choice, as reported by Carey *et al*.[17] Although the MR output for polycrystalline CPP-GMR devices develops gradually, there is still a large gap between the performance of epitaxial CPP-GMR devices and polycrystalline CPP-GMR devices. Thus, further development in polycrystalline CPP-GMR devices will become an urgent issue for the application of CPP-GMR read head.

Citation for this part can be referred to:

Jiamin Chen, S. Li, T. Furubayashi, Y. K. Takahashi, and K. Hono
"Crystal orientation dependence of current-perpendicular-to-plane giant magnetoresistance of pseudo spin-valves with epitaxial $Co_2Fe(Ge_{0.5}Ga_{0.5})$ Heusler alloy layers"
Journal of Applied Physics. **115**, 233905 (2014). [http://dx.doi.org/10.1063/1.4882736]

(b) (110)-oriented CPP-GMR devices with NiAl spacer:

1) B2 NiAl intermetallic compound was applied to a spacer layer of a CPP-GMR pseudo spin-valve with a $Co_2FeGa_{0.5}Ge_{0.5}$(CFGG) FM Heusler alloy. The spin-valve with all-B2 CFGG/NiAl/CFGG trilayer were successfully fabricated in both (001) and (110) orientations with a spacer thickness of 2 and 5 nm.
2) Two differently oriented devices with the same trilayer structure show not only almost the same ΔRA value but also the same tendency of annealing temperature dependence of ΔRA. At the T_a of 450°C, both orientations reach a maximum ΔRA value of 4.34 $m\Omega \cdot \mu m^2$ for the (001)-oriented device with RA of ~48 $m\Omega \cdot \mu m^2$ and 4.14 $m\Omega \cdot \mu m^2$ for the (110)-oriented device with RA of ~50 $m\Omega \cdot \mu m^2$. The same magneto-transport properties, indicating there is no or little orientation dependence of band matching.
3) A thinner NiAl spacer can lead to a slightly higher value of ΔRA due to the short spin diffusion length but further improvement is not possible because of the appearance of the strong interlayer exchange coupling between two FM layers. BCC structure spacer with a longer spin diffusion length will be an effective way to obtain larger MR output independent of the orientation of crystal growth.
4) All-B2-trilayer structure was free of lattice matching influence depending on the crystal orientation. By using all-B2-trilayers structure, the orientation difference problem can be easily solved. Hence, this discovery is useful for read head sensor design.

Citation for this part can be referred to:

Jiamin Chen, T. Furubayashi, Y. K. Takahashi, T.T. Sasaki and K. Hono
"Crystal orientation dependence of band matching in all-B2-trilayer current-perpendicular-to-plane giant magnetoresistance pseudo spin-valves using $Co_2Fe(Ge_{0.5}Ga_{0.5})$ Heusler alloy and NiAl spacer"
Journal of Applied Physics. **117**, 17C119 (2015) [http://dx.doi.org/10.1063/1.4915481]

Reference

[1] J. Higuchi, M. Ohtake, Y. Sato, T. Nishiyama, and M. Futamoto, Jpn. J. Appl. Phys. **50**, 063001 (2011).

[2] A. Sugihara, Y. Sakuraba, K. Yakushiji, S. Yuasa, and K. Takanashi, Jpn. J. Appl. Phys. **50**, 028001 (2011).

[3] R.C.C. Ward, E.J. Grier, and A.K. Petford-Long, J. Mater. Sci. Mater. Electron. **14**, 533 (2003).

[4] C. Müller, H. Mühlbauer, and G. Dumpich, Thin Solid Films **310**, 81 (1997).

[5] U. Geiersbach, A. Bergmann, and K. Westerholt, Thin Solid Films **425**, 225 (2003).

[6] U. Geiersbach, A. Bergmann, and K. Westerholt, J. Magn. Magn. Mater. **240**, 546 (2002).

[7] M. Hattori, Y. Sakuraba, M. Oogane, Y. Ando, and T. Miyazaki, Appl. Phys. Express **1**, 021301 (2008).

[8] K. Özdoğan, B. Aktaş, I. Galanakis, and E. Şaşıoğlu, J. Appl. Phys. **101**, 073910 (2007).

[9] Y.K. Takahashi, A. Srinivasan, B. Varaprasad, A. Rajanikanth, N. Hase, T.M. Nakatani, S. Kasai, T. Furubayashi, and K. Hono, Appl. Phys. Lett. **98**, 152501 (2011).

[10] B.S.D.C.S. Varaprasad, A. Srinivasan, Y.K. Takahashi, M. Hayashi, A. Rajanikanth, and K. Hono, Acta Mater. **60**, 6257 (2012).

[11] T.M. Nakatani, Y. Du, Y.K. Takahashi, T. Furubayashi, and K. Hono, Acta Mater. **61**, 3695 (2013).

[12] S. Li, H.S. Goripati, Y.K. Takahashi, T. Furubayashi, and K. Hono, IEEE Trans. Magn. **49**, 4413 (2013).

[13] H.S. Goripati, T. Furubayashi, Y.K. Takahashi, and K. Hono, J. Appl. Phys. **113**, 043901 (2013).

[14] M.J. Carey, S. Maat, S. Chandrashekariaih, J.A. Katine, W. Chen, B. York, and J.R. Childress, J. Appl. Phys. **109**, 093912 (2011).

[15] J. Chen, S. Li, T. Furubayashi, Y.K. Takahashi, and K. Hono, J. Appl. Phys. **115**, 233905 (2014).

[16] N. Hase, T.M. Nakatani, S. Kasai, Y.K. Takahashi, T. Furubayashi, and K. Hono, J. Magn. Magn. Mater. **324**, 440 (2012).

[17] M.J. Carey, S. Maat, S. Chandrashekariaih, J.A. Katine, W. Chen, B. York, and J.R. Childress, J. Appl. Phys. **109**, 093912 (2011).

[18] Y. Du, T.M. Nakatani, Y.K. Takahashi, N. Hase, T. Furubayashi, and K. Hono, J. Appl. Phys. **114**, 053910 (2013).

[19] T.M. Nakatani, Y. Du, Y.K. Takahashi, T. Furubayashi, and K. Hono, Acta Mater. **61**, 3695 (2013).

[20] T.M. Nakatani, Y.K. Takahashi, T. Ishikawa, M. Yamamoto, and K. Hono, J. Magn. Magn. Mater. **322**, 357 (2010).

[21] Y. Du, B.S.D.C.S. Varaprasad, Y.K. Takahashi, T. Furubayashi, and K. Hono, Appl. Phys. Lett. **103**, 202401 (2013).

Chapter 4 Development of new $Co_2(Fe_{1-x}Ti_x)Si$ Heusler alloys thin film with high spin polarization and high $L2_1$ order

4.1 Introduction

Half-metallic ferromagnets have attracted much attention as key materials to develop spin-polarized current sources for spintronics devices. Among various classes of half-metallic materials, Co-based Heusler alloys have drawn considerable interest due to their theoretically predicted half-metallicity, high spin polarization and high Curie temperatures. Over the past few decades, there have been a number of studies on large tunneling magnetoresistance (TMR), giant magnetoresistance (GMR), and spin-accumulation effects using Co-based Heusler compounds[1–3]. Although large MR ratios over 50% at room temperature have been observed in current-perpendicular-to-plane giant magnetoresistive (CPP-GMR) devices using epitaxial $Co_2Fe(Ga_{0.5}Ge_{0.5})$ (CFGG)[4,5] and $Co_2(Fe_{0.4}Mn_{0.6})Si$ (CFMS)[6] Heusler ferromagnetic (FM) layers, there are still remaining issues for practical applications. For instance, the requirement of high annealing temperature (over 500℃) for achieving high degree of $L2_1$ order in these Heusler alloys is a problem for processing practical polycrystalline CPP-GMR read sensors for hard disk drives. Although it was theoretically predicted that B2 order is enough for obtaining half-metallic band gap in some of the Co-based Heusler alloys[7,8], MR output in the CPP-GMR devices with CFGG and CFMS clearly enhances with improved $L2_1$-order by annealing above 500°C (see **Fig. 4-1**). Therefore, finding a new Heusler alloy that exhibits high spin polarization at room temperature (RT) by annealing at lower temperature is strongly desired.

Among the half-metallic Heusler family, Co_2FeSi (CFS) has been extensively investigated because of the merits of highest Curie temperature (1100 K), highest magnetic moment (6 μ_B) and large exchange stiffness[9,10]. Unfortunately, large degradation of spin-polarization at around room temperature was experimentally observed from the CPP-GMR devices with Co_2FeSi electordes[11] and anisotropic magnetoresistance (AMR) in the Co_2FeSi film[12]. Sakuraba *et al*. claimed that the Fermi level is located near the edge of conduction band (CB) in Co_2FeSi from the analysis of the temperature dependence of AMR[12]. Bombor *et al*. also reported small energy splitting (~10 meV) between Fermi level (E_F) and the half-metallic CB edge from the analysis of temperature dependence of resistivity[13]. Therefore, such small energy

difference between E_F and CB edge (defined as ΔE_{CB} hereafter) can be an origin for the degradation of half-metallicity in Co_2FeSi at RT. In Sakuraba *et al.*'s paper, they also suggested from their systematic study of AMR in Co_2YZ (Y = Mn, Fe, Z = Al, Si, Ga, Ge) films that the Co_2YZ with valence electron number N_v of 28.8 to 29.4 shows small temperature dependence of spin-polarization because E_F is located around the center of half-metallic gap. Based on this discovery, we propose a partial substitution of Fe (N_v = 8) with Ti (N_v = 4) in Co_2FeSi (N_v = 30) Heusler alloy to tune N_v to around 29 for improving its half-metallic property at room temperature. In addition to that, according to the first-principles calculations on the formation energy of chemical disorder in Co_2YZ (Y = Ti, V, Cr, Mn, Fe) compounds by Miura *et al.* [14], Co_2TiSi Heusler alloy is expected to have high spin polarization originating from the clear half-metallic band gap. They also predicted that the formation energy of the anti-site disorder between Co and Y elements is high, suggesting a possibility to obtain high degree of $L2_1$ order at low annealing temperature. Therefore, by combining Co_2FeSi and Co_2TiSi, a new Heusler alloy $Co_2(Fe_{1-x}Ti_x)Si$ (CFTS) could be a promising Heusler alloy which has both high spin polarization and high driving force for $L2_1$-order even at low annealing temperature.

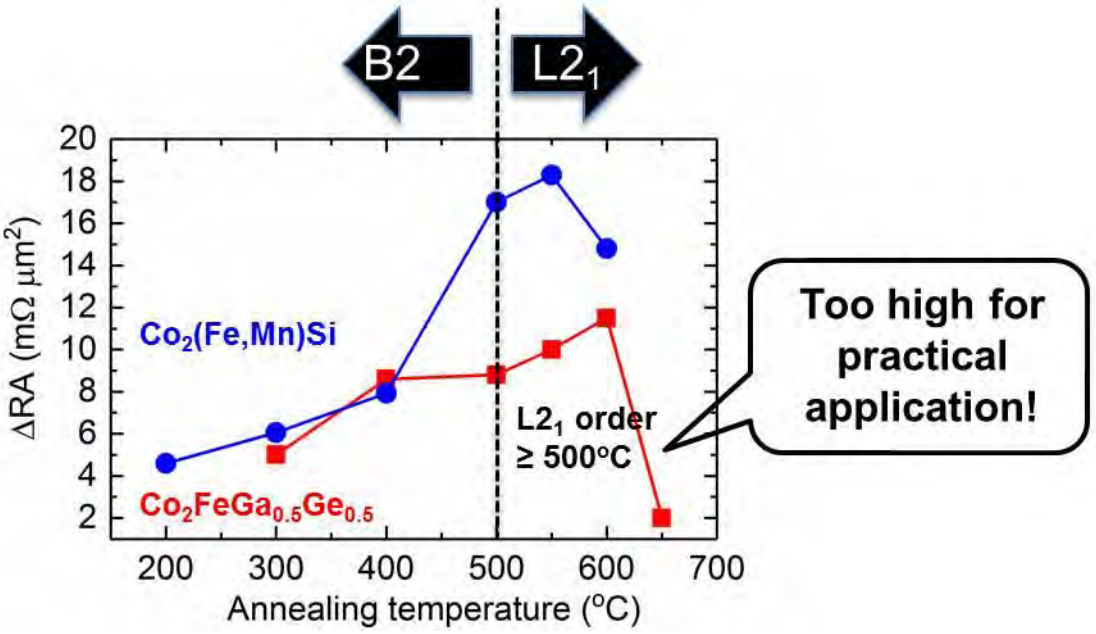

Fig. 4-1 Annealing temperature dependence of MR output of CFGG and CFMS Heusler alloy. By courtesy of Dr. Nakatani and S. Li.

This chapter describes a new series of $Co_2(Fe_{1-x}Ti_x)Si$ Heusler alloys thin film prepared by the co-sputtering technique and their various properties such as electronic structure, chemical ordering, spin-dependent transport properties and magnetic properties were investigated systematically.

4.2 Experiment details

As shown in **Fig. 4-2**, a series of $Co_2(Fe_{1-x}Ti_x)Si$ thin films, denoted as CFTS, were grown on MgO (001) single crystalline substrates with layer structure of MgO(001)-subs./$Co_2(Fe_{1-x}Ti_x)Si$ (50nm), x = 0, 0.1, 0.2, 0.3, 0.6, 1 by co-sputtering Co_2FeSi and Co_2TiSi targets in a ultra-high vacuum (UHV) magnetron sputtering system. The MgO substrate was cleaned by chemical washing followed by thermal cleaning at 600°C in vacuum. All the films were deposited at room temperature and subsequently annealed at temperatures ranging from 400 to 650°C for 30 minutes after the deposition. The actual alloy composition was analyzed by inductively coupled plasma (ICP) analyses. The results show $Co_{2.01}Fe_{1.06}Si_{0.93}$ $Co_{2.01}Fe_{0.96}Ti_{0.09}Si_{0.94}$ $Co_{2.01}Fe_{0.85}Ti_{0.19}Si_{0.95}$ $Co_{2.02}Fe_{0.74}Ti_{0.28}Si_{0.96}$ $Co_{2.02}Fe_{0.42}Ti_{0.56}Si_{0.99}$ and $Co_{2.03}Ti_{0.93}Si_{1.04}$ for the films with nominal x = 0, 0.1, 0.2, 0.3,0.6 and 1, respectively. The calculated N_v are shown in Table 4-1.

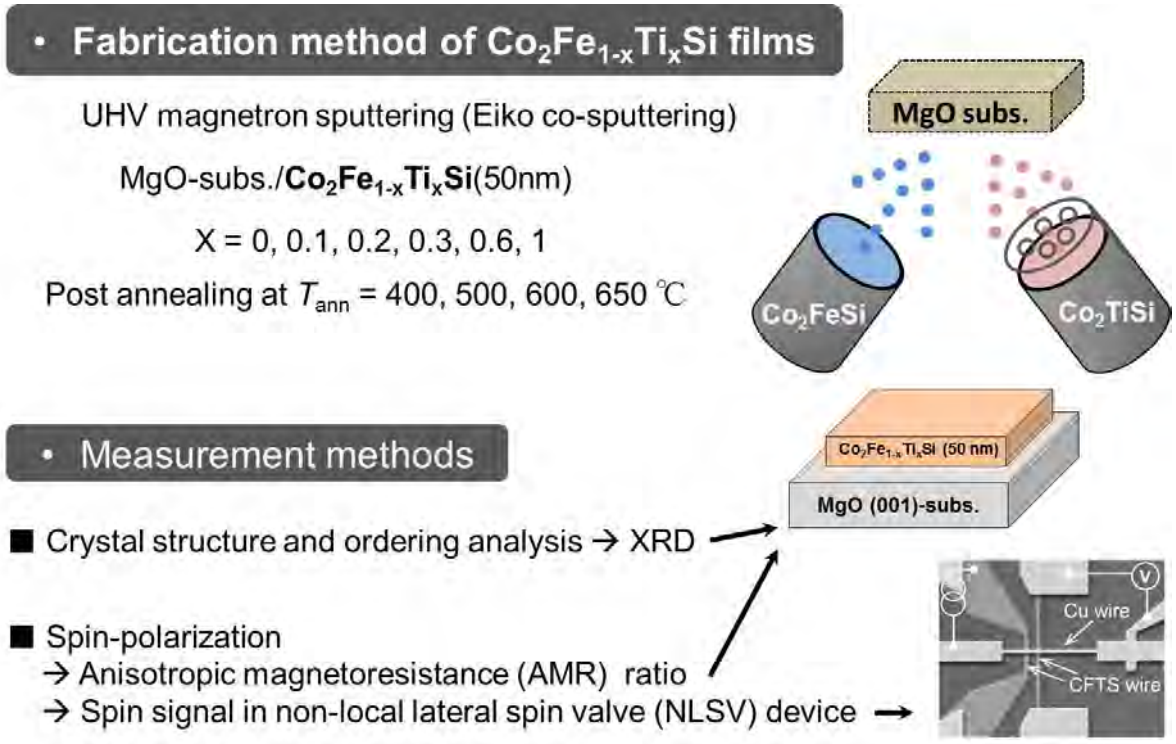

Fig. 4-2 Illustration of experiment details.

TABLE 4-1. The list of nominal and actual composition and N_v of $Co_2Fe_{1-x}Ti_xSi$ series films fabricated for this study.

Nominal composition	Nominal N_V	Actual composition	Actual N_V
Co_2FeSi	30.0	$Co_{2.01}Fe_{1.06}Si_{0.93}$	30.3
$Co_2Fe_{0.9}Ti_{0.1}Si$	29.6	$Co_{2.01}Fe_{0.96}Ti_{0.09}Si_{0.94}$	29.9
$Co_2Fe_{0.8}Ti_{0.2}Si$	29.2	$Co_{2.01}Fe_{0.85}Ti_{0.19}Si_{0.95}$	29.5
$Co_2Fe_{0.7}Ti_{0.3}Si$	28.8	$Co_{2.02}Fe_{0.74}Ti_{0.28}Si_{0.96}$	29.1
$Co_2Fe_{0.4}Ti_{0.6}Si$	27.6	$Co_{2.02}Fe_{0.42}Ti_{0.56}Si_{0.99}$	27.8
Co_2TiSi	26	$Co_{2.03}Ti_{0.93}Si_{1.04}$	26.2

The crystal structure of the films was examined by 4-axis X-ray diffraction (XRD) using Cu-Kα radiation. The ratio of $L2_1$-superlattice peaks intensity to fundamental peak intensity $\alpha_{obs}^{L2_1}$ was evaluated by using the following formulas:

$$\alpha_{obs}^{L2_1} = \frac{I_{obs}(111)/I_{obs}(004)}{I_{cal}(111)/I_{cal}(004)}, \quad (1),$$

where $I_{obs}(111)$ and $I_{obs}(004)$ are the integrated intensity of observed $L2_1$-superlattice peaks and corresponding fundamental peaks, respectively. $I_{cal}(hkl)$ represents the calculated (hkl) peak intensity by assuming a perfect $L2_1$ ordered structure in every CFTS with different x. Spin polarization of CFTS films were experimentally studied by measuring AMR in the CFTS single layer films and by measuring spin-accumulation signal ΔR_s in non-local lateral spin valve (NLSV) devices with the CFTS films. Previous studies clearly indicated that the spin-polarization in Co-based Heusler alloys can be qualitatively investigated from the sign and magnitude of AMR ratio[8,12], which agrees well with the comprehensive theoretical model proposed by Kokado *et al*[15]. The AMR effect was measured at 10, 100, 200 and 300 K in Physical Property Measurement System (PPMS) under an applied electric current I of 1 mA to the <110> direction of the epitaxial CFTS thin film. A magnetic field of 0.5 T was rotated within in-plane directions. The spin polarization was also quantitatively evaluated from ΔR_s in NLSVs based on the one-dimensional spin diffusion model[16]. The NLSV devices with parallel spin-injection and detection wires bridged by an orthogonal Cu channel wire were prepared by microfabricating $Co_2Fe_{1-x}Ti_xSi$ (x = 0, 0.1 and 0.2) films annealed at. The surfaces of CFTS wires were cleaned by moderate in-situ Ar ion milling just before

depositing Cu channel to obtain transparent interfaces between CFTS and Cu channel wires. The thickness t_{CFTS} and width w_{CFTS} of the CFTS wires were varied between 30 nm and 157 nm, and the Cu wire thickness was around 100 nm with an wire width w_{Cu} of 133 nm. Total 24 devices having different center-to-center distances d, from 450 to 1350 nm, between two CFTS wires were patterned on one substrate to evaluate spin-polarization from the fitting spin signals based one dimensional spin-diffusion model[16]. The electrical measurement was performed in a non-local configuration with DC reversal method at 300 K.

4.3 First principles calculations of Density Of States (DOS)

To understand the effect of Ti substitution for Fe in Co_2FeSi, we carried out first-principles calculations on the basis of the density-functional theory (DFT) and the coherent potential approximation (CPA), which are implemented in the spin-polarized relativistic full-potential Korringa-Kohn-Rostoker (SPR-KKR) code[17]. In particular, the CPA can properly treat the disorder between Fe and Ti atoms in $L2_1$ ordered $Co_2(Fe_{1-x}Ti_x)Si$. In the calculations, we adopted the generalized-gradient approximation (GGA)[18] for the exchange-correlation energy and used 250 **k** points in the irreducible part of the Brillouin zone. It has been demonstrated that the Coulomb interaction U in the transition-metal ions must be taken into consideration to reproduce experimental values of the magnetic moment in Co_2FeSi[19]. Thus, by means of the GGA+U method, we considered the interaction U of 3 eV for the 3d states of Co, Fe, and Ti atoms, which was shown to be an appropriate value for describing Co_2FeSi[19]. We also set the lattice cnstant a of $Co_2(Fe_{1-x}Ti_x)Si$ using the equation $a=(1-x)\times a_{CFS}+x\times a_{CTS}$, where a_{CFS}=0.56262 nm and a_{CTS}=0.57436 nm are the lattice constants of Co_2FeSi and Co_2TiSi, respectively, determined by the DFT-based structure optimization.

In **Fig. 4-3**(a) and (b), we show the calculated density of states (DOS) for $Co_2(Fe_{1-x}Ti_x)Si$ Heusler alloys with different x. We found that as x increases, the peak just above the Fermi level in the minority-spin DOS (the CB edge of half-metallic gap) shifts towards higher energies, leading to the increase in ΔE_{CB}. We also found that the minority-spin DOS at the Fermi level gradually decreases as x increases, which enhances the spin polarization $P=(D_\uparrow-D_\downarrow)/(D_\uparrow+D_\downarrow)$, where $D_\uparrow$ and $D_\downarrow$ are the majority- and minority-spin DOS at the Fermi level [See the inset of **Fig. 4-3(b)**]. From these results, we can conclude that Ti substitution into the Fe

site improves the half-metallicity of Co_2FeSi. Note that there might be a discrepancy in ΔE_{CB} between this calculation and the actual one because ΔE_{CB} strongly depends on the given Coulomb interaction U which has a large uncertainty[19]. However, we can expect an enhancement of spin-polarization at RT by the Ti substitution for Fe in Co_2FeSi since the increase in ΔE_{CB} with Ti substitution always appears regardless of the value of U. Although Co_2TiSi is predicted to have the highest spin-polarization with the largest ΔE_{CB}, high spin-polarization at RT is not unlikely in Co_2TiSi because of its low Curie temperature ~ 370 K.

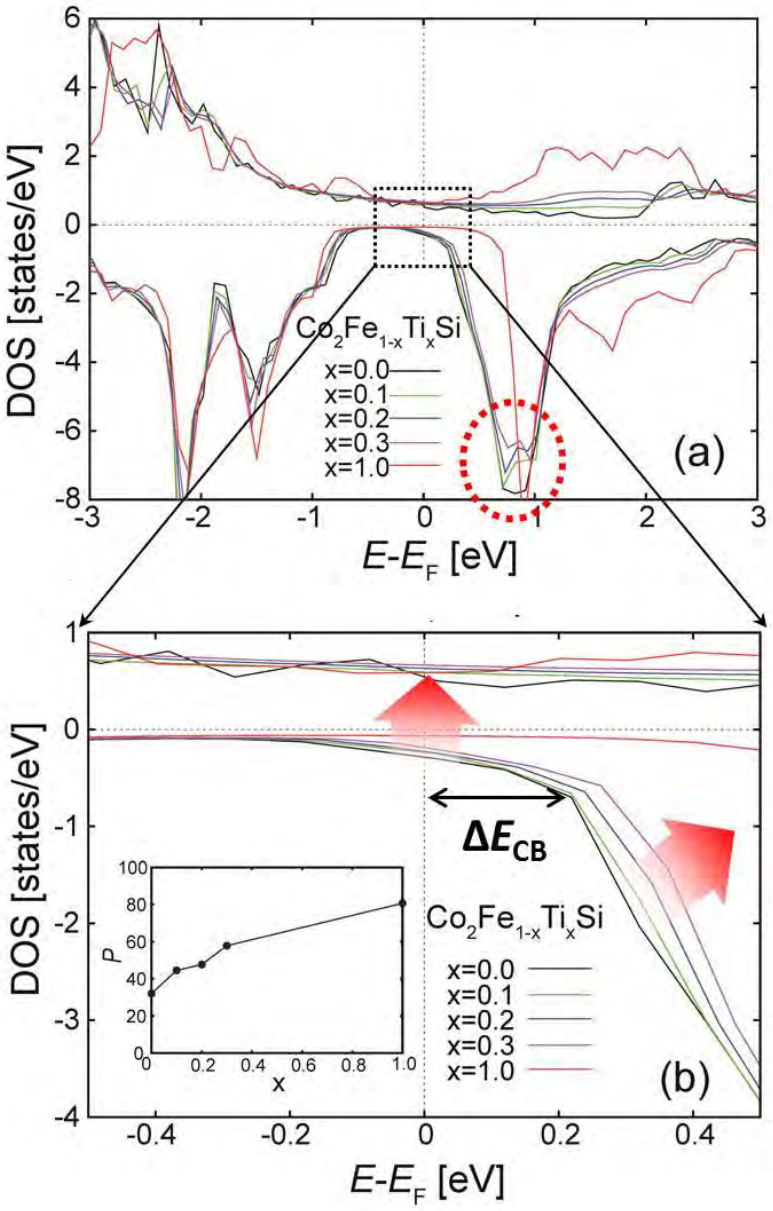

Fig. 4-3 (a) The energy dependences of the DOS for $Co_2(Fe_{1-x}Ti_x)Si$ Heusler alloys with different x. (b) The enlarged view of Fig. 4-3(a) around the Fermi level E_F. The inset shows the x dependence of the spin polarization P. Courtesy of K. Masuda and Y. Miura.

4.4 Crystal structure characterization

4.4.1 XRD profile analysis

The XRD patterns for 50-nm-thick CFTS epitaxial films on MgO (001) single crystal substrate annealed at 650°C with different *x* are shown in **Fig. 4-4**. The strong (002) super-lattice peak, indicating a highly B2-orderd structure, is observed in all the CFTS films. The position of (004) fundamental peak gradually shifts toward higher 2θ angles with increasing *x*, suggesting a reduction of out-of-plane lattice constant (from 0.565 nm for Co_2FeSi to 0.555 nm for Co_2TiSi) with higher Ti content.

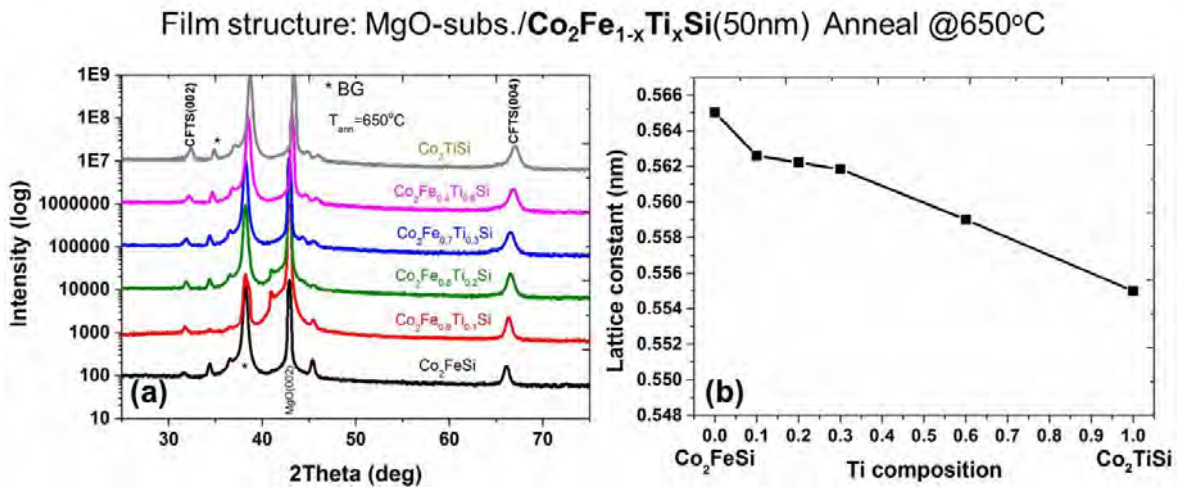

Fig. 4-4 (a) XRD patterns for 50 nm thick $Co_2Fe_{1-x}Ti_xSi$ films annealed at 650°C with x from 0 to 1. (b) Dependence of Ti composition on out-of-plane lattice constant of CFTS films.

4.4.2 Degree of $L2_1$ order

In order to check the degree of $L2_1$ order of the CFTS thin films, the $L2_1$-superlattice (111) diffraction was measured by tilting the surface normal direction with 54.7°. The ratio of $L2_1$-superlattice peaks intensity to fundamental peak intensity $\alpha_{obs}^{L2_1}$ was evaluated by using the following formulas:

$$\alpha_{obs}^{L2_1} = \frac{I_{obs}(111)/I_{obs}(004)}{I_{cal}(111)/I_{cal}(004)}, \quad (2),$$

where $I_{obs}(111)$ and $I_{obs}(004)$ are the integrated intensity of observed $L2_1$-superlattice peaks and corresponding fundamental peaks, respectively. $I_{cal}(hkl)$ represents the calculated (hkl) peak intensity by assuming a perfect $L2_1$ ordered structure in every CFTS with different *x*. The calculated $\alpha_{obs}^{L2_1}$ is plotted in **Fig. 4-5** as a function of Ti composition. In the case of the Co_2FeSi thin film, a high annealing temperature of

650 °C was needed to achieve the $L2_1$ ordered structure. When substituting 10 % of Fe with Ti, we found the $L2_1$ order at 500 °C. The kinetic $L2_1$ ordering temperature is further reduced to 400 °C for x=0.2. Thereafter, the $\alpha_{obs}^{L2_1}$ value is almost saturated for x>0.2. These results indicate that the kinetics for $L2_1$ ordering can be significantly improved by substituting a small amount of Fe with Ti (x=0.1 to 0.3) in Co_2FeSi, which can be explained by higher tolerance for Co-related atomic disorder in Co_2Ti-based Heusler alloys compared with Co_2Fe-based Heusler alloys as suggested from the calculation of formation energy[14].

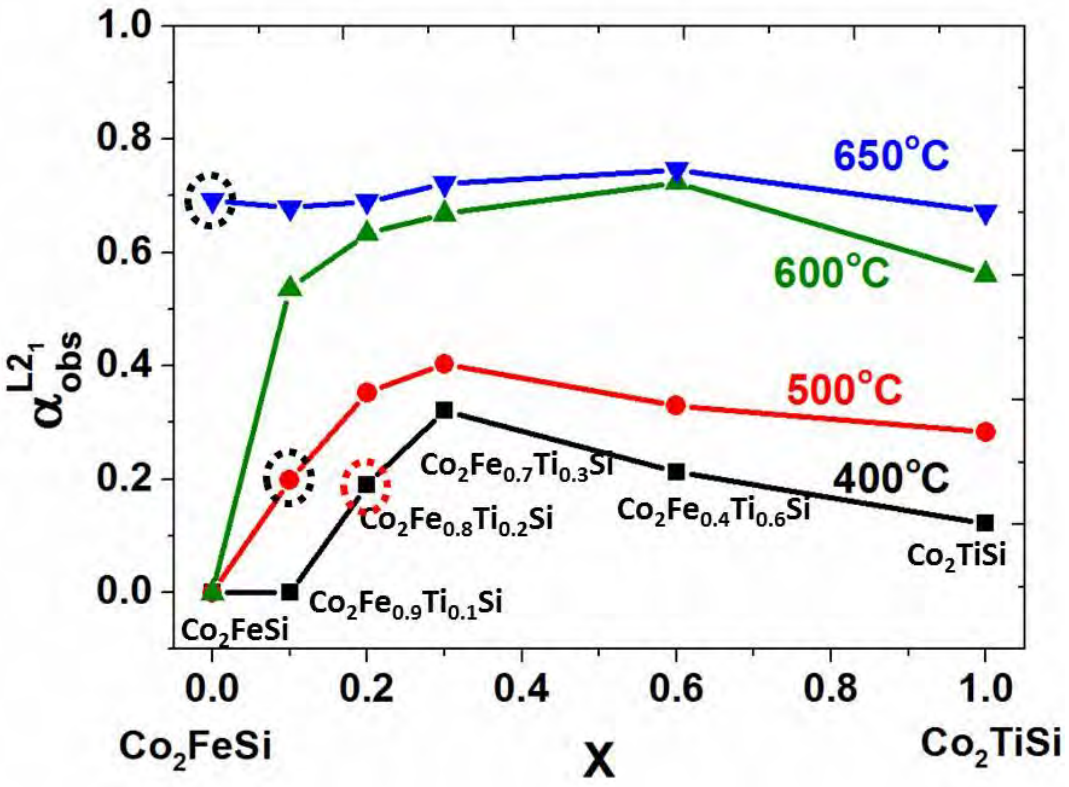

Fig. 4-5 Dependence of $L2_1$ ordering of $Co_2Fe_{1-x}Ti_xSi$ films on annealing temperature and Ti composition.

It is important to point out that annealing above 500°C is necessary to obtain a high $L2_1$ order for the Co_2MnZ and Co_2FeZ (Z = Al, Si, Ge, Ga) Heusler thin films. But for Our CFTS Heusler alloy, clear $L2_1$ order was confirmed even at 400°C as shown in **Fig. 4-6**. In fact, high spin-polarization was reported in $L2_1$ ordered $Co_2Fe(Ga_{0.5}Ge_{0.5})$ (CFGG)[4,7], $Co_2(Fe_{0.4}Mn_{0.6})Si$ (CFMS)[8,12,20,21] and $Co_2Mn(Ga_{0.25}Ge_{0.75})$ (CMGG)[22,23]. This suggests that the partial Ti substitution for Mn/Fe in various $Co_2(Fe,Mn)Z$ is promising for reducing the kinetic ordering temperature, which is useful for processing read head sensors due to the low temperature tolerance for permalloy shield[24].

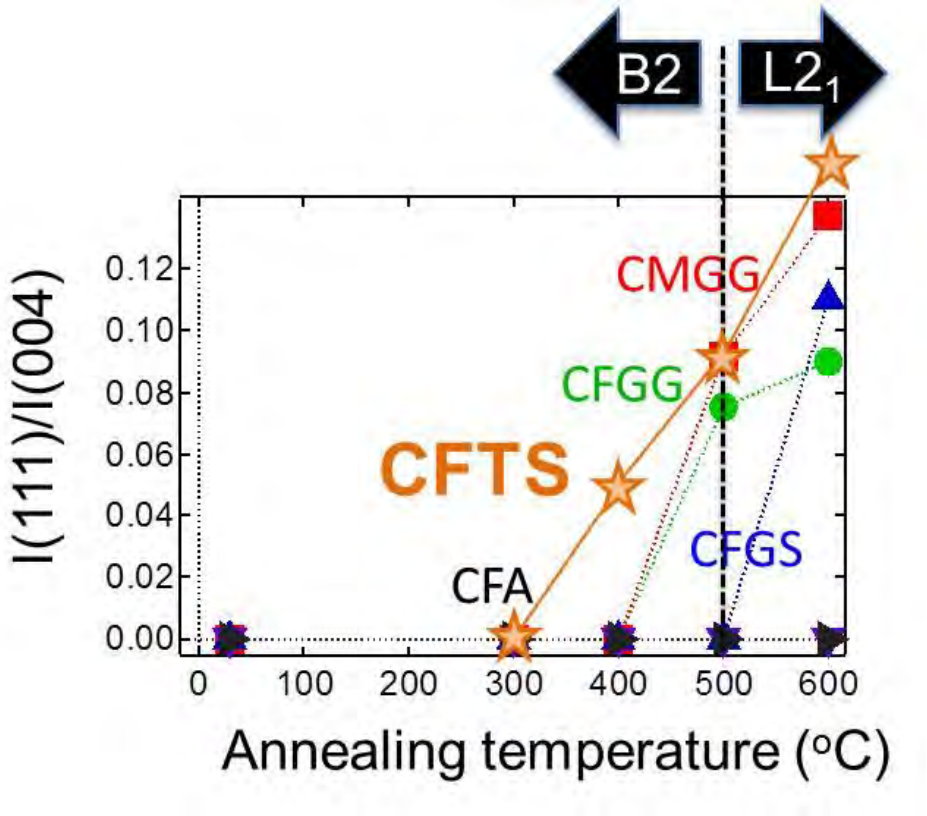

Fig. 4-6 Annealing temperature dependence of the *I*(111)/*I*(004) intensity ratio in CFTS, CFA, CFGS, CFGG and CMGG films. Data except CFTS are from Ref. 12.

4.5 Anisotropic Magnetoresistance (AMR) measurements

4.5.1 Brief introduction of AMR effect

Anisotropic magnetoresistance (AMR) was discovered by W. Thomson one and a half centuries ago[25]. By applying magnetic field along or across the direction of electric current in ferromagnetic conductors (iron or nickel), a few percent change in their resistance (*R*) can be observed. The effect arises from the simultaneous action of magnetization and spin-orbit interaction and its detailed mechanism depends on the material. The anisotropic magnetoresistance can be quantitatively described as the following equation:

$$\text{AMR ratio} = \frac{\Delta\rho}{\rho} = \frac{\rho_{\parallel} - \rho_{\perp}}{\rho_{\perp}} \times 100\%, \qquad (3),$$

Where $\rho_{\parallel}(\rho_{\perp})$ is the resistivity of the film when the electric current *I* parallel (perpendicular) to the magnetization. The AMR effect is used in a wide array of sensors for measurement of Earth's magnetic field (electronic compass), for electric current measuring (by measuring the magnetic field created around the conductor), for traffic detection and for linear position and angle sensing.

Recently, Kokado *et al.* have developed a new theoretical model to analyze AMR effect in various kinds of ferromagnetic (FM) materials, which is considered to be a facile way to investigate the spin-polarization of ferromagnetic materials at room temperature[15,26]. In their theoretical framework, *s-d* electron scattering, which is the origin of AMR, dominantly occurs from s↑ to d↑ sates or s↓ to d↓ states in half-metallic materials, resulting in a negative sign of AMR ratios. Namely, an electric resistance in the parallel condition ($M // I$, where M and I represent magnetization and electric current, respectively) is smaller than that in the perpendicular condition ($M \perp I$). According to their prediction, a measurement of AMR signals of a target ferromagnetic film provides information of a half-metallic nature of the film without any micro-fabrications. Following their prediction, Yang *et al.* have systematically studied AMR effect in $Co_2(Fe_xMn_{1-x})Si$ film and clearly found a sign change of AMR from negative to positive when x became larger than 0.8, suggesting a disappearance of half-metallic nature for $x>0.8$[8]. Thereafter, Sakuraba *et al.* have investigated AMR effect in various Co_2MnZ and Co_2FeZ Heusler epitaxial thin film in more detail and found an interesting correlation between magnitude of AMR ratio and total valence electron number (N_v). They also demonstrated that there is a positive correlation between the magnitude of negative AMR ratio and magnetoresistive output of CPP-GMR devices using the Heusler compounds.

Based on their discovery, we studied spin polarization of CFTS films by measuring AMR effect in the CFTS single layer films in our study. The AMR effect was measured at 10, 100, 200 and 300 K in Physical Property Measurement System (PPMS) under an applied electric current I of 1 mA to the <110> direction of the epitaxial CFTS thin film. A magnetic field of 0.5 T was rotated within in-plane directions.

4.5.2 AMR effect in CFTS

Fig. 4-7 plots the dependence of AMR ratio on Ti composition at 10 and 300 K for all CFTS films annealed at 650 °C in which the similar degree of $L2_1$-ordering was confirmed as shown in **Fig. 4-5**. Clear twofold symmetric curves can be observed for all CFTS films as shown in the inset figures. The AMR ratio of Co_2FeSi exhibited positive value at 300 K and negative value at 10 K, which is consistent with the previous study[7]. Interestingly, the sign of AMR ratio at 300 K suddenly changes from positive to negative

between x=0 and x=0.1. The magnitude of negative AMR ratio gradually increases with increasing x and reaches a maximum of -0.09 % at 300 K and -0.13 % at 10 K in $Co_2Fe_{0.8}Ti_{0.2}Si$. According to the comprehensive theoretical model developed by Kokado *et al.*[15], the sign of AMR ratio in ferromagnetic materials can provide information on its half-metallic nature, *i.e.*, half-metallic ferromagnets always show negative AMR ratio ($\rho_{\perp} > \rho_{//}$). Therefore, this AMR result of Co_2FeSi indicates that Co_2FeSi is half-metal only at low temperature and its half-metallic nature disappears at 300 K, which can be explained by the effect of thermal fluctuation of electron occupancy around E_F at 300 K. Previous experimental results on the CPP-GMR effect using Co_2FeSi also showed similar tendency against temperature[6], *i.e.*, the large temperature dependence of MR outputs of Co_2FeSi/Ag/Co_2FeSi CPP-GMR devices. The sign change of the AMR ratio at 300 K from Co_2FeSi (+) to $Co_2(Fe_{0.9}Ti_{0.1})Si$ (-) can be interpreted as the result of the improved spin-polarization at room temperature due to the shifting of E_F by the small amount of Ti substitution, which corresponds well to the calculation result of DOS shown in **Fig. 4-3**.

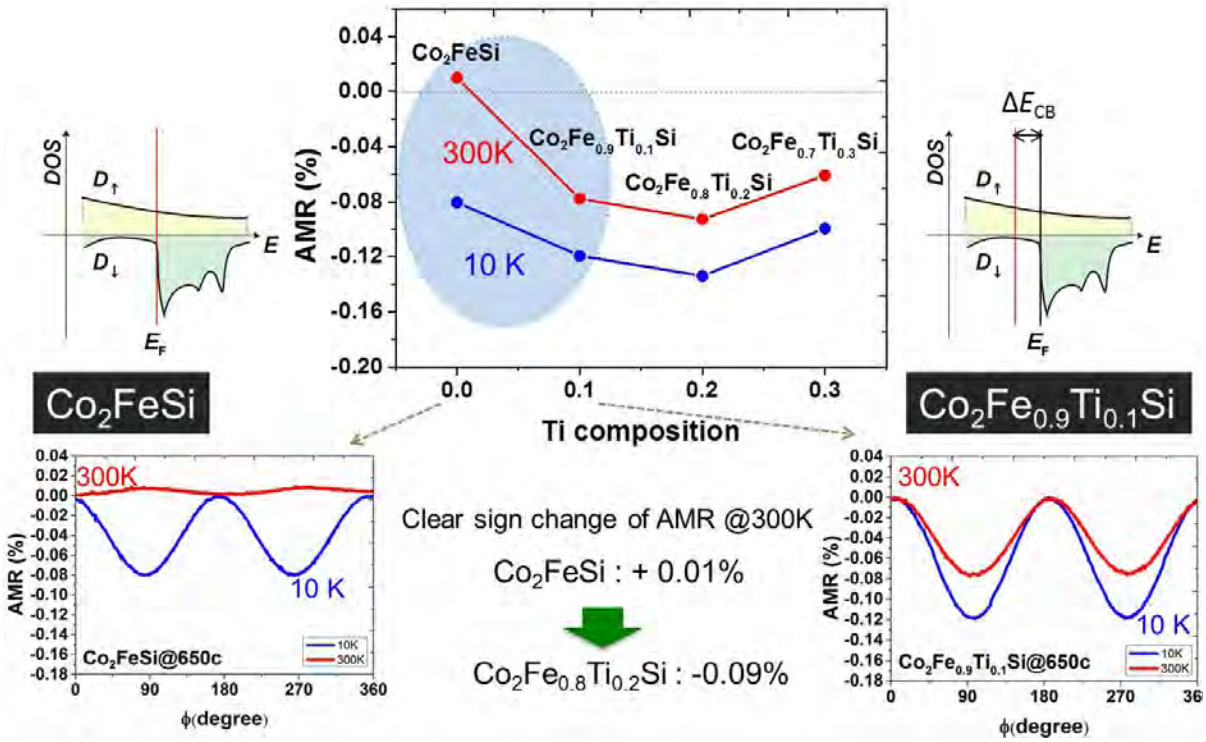

Fig. 4-7 Dependence of AMR ratio on the Ti composition in $Co_2Fe_{1-x}Ti_xSi$ films. The bottom two figures show in-plane relative angle ϕ dependences of AMR ratio in the Co_2FeSi and $Co_2Fe_{0.9}Ti_{0.1}Si$ films.

4.5.3 Temperature dependence of AMR in CFTS

In order to see the effect of thermal fluctuation on half-metallic nature of CFTS more clearly, we investigated the temperature dependence of the AMR effect in the CFTS films in **Fig. 4-8**. The temperature dependence of the AMR ratio includes the temperature dependence of resistivity $\rho(T)$ and the resistivity change originating from the AMR effect, $\Delta\rho(T)$. Whereas the origin of $\rho(T)$ are thermally excited phonon and temperature-independent impurity scattering, $\Delta\rho(T)$ mainly originates from *s-d* scattering via impurity[15]. Therefore, we compare the temperature dependence of normalized $\Delta\rho(T)$ at 10 K, *i.e.*, $\Delta\rho(T)/\Delta\rho(10\text{ K})$, in which the effect of thermally excited phonon-induced scattering and the amount of impurities can be eliminated to see how conductive *s* and localized *d* electronic states contribute to AMR change with temperature in the CFTS films. As shown in **Fig. 4-8**, Co_2FeSi shows the largest temperature dependence of $\Delta\rho$ in all the CFTS films and the temperature dependence can be gradually suppressed by increasing *x* in $Co_2(Fe_{1-x}Ti_x)Si$. This result suggests that ΔE_{CB} increases with increasing Ti composition and the localized *d*-state forming the conduction band of half-metallic gap, which is consistent with the calculated DOS in **Fig. 4-3**.

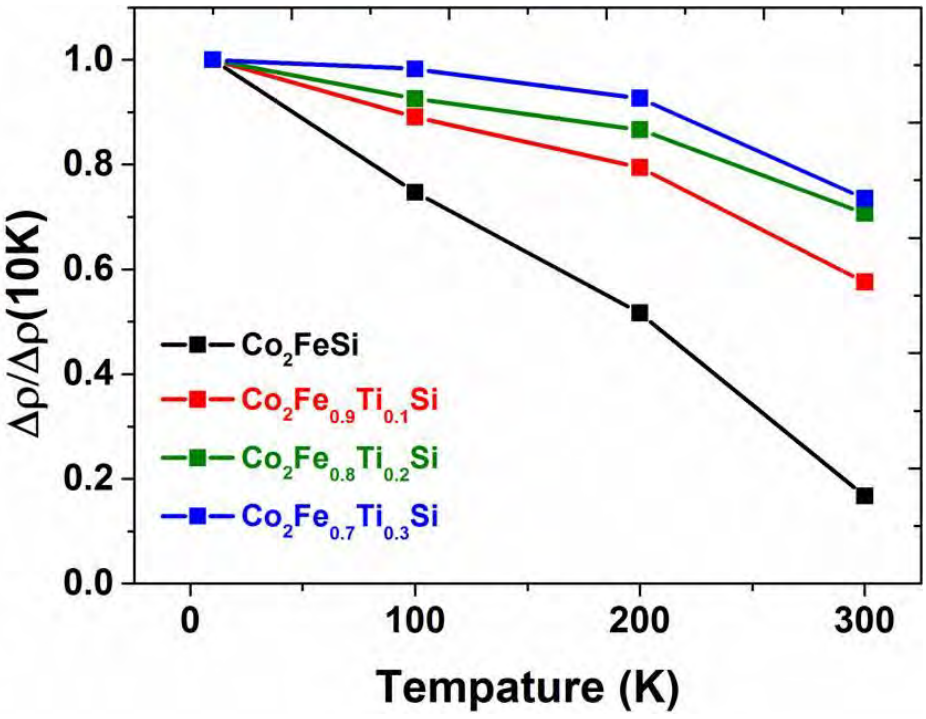

Fig. 4-8 Temperature dependence of normalized resistivity change in $Co_2Fe_{1-x}Ti_xSi$ films.

4.6 CPP-GMR devices with CFTS

Since clear improvement of spin polarization was confirmed both from first principal calculation of DOS and AMR measurement, we then tried to apply CFTS as ferromagnetic layer in CPP-GMR devices to enhance MR property. But unfortunately, the results are disappointing. As shown in **Fig. 4-9 (a)**, the MR ratio decreases rapidly as Ti content increases when CPP-GMR devices were fabricated with CFTS(10 nm)/Ag(5 nm)/CFTS(10 nm) tri-layer structure, which is opposite to what we expected. To find out the reason for that, TEM observation for microstructure analysis was conduct. As shown in the HAADF image in **Fig. 4-9 (b)-(d)**, pin hole-like structure appears in the upper CFTS layer and becomes more and more serious as Ti composition increases.

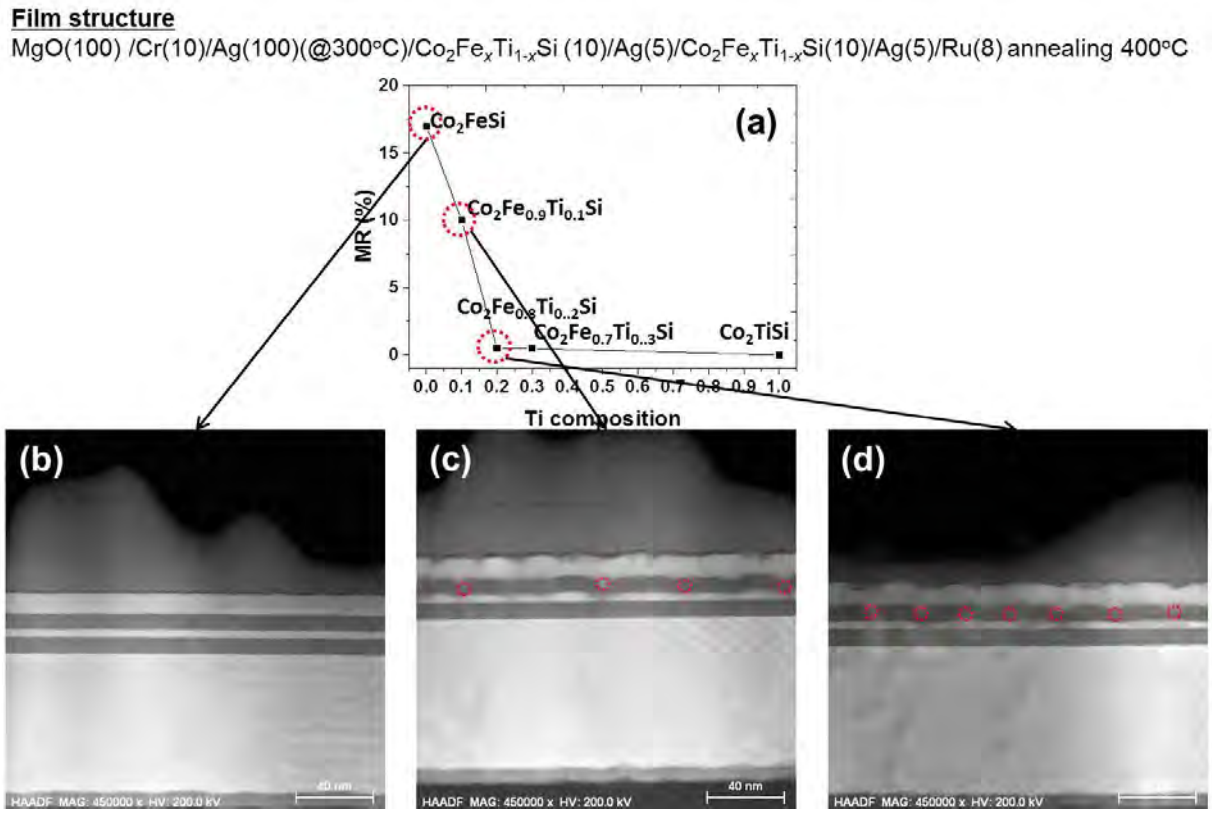

Fig. 4-9 (a) MR ratio as a function of Ti composition. HAADF image for CPP-GMR device with ferromagnetic electrode of (b) Co_2FeSi, (c) $Co_2(Fe_{0.9}Ti_{0.1})Si$, (d) $Co_2(Fe_{0.8}Ti_{0.2})Si$.

The EDS mapping results shown in **Fig. 4-10** indicate that the formation of pin hole-like structure is due to the interdiffusion of Ag element into the top CFTS layer. The origin of such interdiffusion is still not fully understood, but could be attributed to the possibility of alloy forming between Ag and Ti as shown in the phase diagram in **Fig. 4-11**[30]. Therefore, although CFTS Heusler itself is a high spin-polarized material

for spintronic devices, combining CFTS FM layer with Ag spacer is not a good choice for CPP-GMR device improvement. The proposed solutions are trying CPP-GMR devices with CFTS FM layer and other spacer materials, such as Cu, NiAl or non-magnetic Heusler alloy.

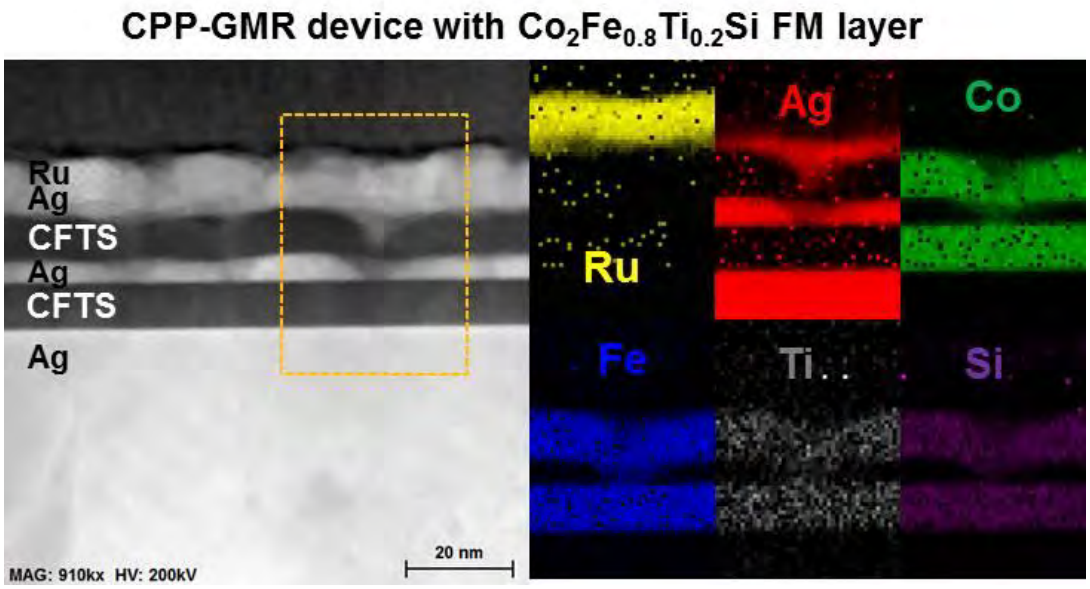

Fig. 4-10 EDS mapping images for CPP-GMR device with $Co_2(Fe_{0.8}Ti_{0.2})Si$ ferromagnetic layer.

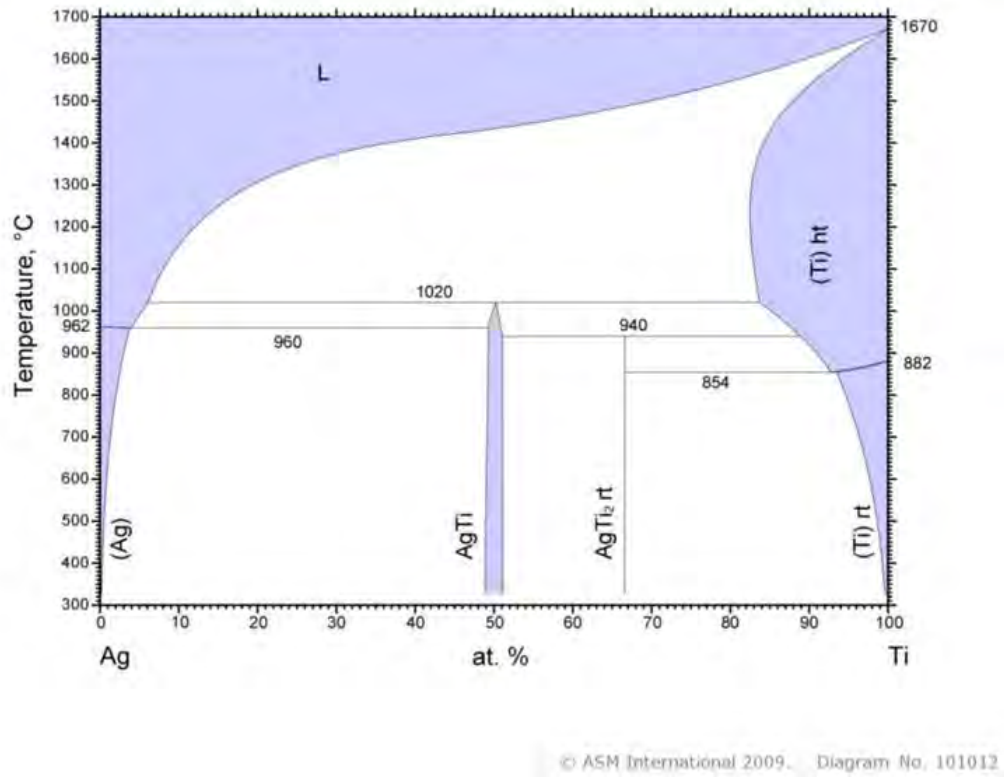

Fig. 4-11 Phase diagram of Ti and Ag binary alloy. [30]

4.7 Non-local lateral spin valve (NLSV) devices with CFTS

Although the improvement of spin-polarization at RT in CFTS Heusler alloy thin films could be qualitatively confirmed by the sign change of AMR ratios of $Co_2(Fe_{1-x}Ti_x)Si$ with x=0 to x=0.1 and the suppression of the temperature dependence of $\Delta\rho$ with increasing x, AMR measurement cannot give actual spin polarization of CFTS Heusler alloy quantitatively. Moreover, CPP-GMR devices with CFTS Heusler alloy cannot work for spin polarization evaluation due to the interdiffusion of Ag and Ti. Therefore, we try to evaluate the spin polarization by measuring spin signals of Non-local lateral spin valve (NLSV) devices.

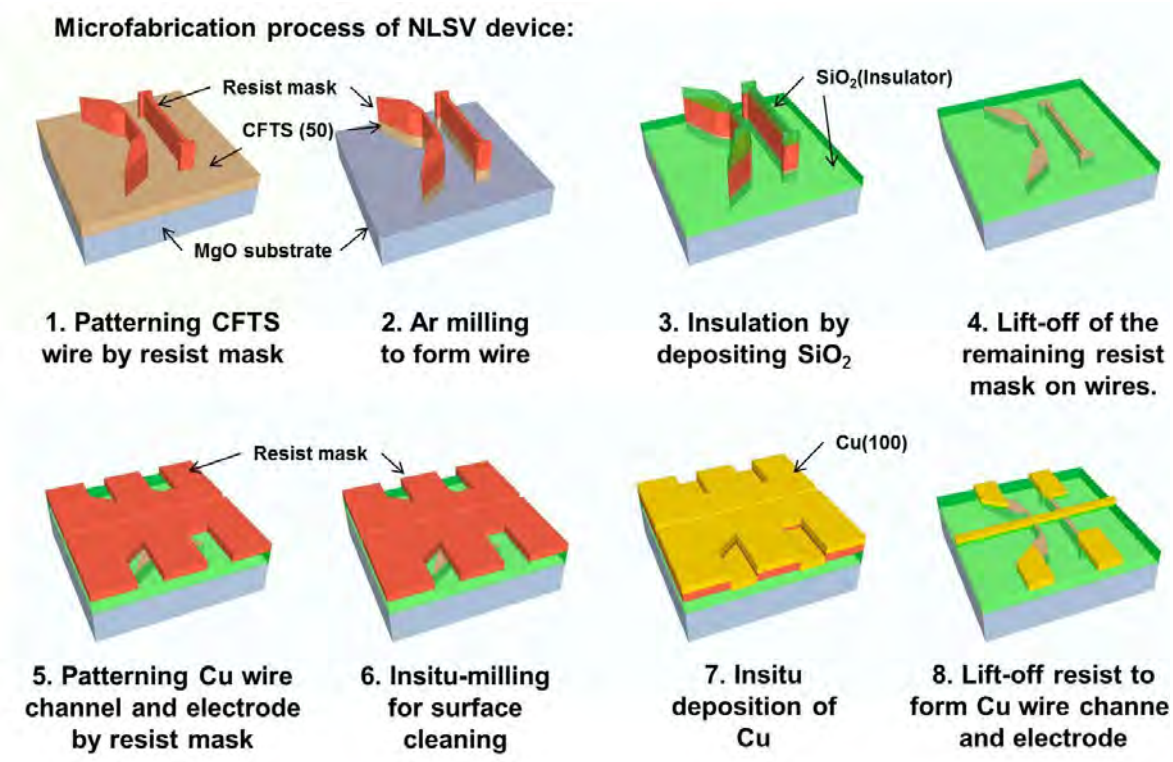

Fig. 4-12 Microfabrication process of NLSV device.

4.7.1 Microfabrication process of NLSV device

Fig. 4-12 shows the microfabrication process details of NLSV device. The NLSV devices with parallel spin-injection and detection wires bridged by an orthogonal Cu channel wire were prepared by microfabricating $Co_2Fe_{1-x}Ti_xSi$ (x = 0, 0.1 and 0.2) films annealed at 650°C. The surfaces of CFTS wires were cleaned by moderate in-situ Ar ion milling just before depositing Cu channel to obtain transparent interfaces between CFTS and Cu channel wires. The thickness t_{CFTS} and width w_{CFTS} of the CFTS wires

were varied between 30 nm and 157 nm, and the Cu wire thickness was around 100 nm with a wire width w_{Cu} of 133 nm. Total 24 devices having different center-to-center distances d, from 450 to 1350 nm, between two CFTS wires were patterned on one substrate to evaluate spin-polarization. The electrical measurement was performed in a non-local configuration with DC reversal method at 300 K.

4.7.2 Spin signal of NLSV device

In order to confirm the enhancement of spin-polarization by the Fe substitution with Ti in CFS as suggested from the AMR measurements more quantitatively, we evaluated the spin polarization by measuring spin signals of NLSV devices using the single layer CFTS films. As shown in the inset of **Fig. 4-13**, we measured the spin accumulation signal ΔR_s by flowing a dc current from one CFTS wire to the left side of Cu wire. **Fig. 4-13** shows the d dependence of ΔR_s. ΔR_s increases with increasing x, indicating the enhancement of spin-polarization. In order to quantify the value of spin-polarization, observed ΔR_s - d were fitted by the one-dimensional spin diffusion model[16], given as

$$\Delta R_s = 4R_{Cu}\frac{\left(\frac{P_{CFTS}}{1-{P_{CFTS}}^2}\frac{R_{CFTS}}{R_{Cu}}\right)^2 e^{\left(-\frac{d}{\lambda_{Cu}}\right)}}{\left(1+\frac{2}{1-{P_{CFTS}}^2}\frac{R_{CFTS}}{R_{Cu}}\right)^2 - e^{\left(-\frac{2d}{\lambda_{Cu}}\right)}},$$

Where $R_{CFTS} = \rho_{CFTS}\lambda_{CFTS}/A_J$ and $R_{Cu} = \rho_{Cu}\lambda_{Cu}/A_{Cu}$ are the spin resistance of CFTS and Cu, respectively. $\rho_{CFTS(Cu)}$, $\lambda_{CFTS(Cu)}$, A_J and A_{Cu} correspond to the resistivity of CFTS(Cu), the spin diffusion length of CFTS(Cu), the area of CFTS/Cu interfaces and the cross-sectional area of the Cu wires, respectively. P_{CFTS} is the spin polarizations of CFTS wires. ρ_{CFTS} was evaluated to be 55, 38 and 26 μΩcm for x = 0.0, 0.1 and 0.2, respectively. Previous study on the CPP-GMR device using epitaxial $Co_2FeAl_{0.5}Si_{0.5}$ (CFAS) electrodes estimated that λ_{CFAS} = 2.2 nm and ρ_{CFAS} = 71.0 μΩcm at RT[31], which results in $\rho_{CFAS}\lambda_{CFAS}$= 1.56 ×10^{-5} μΩcm^2. Based on the inverse proportional relationship between ρ and λ [32] and similar constituents between CFTS and CFAS, we assumed the $\rho_{CFTS}\lambda_{CFTS}$ = $\rho_{CFAS}\lambda_{CFAS}$ = 1.56 ×10^{-5} μΩcm^2, for x = 0.0, 0.1 and 0.2. ρ_{Cu} of Cu wire is experimentally measured to be around 4.7 μΩcm at 300K. Assuming λ_{Cu} is the same for all devices, the fitting result gives spin polarization of $P_{Co_2FeSi} = 0.61$, $P_{Co_2Fe_{0.9}Ti_{0.1}Si} = 0.65$, and $P_{Co_2Fe_{0.8}Ti_{0.2}Si} = 0.70$, respectively with λ_{Cu} = 315 nm.

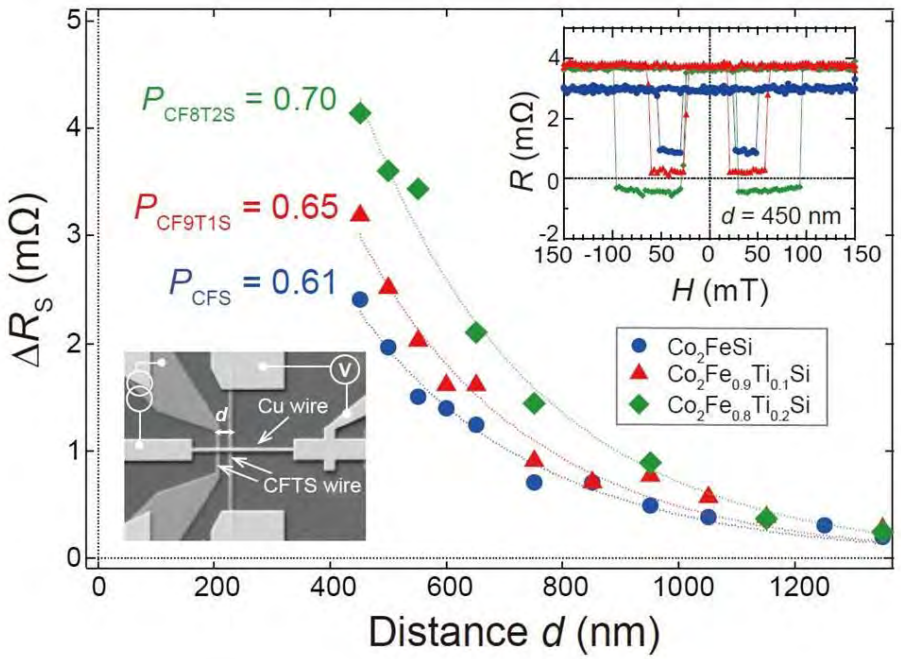

Fig. 4-13 Spin signal ΔR_s as a function of wire distance d for each $Co_2Fe_{1-x}Ti_xSi$ device. Dashed line indicates the fitting result by the one dimensional spin diffusion model. The insets show SEM image of typical LSV device and the R-H curves for the devices with d = 450 nm.

This result indicates that Ti substitution for Fe in the Co_2FeSi Heusler alloy gives an enhancement of spin polarization at RT, which agrees well with our first-principle calculation and the AMR measurement.

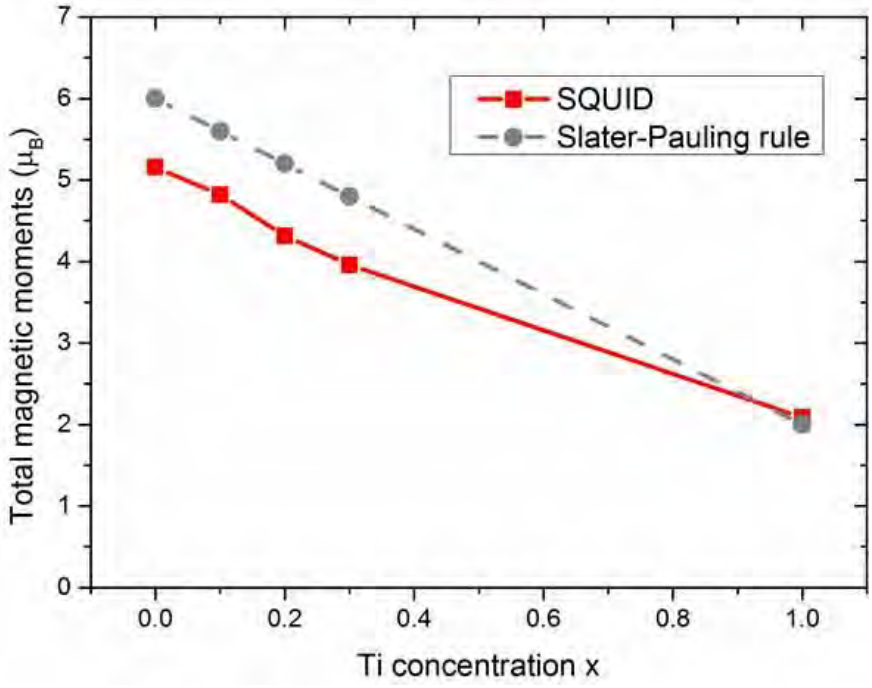

Fig. 4-14 Total magnetic moments for $Co_2Fe_{1-x}Ti_xSi$ measured at 10K with SQUID as a function of Ti concentration. The dash line indicates the Slater-Pauling rule.

4.8 Magnetic property

Fig. 4-14 shows the magnetic moments per unit cell of CFTS thin films measured at 10K. As shown in the figure, the total magnetic moments measured by SQUID decreases linearly with increasing *x*. This tendency is in good agreement with the total magnetic moments calculated by the Slater-Pauling rule. However, remarkable difference can be found between the experimental values and the Slater-Pauling rule. Such difference can be understood by the presence of *A*2 or *B*2 disorder in the CFTS films. *B*2 disorder in Co_2FeSi samples is unavoidable, leading to a decreased magnetic moment compared with the perfect $L2_1$ structure. As mentioned previously, substituting Fe with Ti can improve the degree of $L2_1$ order; therefore, the difference between the experimentally measured value and Slater-Pauling rule becomes smaller as Ti concentration increases. Note that too much Ti substitution in Co_2FeSi will cause a side effect, i.e., decrease in Curie temperature from Co_2FeSi (1100K)[9] to Co_2TiSi (380K)[33] . All the CFTS thin films exhibit soft magnetic properties at 10K as shown in the *M-H* curve in **Fig. 4-15**.

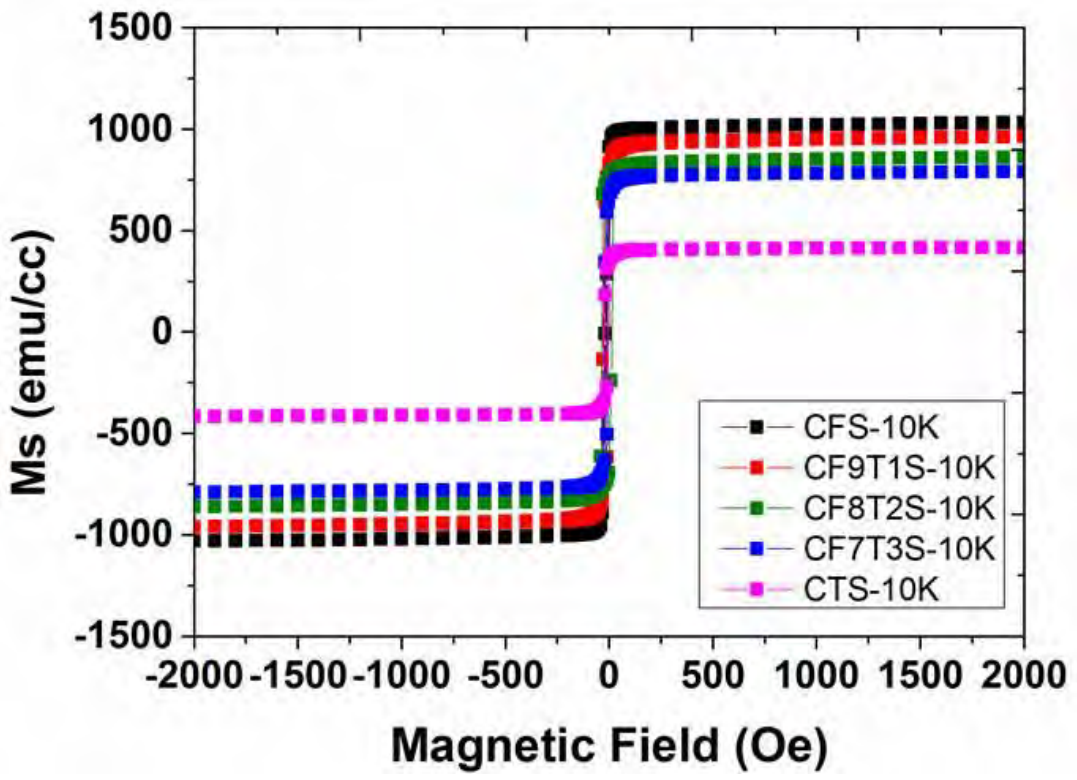

Fig. 4-15 magnetization curves of CFTS alloy measured at 10K.

4.9 Summary of this chapter

In this chapter, we fabricated a series of Heusler alloys, $Co_2(Fe_{1-x}Ti_x)Si$ ($0 \le x \le 1$), and their electronic states, crystal structure, and spin-dependent transport properties were systematically investigated. The summaries are as follow:

1) First-principles calculations of DOS predicted that the minority-spin DOS forming CB edge of half-metallic gap is located near Fermi level in Co_2FeSi, which shifts toward higher energies with increasing *x*, suggesting the improvement of spin-polarization at room temperature by the substitution of Fe with Ti.
2) The improvement of spin-polarization at RT were qualitatively confirmed by the sign change of AMR ratios of $Co_2(Fe_{1-x}Ti_x)Si$ with x=0 to x=0.1 and the suppression of the temperature dependence of $\Delta\rho$ with increasing *x*.
3) We also evaluated the spin polarization of CFTS by measuring non-local spin signals of the NLSV devices with CFTS thin films wires. The one-dimensional model fitting of the spin signals suggested that the spin-polarization at room temperature increases from 0.61 for Co_2FeSi to 0.70 for $Co_2Fe_{0.8}Ti_{0.2}Si$.
4) We also confirmed that the kinetic $L2_1$-ordering temperature decreases from 650 ºC for Co_2FeSi to 400 ºC for $x > 0.2$, which is promising feature for various spintronic applications that have a limitation for annealing temperature.

Citation for this part can be referred to:

Jiamin Chen, Y. Sakuraba, K. Masuda, Y. Miura, S. Li, S. Kasai, T. Furubayashi, K. Hono
"Enhancement of $L2_1$ order and spin-polarization of Co_2FeSi thin film by substitution of Fe with Ti"
Applied Physics Letters. **110**, 242401 (2017) [http://dx.doi.org/10.1063/1.4985237]

Reference

[1] S. Kämmerer, A. Thomas, A. Hütten, and G. Reiss, Appl. Phys. Lett. **85**, 79 (2004).

[2] Y. Sakuraba, J. Nakata, M. Oogane, H. Kubota, Y. Ando, A. Sakuma, and T. Miyazaki, Jpn. J. Appl. Phys. **44**, L1100 (2005).

[3] T. Iwase, Y. Sakuraba, S. Bosu, K. Saito, S. Mitani, and K. Takanashi, Appl. Phys. Express **2**, 063003 (2009).

[4] S. Li, Y.K. Takahashi, T. Furubayashi, and K. Hono, Appl. Phys. Lett. **103**, 042405 (2013).

[5] Y.K. Takahashi, A. Srinivasan, B. Varaprasad, A. Rajanikanth, N. Hase, T.M. Nakatani, S. Kasai, T. Furubayashi, and K. Hono, Appl. Phys. Lett. **98**, 152501 (2011).

[6] Y. Sakuraba, M. Ueda, Y. Miura, K. Sato, S. Bosu, K. Saito, M. Shirai, T.J. Konno, and K. Takanashi, Appl. Phys. Lett. **101**, 252408 (2012).

[7] B.S.D.C.S. Varaprasad, A. Srinivasan, Y.K. Takahashi, M. Hayashi, A. Rajanikanth, and K. Hono, Acta Mater. **60**, 6257 (2012).

[8] F.J. Yang, Y. Sakuraba, S. Kokado, Y. Kota, A. Sakuma, and K. Takanashi, Phys. Rev. B **86**, (2012).

[9] S. Wurmehl, G. Fecher, H. Kandpal, V. Ksenofontov, C. Felser, H.-J. Lin, and J. Morais, Phys. Rev. B **72**, 184434 (2005).

[10] O. Gaier, J. Hamrle, S. Trudel, B. Hillebrands, H. Schneider, and G. Jakob, J. Phys. Appl. Phys. **42**, 232001 (2009).

[11] T. Furubayashi, T.M. Nakatani, H.S. Goripati, H. Sukegawa, Y.K. Takahashi, K. Inomata, and K. Hono, J. Appl. Phys. **114**, 123910 (2013).

[12] Y. Sakuraba, S. Kokado, Y. Hirayama, T. Furubayashi, H. Sukegawa, S. Li, Y.K. Takahashi, and K. Hono, Appl. Phys. Lett. **104**, 172407 (2014).

[13] D. Bombor, C.G.F. Blum, O. Volkonskiy, S. Rodan, S. Wurmehl, C. Hess, and B. Büchner, Phys. Rev. Lett. **110**, (2013).

[14] Y. Miura, M. Shirai, and K. Nagao, J. Appl. Phys. **99**, 08J112 (2006).

[15] S. Kokado, M. Tsunoda, K. Harigaya, and A. Sakuma, J. Phys. Soc. Jpn. **81**, 024705 (2012).

[16] S. Takahashi and S. Maekawa, Phys. Rev. B **67**, (2003).

[17] H. Ebert, D. Ködderitzsch, and J. Minár, Rep. Prog. Phys. **74**, 096501 (2011).

[18] J.P. Perdew, K. Burke, and M. Ernzerhof, Phy Rev Lett **77**, 3865 (1996).

[19] H.C. Kandpal, G.H. Fecher, C. Felser, and G. Schönhense, Phys. Rev. B **73**, (2006).

[20] T. Kubota, S. Tsunegi, M. Oogane, S. Mizukami, T. Miyazaki, H. Naganuma, and Y. Ando, Appl. Phys. Lett. **94**, 122504 (2009).

[21] S. Takahashi, Y. Sonobe, and K. Takanashi, U.S. patent 0,188,034 (2015).

[22] B.S.D. Varaprasad, A. Rajanikanth, Y.K. Takahashi, and K. Hono, Acta Mater. **57**, 2702 (2009).

[23] Y.K. Takahashi, N. Hase, M. Kodzuka, A. Itoh, T. Koganezawa, T. Furubayashi, S. Li, B.C.S. Varaprasad, T. Ohkubo, and K. Hono, J. Appl. Phys. **113**, 223901 (2013).

[24] M.J. Carey, S. Maat, S. Chandrashekariaih, J.A. Katine, W. Chen, B. York, and J.R. Childress, J. Appl. Phys. **109**, 093912 (2011).

[25] W. Thomson, Proc. R. Soc. Lond. **8**, 546 (1856).

[26] S. Kokado and M. Tsunoda, Adv. Mater. Res. **750–752**, 978 (2013).

[27] T. Furubayashi, T.M. Nakatani, H.S. Goripati, H. Sukegawa, Y.K. Takahashi, K. Inomata, and K. Hono, J. Appl. Phys. **114**, 123910 (2013).

[28] M. Oogane, M. Shinano, Y. Sakuraba, and Y. Ando, J. Appl. Phys. **105**, 07C903 (2009).

[29] Z. Gercsi, A. Rajanikanth, Y.K. Takahashi, K. Hono, M. Kikuchi, N. Tezuka, and K. Inomata, Appl. Phys. Lett. **89**, 082512 (2006).

[30] M. Li, C. Li, F. Wang, and W. Zhang, Calphad **29**, 269 (2005).

[31] T.M. Nakatani, T. Furubayashi, S. Kasai, H. Sukegawa, Y.K. Takahashi, S. Mitani, and K. Hono, Appl. Phys. Lett. **96**, 212501 (2010).

[32] J. Bass and W.P. Pratt, J. Phys. Condens. Matter **19**, 183201 (2007).

[33] J. Barth, G.H. Fecher, B. Balke, S. Ouardi, T. Graf, C. Felser, A. Shkabko, A. Weidenkaff, P. Klaer, H.J. Elmers, H. Yoshikawa, S. Ueda, and K. Kobayashi, Phys. Rev. B **81**, (2010).

Chapter 5 Realization of high quality epitaxial CPP-GMR pseudo spin-valves on Si(001) wafer using NiAl buffer layer

5.1 Introduction

Up to now, as described in the previous two chapters, substantial large MR ratios at room temperature (RT) was realized in fully epitaxial CPP-GMR devices with the usage of the Co-based Heusler alloys such as Co_2MnSi (CMS)[1], $Co_2Mn(Ga_{0.25}Ge_{0.75})$ (CMGG)[2], $Co_2(Fe_{0.4}Mn_{0.6})Si$ (CFMS)[3] and $Co_2Fe(Ga_{0.5}Ge_{0.5})$ (CFGG)[4]. Such a high MR output in a low resistance device has already satisfies the MR performance required for the areal density of 2 Tbit/in^2 according to the simulation by Takagishi *et al.*[5] However, all of these high MR outputs have only been demonstrated for the epitaxial CPP-GMR pseudo spin-valves (PSVs) grown on unpractical MgO single crystalline substrates, which are too expensive for mass production and cannot be realized with current semiconductor industry processes. On the other hand, for industrial viability, polycrystalline CPP-GMR devices that grown on thermal-oxidized Si substrate have been used,[6–8] but unfortunately, the MR output of polycrystalline devices are much lower than those of epitaxial devices that were grown on MgO substrates. The existence of grain boundary and inferior layer roughness are considered to be possible reasons for such large discrepancy of MR outputs between polycrystalline and single crystalline (epitaxial) devices. Therefore, it is strongly desired to develop industrial viable high performance epitaxial CPP-GMR devices on a Si single crystalline substrate to satisfy practical application requirement. The main concept is described in **Fig. 5-1**. In addition, single crystalline devices on Si substrate also enable us to utilize a wafer bonding technology,[9] that can be a solution to overcome the obstacles of present fabrication process of practical devices such as a limitation of annealing temperature.

Actually, growing high quality epitaxial CPP-GMR device on Si(001) single crystalline substrate is not that easy. For instance, the growth of high quality epitaxial ferromagnetic (FM) films on Si has puzzled scientists for decades mainly because of the very high reactivity between most transition metals and silicon, which results in the formation of silicide and **Fig. 5-2** shows one of the examples. Many materials have been tried in the previous studies to use as a buffer layer but problems such as serious intermixing, large surface roughness, low thermal stability and large lattice mismatch with 3*d* FM layer still exist.[10–12]

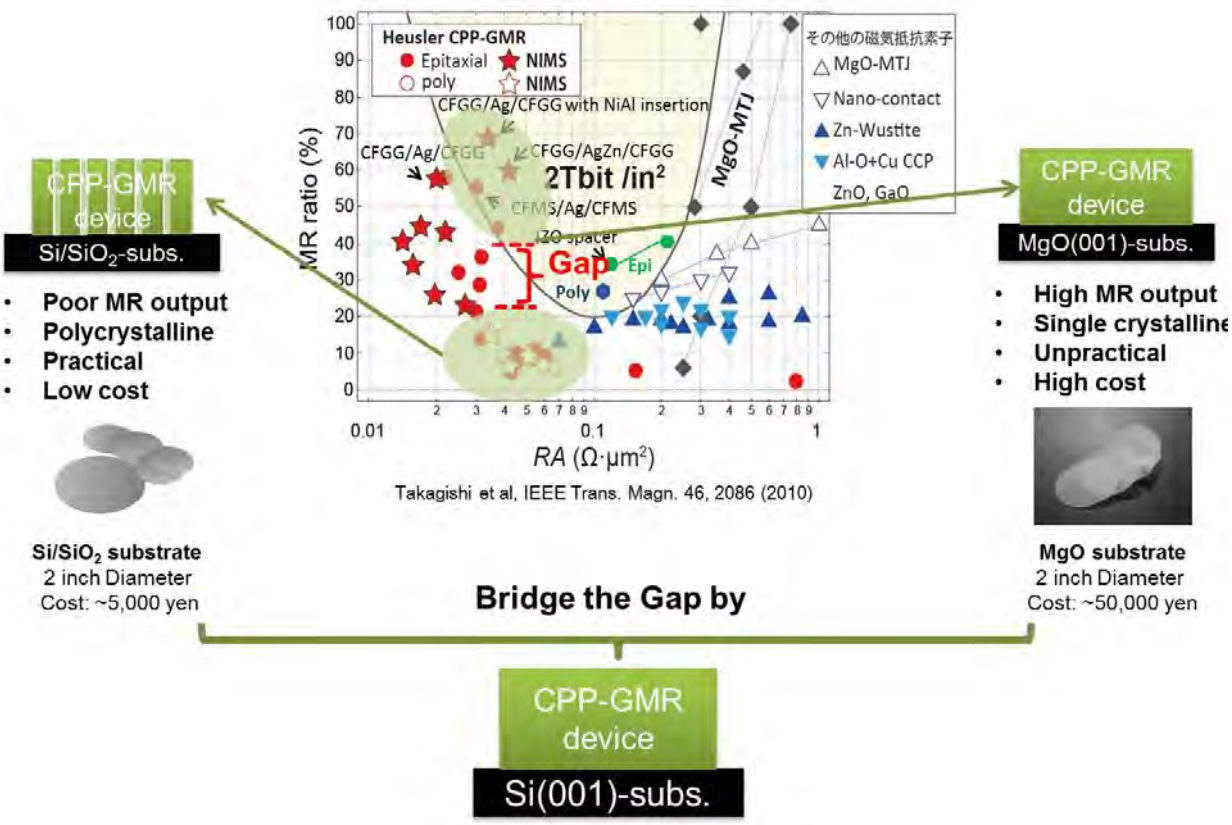

Fig. 5-1 Background introduction of this chapter.

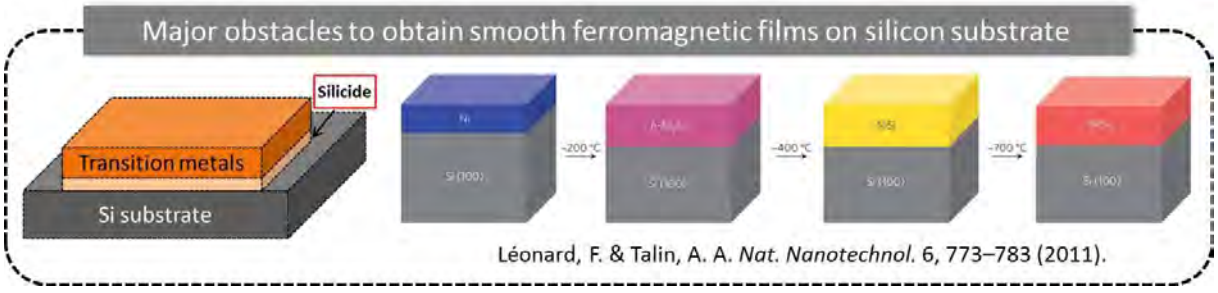

Fig. 5-2 Silicide formation problem in Ni-Si system.

In this chapter, we describe the usage of NiAl as a buffer material for the growth of high quality fully epitaxial CPP-GMR devices on Si single crystalline wafer. NiAl has merits including high thermal stability with a melting point up to 1620°C,[13] relatively small lattice mismatch (~6%) with Si substrate and almost perfect lattice matching (less than 1%) with Co-based Heusler alloys.[14,15]

5.2 Buffer material selection

To obtain fully epitaxial growth of ferromagnetic layer on Si, a buffer material which satisfies the following requirement is needed: (1) Small lattice mismatch with both the Si substrate and ferromagnetic layer; (2) Stable enough to avoid mixture with other layer during annealing process. (3) Easy to fabricate via sputtering method. Therefore, selecting a suitable buffer material is the most crucial issue for the growth of epitaxial CPP-GMR device on Si(001) single crystalline substrate. **Table 5-1** lists all the buffer material candidates that we have considered. After trying many materials, we found NiAl and TiN promising.

TABLE 5-1. The list of buffer candidates.

Materials	Space group	Lattice constant a (nm)	Lattice constant b (nm)	Lattice constant c (nm)	Min misfit with Si (%)	Min misfit with CFGG (%)
Si	Fd-3m O2 (227)	0.543	0.543	0.543	0.0	5.4
TaN	Fm-3m (225)	0.43443	0.43443	0.43443	13.1	7.0
AlN	F-43m (216)	0.434	0.434	0.434	13.0	6.9
TiN	Fm-3m (225)	0.4236	0.4236	0.4236	10.3	4.4
MgO	Fm-3m (225)	0.42101	0.42101	0.42101	9.6	3.7
Ag	Fm-3m (225)	0.4086	0.4086	0.4086	6.4	0.7
Au	Fm-3m (225)	0.40839	0.40839	0.40839	6.4	0.6
Al	Fm-3m (225)	0.4048	0.4048	0.4048	5.4	0.3
Pt	Fm-3m (225)	0.3923	0.3923	0.3923	2.2	3.3
Ir	Fm-3m (225)	0.384	0.384	0.384	0.0	5.4
Cu	Fm-3m (225)	0.3614	0.3614	0.3614	5.9	11.0
Ta	Im-3m (229)	0.3308	0.3308	0.3308	13.8	15.3
Ti	Im-3m (229)	0.3276	0.3276	0.3276	14.7	14.1
	$P6_3/mmc$ (194)	0.291	0.291	0.459	7.2	1.4
Mg	$P6_3/mmc$ (194)	0.3211	0.3211	0.523	16.4	11.9
	Im-3m (229)	0.33381	0.33381	0.33381	13.1	16.3
GaN	$P6_3mc$ (186)	0.3181	0.3181	0.5177	17.2	10.8
W	Im-3m (229)	0.316	0.316	0.316	16.4	10.1
Mo	Im-3m (229)	0.3096	0.3096	0.3096	14.0	7.9
V	Im-3m (229)	0.302	0.302	0.302	11.2	5.2
Cr	Im-3m (229)	0.29006	0.29006	0.29006	6.8	1.1
NiAl	Pm-3m (221)	0.2886	0.2886	0.2886	6.3	0.6
Fe	Im-3m (229)	0.28654	0.28654	0.28654	5.5	0.2

Ru	**$P6_3/mmc$ (194)**	**0.2706**	**0.2706**	**0.4282**	**0.3**	**5.7**
Zn	**$P6_3/mmc$ (194)**	**0.2667**	**0.2667**	**0.4939**	**1.8**	**7.1**
Ni	**$P6_3/mmc$ (194)**	**0.265**	**0.265**	**0.432**	**2.4**	**7.7**
	Fm-3m (225)	**0.3518**	**0.3518**	**0.3518**	**8.4**	**13.3**
Co	**$P6_3/mmc$ (194)**	**0.24933**	**0.24933**	**0.4019**	**8.2**	**13.1**
	Fm-3m (225)	**0.35367**	**0.35367**	**0.35367**	**7.9**	**12.9**
…						

5.2.1 TiN buffer layer

In the previous study, there are several papers reporting successful epitaxial growth of thin films on Si(100) using TiN buffer layer with different fabrication methods as shown in **Fig. 5-3**.[16–18]

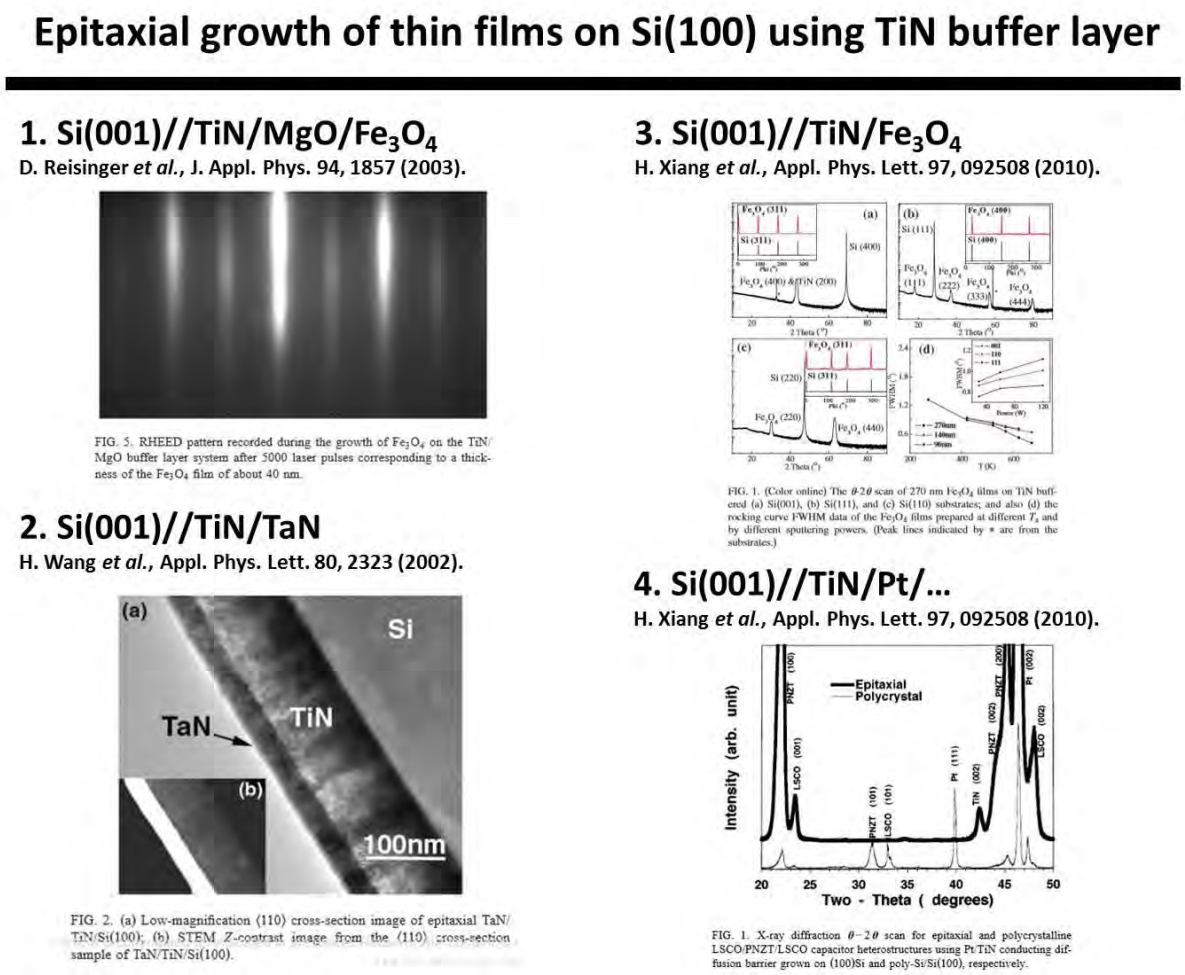

Fig. 5-3 Different papers about epitaxial growth of thin films on Si(100) using TiN buffer layer.

Following their studies, we also try to grow epitaxial TiN layer on Si(001) single crystalline substrate by reactive sputtering Ti with N_2 atmosphere (Ar: 16 sccm + N_2: 2 sccm). **Fig. 5-4** shows RHEED patterns and AFM results of TiN thin films sputtered at different conditions. When TiN thin film was deposited with elevated substrate temperature of 500 ℃ and target to substrate distance T_s=150 mm, RHEED pattern shows polycrystalline feature as indicated in **Fig. 5-4(a)**. As T_s reduces from 150 to 100 mm, TiN layer tend to show better crystallinity, but still polycrystalline. And the surface roughness becomes worse. When substrate temperature increases from 500 ℃ to 600 ℃, crystallinity can be further improved but still not

epitaxial growth. But interestingly, surface roughness becomes better in this deposition condition, which is different from the normal case that surface roughness increases as deposition temperature increases.

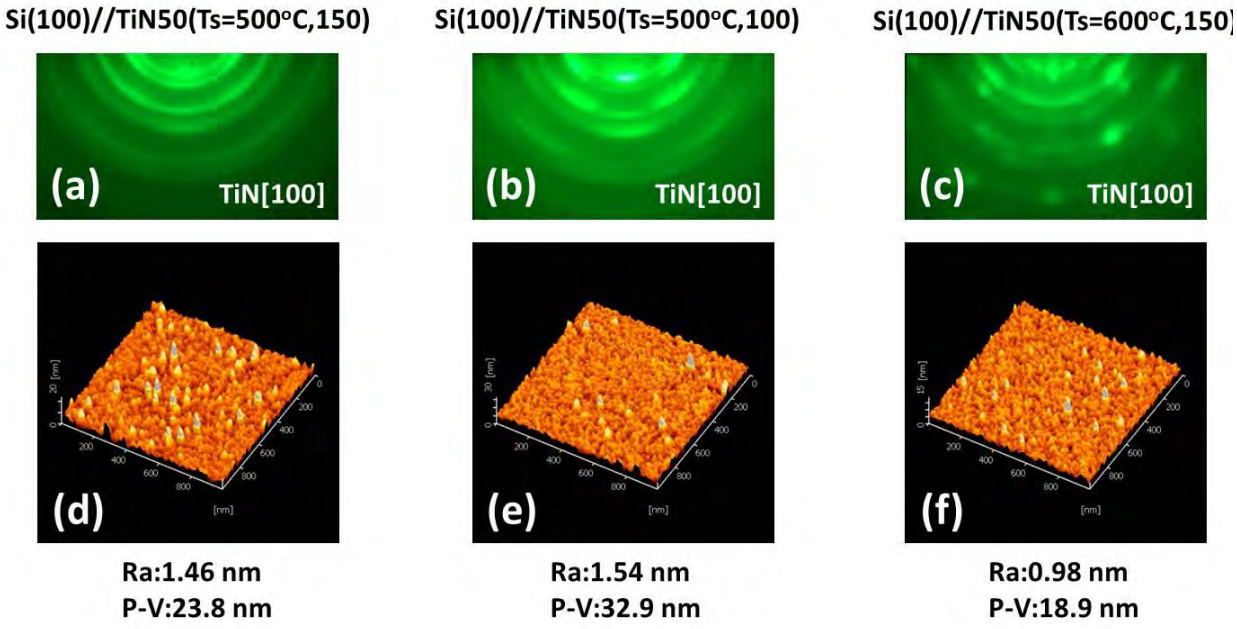

Fig. 5-4 RHEED patterns and AFM results of TiN thin films sputtered at different conditions.

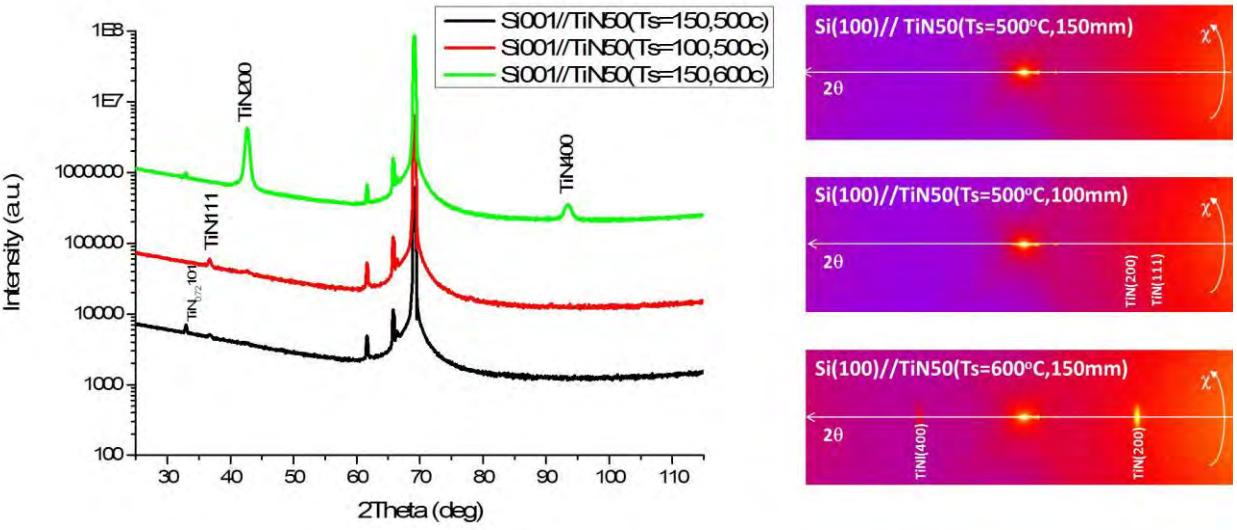

Fig. 5-5 *θ-2θ* XRD profiles and corresponding two-dimensional diffraction images of 50 nm thick TiN layer on Si(001) substrate with different sputter conditions.

Fig. 5-5 shows the XRD patterns for the TiN thin films deposited with previous three conditions. As shown in the figure, TiN sputtered with elevated substrate temperature of 500 ℃ and T_s=150 mm displays only a very weak $TiN_{0.72}$(101) peak, indicating insufficient nitride. When T_s reduces from 150 to 100 mm, $TiN_{0.72}$(101) peak disappears and TiN(111) peak appears instead. For the one that deposited at 600 ℃ and T_s=150 mm, although strong TiN(200) peak can be seen, it is still far from nice epitaxial growth as indicated from the RHEED pattern. Overall, epitaxial growth could be obtained probably by depositing at higher substrate temperature. However, such high deposition temperature will lead to rough surface and cannot be practical. Therefore, better buffer material other than TiN need to be found.

5.2.2 NiAl buffer layer

From the results obtained for TiN so far, it seem that it is not a good candidate for the growth of high quality fully epitaxial CPP-GMR devices on Si single crystalline substrate. Hence, we shift our focus to NiAl. As mentioned in Chapter 3, we come to understand that NiAl is a good buffer layer which can provide a flat and good lattice matching interface for Heusler alloy. More importantly, NiAl holds a lot of merits such as high thermal stability with a melting point up to 1620°C,[13] relatively small lattice mismatch (~6%) with Si substrate. Due to these physical and chemical properties of NiAl, we try it on Si substrate for epitaxial growth.

First, single NiAl layer was made with different deposition temperature changing from 300 to 600 ℃. **Fig. 5-6** shows the XRD patterns accompanied with RHEED patterns for samples with single 50 nm thick NiAl layers deposited on a Si(001) substrate at different temperatures. At the deposition temperature of T_s=300°C, NiAl(011) and NiAl(022) peaks appear, indicating the NiAl layer grows with the (011) orientation in the out-of-plane direction, which is different from the (001) orientation of Si substrate. A very broad NiAl(011) peak shown in the two dimension XRD image suggests that the crystallinity is low at this deposition temperature. A RHEED pattern taken along the NiAl[100] azimuth gives a rings-centered pattern, which means a polycrystalline growth of the NiAl layer. When deposition temperature increases to T_s = 400°C, the NiAl(011) and NiAl(022) peaks disappear; instead, the NiAl(001) and NiAl(002) peaks

appear. The appearance of NiAl(001) peak suggests that the NiAl has *B*2 ordered structure and its crystal orientation becomes (001) to the out-of-plane direction. The spotty peak shown in the 2D XRD image indicates a significant improvement in the crystallinity of the film. The RHEED pattern also becomes streaky, demonstrating the start of epitaxial growth. Note that there is a small satellite peak at around 33 degree near NiAl(001) peak at this deposition temperature. The satellite peak is probably coming from the formation of metastatic silicide Ni_3Si_2 when we increase the deposition temperature, because Ni_3Si_2(330) peak has a peak position of ~33 degree. Details of how this metastatic silicide forms according to different deposition temperature are still unclear and need to be further studied. When the T_s further increases up to 500 and 600°C, the peak intensities for NiAl(001) and NiAl(002) become stronger and the small satellite peaks disappear. The streaks in the diffraction pattern become sharper and more intense.

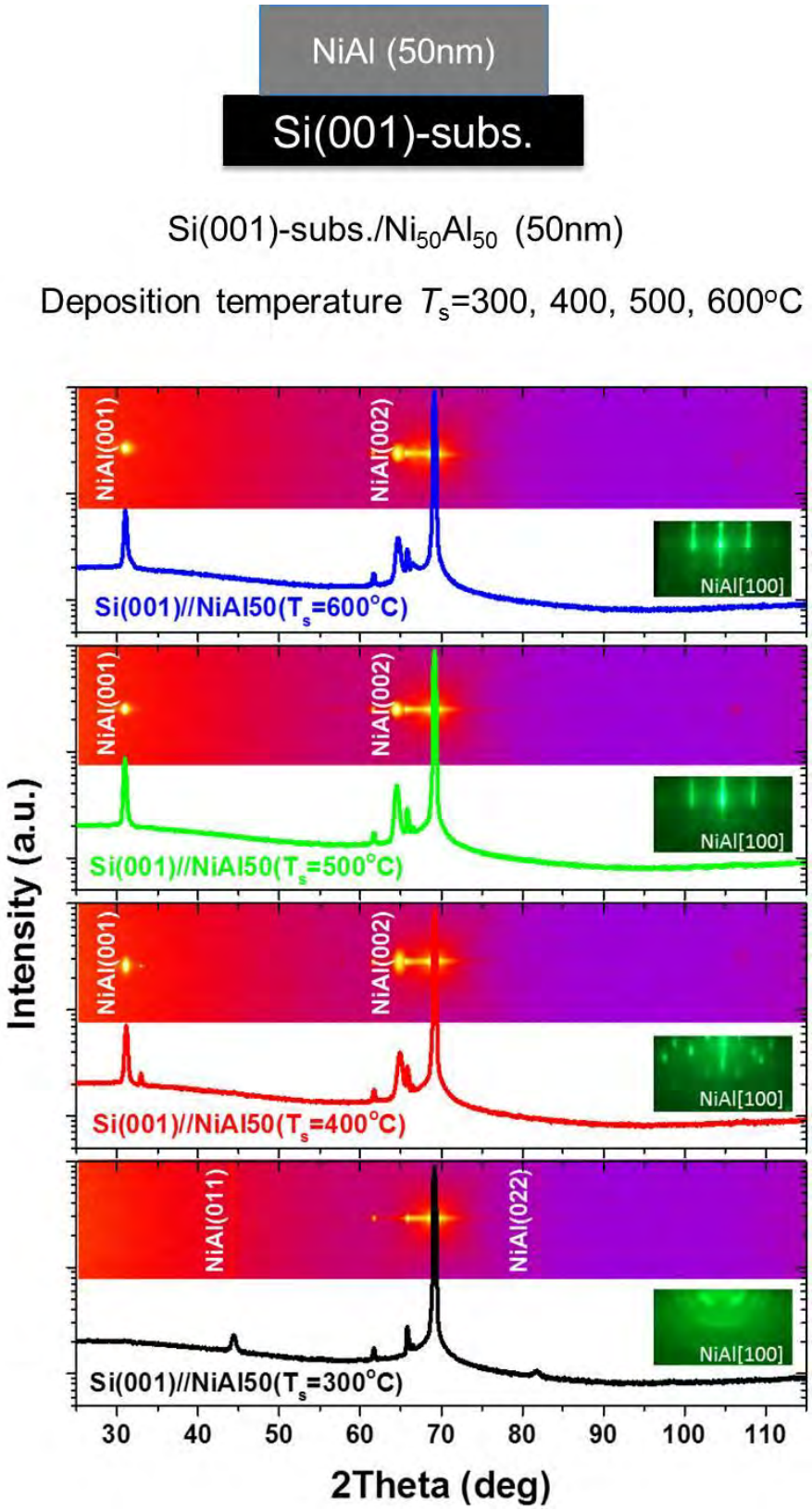

Fig. 5-6 *θ-2θ* XRD profiles and corresponding two-dimensional diffraction images of 50 nm thick NiAl layer on Si(001) substrate with deposition temperature ranging from 300 to 600°C. Insets are RHEED patterns taken along <100> azimuth of each deposition temperature.

5.3 Surface roughness improvement by Ag layer

In order to integrate CPP-GMR devices on Si substrates, it is important to control the surface roughness of each layer. Indeed, the bottom buffer layer, which also serves as a bottom electrode for the devices and a support for upper layer growth, should have a surface roughness as small as possible. **Fig. 5-7** plots the surface roughness as a function of deposition temperature (T_s) for NiAl layer. As shown in the figure, both surface roughness average (R_a) value and peak to valley (P_v) value rise as T_s increase, which means higher deposition temperature leads to poorer layer surface roughness. Deposition temperature T_s = 500°C for NiAl layer is the optimal condition by considering both epitaxial growth and smooth layer surface for our CPP-GMR devices in this study. For the sake of further improvement of bottom buffer layer surface roughness, Ag layer was deposited on the top of NiAl owing to its good lattice matching with NiAl. After the deposition of 50 nm Ag, both R_a and P_v reduce from 2.19 nm and 24.1 nm to 0.94 nm and 12.3 nm. A good epitaxial growth can be maintained as confirmed by the streaky RHEED pattern showing in inset of **Fig. 5-8**. According to our previous studies on CPP-GMR, applying post annealing process can significantly ameliorate the surface roughness of Ag layer. As shown in **Fig. 5-8**, both R_a and P_v fall strikingly as post annealing temperature (T_a) enhances. At the annealing temperature T_a = 600°C, surface roughness starts to be deteriorated due to serious formation of silicide at the interface between NiAl and Si, which will be discussed from the microstructure analysis in later section. Therefore, post annealing temperature T_a = 500°C is selected for the following growth of CPP-GMR devices.

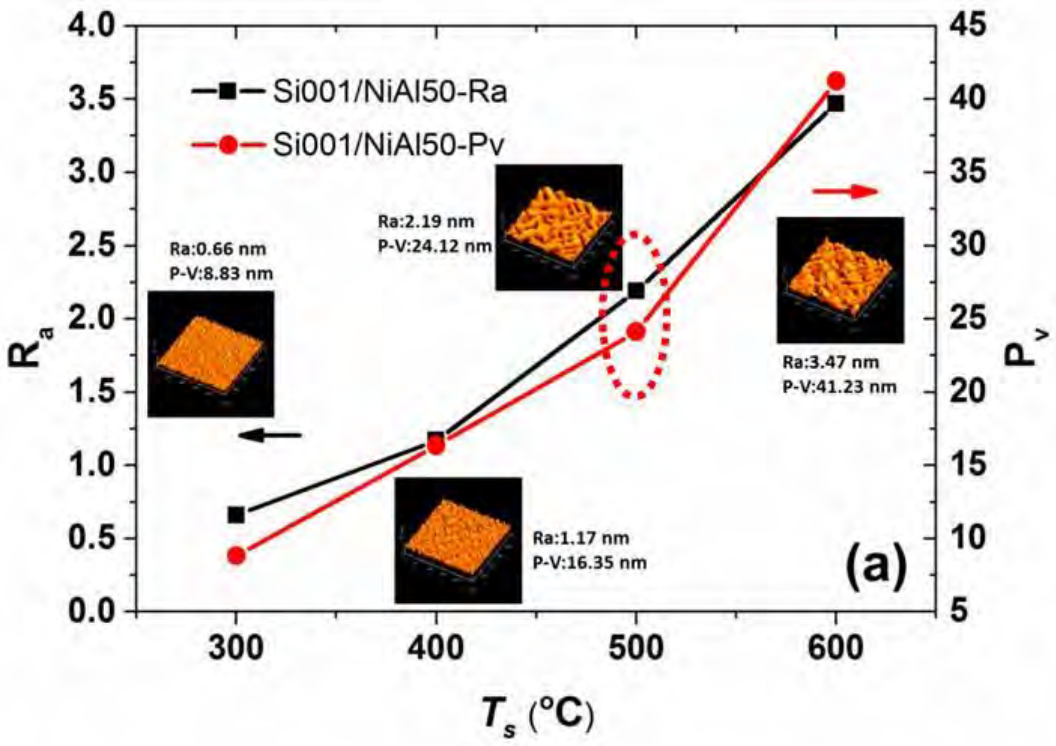

Fig. 5-7 Surface roughness measured by AFM of the film stacks (a) Si(001)//NiAl(50 nm). Insets are surface structure of each deposition temperature.

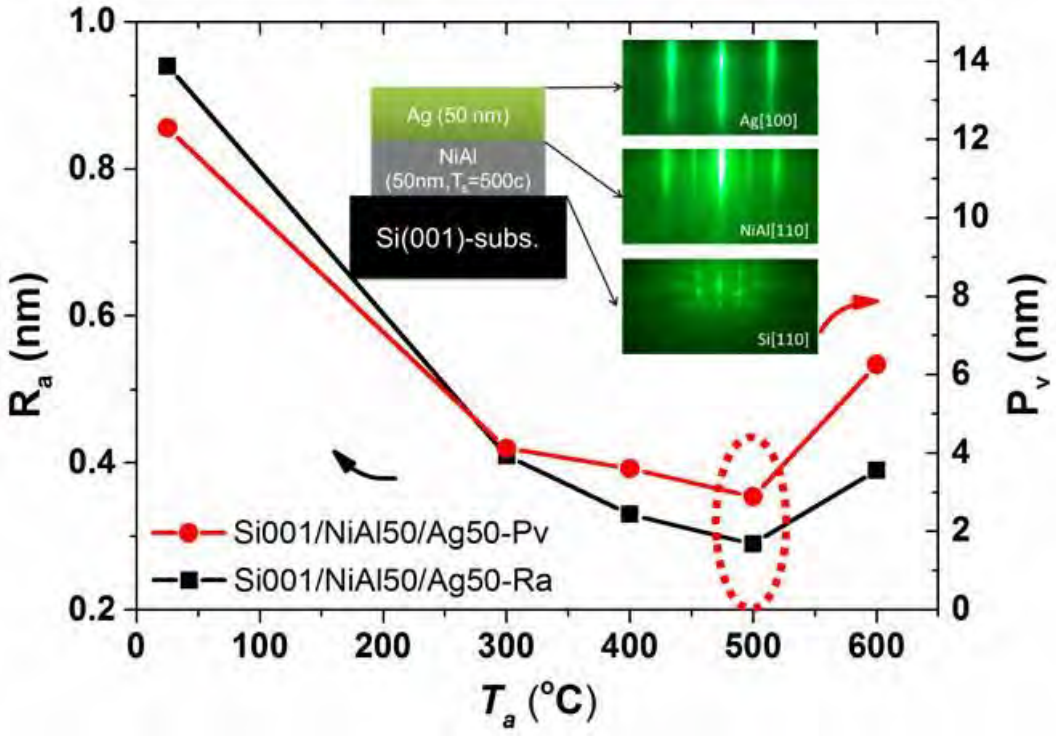

Fig. 5-8 Surface roughness measured by AFM of the film stacks Si(001)//NiAl(50 nm)/Ag(50 nm). Insets are sample structure illustration.

5.4 Si(001)-based CPP-GMR using NiAl buffer layer

5.4.1 Experiment details

A fully epitaxial multi-layer stack of NiAl(50)/Ag(50)/CFGG(10)/Ag(5)/CFGG(10) /Ag(5)/Ru(8) (thickness in nm) was deposited onto Si(001) single-crystalline substrates using the ultrahigh vacuum magnetron sputtering system with a base pressure lower than 5×10^{-7} Pa. The Si substrates were chemically etched using 3% HF acid water solution to remove the thin SiO_2 surface layer formed from natural oxidation of Si. Before the deposition of thin film, substrates were heated at 600°C for 30 min inside the sputtering chamber for thermal cleaning. The clean and smooth Si surface was confirmed by observing reconstructed 2×1 patterns detected from reflection high-energy electron diffraction (RHEED) (see in **Fig. 5-8**). Firstly, 50 nm thick NiAl was deposited on Si substrate by reactive deposition epitaxy (RDE) method[19,20], *i.e.*, by deposition onto a heated substrate, with an elevated temperature ranging from T_s =300 to 600°C. The composition of NiAl alloy target is $Ni_{0.5}Al_{0.5}$. Thereafter, 50 nm thick Ag was deposited at RT on the NiAl layer to serve as a bottom electrode for an MR measurement. The Ag layer was *in-situ* annealed at 300-600°C after the deposition to improve the surface roughness. The CFGG layer was sputter deposited using an alloy target with a composition of $Co_{49.3}Fe_{24.6}Ga_{12.9}Ge_{13.2}$ measured by inductively coupled plasma analysis. After the deposition of a top CFGG layer, the films were post-annealed again at 350-550°C inside the chamber for 30 min to promote the chemical order of CFGG. Finally, Ag/Ru capping layer was deposited at RT to avoid oxidation.

The surface structure of each layer was characterized by RHEED and the whole multilayer crystal structure was examined by 4-axis X-ray diffraction (XRD) using Cu-*K*α radiation. The surface morphology was measured by means of atomic force microscopy (AFM). Cross-sectional transmission electron microscopy (TEM) and aberration-corrected scanning TEM (STEM) were employed to characterize the microstructure of the film stacks. For CPP-GMR measurements, the film stacks were micro-fabricated into elliptical pillars with dimensions ranging from 70×140 to 200×400 nm^2 by electron beam lithography and Ar ion etching. The actual area of the pillar was measured by scanning electron microscopy (SEM) to enable the calculation of the resistance-area product (*RA*) and the resistance change-area product (Δ*RA*). The

magnetoresistance was measured by the direct current four-probe method at 300K with a constant current of 100 μA and a magnetic field along the <110> direction of the epitaxial CFGG layer. The MR ratio was determined using the equation of $\mathrm{MR} = (R_{ap} - R_p)/R_p$, where $R_{ap}(R_p)$ represents the device resistance when the two CFGG layers exhibit the antiparallel (parallel) magnetization configuration.

5.4.2 Crystal structure characterization

5.4.2.1 XRD

Fig. 5-9 shows the XRD patterns for the samples with the stack structure of Si(001) sub.//NiAl(50)/Ag(50)/CFGG(10)/Ag(5)/CFGG(10) /Ag(5)/Ru(8) (thickness in nm) at the as-deposited state and annealed at 400°C, respectively. Clear epitaxial growth with (001) orientation in the out-of-plane direction of each layer can be confirmed in both samples.

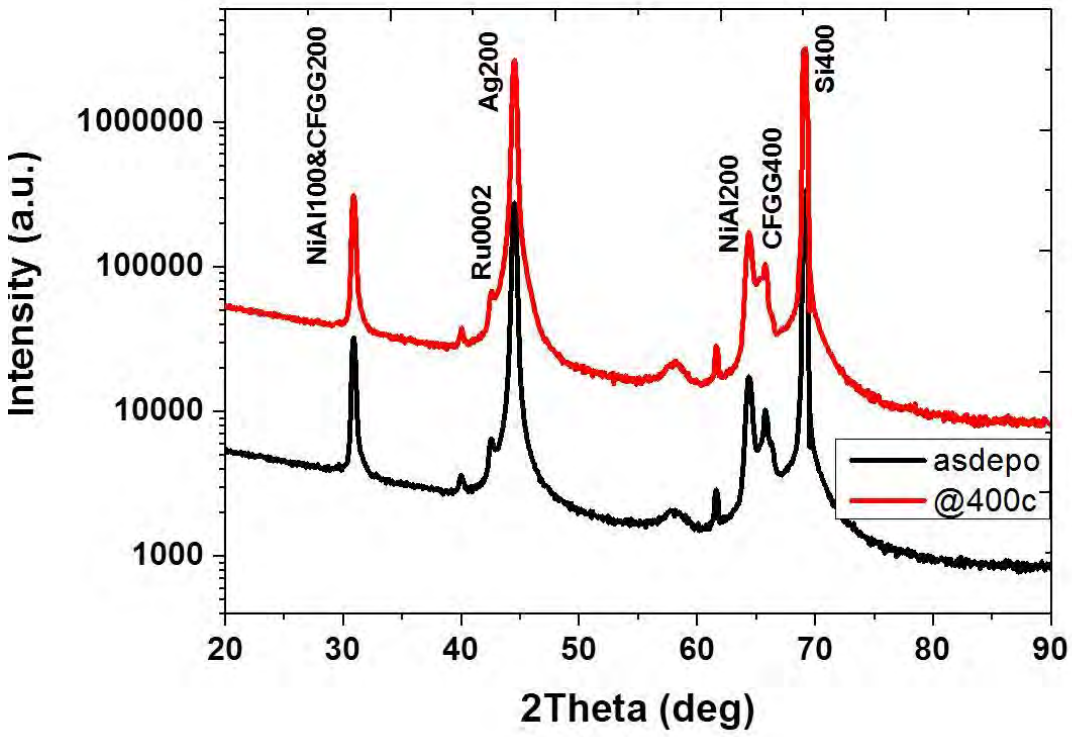

Fig. 5-9 XRD patterns for the samples with the stack structure of Si(001) sub.//NiAl(50)/Ag(50)/CFGG(10)/Ag(5)/CFGG(10) /Ag(5)/Ru(8) (thickness in nm) at the as-deposited state and annealed at 400°C, respectively.

To determine the in-plane crystallographic orientations relationships, XRD pole-figure measurements were performed from Si(022), NiAl(011), Ag(022) and CFGG(022) fundamental diffractions, as shown in **Fig. 5-10**. From the figure, a 45° shift of the Ag(022) peak was observed because of the better lattice matching. From the XRD pole-figures, the epitaxial relationship of Si(001)[110]//NiAl(001)[110]//Ag(001)[100]//CFGG(001)[110] for all the layers was determined.

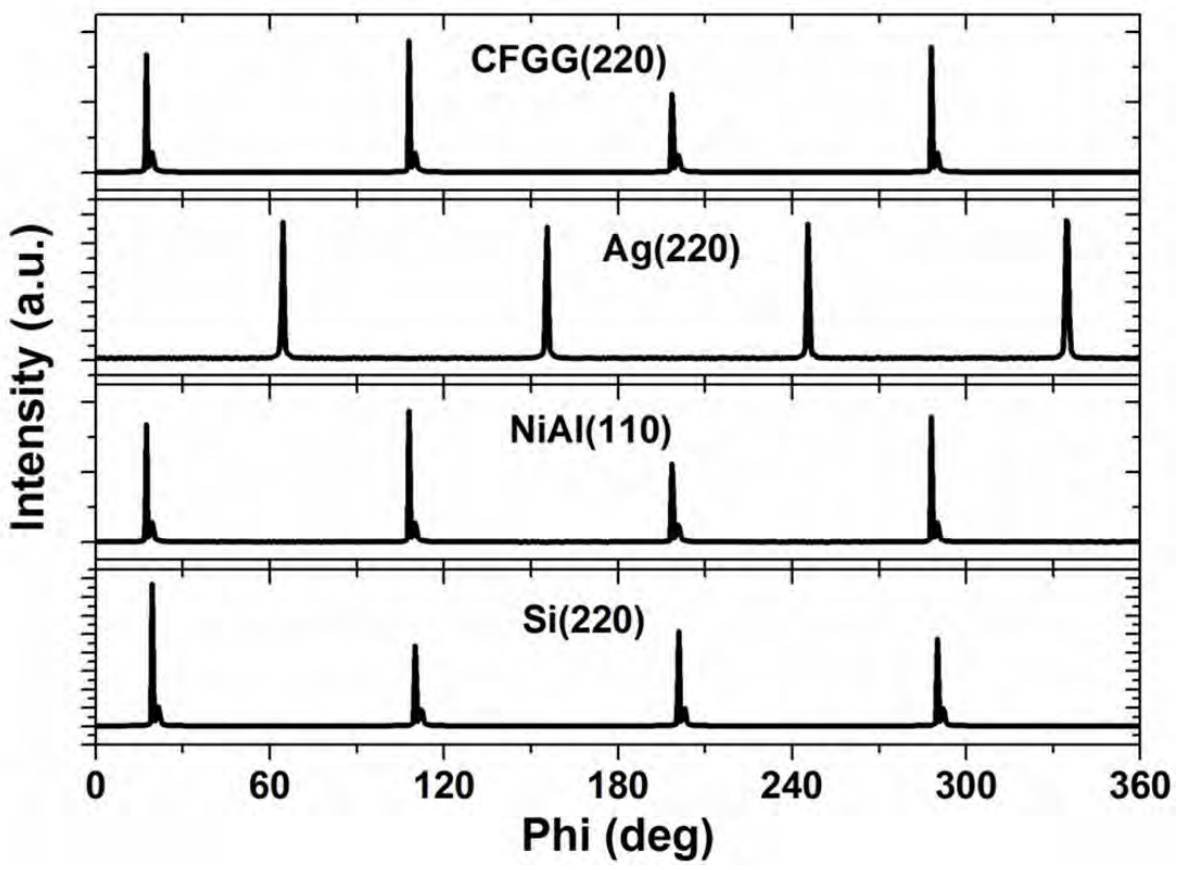

Fig. 5-10 XRD pole-figure measurements for Si(022), NiAl(011), Ag(022) and CFGG(022) peaks.

5.4.2.2 RHEED

Since the NiAl (011) and CFGG (022) fundamental peaks overlap due to the almost identical out-of-plane lattice parameters of a_{CFGG}=0.287 nm and a_{NiAl}=0.289 nm, we have to further verify the orientation relationships by RHEED. **Fig. 5-11** shows the stacking structure for the whole CPP-GMR devices and the RHEED patterns for each layer. The RHEED patterns confirm the epitaxial relation as previously described. Even though a relatively large lattice mismatch of ~6% exists at the NiAl($2a_{NiAl}$=0.578 nm)/Si(a_{Si}=0.543 nm) interface, a nice streaky pattern of NiAl can still be obtained. The diffraction pattern of the 50 nm Ag buffer layer becomes more intense after post-annealing at 500°C. The top CFGG layer shows very broad streak in the as-deposited state; the pattern streak turns into narrow and super-lattice streak appears after post-annealing at 400°C. Such variation can be explained by the improvement of surface roughness and promotion of chemical ordering in the CFGG layers.

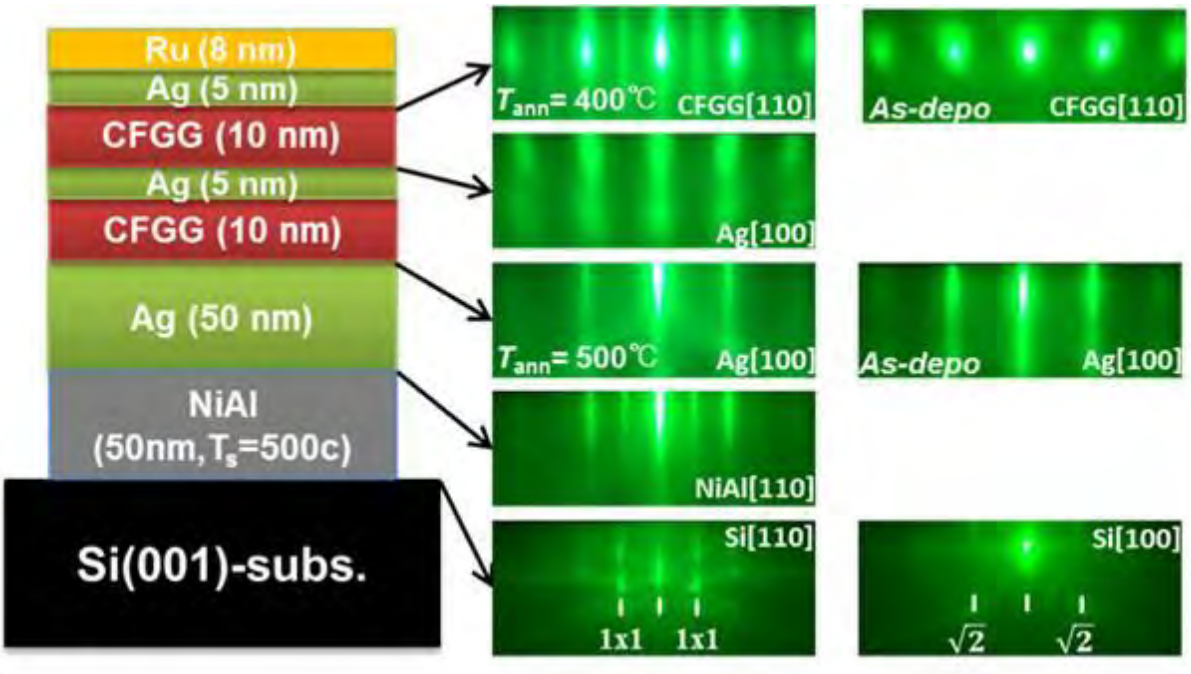

Fig. 5-11 Structure illustrations of whole CPP-GMR film stack and corresponding RHEED patterns for each layer.

5.4.3 Magneto-transport properties

5.4.3.1 Measurement of the lead resistance

The resistance of the devices was plotted as a function of the inverse of CPP-GMR pillar area (**Fig. 5-12**). The lead resistance is calculated to be 0.76Ω according to the formula of $R_{device} = \rho \cdot l \cdot \frac{1}{A} + R_{lead}$, where the ρ was the average resistivity of the pillar, l was the thickness of the pillar and A is the area of the pillar. Note that the lead resistance here is higher than that in the case of MgO-based CPP-GMR device, simply because the bottom electrode layer of Ag is reduced from 100 to 50 nm.

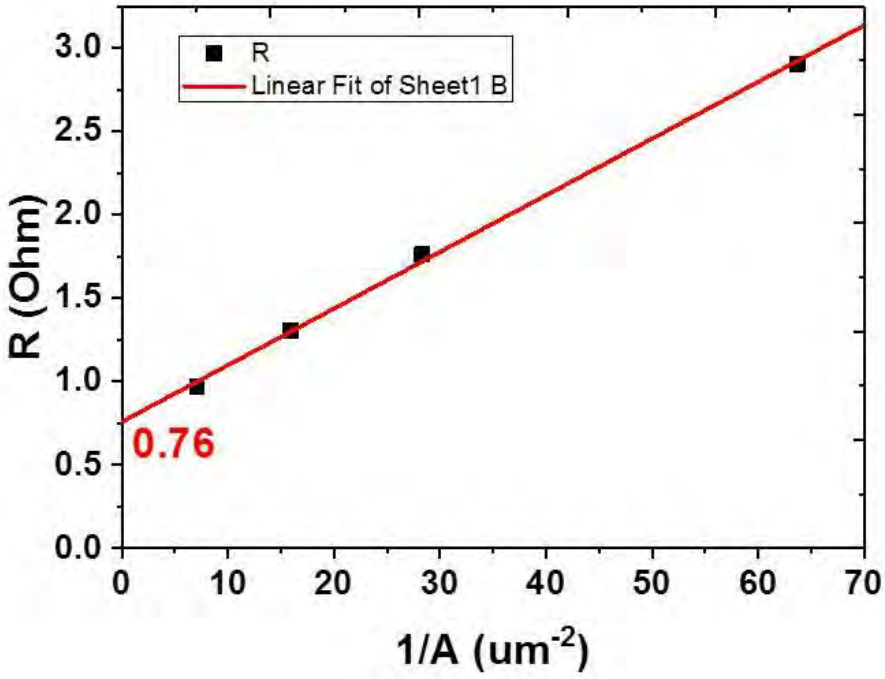

Fig. 5-12 Resistance of the CPP-GMR devices as a function of the inverse of CPP-GMR pillar area.

5.4.3.2 Room temperature magneto-transport properties

CPP-GMR devices were microfabricated by using film stack shown in **Fig. 5-11.** The magnetoresistance was measured by the direct current four-probe method at 300K with a constant current of 100 μA and a magnetic field along the <110> direction of the epitaxial CFGG layer. **Fig. 5-13** summarizes the MR outputs of resistance change-area product (ΔRA) for the epitaxial CPP-GMR devices grown on a Si(001) substrate (red star) as a function of annealing temperature. The results of the epitaxial CPP-GMR devices on an

MgO(001) substrate (black square)[21] and the polycrystalline CPP-GMR devices on a Si/SiO_2 substrate (grey square, green circle and blue triangle)[7] are also shown for comparison. For the CPP-GMR devices grown on a Si(001) substrate, the MR output enhances as the post-annealing temperature increases and reaches a maximum of 8.6 mΩμm^2 at 400°C. Thereafter, the MR output descends as the post-annealing temperature rises above 400°C. The drop of MR output at high annealing temperature stems from the formation of a nickel silicide layer at the NiAl/Si interface and corresponding interdiffusion through the multilayer structure, which will be further discussed from TEM characterization in section 5.4.4. It is important to point out that for the post-annealing temperature up to 400°C, the CPP-GMR devices grown on a Si(001) substrate presents comparable MR outputs with those grown on an MgO(001) substrate. This means we can replace the expansive impractical MgO substrate with the Si substrate to achieve high performance epitaxial CPP-GMR devices for practical sensor applications, which is a great breakthrough. More importantly, by combining this epitaxial Si/NiAl template with the wafer bonding technique[9], various types of spintronic devices such as CPP-GMR, magnetic tunnel junctions, spin-field-effect transistors and lateral spin valves can be grown on a Si substrate and easily attached to other integrated circuits or magnetic shield layers, which is promising for next-generation spintronic applications based on epitaxial devices. MR output obtained for the optimal annealing temperature of 400°C for the epitaxial CPP-GMR devices is about 40% higher than that for the polycrystalline CPP-GMR devices. Such a large discrepancy of the MR outputs between polycrystalline and single crystalline devices could be attributed to the existence of grain boundaries and inferior layer roughness in the polycrystalline devices. Recently, *Du et. al.*[22] have reported the usage of $(Mg_{0.5}Ti_{0.5})O$ buffer layer to enhance the MR output in polycrystalline CFGG/Ag/CFGG device by controlling the crystal orientation and improving the interfacial roughness. Although they had improved the interfacial roughness, the enhancement of MR output was limited. Therefore, the existence of grain boundary may be more responsible for the discrepancy. According to the Valet-Fert model, ΔRA can be expressed by $\Delta RA \sim 2\frac{\beta^2}{1-\beta^2}\rho_F t_F + 2\frac{\gamma^2}{1-\gamma^2}AR_{F/N}$, where β, ρ_F, and t_F are the bulk spin asymmetry, resistivity and layer thickness of CFGG, and γ and $AR_{F/N}$ are the interfacial spin asymmetry and interfacial resistance at the CFGG/Ag interface, respectively. The existence of grain boundaries in the FM layers in the polycrystalline

devices can produce a spin-independent electron scattering channel when the current is applied to the devices, which will degrade the spin electron selection function of the spin valve device. Since β is closely related to the spin polarization of an FM layer, the MR output in polycrystalline CPP-GMR devices will consequently behave inferior to that in epitaxial CPP-GMR devices. Since we are able to improve interfacial roughness and eliminate grain boundaries in epitaxial CPP-GMR devices growth on Si substrate, the gap between practical low performance polycrystalline CPP-GMR devices and impractical high performance epitaxial CPP-GMR device can be filled in by using the Si//NiAl template.

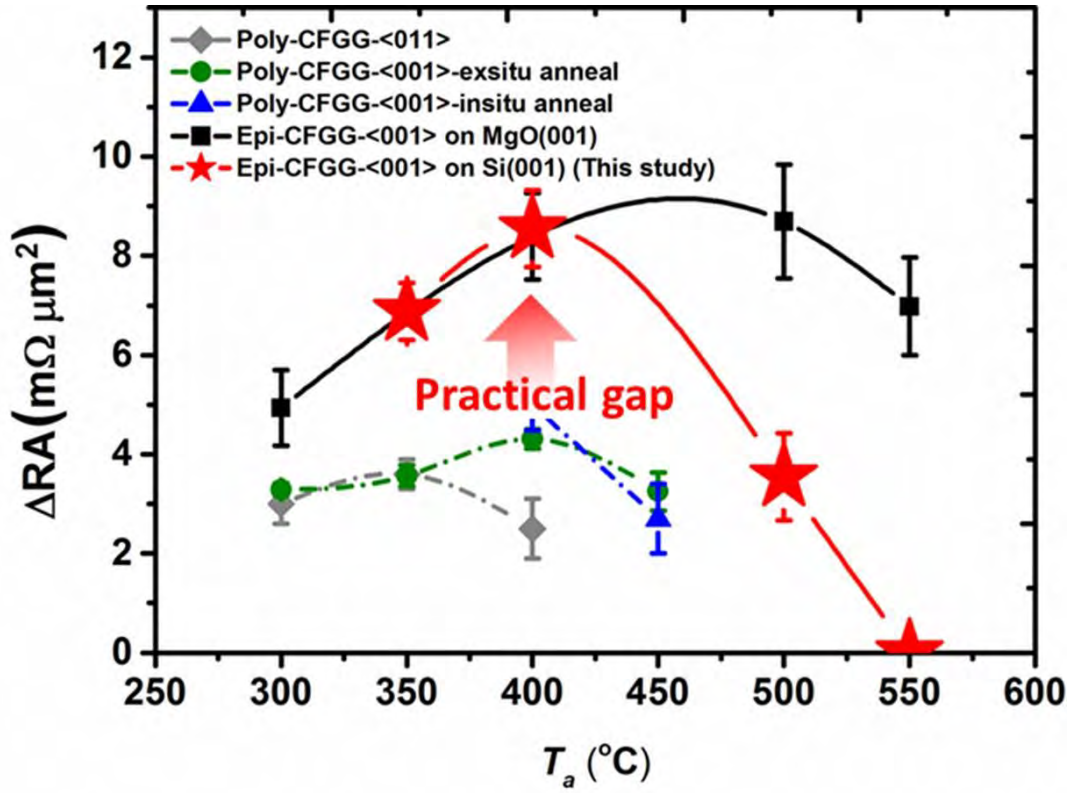

Fig. 5-13 Annealing temperature dependence of ΔRA for epitaxial CPP-GMR devices on Si(001) substrate (red star), epitaxial CPP-GMR devices on MgO(001) substrate (black square)[21] and polycrystalline CPP-GMR devices on Si/SiO_2 substrate (grey square, green circle and blue triangle).[7]

Fig. 5-14 depicts the typical MR curve at 300K of CPP-GMR device fabricated on a Si(001) substrate annealed at optimal temperature of 400°C. Our CFGG/Ag/CFGG CPP-GMR device shows an average MR ratio of 27.8% and ΔRA of 8.6 $m\Omega\mu m^2$ with RA_p of 29.6 $m\Omega\mu m^2$. Both the MR ratio and ΔRA value are nearly the same with those of the CFGG/Ag/CFGG CPP-GMR device grown on an MgO(001) substrate reported previously[4,21], but much higher than those reported for the polycrystalline all metallic CPP-GMR

device. More importantly, higher MR output of Si-based CPP-GMR device can be expected by using high spin-polarized Heusler alloy (e.g. CFMS[3]) and new spacer (e.g.In-Zn-O[25]).

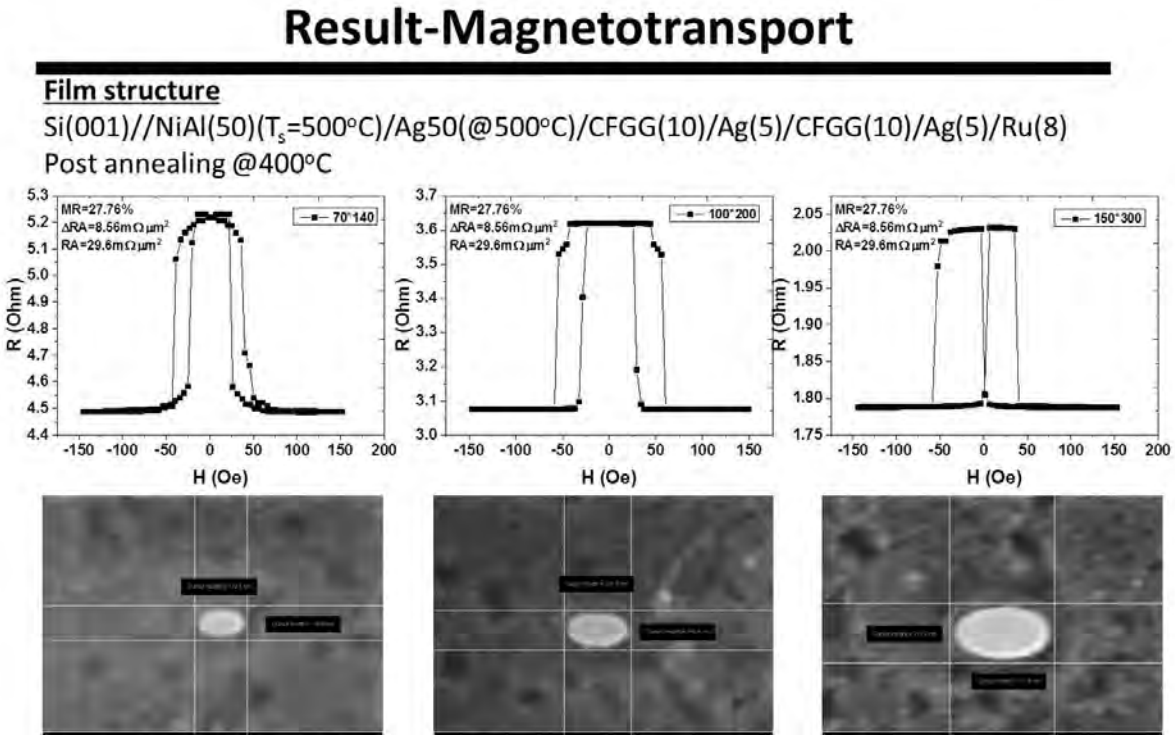

Fig. 5-14 Typical MR curves and pillar SEM images of CPP-GMR devices annealed at optimal temperature 400°C.

5.4.4 Microstructure

In order to clarify the layer structure and the reason for the reduction in the MR output for the annealing temperature above 400°C using the Si(001) substrate, cross sectional TEM observation was made. The high-angle annular dark-field (HAADF)-STEM image in **Fig. 5-15(a)** shows a uniform layer structure for the device annealed at the optimal temperature of 400°C. The nano-beam diffraction patterns and magnified high resolution HAADF image of tri-layer region confirm the epitaxial growth and the crystal structure of each layer as determined by the XRD results. Note that at the interface between Si and NiAl layers, a layer of ~10 nm thick silicide is formed. The silicide is identified to be $NiSi_2$ as shown in the corresponding nano-beam diffraction pattern. The appearance of $NiSi_2$ is mainly because the NiAl layer was deposited while heating the Si substrate up to 500°C, which is a temperature high enough for the reaction between Ni and Si. **Fig. 5-**

15(b) and **(c)** show the EDS elemental mapping results for the enlarged CFGG/Ag/CFGG trilayer region. All the layers are well-defined and the interfaces are sharp. On the other hand, the HAADF-STEM image obtained from the device annealed at 550°C in **Fig. 5-15(d)** shows that the silicide layer is twice as thick as that in the device annealed at 400°C, suggesting the formation of $NiSi_2$ is much more pronounced. The layer structure becomes messy and the roughness of the interface increases. The EDS mapping results for the enlarged trilayer region in **Fig. 5-15(e)** and **(f)** indicate the excess Al rejected from the $NiSi_2$ layer diffuse into the bottom CFGG layer. Also the Ag spacer becomes thicker as the result of the diffusion of Ag from the bottom electrode layer. The diffusion of Al and Si in the bottom CFGG layer destroys the half-metallicity of the bottom CFGG layer, leading to a significant drop of MR output as shown in **Fig. 5-13**. In order to further improve the high temperature tolerance of CPP-GMR devices on the Si substrate, more stable buffer material needs to be developed. Nevertheless, a thermal tolerance of 400°C is high enough to attain high MR output from the CFGG/Ag/CFGG pseudo spin-valves (PSVs).

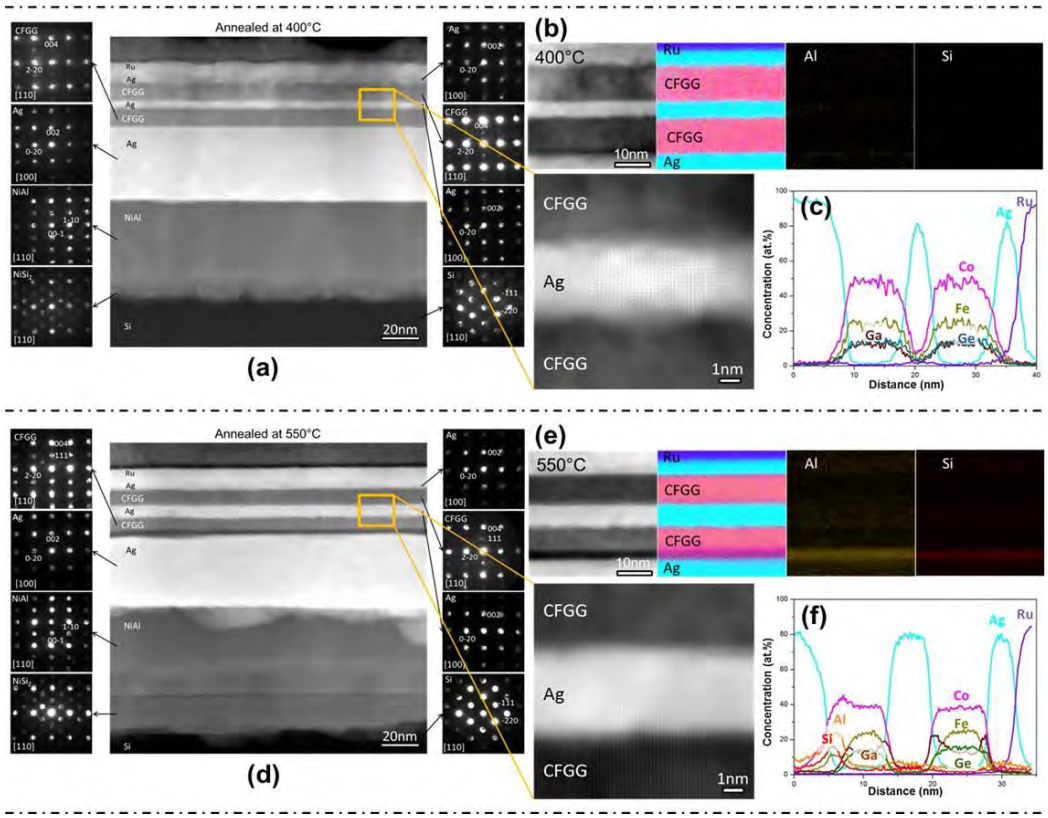

Fig. 5-15 (a) (d) HAADF-STEM images together with nano-beam diffraction patterns (NBDPs) (b) (e) EDS mappings and (c) (f) Line scan analysis for epitaxial CPP-GMR devices on Si(001) substrate annealed at 400°C and 550°C, respectively.

5.5 Further improvement by CoFe insertion

So far, by using NiAl as a buffer material, we have successfully achieved fully epitaxial growth and obtain comparable high MR ratio on Si(001) substrate up to 400°C. But serious formation of silicide and element diffusion prevent further improvement of MR property at higher annealing temperature. To overcome this problem, we come up with an idea that we may probably enhance the thermal stability of buffer layer by inserting a CoFe layer between Ag and NiAl as shown in **Fig. 5-16** due to a good lattice matching with both Ag and NiAl. We also believe that CoFe insertion layer may be able to absorb or block Al diffusion by forming alloy. Actually, CoFe insertion layer had been widely used as a method to improve MR ratio in both CPP-GMR and TMR devices.[23–26]

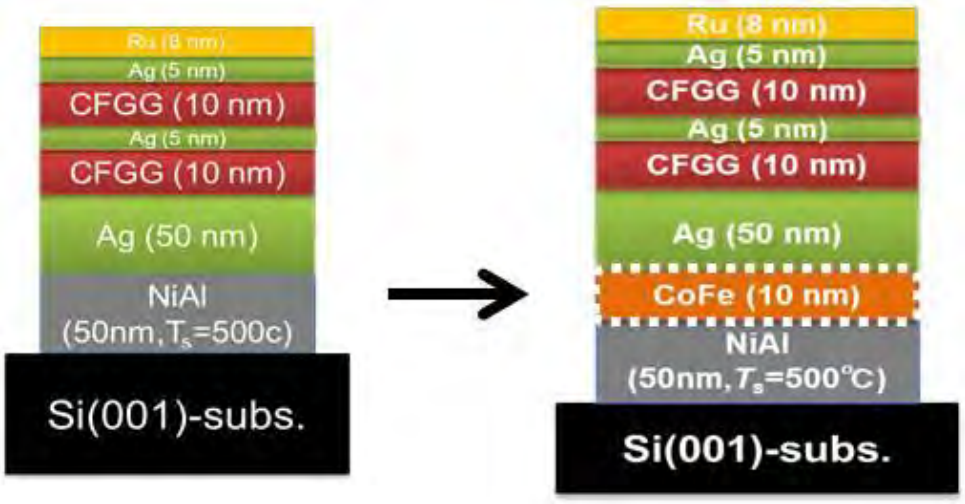

Fig. 5-16 Illustration of CoFe insertion strategy.

After the insertion, fully epitaxial was maintained as confirmed by the RHEED patterns for each layers shown in **Fig. 5-17**. Interestingly, the MR output improve significantly as shown in **Fig. 5-18**, especially at high annealing temperature of 500°C. **Fig. 5-19(a)** summarizes the MR outputs of devices with and without CoFe insertion as a function of annealing temperature. Nice and uniform multilayer structure without any interdiffusion can be seen in **Fig. 5-19(b)**. When we compare the microstructure of these two devices with/without CoFe insertion layer in **Fig. 5-19(b)** and **(c)**, to our surprise, we found that CoFe insertion layer can just acted as a diffusion barrier and suppressed the formation of silicide at NiAl/Si interface instead of absorbing Al element to form CFA alloy during the high-temperature annealing!

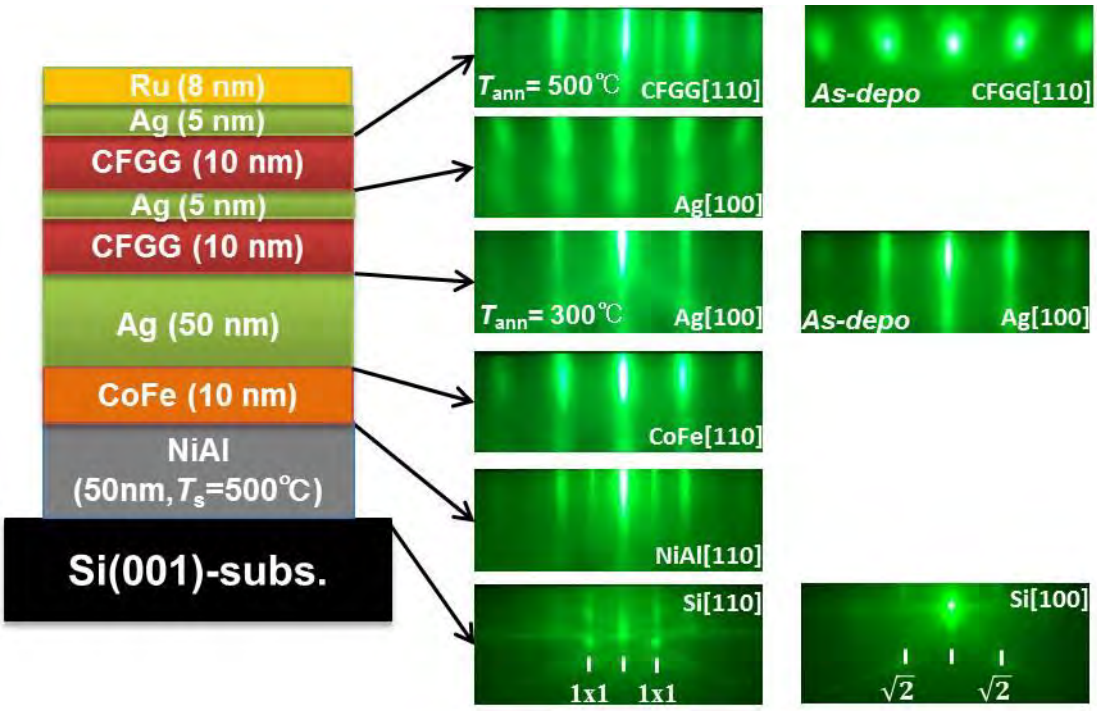

Fig. 5-17 Structure illustrations of whole CPP-GMR film stack and corresponding RHEED patterns for each layer.

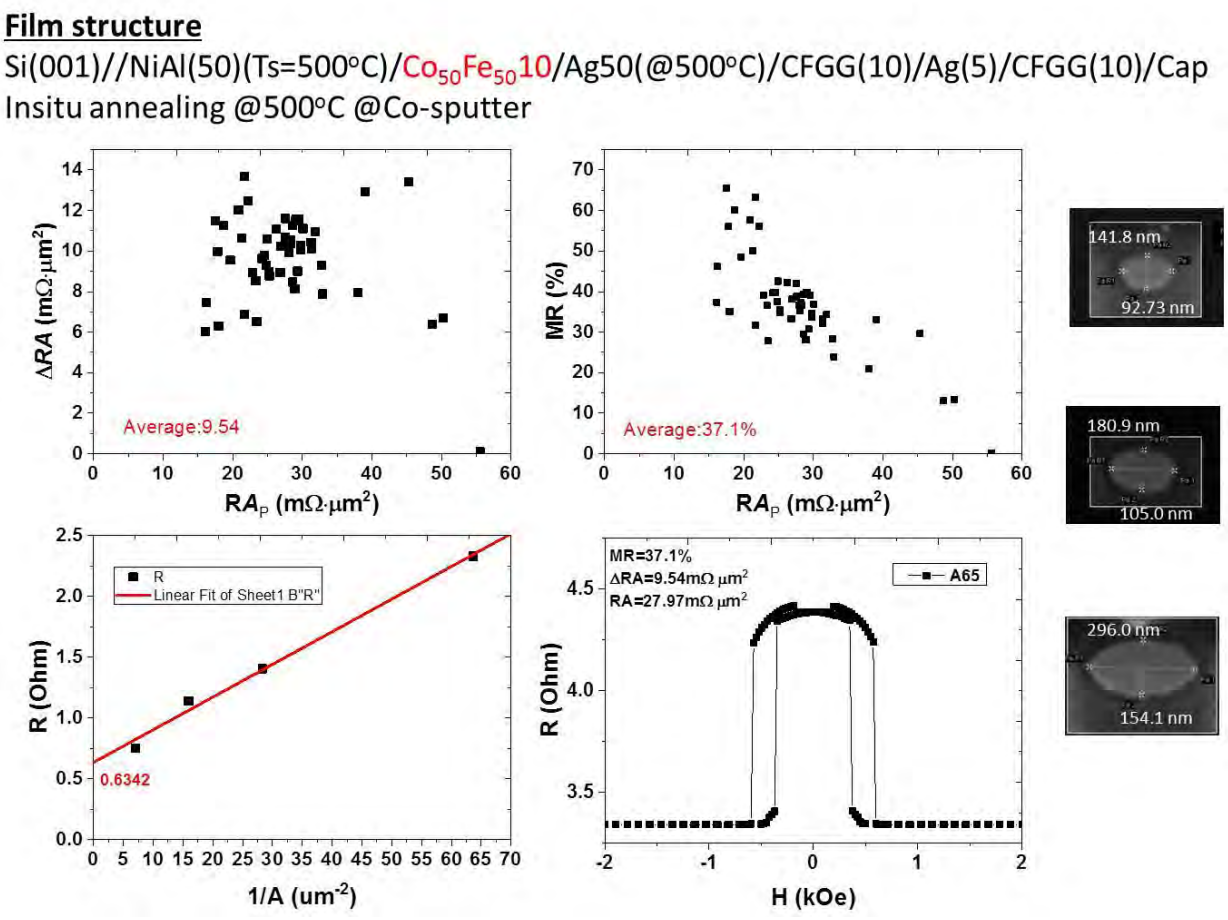

Fig. 5-18 Magneto-transport properties of CPP-GMR device on Si(001) substrate with CoFe insertion layer annealed at 500°C.

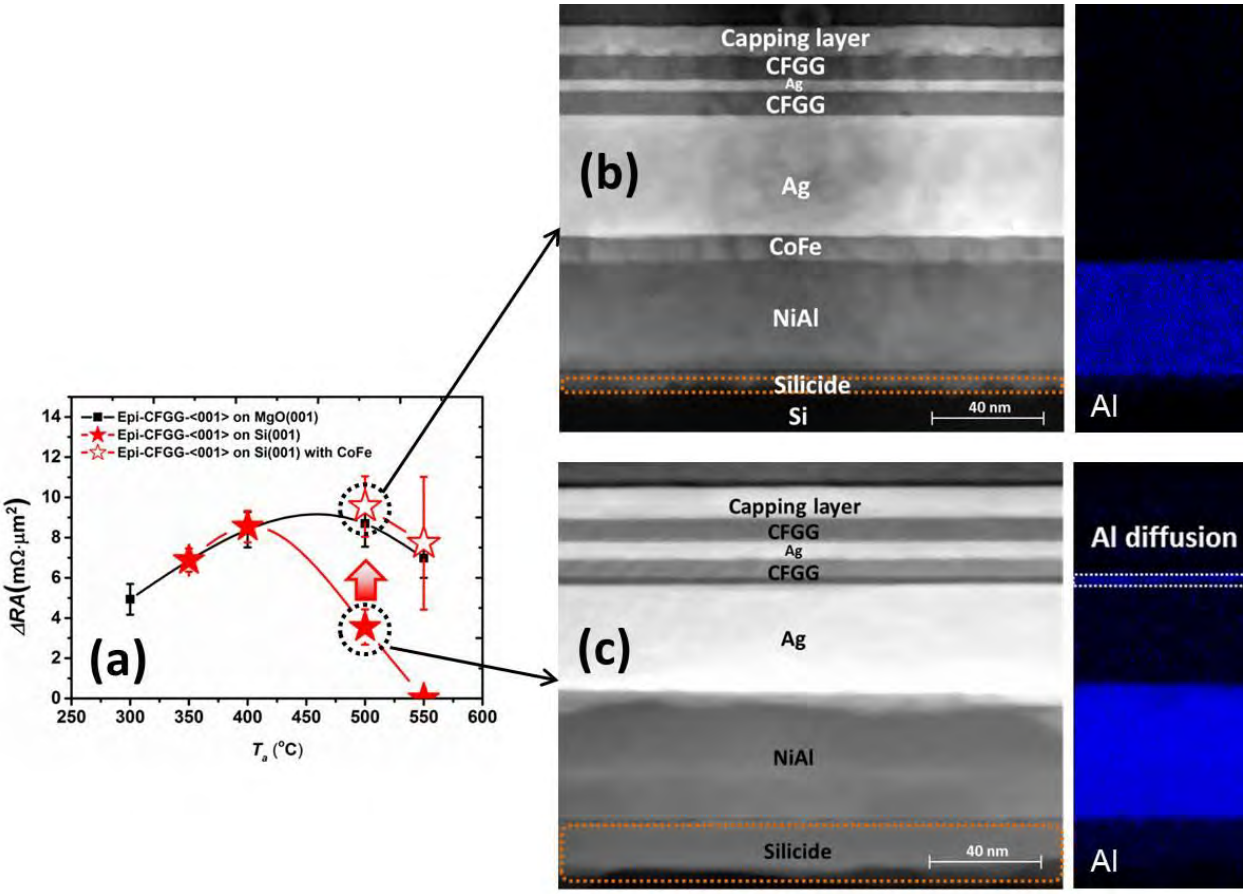

Fig. 5-19 (a) Annealing temperature dependence of Δ*RA* for different epitaxial CPP-GMR devices. (b) and (c) HAADF-STEM images together with EDS mappings for devices w/wo CoFe insertion layer, respectively.

5.6 Summary of this chapter

In this chapter, we investigated the use of a NiAl buffer layer for the integration of CPP-GMR devices on a Si(001) single crystalline substrate. The summaries are as follow:

1) By undertaking a NiAl deposition on silicon at a temperature of 500°C, a smooth and epitaxial *B*2-NiAl layer with highly (001)-orientation was demonstrated.
2) The surface roughness of NiAl was further improved by depositing Ag on the NiAl layer and applying subsequent post-annealing process.
3) High quality epitaxial CPP-GMR device on Si(001) substrate was realized by using NiAl buffer layer for the first time.
4) The epitaxial CPP-GMR of CFGG/Ag/CFGG structure grown on the NiAl-buffered Si(001) substrate exhibited a high MR ratio of 27.8% and ΔRA of 8.6 $m\Omega\mu m^2$, which is comparable with those of the devices grown on an MgO(001) substrate. Such results demonstrated the feasibility of growing epitaxial CPP-GMR on Si wafers, which can exhibit much higher MR output than polycrystalline devices that are deposited on amorphous buffered industrially standard chemical-mechanical-polished substrates. This gives a potential for developing industrially viable single crystalline CPP-GMR devices on Si wafer for allowing higher temperature annealing in combination with the wafer bonding technology.
5) Thermal stability and MR property of CPP-GMR device on Si(001) substrate were further improved by CoFe insertion.
6) CoFe insertion layer can act as a diffusion barrier and suppressed the formation of silicide at NiAl/Si interface during the high-temperature annealing.

Citation of this part can be referred to:

Jiamin Chen, J. Liu, Y. Sakuraba, H. Sukegawa, S. Li and K. Hono
"Realization of high quality epitaxial current-perpendicular-to-plane giant magnetoresistive pseudo spin-valves on Si(001) wafer using NiAl buffer layer"
APL Materials. **4**, 056104 (2016) [http://dx.doi.org/10.1063/1.4950827]

Reference

[1] Y. Sakuraba, K. Izumi, T. Iwase, S. Bosu, K. Saito, K. Takanashi, Y. Miura, K. Futatsukawa, K. Abe, and M. Shirai, Phys. Rev. B **82**, (2010).

[2] Y.K. Takahashi, N. Hase, M. Kodzuka, A. Itoh, T. Koganezawa, T. Furubayashi, S. Li, B.C.S. Varaprasad, T. Ohkubo, and K. Hono, J. Appl. Phys. **113**, 223901 (2013).

[3] J. Sato, M. Oogane, H. Naganuma, and Y. Ando, Appl. Phys. Express **4**, 113005 (2011).

[4] Y.K. Takahashi, A. Srinivasan, B. Varaprasad, A. Rajanikanth, N. Hase, T.M. Nakatani, S. Kasai, T. Furubayashi, and K. Hono, Appl. Phys. Lett. **98**, 152501 (2011).

[5] M. Takagishi, K. Yamada, H. Iwasaki, H.N. Fuke, and S. Hashimoto, Magn. IEEE Trans. On **46**, 2086 (2010).

[6] M.J. Carey, S. Maat, S. Chandrashekariaih, J.A. Katine, W. Chen, B. York, and J.R. Childress, J. Appl. Phys. **109**, 093912 (2011).

[7] Y. Du, B.S.D.C.S. Varaprasad, Y.K. Takahashi, T. Furubayashi, and K. Hono, Appl. Phys. Lett. **103**, 202401 (2013).

[8] T.M. Nakatani, Y. Du, Y.K. Takahashi, T. Furubayashi, and K. Hono, Acta Mater. **61**, 3695 (2013).

[9] H. Takagi, K. Kikuchi, R. Maeda, T.R. Chung, and T. Suga, Appl. Phys. Lett. **68**, 2222 (1996).

[10] W. Yang, D.N. Lambeth, L. Tang, and D.E. Laughlin, J. Appl. Phys. **81**, 4370 (1997).

[11] D.K. Fork, F.A. Ponce, J.C. Tramontana, and T.H. Geballe, Appl. Phys. Lett. **58**, 2294 (1991).

[12] P. Tiwari, X.D. Wu, S.R. Foltyn, Q.X. Jia, I.H. Campbell, P.A. Arendt, R.E. Muenchausen, D.E. Peterson, T.E. Mitchell, and J. Narayan, Appl. Phys. Lett. **65**, 2693 (1994).

[13] Y. Dutchak and V. Chekh, J Phys Chem **55**, 1326 (1981).

[14] J. Chen, T. Furubayashi, Y.K. Takahashi, T.T. Sasaki, and K. Hono, J. Appl. Phys. **117**, 17C119 (2015).

[15] J. Chen, S. Li, T. Furubayashi, Y.K. Takahashi, and K. Hono, J. Appl. Phys. **115**, 233905 (2014).

[16] D. Reisinger, M. Schonecke, T. Brenninger, M. Opel, A. Erb, L. Alff, and R. Gross, J. Appl. Phys. **94**, 1857 (2003).

[17] H. Wang, A. Tiwari, A. Kvit, X. Zhang, and J. Narayan, Appl. Phys. Lett. **80**, 2323 (2002).

[18] H. Xiang, F. Shi, M.S. Rzchowski, P.M. Voyles, and Y.A. Chang, Appl. Phys. Lett. **97**, 092508 (2010).

[19] J.E. Mahan, K.M. Geib, G.Y. Robinson, R.G. Long, Y. Xinghua, G. Bai, M.-A. Nicolet, and M. Nathan, Appl. Phys. Lett. **56**, 2126 (1990).

[20] S. Olive Mendez, V. Le Thanh, A. Ranguis, and J. Derrien, Appl. Surf. Sci. **254**, 6040 (2008).

[21] S. Li, Y.K. Takahashi, T. Furubayashi, and K. Hono, Appl. Phys. Lett. **103**, 042405 (2013).

[22] Y. Du, T. Furubayashi, Y. Takahashi, Y. Sakuraba, and K. Hono, IEEE Trans. Magn. 1 (2015).

[23] N. Hase, T.M. Nakatani, S. Kasai, Y.K. Takahashi, and K. Hono, J. Appl. Phys. **109**, 07E112 (2011).

[24] Y. Du, T.M. Nakatani, Y.K. Takahashi, N. Hase, T. Furubayashi, and K. Hono, J. Appl. Phys. **114**, 053910 (2013).

[25] T. Scheike, H. Sukegawa, K. Inomata, T. Ohkubo, K. Hono, and S. Mitani, Appl. Phys. Express **9**, 053004 (2016).

[26] T. Scheike, H. Sukegawa, T. Furubayashi, Z. Wen, K. Inomata, T. Ohkubo, K. Hono, and S. Mitani, Appl. Phys. Lett. **105**, 242407 (2014).

Chapter 6 Fabrication of Single Crystalline Magnetoresistive Sensors on Polycrystalline Electrode using Three-Dimensional Integration Technology

6.1 Introduction

As discussed in last several chapters, a CPP-GMR device inherently possesses low *RA* due to its all-metallic structure; however, the MR ratio used to be too small for any applications. Recently, substantially large MR ratios (>80%) and ultralow *RA* of 0.05 $\Omega\mu m^2$, which satisfy the requirements for >2 Tbit/in^2,[1] have been realized in CPP-GMR devices with Co-based Heusler alloys such as Co_2MnSi and $Co_2Fe(Ga_{0.5}Ge_{0.5})$ (CFGG)[2,3] that exhibit half-metallic behavior. However, the following three critical issues still hinder practical applications of the CPP-GMR devices. First, MR ratios > 30–50% have been achieved only in (001)-oriented epitaxial CPP-GMR devices grown on unpractical MgO(001) substrates. Secondly, epitaxial device cannot be grown on permalloy shield with current read head sensor fabrication process. Thirdly, high-temperature annealing over 500°C for Heusler alloy is indispensable to obtain the high MR ratios. Such high-temperature annealing is not compatible with the conventional fabrication processes of read heads because it damages the permalloy magnetic shield and destroy layered structure of polycrystalline devices.

The first problem was successfully solved by using NiAl buffer layer for high quality epitaxial growth of CPP-GMR devices on Si(001) single crystalline substrate as described in chapter 5. In this chapter, we describe how to overcome the remaining two critical issues by developing new three-dimensional integration technology concept. This concept is based on direct wafer bonding and backside silicon removal process, which enable integration of high-performance epitaxial CPP-GMR devices on polycrystalline electrode for sensor applications.

6.2 Epitaxial CPP-GMR device on Polycrystalline electrode (Ta-Au bonding)

6.2.1 Experimental detail

Epitaxial CPP-GMR devices and polycrystalline electrode are fabricated on two different wafers, respectively. Fully epitaxial CPP-GMR devices with layer structure of NiAl(50)/CoFe(10)/Ag(50)/CFGG(10)/Ag(5)/CFGG(10)/Ag(5)/Au(5) (unit in nm) were deposited onto a ϕ2 inch single-crystal Si(001) wafer using the ultrahigh vacuum magnetron sputtering system. On the ϕ8 inch counter thermally-oxidized Si wafer, a poly-crystalline multilayer was deposited to simulate permalloy bottom electrode. Direct wafer bonding of the epitaxial CPP-GMR film with polycrystalline electrode were performed by using the room-temperature bonding apparatus (MWB-12ST Mitsubishi Heavy Industries). For the first trial, a Ta cap layer was deposited on the permalloy layer to obtain strong adhesion at the bonded interface. Surface oxide layers on the Ta cap layers were sputter-etched *in situ* by Ar ion beam, and the wafers were immediately bonded in a high vacuum. Details of whole process are shown in **Fig. 6-1**.

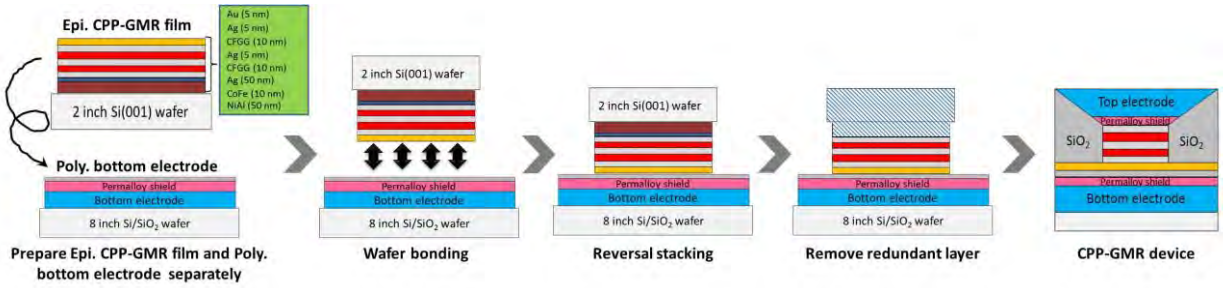

Fig. 6-1 Wafer bonding process in this study. Epitaxial CPP-GMR film on 2inch Si(001) substrate was bonded on poly-crystalline permalloy film deposited on 8 inch Si/SiO2 wafer.

6.2.2 Room-temperature direct wafer bonding

The room –temperature wafer bonding method that used in this study is called "surface-activated bonding" (SAB) [4]. Surface of the wafer is firstly sputter etched by Ar ion beam and then bonded at room temperature in vacuum as shown in **Fig. 6-2**. The etching can remove surface contamination, which make surface atoms stable. After etching, the surface atoms reach active state and their reactivity enables inter-atomic bond formation at RT.

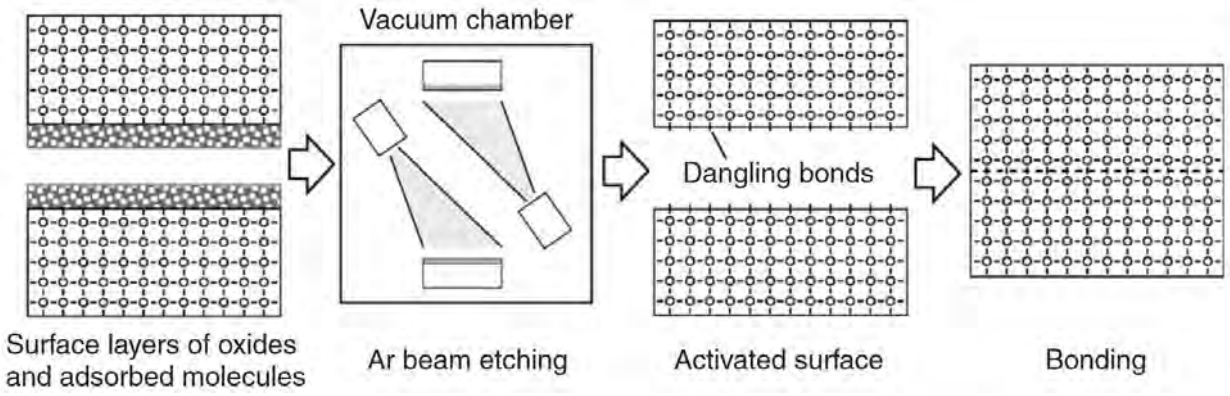

Fig. 6-2 Principle of the surface-activated bonding (SAB)[4].

Fig. 6-3 depicts the detail structure of sample used for wafer bonding. **Fig. 6-4(a)** and **(b)** show the thickness distribution and scanning acoustic microscope image of the bonded wafers, respectively. Both the small total thickness variation and the image without visible voids suggest a successful bonding.

6.2.3 Removal of backside Si substrate

The thinning process flow is shown in **Fig. 6-5**. The 2inch side Si wafer was removed by a high-speed but less damage process. First, coarse grindings were performed using 321- grit wheel until remaining thickness of around 75 μm. Then fine grindings were performed using 8000- grit wheel until remaining thickness of around 15 μm. **Fig. 6-6** shows image of sample right after fine grinding. Next, the residual Si

was selectively removed by wet etching with alkaline solution. To remove Si, tetramethylammonium hydroxide (TMAH)-based solution, which exhibited a high etching selectivity to NiAl layer, was used. Although some edge areas are not perfectly bonded, and point defects can be found in the sample after removing the top Si substrate (see **Fig. 6-7**), most of the areas in the sample are clean enough for the subsequent micro-fabrication of CPP-GMR devices.

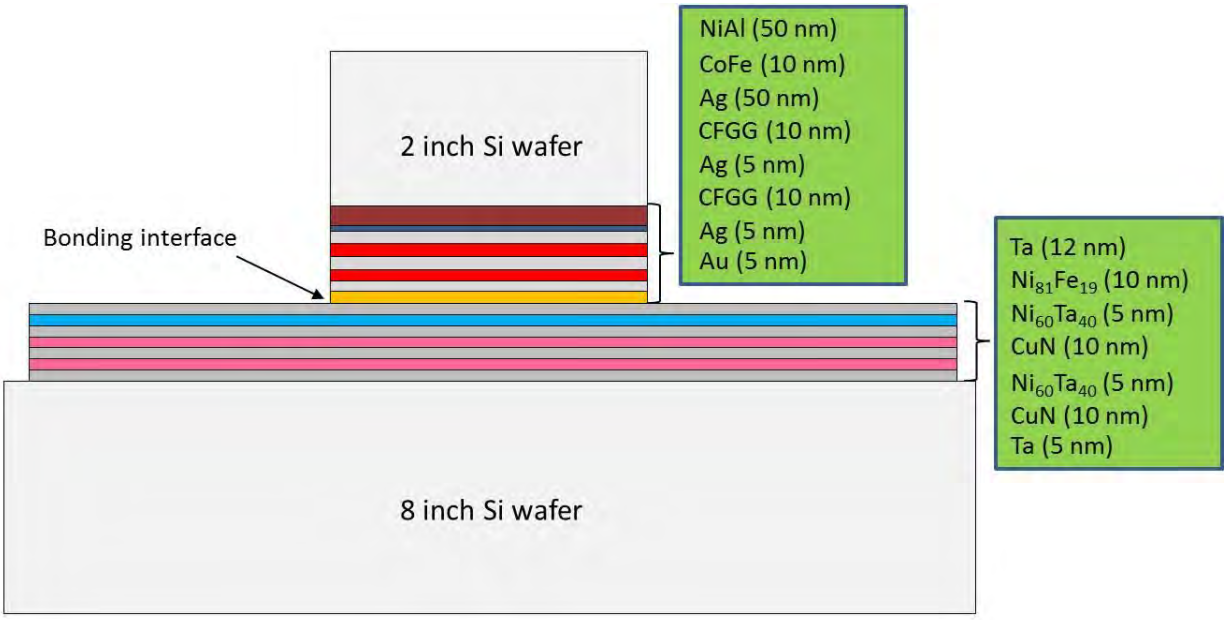

Fig. 6-3 Structure of sample used for wafer bonding

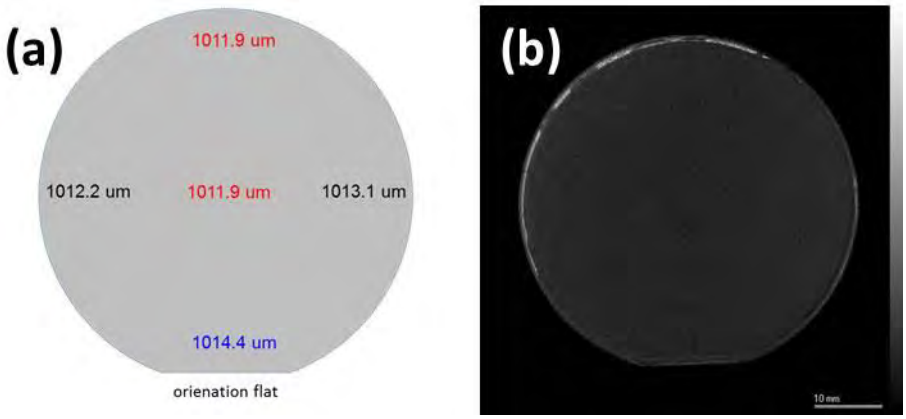

Fig. 6-4 (a) Thickness distribution of 2 inch wafer with 8 inch wafer after wafer bonding. (b) Ultrasonic microscopy image of 2 inch wafer after bonding.

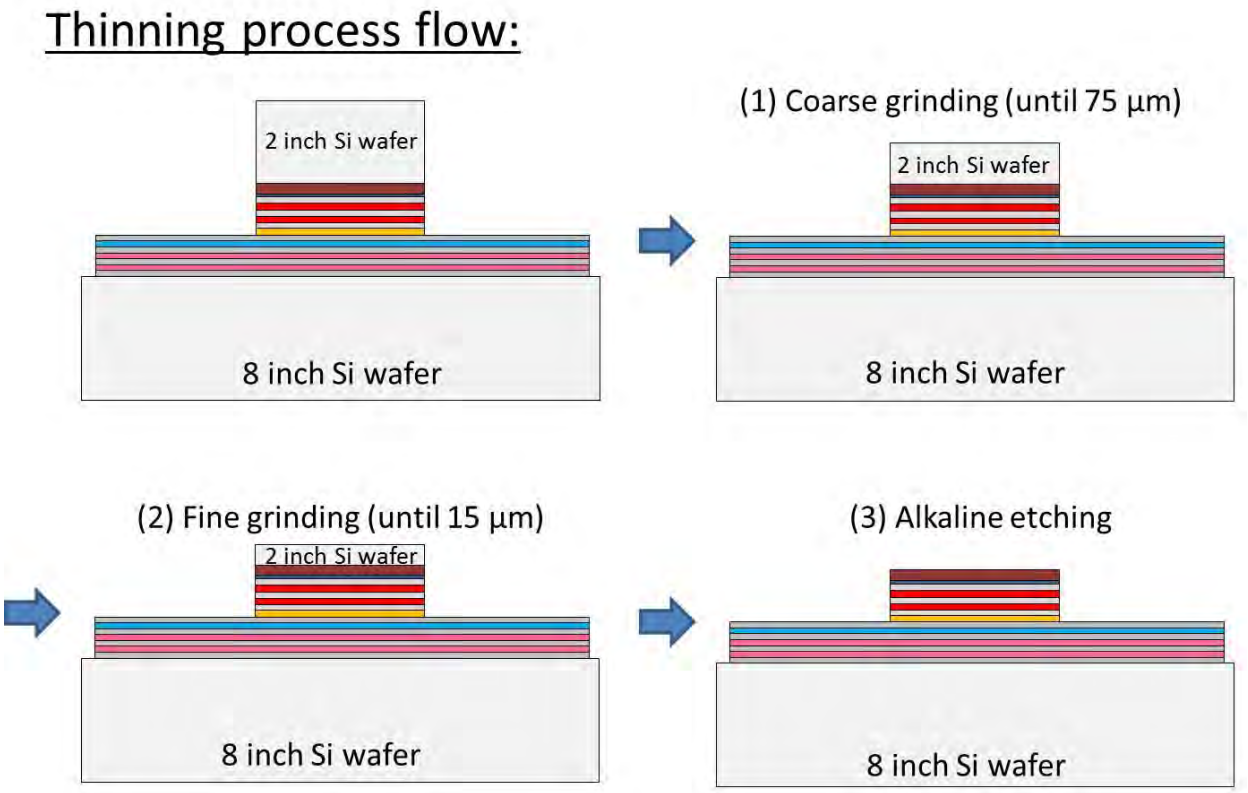

Fig. 6-5 Thinning process flow.

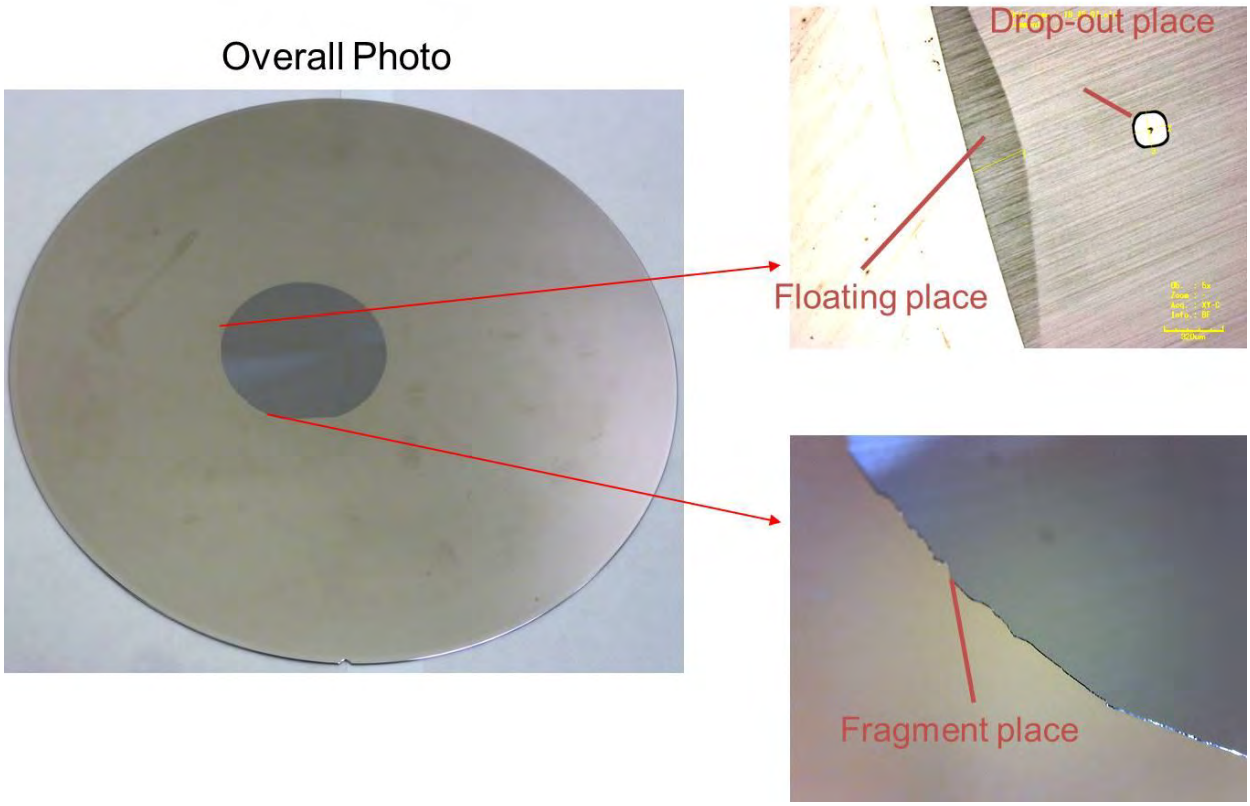

Fig. 6-6 Image after fine grinding.

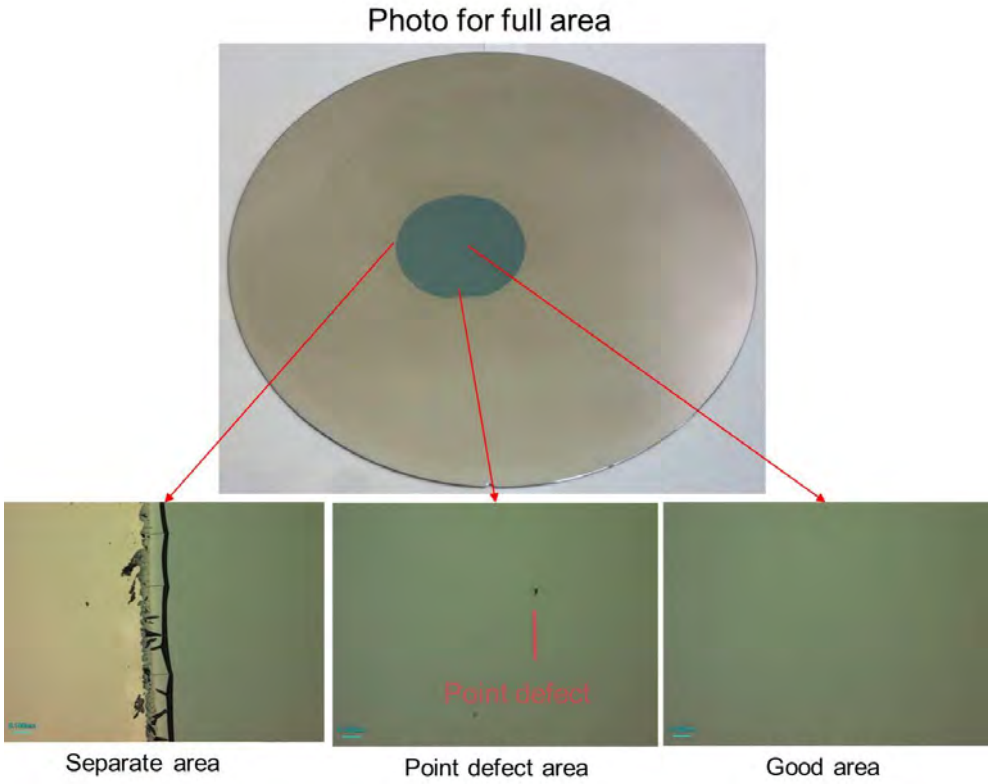

Fig. 6-7 Photos for the sample after grinding and wet etching of top Si substrate.

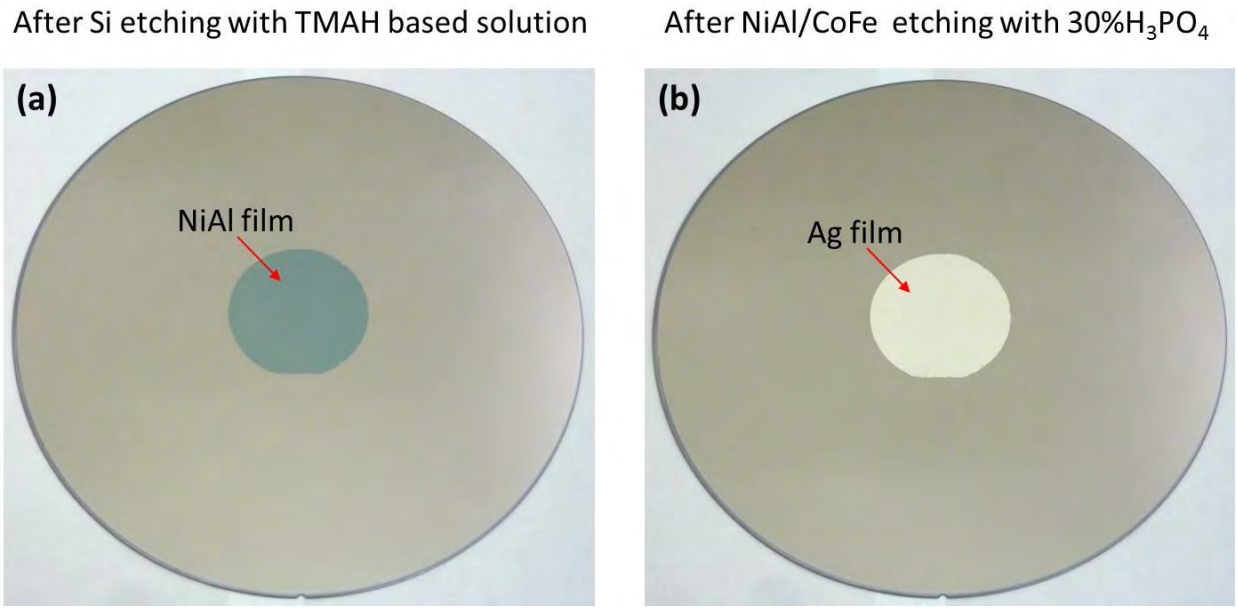

Fig. 6-8 Photos for the sample (a) after Si etching with TMAH+additive and (b) after NiAl/CoFe etching with 30% H_3PO_4.

6.2.4 Removal of redundant layer

Redundant NiAl and CoFe layer, which are original buffer layer of the epitaxial CPP-GMR film, were removed by H_3PO_4 acid with a concentration of 30%. **Fig. 6-8** shows image of the sample before and after wet etching of NiAl and CoFe layer, respectively.

6.2.5 Epitaxial CPP-GMR device on Polycrystalline electrode

After removal of redundant layer, TEM observation of sample was conducted to check the bonding interface condition and surface condition. Microstructure of the bonding interface was analyzed by high-resolution HAADF-STEM and EDS mapping (**Fig. 6-9**). Clean and flat Ag sample surface can be observed, which indicate a successful removal of NiAl and CoFe layer after wet etching. Smooth Ta/Au bonding interface without any voids is observed. In the magnified HAADF image of bonding interface region, a clear bonding is obtained while keeping the single-crystal structure of Au layer on top of amorphous-like Ta layer. The appearance of amorphous-like Ta layer is probably coming from damage of Ar ion beam etching before bonding. Interestingly, such kind of damage was not observed in the Au layer side. Note that this is first demonstration for direct bonding epitaxial MR multilayer film on top of amorphous layer. The EDS mapping images show that the Au/Ta interface is sharp without any oxidation, which means the epitaxial CPP-GMR film is successfully bonded on top of the permalloy bottom electrode.

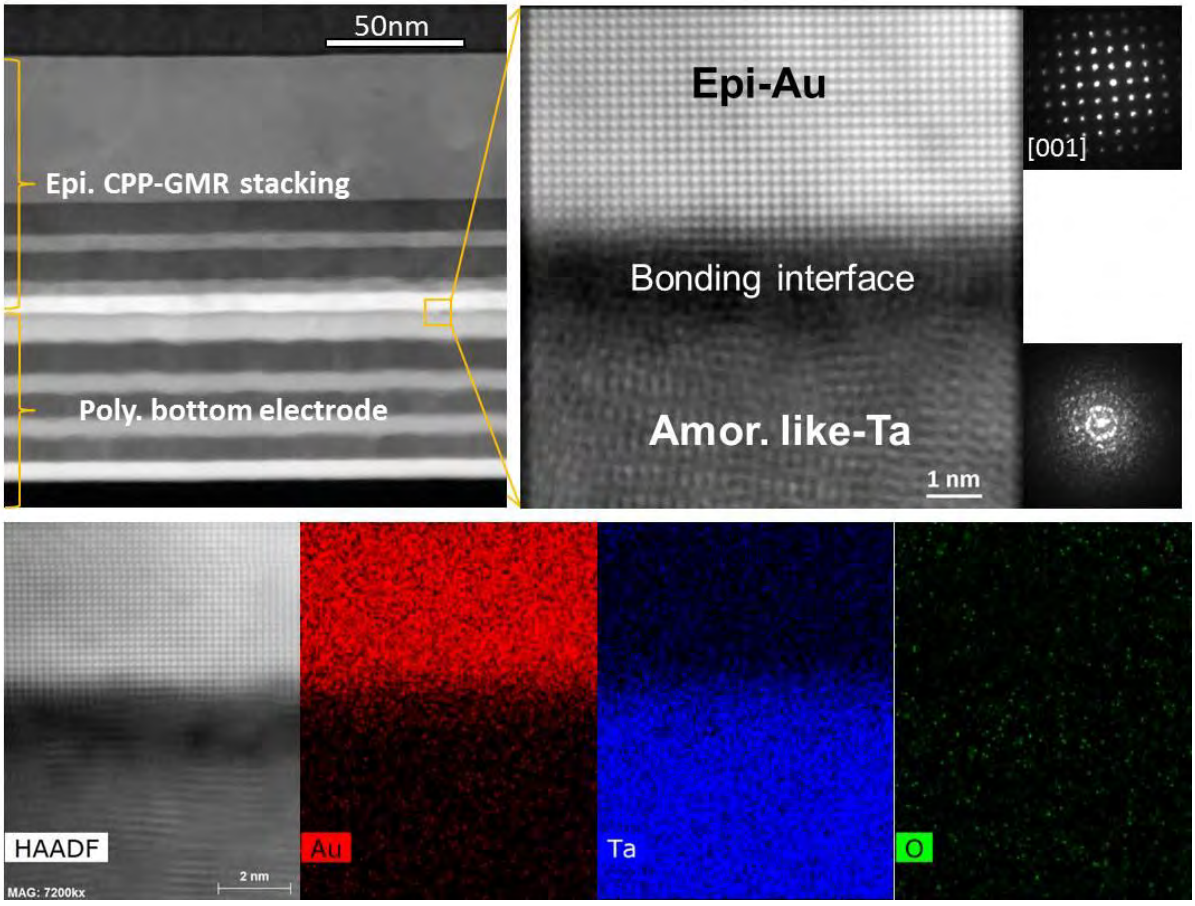

Fig. 6-9 Microstructure analysis of the stacking film after bonding and bonding interface by HR-HAADF STEM. Epitaxial CPP-GMR film is successfully bonded on Ta capping layer without any remarkable defects at the interface.

By using the successful bonded sample, we try to fabricate CPP-GMR device by microfabrication. However, sample right after removal of redundant layer is not directly suitable for CPP-GMR device fabrication. The remaining 50 nm thick Ag surface layer, which is original buffer layer, is too thick for pillar fabrication because redeposition problem may occur at the side wall of the pillar which will significantly degrade MR property of the device. Therefore, reverse sputter needs to be applied to the sample to thin the remaining Ag layer. In addition to that, due to the microfabrication process limit in our lab, EB lithography resist (maN-2403) that we used for making pillar can only work with sample with Ru surface. Hence, before microfabrication, Ru capping layer is necessary right after thinning of Ag layer. We first reverse sputter the bonded sample to reduce Ag layer thickness to around 5nm, then deposit 8nm Ru capping layer without breaking vacuum. Finally, CPP-GMR devices were fabricated by microfabrication process that we always use as described in **Fig. 2-3** in chapter 2. Unfortunately, no MR output was obtained for the 1st trial sample of CPP-GMR devices, and for the 2nd trial sample, only one normal MR loop can be obtained from total 224 devices as shown in **Fig. 6-10**. We speculated that the problem may come from very thin Ag/Au capping layer in the epitaxial CPP-GMR multilayer side.

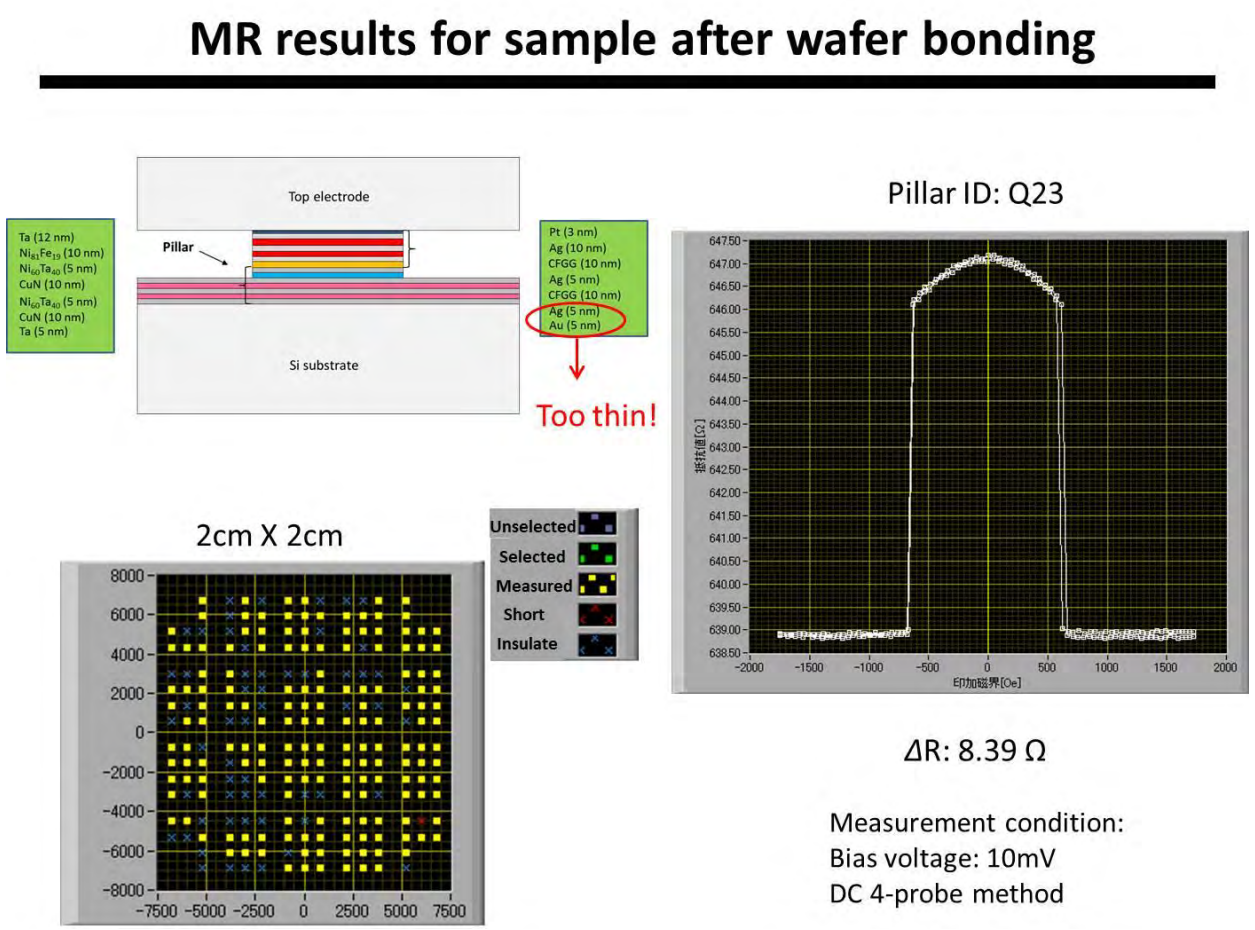

Fig. 6-10 Magneto-resistance measurement results for bonded sample after microfabrication.

In order to clarify what is the reason for the loss of MR output in the devices, microstructure analysis is employed. TEM characterization of sample before microfabrication and after Ru capping layer deposition is shown in **Fig. 6-11**. The tem image shows that interface between Ru and Ag layer is pretty rough. This is probably due to the reverse sputtering, because reverse sputter normally will deteriorate surface roughness of the sample. From the EDS mapping results, some areas of Ag spacer contained CFGG can be seen as indicated as the red dash line in the figure. In the Au layer, some regions mixing with Ag can be found as well. We also checked the microstructure of the pillar after microfabrication showing in **Fig. 6-12**. In the pillar, similar problem can be found and the inter mixing between Ag and Au becomes more serious as shown by the dash circle in **Fig. 6-12**. These microstructures are totally different from the nice multilayer structure that shown in **Fig. 6-9** right after removal of redundant layer. The reason for such big difference could be attributed to solid solution between Ag and Au. Silver and gold are well known to from substitutional solid solution easily for all concentrations even at room temperature due to the same FCC crystal structure and similar lattice constant. During the reverse sputtering or the Ar milling process, sample can get unavoidable heated, which will promote the solid solution of Ag and Au layer. Inter mixing between Ag and Au will lead to the degradation of CFGG/Ag/CFGG trilayer structure, which is the key part for CPP-GMR device, resulting in the loss of MR output. Therefore, more stable capping materials combination maybe needed to reproduce MR output of epitaxial CPP-GMR device even after wafer bonding and microfabrication.

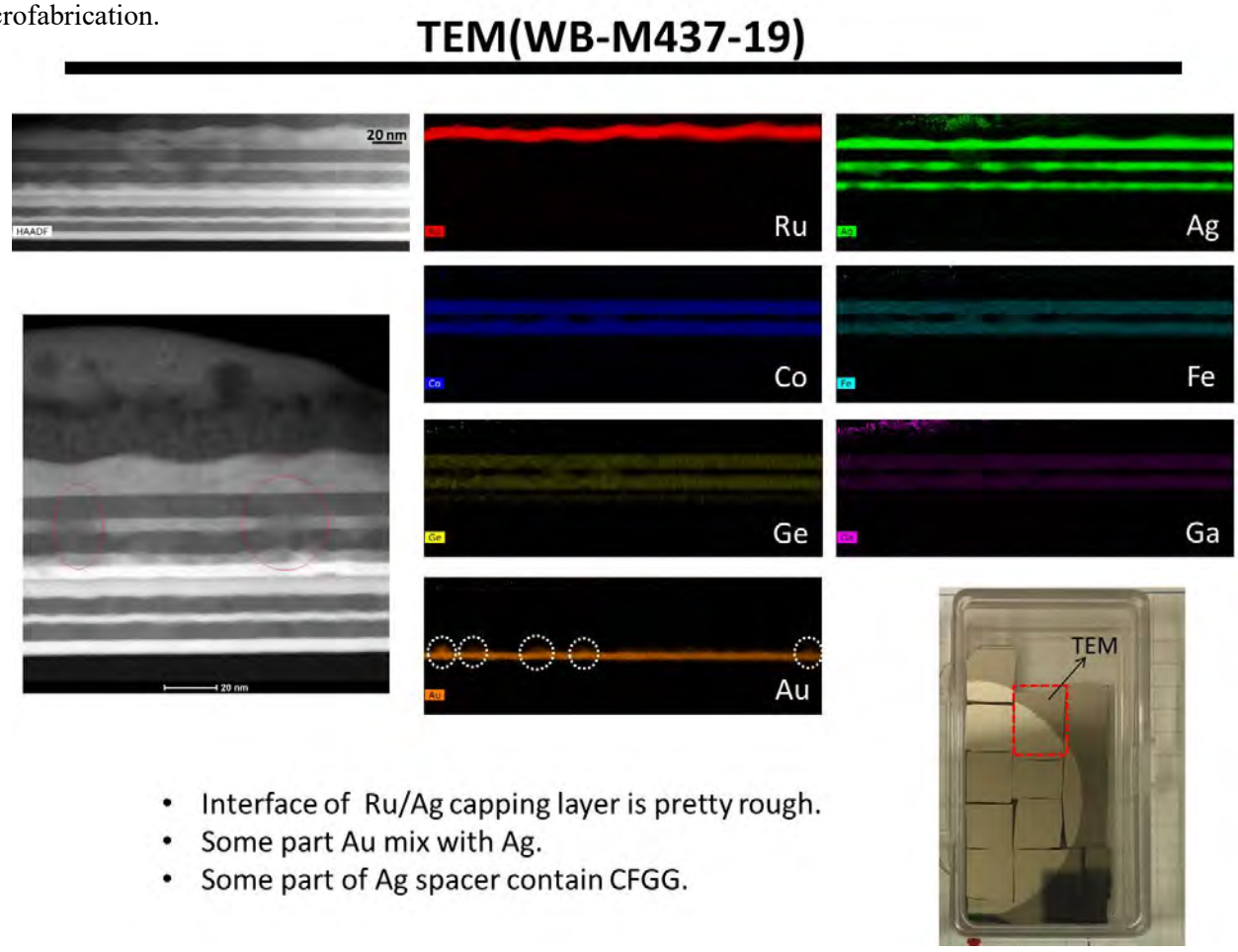

Fig. 6-11 Microstructure of sample before microfabrication and after Ru capping layer deposition.

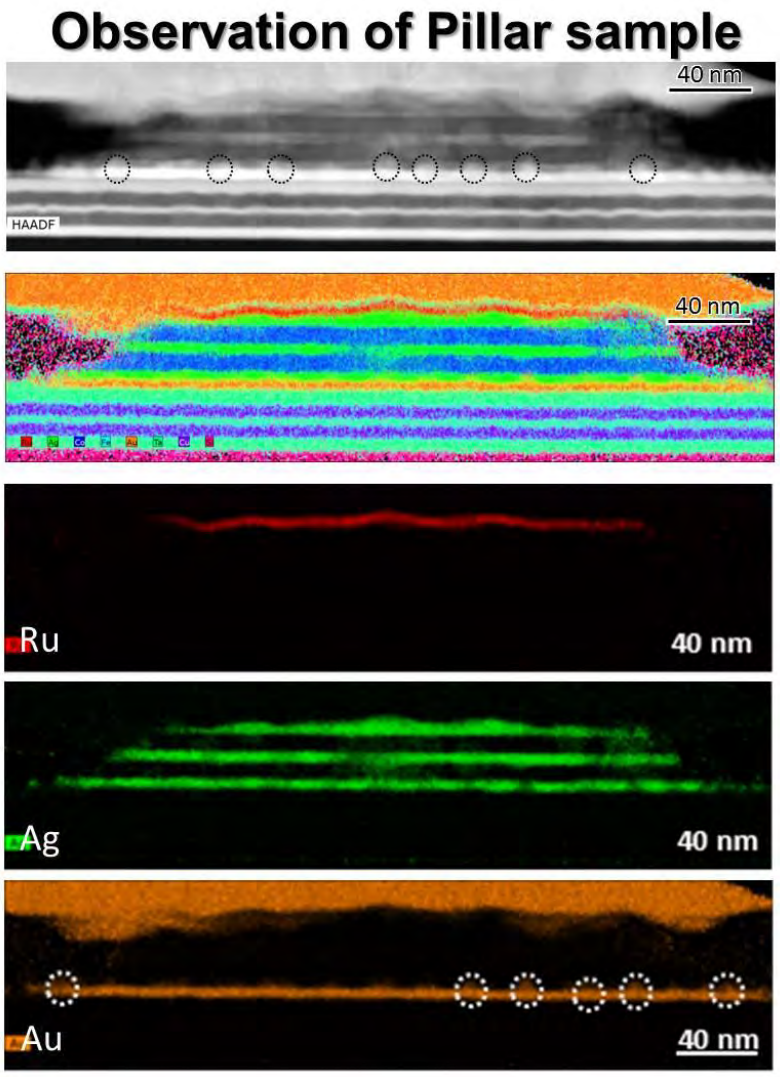

Fig. 6-12 Microstructure of pillar from sample after microfabrication.

6.3 Effect of material selection on bonding interface

After realizing Ag/Au capping is not a good choice for obtaining stable bonding interface, we decided to systematically investigate bonding interface condition dependence on different capping materials for direct wafer bonding processing.

6.3.1 Experimental detail

Epitaxial multilayers was fabricated on 2inch Si(001) single crystalline substrate with three different capping layers (Ta, Au and Ta/Au) to represent epitaxial device (see **Fig. 6-13**). To simply the sample preparation, trilayer structure of CFGG/Ag/CFGG is removed in all samples. All the samples are epitaxial growth as confirmed by RHEED patterns and show smooth surface as indicated by AFM results. The reason why we choose Au and Ta as candidates is because Au and Ta can represent soft and hard material, respectively. On an 8 inch counter wafer, again, a polycrystalline electrode multilayer was stacked. The 2 inch Epi-multilayer and 8 inch Poly-electrode were bonded by a room-temperature bonding apparatus as shown in **Fig. 6-14**.

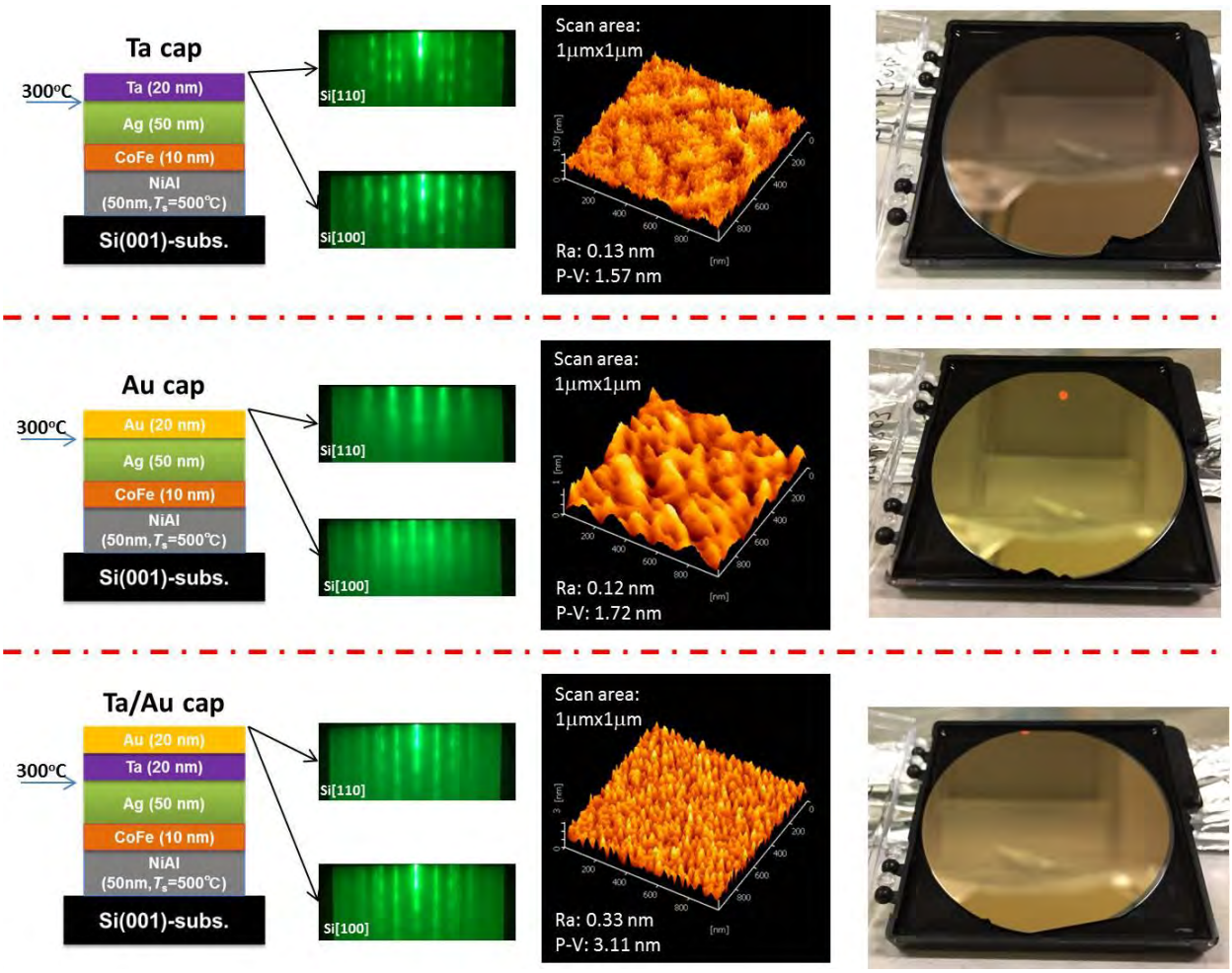

Fig. 6-13 Epitaxial multilayers on 2inch Si(001) single crystalline substrate with three different capping layers (Ta, Au and Ta/Au) and related surface RHEED patterns and surface roughness.

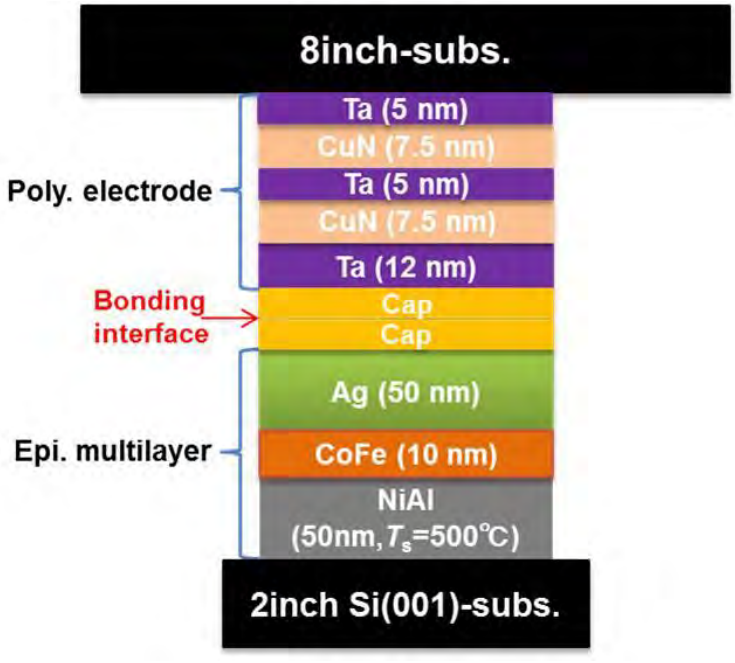

Fig. 6-14 Illustration of Epitaxial multilayers bonded with polycrystalline bottom electrode with different capping layer combinations.

6.3.2 Ta-Au bonding

Here Ta-Au bonding means wafer bonding is conducted between epitaxial multilayer with Ta capping layer on 2inch wafer and polycrystalline electrode with Au capping layer on 8 inch wafer. **Fig. 6-15** shows microstructure of sample with Ta-Au bonding interface. As shown in the low magnification HAADF image, all the layers look uniform. The bonding interface between Ta and Au is clear and well-attached. Note that there is a very thin grey contrast at the Ta/Au bonding interface. This thin grey contrast originated from the amorphous-like Ta damage layer, which is around 5 nm as shown in the high magnification HAADF image. Surface of Ta capping layer changes from single crystalline to amorphous-like after bonding. The bonding interface in this case looks similar with the one that shown in **Fig. 6-9**. No element interdiffusion is observed from the EDS mapping results. Damage at Ta surface is not preferable because it mays cause unexpected electron scattering when current flow through the bonding interface in the device.

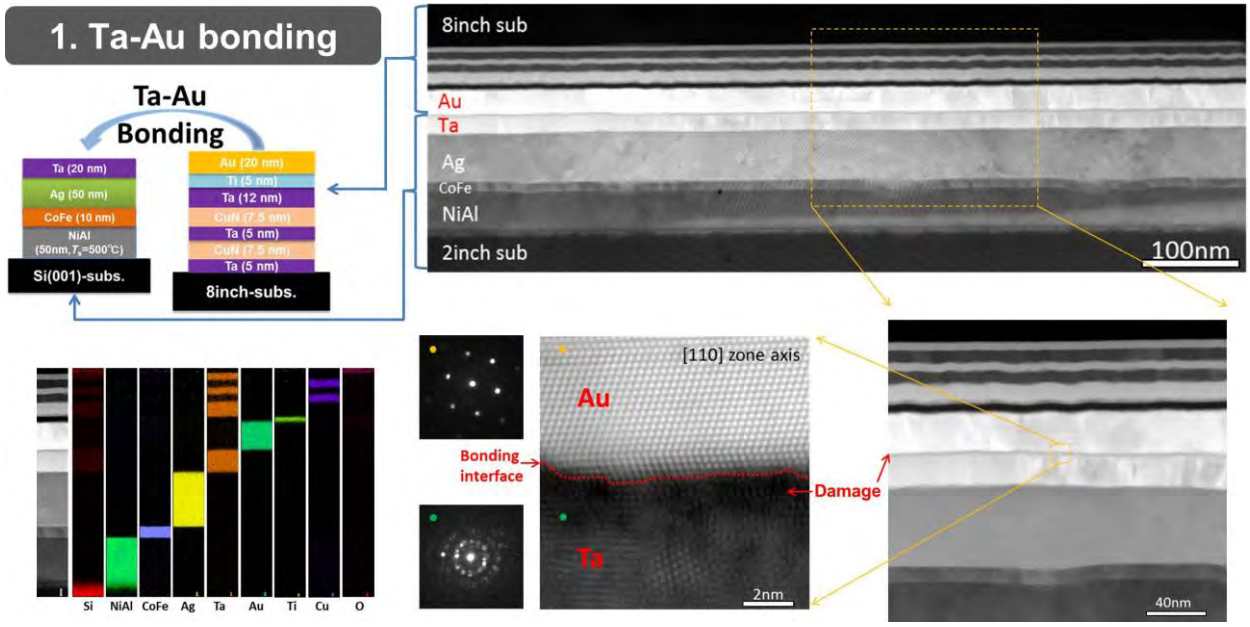

Fig. 6-15 Microstructure analysis of sample with Ta-Au bonding interface.

6.3.3 Au-Ta bonding

Here Au-Ta bonding means wafer bonding is conducted between epitaxial multilayer with Au capping layer on 2inch wafer and polycrystalline electrode with Ta capping layer on 8 inch wafer. **Fig. 6-16** shows microstructure of sample with Au-Ta bonding interface. As shown in the low magnification HAADF image, the bonding interface between Ta and Au is also clear and well-attached. Again, a very thin grey contrast which is coming from amorphous-like Ta damage layer at the Au/Ta bonding interface is observed. It is important to point out that such kind of surface damage can only be observed from Ta side but not in Au side, as confirmed from **Fig. 6-9**, **Fig. 6-15** and **Fig. 6-16**. From the EDS mapping results, a serious intermixing between Ag and Au layer can be found, which makes Ag/Au interface unclear. Surprisingly, recrystallization seems to occur in both Ag and Au layers, which varies both layers from single crystalline before bonding (confirmed by RHEED pattern in **Fig. 6-13**) to polycrystalline after bonding as indicated by two sets of

different nano-beam diffraction patterns. The origin of intermixing and recrystallization may be related the solid solution behavior between silver and gold and the pressure introduced during the bonding process. Note that in the sample that we failed to obtain MR loop after bonding shown in and **Fig. 6-12**, similar Ag and Au intermixing issue occurred. Therefore, this capping materials combination shown in **Fig. 6-16** is not suitable to obtain stable multilayer structure after bonding process.

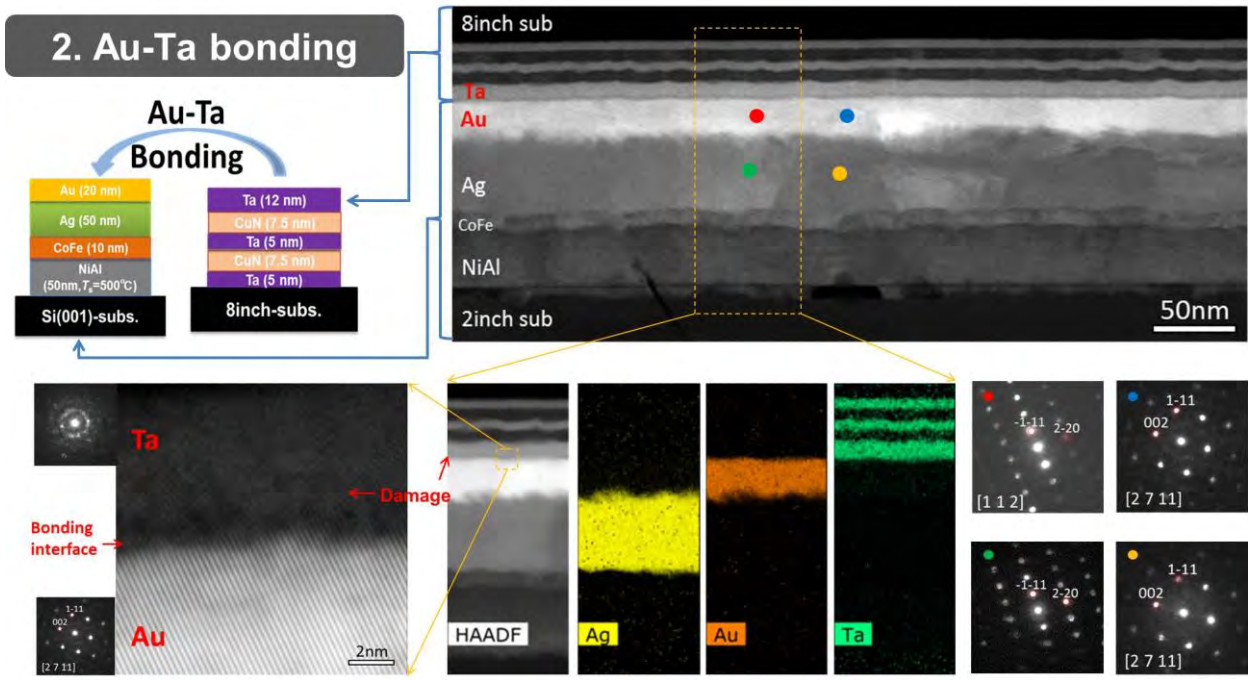

Fig. 6-16 Microstructure analysis of sample with Au-Ta bonding interface.

6.3.4 Au-Au bonding

Here Au-Au bonding means wafer bonding is conducted between epitaxial multilayer with Au capping layer on 2inch wafer and polycrystalline electrode with Au capping layer on 8 inch wafer. **Fig. 6-17** shows microstructure of sample with Au-Au bonding interface. As shown in the low magnification HAADF image, the bonding interface between Au and Au looks perfect. The interface is so well-attached that it is hard to distinguish where it is in low magnification image. In this Au-Au bonding case, no damage grey contrast is observed at the bonding interface. From the high magnification HAADF image, we can clearly see polycrystalline Au is successfully bonded with epitaxial Au. The bonding interface is free of damage and exhibit grain-boundary-like interface. The fast Fourier transform (FFT) filtering image of horizontal direction reveals no out-of-plane dislocation at the bonding interface. All the layers are sharp and uniform. No interdiffusion was found to occur after bonding as demonstrated by the EDS mapping results. Among three bonded samples, Au-Au bonding shows the best bonding interface condition as shown in **Fig. 6-18**.

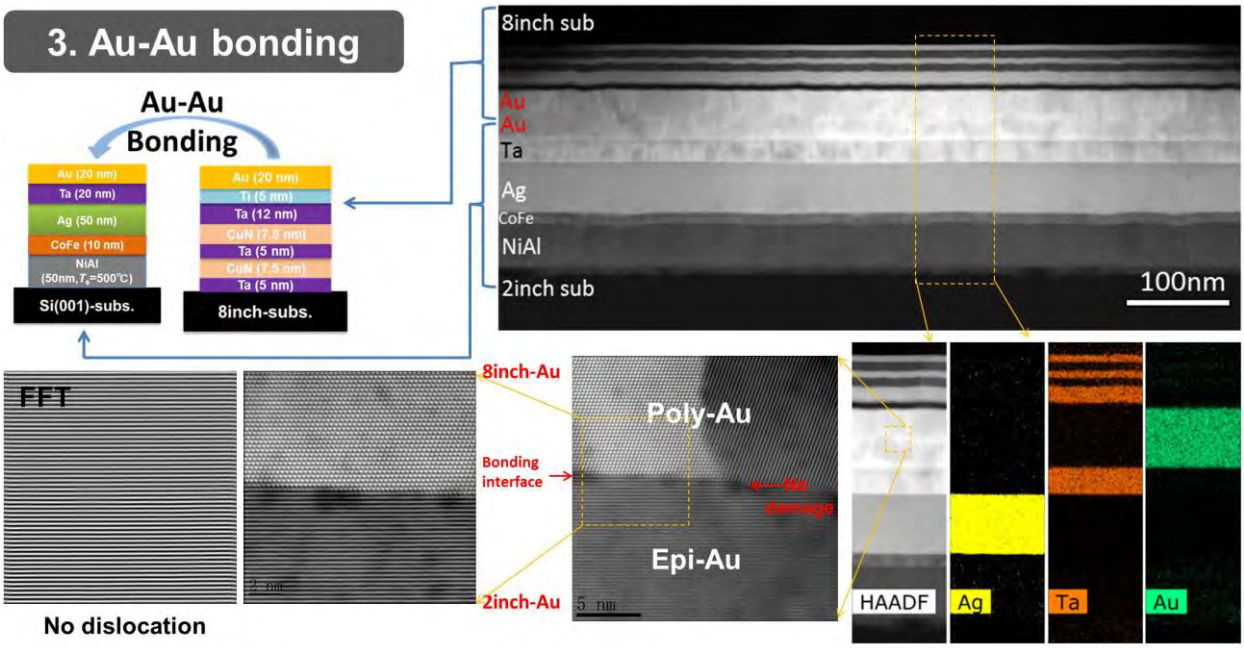

Fig. 6-17 Microstructure analysis of sample with Au-Au bonding interface.

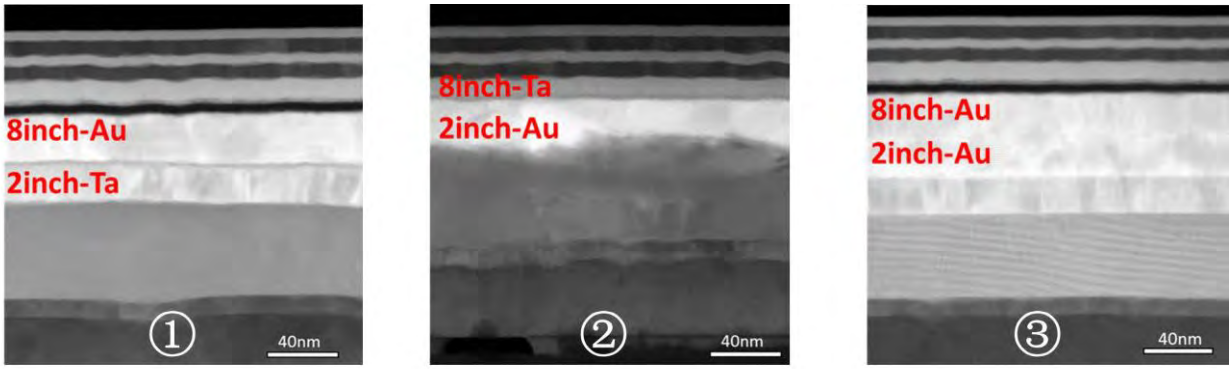

Fig. 6-18 Microstructure comparisons of samples with ①Ta-Au bonding interface, ②Au-Ta bonding interface and ③Au-Au bonding interface.

6.4 Epitaxial CPP-GMR device on Polycrystalline electrode (Au-Au bonding)

After understanding that Au-Au bonding can provide the best condition, we apply the Au-Au bonding process to the sample with CFGG/Ag/CFGG trilayer structure for CPP-GMR device fabrication. The microstructure is shown in **Fig. 6-19**. Uniform multilayer structure is presented as expected. The essential CFGG/Ag/CFGG trilayer structure remains continuous even in large range of region as confirmed in the low magnification HAADF image. With this nice structure, we did microfabrication to make CPP-GMR device and measure its MR property. Finally, similar MR output of Epi-CPP-GMR device is successfully reproduced after bonding process by using Au-Au bonding (see **Fig. 6-20**)! This result for the first time demonstrates the possibility of integrating epitaxial multilayer device on polycrystalline electrode vertically, which is a promising technology not only for utilizing epitaxial CPP-GMR device for ultrahigh-density hard

disk drives (HDDs) read head sensor[5], but also for 3D stacking of epitaxial magnetic tunneling junction (MTJ) in ultrahigh-density MRAM[6].

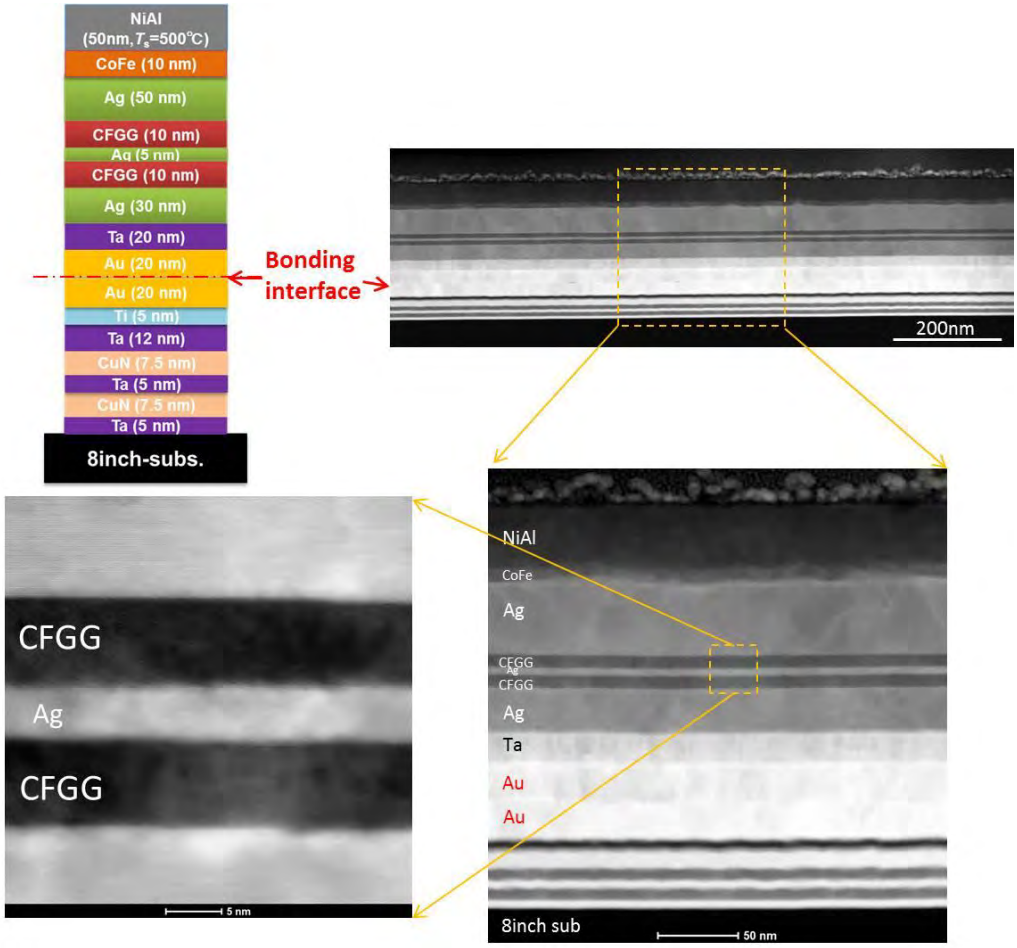

Fig. 6-19 Microstructure of CPP-GMR device with Au-Au bonding interface.

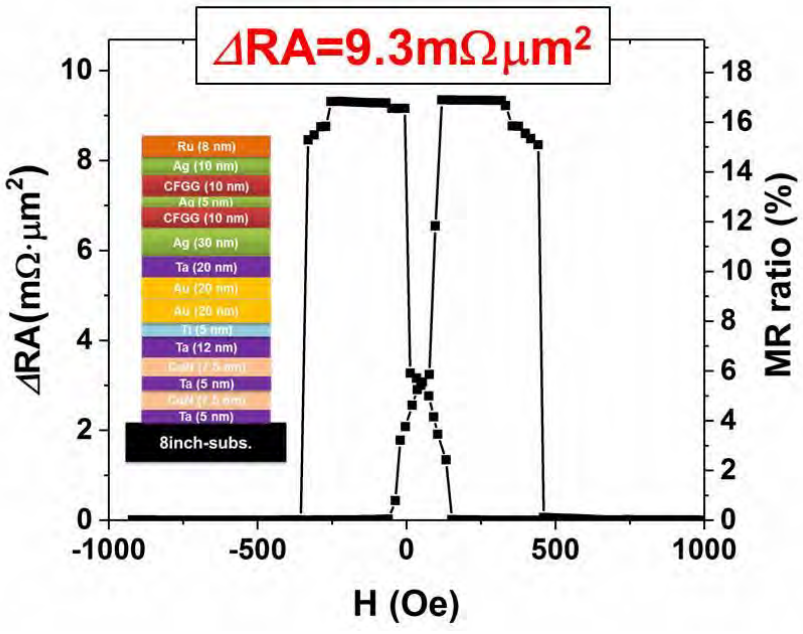

Fig. 6-20 Typical MR curve of CPP-GMR device after Au-Au bonding.

Although ΔRA shows similar value, the MR ratio for the device after bonding is much lower than the one that before bonding if we compare **Fig. 5-18** with **Fig. 6-20**. The reason for that is much higher bottom electrode resistance in the bonded CPP-GMR device compared with the device before bonding due to the usage of high resistivity materials and complicated multilayer structure. As shown in **Fig. 6-21**, lead resistance is estimated to be 1.81 Ω, which is almost 4 times larger than the convention 100 nm thick Ag bottom electrode that we always use. In this study, we didn't focus on optimizing polycrystalline bottom electrode with simple structure to achieve flat surface together with low resistance. If one can improve this part, MR ratio can be further enhanced. Devices resistance presented in **Fig. 6-21** looks pretty scatter. Because of the scattering device resistance, large estimation error may occur if subtracting lead resistance to calculate the real MR ratio so we didn't calculate here. To understand the origin of device scattering, microstructure was analyzed. By looking at the TEM image shown in **Fig. 6-22**, we come to know that such device scattering is mainly because of the inhomogeneous surface morphology, which is caused by the Ar milling process during the removal of redundant NiAl/CoFe and part of Ag layer. Due to the process limit in our lab, Ar milling or reverse sputtering is the only method we can apply to remove redundant layer, during which deterioration of surface roughness is unavoidable. If wet etching process which can produce homogeneous surface is available, better device property can be expected.

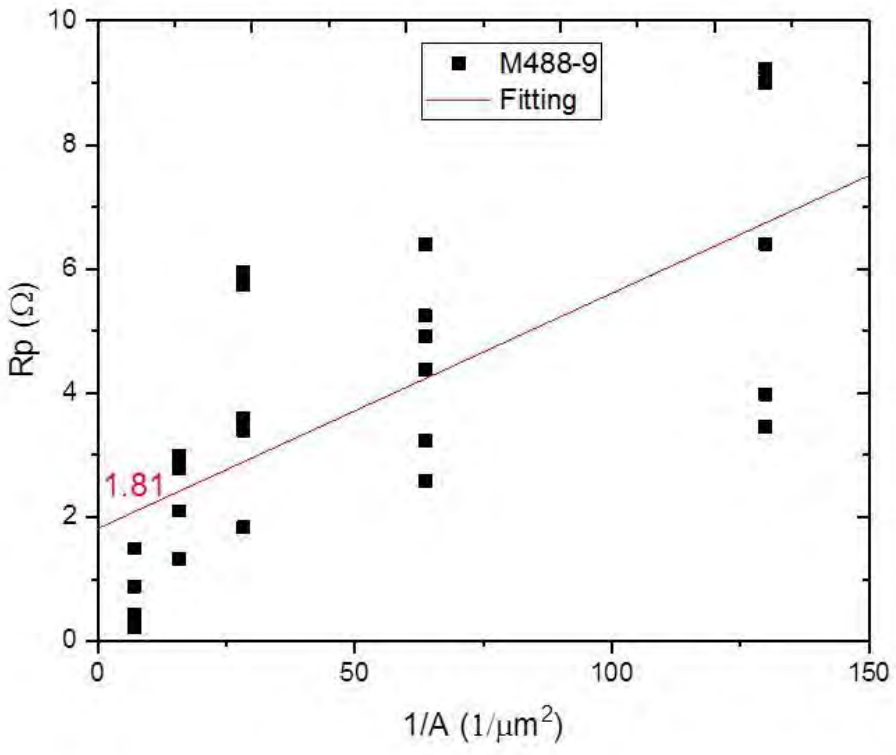

Fig. 6-21 Resistance of the CPP-GMR devices as a function of the inverse of CPP-GMR pillar area.

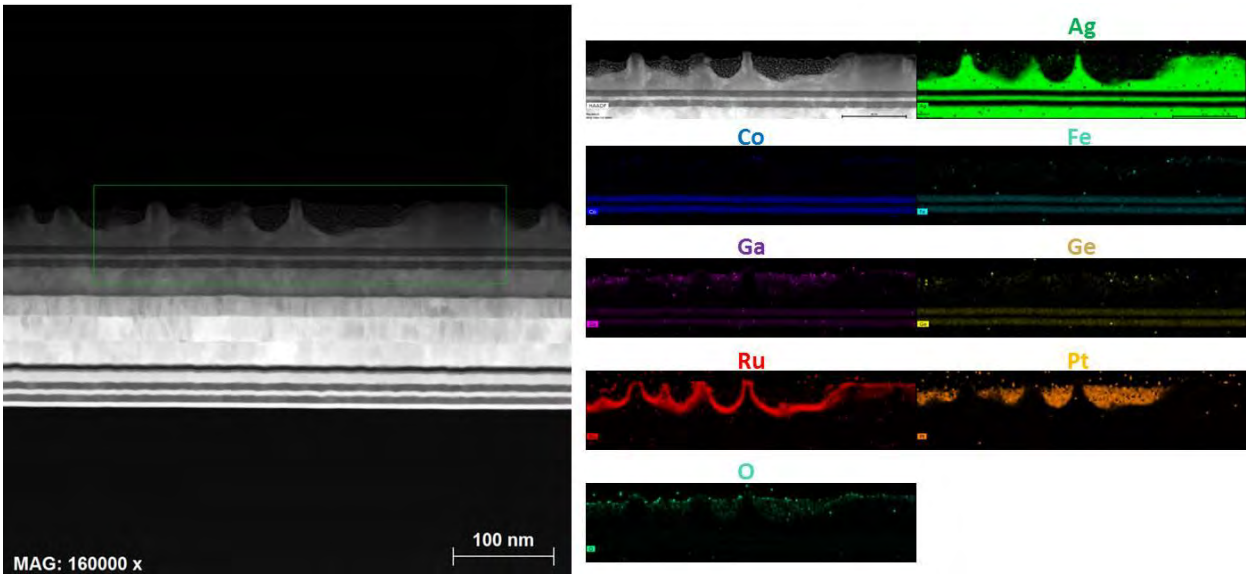

Fig. 6-22 Microstructure of CPP-GMR device after removal of redundant layer and deposition of 8nm Ru.

6.5 Summary of this chapter

In this chapter, fabrication of Single Crystalline Magnetoresistive Sensors on Polycrystalline Electrode using Three-Dimensional Integration Technology was successfully achieved. The summaries are as follow:

1) Integration of epitaxial CPP-GMR device on top of a polycrystalline bottom electrode was realized for the first time by Three-Dimensional Integration Technology based on direct wafer bonding and backside silicon removal process.
2) Bonding interface condition dependence on different capping materials for direct wafer bonding processing was systematically investigated. Among three bonded samples, Au-Au bonding shows the best bonding interface condition. The bonding interface looks perfect, free of damage and grain-boundary like. All layer structure remains uniform after bonding. In the case of Ta-Au bonding, layer structure seriously deteriorates in 2inch side because of mixing between Ag and Au layer. Damage can be always seen at the bonding interface of Ta side but not in Au side in both Au-Ta bonding and Ta-Au bonding.
3) Similar MR output of Epi-CPP-GMR device is successfully reproduced after bonding process by using Au-Au bonding, which is a promising technology not only for utilizing epitaxial CPP-GMR device for ultrahigh-density hard disk drives (HDDs) read head sensor, but also for 3D stacking of epitaxial magnetic tunneling junction (MTJ) in ultrahigh-density MRAM.
4) Better device property after bonding can be expected if further process optimization is available.

Reference

[1] M. Takagishi, K. Yamada, H. Iwasaki, H.N. Fuke, and S. Hashimoto, Magn. IEEE Trans. On **46**, 2086 (2010).
[2] Y. Sakuraba, K. Izumi, T. Iwase, S. Bosu, K. Saito, K. Takanashi, Y. Miura, K. Futatsukawa, K. Abe, and M. Shirai, Phys. Rev. B **82**, (2010).
[3] S. Li, Y.K. Takahashi, T. Furubayashi, and K. Hono, Appl. Phys. Lett. **103**, 042405 (2013).
[4] H. Takagi and R. Maeda, J. Cryst. Growth **292**, 429 (2006).
[5] J. Chen, J. Liu, Y. Sakuraba, H. Sukegawa, S. Li, and K. Hono, APL Mater. **4**, 056104 (2016).
[6] K. Yakushiji, H. Takagi, N. Watanabe, A. Fukushima, K. Kikuchi, Y. Kurashima, A. Sugihara, H. Kubota, and S. Yuasa, Appl. Phys. Express **10**, 063002 (2017).

Chapter 7 Summary and future perspectives

Current-perpendicular-to-plane (CPP) giant magnetoresistance (GMR) device has been considered to be next generation read head sensor for future ultra-high density hard disk drives (HDD) exceeding 2Tbit/in^2 owing to its intrinsic low device resistant. A lot of progress has been carried out in this field but further efforts to promote development in fundamental studies and build up a "bridge" between fundamental studies and practical applications are still strongly desired. For that purpose, this thesis was conducted to develop high performance and practical applicable Heusler-alloy-based CPP-GMR device by investigating new materials and new concept of processing. The specific objectives are (1) To establish a fabrication process for (110)-oriented epitaxial CPP-GMR devices and investigate its crystallographic orientation dependence of MR output, (2) To search for new highly spin-polarized Heusler alloy with high driving force for $L2_1$-order even at low annealing temperature for CPP-GMR device application, (3) To grow high quality epitaxial CPP-GMR device on Si(001) wafer by selecting appropriate buffer materials, and (4) To fabricate single crystalline CPP-GMR device on polycrystalline electrode using wafer bonding technology. These four missions are described from Chapter 3 to Chapter 6, respectively. The results are summarized as follow:

1) The fabrication process of (110)-oriented epitaxial CPP-GMR device was established.
   For Ag and Cu spacer, fully epitaxial CPP-GMR devices with a (110)-oriented CFGG Heusler alloy and a (111)-oriented spacer were developed, and the MR properties are compared with those reported for the CPP-GMR devices with a (001)-oriented CFGG layer. Significant degradation of the MR output is observed for the (110)-oriented devices with the (111)-oriented Ag spacer compared with the (100)-oriented devices. In contrast, the (110)-oriented device exhibits a higher MR output with a (111)-oriented Cu spacer, suggesting that an improvement of the GMR ratio can be obtained by selecting an appropriate orientation relationship to tune the lattice mismatch between the FM layer and the spacer. The (110)-oriented PSVs demonstrate a ΔRA value of 4.1 mΩ·μm^2 with a Cu spacer at 350°C and 3.7 mΩ·μm^2 with an Ag spacer at 450°C.
   For NiAl spacer, The spin-valve with all-B2 CFGG/NiAl/CFGG trilayer were successfully fabricated in both (001) and (110) orientations with a spacer thickness of 2 and 5 nm. Two different oriented devices with the same trilayer structure show the same magneto-transport properties, indicating there is no or very small orientation dependence of band matching on MR output. A thinner NiAl spacer can lead to a slightly higher value of ΔRA due to the short spin diffusion length but further improvement is not available because of the appearance of the strong interlayer exchange coupling. BCC structure spacer with longer spin diffusion length will be an effective way to enhance the MR output for the CPP-GMR read head in the future. Negligibly small dead layer thickness from magnetization property measurement and flat and strain free interface from TEM observation show that the interface condition is good for CFGG/NiAl combination regardless of the orientation of the film.

2) A series of Heusler alloys, $Co_2(Fe_{1-x}Ti_x)Si$ ($0 \le x \le 1$) were fabricated, and their electronic states, crystal structure, and spin-dependent transport properties were systematically investigated. First-

principles calculations of DOS predicted that the minority-spin DOS forming CB edge of half-metallic gap is located near Fermi level in Co_2FeSi, which shifts toward higher energies with increasing x, suggesting the improvement of spin-polarization at room temperature by the substitution of Fe with Ti. The improvement of spin-polarization at RT were qualitatively confirmed by the sign change of AMR ratios of $Co_2(Fe_{1-x}Ti_x)Si$ with x=0 to x=0.1 and the suppression of the temperature dependence of $\Delta\rho$ with increasing x. We also evaluated the spin polarization of CFTS by measuring non-local spin signals of the NLSV devices with CFTS thin films wires. The one-dimensional model fitting of the spin signals suggested that the spin-polarization at room temperature increases from 0.61 for Co_2FeSi to 0.70 for $Co_2Fe_{0.8}Ti_{0.2}Si$. We also confirmed that the kinetic $L2_1$-ordering temperature decreases from 650 ºC for Co_2FeSi to 400 ºC for $x > 0.2$, which is promising feature for various spintronic applications that have a limitation for annealing temperature.

3) The use of a NiAl buffer layer for the integration of CPP-GMR devices on a Si(001) single crystalline substrate was realized. By undertaking a NiAl deposition on silicon at a temperature of 500°C, a smooth and epitaxial *B*2-NiAl layer with highly (001)-orientation was demonstrated, indicating that NiAl can act as a template for epitaxial CPP-GMR devices. The surface roughness of NiAl was further improved by depositing Ag on the NiAl layer and applying subsequent post-annealing process. The epitaxial CPP-GMR of CFGG/Ag/CFGG structure grown on the NiAl-buffered Si(001) substrate exhibited a high MR ratio of 27.8% and ΔRA of 8.6 $m\Omega\mu m^2$, which is comparable with those of the devices grown on an MgO(001) substrate. This work demonstrated the feasibility of growing epitaxial CPP-GMR on Si wafers, which can exhibit much higher MR output than polycrystalline devices that are deposited on amorphous buffered industrially standard chemical-mechanical-polished substrates. This gives a potential for developing industrially viable single crystalline CPP-GMR devices on Si wafer for allowing higher temperature annealing in combination with the wafer bonding technology.

4) Integration of epitaxial CPP-GMR device on top of a polycrystalline bottom electrode was realized for the first time by Three-Dimensional Integration Technology based on direct wafer bonding and backside silicon removal process. Bonding interface condition dependence on different capping materials for direct wafer bonding processing was systematically investigated. Among three bonded samples, Au-Au bonding shows the best bonding interface condition. The bonding interface looks perfect, free of damage and grain-boundary like. All layer structure remains uniform after bonding. In the case of Ta-Au bonding, layer structure seriously deteriorates in 2inch side because of mixing between Ag and Au layer. Damage can be always seen at the bonding interface of Ta side but not in Au side in both Au-Ta bonding and Ta-Au bonding. Similar MR output of Epi-CPP-GMR device is successfully reproduced after bonding process by using Au-Au bonding, which is a promising technology not only for utilizing epitaxial CPP-GMR device for ultrahigh-density hard disk drives (HDDs) read head sensor, but also for 3D stacking of epitaxial magnetic tunneling junction (MTJ) in ultrahigh-density MRAM.

This study shows great potential of future application of Heusler-alloy-based CPP-GMR device as read head sensor in ultra-high density hard disk drive. However, current research status in this field is still far from practical application level. Therefore, further development of new materials and new processing are required. From the study in chapter 3 of this thesis, we come to know that spacer material with good lattice and band matching with ferromagnetic layer material is essential to achieve high interfacial spin scattering asymmetry γ as indicated in Valet-Fert model. Recently, new spacer materials such as Ag-alloy[1,2] and semiconductor[3,4] have been reported, sending message that there is still a large room to improve MR output by new spacer material searching. Ag-Alloy, semiconductor material and nonmagnetic Heusler alloy are all promising direction for spacer materials investigation. For the ferromagnetic layer material, Heusler alloy is definitely a good candidate to obtain large bulk spin scattering asymmetry β, which is a key factor for MR output enhancement. In chapter 4, $Co_2(Fe_{1-x}Ti_x)Si$ Heusler that we have studied show impressive feature of low $L2_1$ ordering temperature down to 400 ºC, which is promising for practical application. But unfortunately, spin polarization of $Co_2(Fe_{1-x}Ti_x)Si$ is still lower than previous reported high spin-polarized Heusler alloy such as CFGG and CFMS. Better Heusler alloy needs to be developed. Actually, there are still a lot of unexplored materials hiding inside the Heusler alloy family. Up to now, only small amount of quaternary Heusler alloys have been systematically studied and there is little report about quinary Heusler alloy. Thus, more investigations in this filed could be promising for realizing higher MR output. From the practical point of view, epitaxial growth of CPP-GMR device on Si substrate described in chapter 5 enable us to develop industrially viable high performance single crystalline CPP-GMR devices without relying on unpractical expensive MgO substrate. It is also interesting to use NiAl buffer layer for developing epitaxial MTJs on Si substrate for next generation MRAMs application. Currently, annealing temperature in read head fabrication process is mainly limited by the thermal stability of soft magnetic shield layer (typically permalloy). Three dimension integration technology described in chapter 6 has provided us a new concept of processing to solve the problem of annealing temperature limit, so that more freedom of material selection can be obtained to achieve higher CPP-(G)MR output. Actually, this technology can also be extended to various spintronic application based on single crystalline devices.

Reference

[1] Y. Du, T. Furubayashi, T.T. Sasaki, Y. Sakuraba, Y.K. Takahashi, and K. Hono, Appl. Phys. Lett. **107**, 112405 (2015).
[2] T. Kubota, Y. Ina, M. Tsujikawa, S. Morikawa, H. Narisawa, Z. Wen, M. Shirai, and K. Takanashi, J. Phys. Appl. Phys. **50**, 014004 (2017).
[3] S. Kasai, Y.K. Takahashi, P.-H. Cheng, Ikhtiar, T. Ohkubo, K. Kondou, Y. Otani, S. Mitani, and K. Hono, Appl. Phys. Lett. **109**, 032409 (2016).
[4] T. Nakatani, G. Mihajlović, J.C. Read, Y. Choi, and J.R. Childress, Appl. Phys. Express **8**, 093003 (2015).

Acknowledgements

The work involved in this PhD thesis was accomplished at the Research Center for Magnetic and Spintronic Materials in National Institute for Materials Science in Tsukuba, supported by JSPS KAKENHI Grant Number JP17J01091. Therefore, I want to express my gratitude to the joint program of University of Tsukuba and National Institute for Materials Science for offering me the Graduate Research Assistantship that has been supporting my daily life for the first two and a half years, and I would also like to thank Japan Society for the Promotion of Science for providing me the DC2 scholarship for the rest of my Ph.D. study.

I am so lucky that I have the opportunity to live and study in Tsukuba. The past five years studying (Master & Ph.D.) here will become a wonderful memory for the rest of my life. And there are a lot of people I would like to thank.

The very first one would be my supervisor Prof. Kazuhiro Hono. I would like to express my sincerest gratitude to him, for his continuous guidance and encouragement in the last five years academic study (Master & Ph.D.). It is his instructions and patient teaching that make the research interesting and meaningful for me. His positive and rigorous attitude towards science and academy sets up a good example for me, and I have learnt not only how to do research, but also how to be a real researcher here.

I would like to give my deepest gratitude to Prof. Shinji Kuroda, Prof. Seiji Mitani, and Prof. Hideto Yanagihara, who are the committee members of my Ph.D. defence, for spending a lot of time examining my Ph.D. thesis and providing me helpful suggestions.

I would also like to give my deepest gratitude to Dr. Yuya Sakuraba and Dr. Takao Furubayashi, who had taken care of my research work since I came to NIMS. Thanks a lot for teaching me experimental skills and useful knowledge. Without your valuable guidance and discussion, I would not be able to fulfil my research.

I must also thank Dr. Yukiko Takahashi and Dr. Taisuke Sasaki who patiently gave me advice on my academic work and taught me experiment skill about the TEM observation.

I also have to express my appreciation to Dr. S. Li and Mr. Bunpei Masaoka, who constantly helped me with experiment on my study. Many thanks to Dr. Hiroaki Sukegawa, Dr. Shinya Kasai, Dr. Tomoya Nakatani and Dr. Zhenchao Wen for giving valuable suggestions on my study. Thanks other CMSM members for daily discussion.

Finally, I want to say thanks to all my families, especially to my dear wife, Wentian Ma. You are the only one who is always by my side to support me through this long process. It is your indispensable supports that help me overcome all the difficulties in the past five years. I cannot emphasize how important that you were to me.

There are just too many people I should thank and I know I am probably forgetting someone. So again, I just want to say thank you to everyone who helped me, supported me.

Appendix: Publication

1. **Jiamin Chen**, S. Li, T. Furubayashi, Y. K. Takahashi, and K. Hono
   "Crystal orientation dependence of current-perpendicular-to-plane giant magnetoresistance of pseudo spin-valves with epitaxial $Co_2Fe(Ge_{0.5}Ga_{0.5})$ Heusler alloy layers"
   Journal of Applied Physics. **115**, 233905 (2014).

2. **Jiamin Chen**, T. Furubayashi, Y. K. Takahashi, T.T. Sasaki and K. Hono
   "Crystal orientation dependence of band matching in all-B2-trilayer current-perpendicular-to-plane giant magnetoresistance pseudo spin-valves using $Co_2Fe(Ge_{0.5}Ga_{0.5})$ Heusler alloy and NiAl spacer"
   Journal of Applied Physics. **117**, 17C119 (2015)

3. **Jiamin Chen**, J. Liu, Y. Sakuraba, H. Sukegawa, S. Li and K. Hono
   "Realization of high quality epitaxial current-perpendicular-to-plane giant magnetoresistive pseudo spin-valves on Si(001) wafer using NiAl buffer layer"
   APL Materials. **4**, 056104 (2016)

4. **Jiamin Chen**, Y. Sakuraba, K. Masuda, Y. Miura, S. Li, S. Kasai, T. Furubayashi, K. Hono
   "Enhancement of $L2_1$ order and spin-polarization of Co_2FeSi thin film by substitution of Fe with Ti"
   Applied Physics Letters. **110**, 242401 (2017)

5. S. Li, Y. K. Takahashi, Y. Sakuraba, N. Tsuji, H. Tajiri, Y. Miura, **Jiamin Chen**, T. Furubayashi and K. Hono
   "Large enhancement of bulk spin polarization by suppressing Co_{Mn}-antisites effect in $Co_2Mn(Ge_{0.75}Ga_{0.25})$ Heusler alloy "
   Applied Physics Letters. **108**, 122404 (2016)

6. S. Li, Y. K. Takahashi, Y. Sakuraba, **Jiamin Chen**, T. Furubayashi, O. Mryasov, S. Faleev and K. Hono
   "Current-perpendicular-to-plane giant magnetoresistive properties in $Co_2Mn(Ge_{0.75}Ga_{0.25})/Cu_2TiAl/Co_2Mn(Ge_{0.75}Ga_{0.25})$ all-Heusler alloy pseudo spin valve"
   Journal of Applied Physics. **119**, 093911 (2016)

Appendix: International conference presentation

1. **Jiamin Chen**, Y. Sakuraba, K. Masuda, Y. Miura, S. Li, S. Kasai, T. Furubayashi and K. Hono
   "Enhancement of $L2_1$ ordering and spin-polarization of Co_2FeSi thin film by substitution of Fe with Ti"
   The 62nd Annual Conference on Magnetism and Magnetic Materials (MMM), November 6-November 10, 2017, Pittsburgh, USA
   Best Student Award Oral presentation: BE-02

2. **Jiamin Chen**, Y. Sakuraba, K. Yakushiji, H. Takagi, Y. Kurashima, N. Watanabe, K. Kikuchi, S. Yuasa and K. Hono
   "Effect of material selection on bonding interface for direct wafer bonding processing of epitaxial magnetoresistive devices"
   The 3rd ImPACT International Symposium, September 23th-25th, 2017, Sendai, Japan
   Poster presentation: 21

3. **Jiamin Chen**, J.Liu, Y. Sakuraba, H. Sukegawa, S. Li, and K. Hono
   "Realization of high quality epitaxial current-perpendicular-to-plane giant magnetoresistive pseudo spin-valves on Si(001) wafer using NiAl buffer layer"
   The 28th Magnetic Recording Conference (TMRC), August 3th, 2017, Tsukuba, Japan
   Poster presentation: BP-19

4. **Jiamin Chen**, Y. Sakuraba, J. Liu, K. Yakushiji, H. Takagi, N. Watanabe, A. Fukushima, K. Kikuchi, S. Yuasa, and K. Hono
   "Fabrication of Single Crystalline Magnetoresistive Sensors on Polycrystalline Electrode using Three-Dimensional Integration Technology"
   IEEE International Magnetics Conference (INTERMAG), April 27th, 2017, Dublin, Ireland
   Oral presentation: FE-03

5. **Jiamin Chen**, Y. Sakuraba, J. Liu, K. Yakushiji, H. Takagi, N. Watanabe, K. Kikuchi, S. Yuasa, and K. Hono
   "Fabrication of Single Crystalline Magnetoresistive Sensors on Polycrystalline Electrode using Three-Dimensional Integration Technology"
   The 2016 IEEE International Electron Devices Meeting (IEDM), December 6th, 2016, San Francisco, USA
   Poster presentation: MRAM poster session No.13

6. **Jiamin Chen**, J.Liu, Y. Sakuraba, H. Sukegawa, S. Li, and K. Hono
   "Realization of high quality epitaxial current-perpendicular-to-plane giant magnetoresistive pseudo spin-valves on Si(001) wafer using NiAl buffer layer"
   The 61st Annual Conference on Magnetism and Magnetic Materials (MMM), October 31-November 4, 2016, New Orleans, USA
   Oral presentation: GH-02

7. **Jiamin Chen**, J.Liu, Y. Sakuraba, H. Sukegawa, S. Li, and K. Hono
   "Realization of high quality epitaxial current-perpendicular-to-plane giant magnetoresistive pseudo spin-valves on Si(001) wafer using NiAl buffer layer"
   The 2nd ImPACT International Symposium, September 30th, 2016, Tsukuba, Japan
   Poster presentation: 21

8. **Jiamin Chen**, T. Furubayashi, Y. K. Takahashi, T.T. Sasaki and K. Hono
   "*Crystal orientation dependence of band matching in all-B2-trilayer current-perpendicular-to-plane giant magnetoresistance pseudo spin-valves using $Co_2Fe(Ge_{0.5}Ga_{0.5})$ Heusler alloy and NiAl spacer*"
   The 59th Annual Conference on Magnetism and Magnetic Materials (MMM), November 3-7, 2014, Honolulu, Hawaii, USA
   Oral presentation: CC-02

9. **Jiamin Chen**, S. Li, T. Furubayashi, Y. K. Takahashi, and K. Hono
"*Structural and magneto-transport properties of CPP-GMR pseudo spin-valves with (110) epitaxial layers of $Co_2Fe(Ge_{0.5}Ga_{0.5})$ Heusler alloy*"
The 58th Annual Conference on Magnetism and Magnetic Materials (MMM), November 4-8, 2013, Denver, Colorado, USA
Oral presentation: HC-13

Appendix: Domestic conference presentation

1. **Jiamin Chen**, Y. Sakuraba, K. Masuda, Y. Miura, S. Li, S. Kasai, T. Furubayashi and K. Hono
"Enhancement of $L2_1$ ordering and spin-polarization of Co_2FeSi thin film by substitution of Fe with Ti"
The 161st Fall Annual Meeting of the Japan Institute of Metals and Materials (JIM), September 8th, 2017, Hokkaido University, Japan
Oral presentation: S6・22

2. **Jiamin Chen**, Y. Sakuraba, J. Liu, K. Yakushiji, H. Takagi, N. Watanabe, A. Fukushima, K. Kikuchi, S. Yuasa, and K. Hono
"Fabrication of Single Crystalline Magnetoresistive Sensors on Polycrystalline Electrode using Three-Dimensional Integration Technology"
The 64th Japan Society of Applied Physics (JSAP) Spring Meeting, March 14th, 2017, Yokohama, Japan
Oral presentation: 14a-501-10

3. **Jiamin Chen**, Y. Sakuraba, Y. Miura, S. Li, T. Furubayashi, and K. Hono
"Enhancement of $L2_1$ ordering and spin-polarization of Co_2FeSi thin film by substitution of Fe with Ti"
2016 Tsukuba Global Science Week (TGSW), September 17th, 2016, Tsukuba, Japan
Poster presentation: P19

4. **Jiamin Chen**, J.Liu, Y. Sakuraba, H. Sukegawa, S. Li, and K. Hono
"Realization of high quality epitaxial current-perpendicular-to-plane giant magnetoresistive pseudo spin-valves on Si(001) wafer using NiAl buffer layer"
The 77th Japan Society of Applied Physics (JSAP) Autumn Meeting, September 15th, 2016, Niigata, Japan
Oral presentation: 15a-C41-2

5. **Jiamin Chen**, J.Liu, Y. Sakuraba, H. Sukegawa, S. Li, and K. Hono
"Realization of high quality epitaxial current-perpendicular-to-plane giant magnetoresistive pseudo spin-valves on Si(001) wafer using NiAl buffer layer"
The 40th Annual Conference on MAGNETICS in Japan (MSJ), September 6th, 2016, Kanazawa University, Japan
Oral presentation: 06aA-6

6. **Jiamin Chen**, Y. Sakuraba, Y. Miura, T. Furubayashi, and K. Hono
"Enhancement of $L2_1$ ordering and spin-polarization of Co_2FeSi thin film by substitution of Fe with Ti"
The 63rd Japan Society of Applied Physics (JSAP) Spring Meeting, March 19th, 2016, Ookayama Campus, Tokyo Inst. of Tech., Japan
Poster presentation: 19p-P1-16

7. **Jiamin Chen**, Y. Sakuraba, Y. Miura, T. Furubayashi, Y. K. Takahashi, and K. Hono
"Enhancement of $L2_1$ ordering and spin-polarization of Co_2FeSi thin film by substitution of Fe with Ti"
The 157th Fall Annual Meeting of the Japan Institute of Metals and Materials (JIM), September 16th, 2015, Ito Campus, Kyushu University, Japan
Oral presentation: S4・25

8. **Jiamin Chen**, T. Furubayashi, Y. K. Takahashi, T.T. Sasaki and K. Hono
"*Crystal orientation dependence of band matching in all-B2-trilayer current-perpendicular-to-plane giant magnetoresistance pseudo spin-valves using $Co_2Fe(Ge_{0.5}Ga_{0.5})$ Heusler alloy and NiAl spacer*"
The 62nd Japan Society of Applied Physics (JSAP) Spring Meeting, March 11th, 2015, Shonan Campus, Tokai University, Japan
Oral presentation: 9p-P1-16

9. **Jiamin Chen**, T. Furubayashi, Y. K. Takahashi, T.T. Sasaki and K. Hono
"*Crystal orientation dependence of band matching in all-B2-trilayer current-perpendicular-to-plane*

giant magnetoresistance pseudo spin-valves using $Co_2Fe(Ge_{0.5}Ga_{0.5})$ Heusler alloy and NiAl spacer"
The 38th Annual Conference on MAGNETICS in Japan (MSJ), September 4th, 2014, Hiyoshi Campus, Keio University, Japan
Oral presentation: 4pD-3

10. **Jiamin Chen**, S. Li, T. Furubayashi, Y. K. Takahashi, and K. Hono
"*Structural and magneto-transport properties of CPP-GMR pseudo spin-valves with (110) epitaxial layers of $Co_2Fe(Ge_{0.5}Ga_{0.5})$ Heusler alloy*"
The 61st Japan Society of Applied Physics (JSAP) Spring Meeting, March 20th, 2014, Sagamihara Campus, Aoyama Gakuin University, Japan
Oral presentation: 20a-E7-6

11. **Jiamin Chen**, S. Li, T. Furubayashi, Y. K. Takahashi, and K. Hono
"*Structural and magneto-transport properties of CPP-GMR pseudo spin-valves with (110) epitaxial layers of $Co_2Fe(Ge_{0.5}Ga_{0.5})$ Heusler alloy*"
The 37th Annual Conference on MAGNETICS in Japan (MSJ), September 3rd, 2013, Sapporo, Hokkaido, Japan
Oral presentation: 3pC-3